

# MRI and NMR Investigations of Transport in Soft Materials and Explorations of Electron- Nuclear Interactions for Liquid-State Dynamic Nuclear Polarization

**Xiaoling Wang**

Dissertation submitted to the faculty of Virginia Polytechnic Institute and  
State University in partial fulfillment of the requirements for the degree of

Doctor of Philosophy  
In  
Chemistry

Louis A. Madsen  
Harry C. Dorn  
Harry W. Gibson  
T. Daniel Crawford

June 8, 2015  
Blacksburg, Virginia

Keywords: time-resolved microMRI, diffusion, nanoparticles, collagen,  
polyplex, gene delivery, free polymer quantification, pulsed-field-gradient  
NMR, molecular weight, polyelectrolytes, liquid-state dynamic nuclear  
polarization, Overhauser effect, supercritical fluid CO<sub>2</sub>, hyperfine coupling,  
density functional theory

# MRI and NMR Investigations of Transport in Soft Materials and Explorations of Electron-Nuclear Interactions for Liquid-State Dynamic Nuclear Polarization

Xiaoling Wang

## ABSTRACT

The first part of this dissertation (Chapters 1 to 4) describes the use of magnetic resonance techniques for polymeric material characterizations in solutions, with emphasis on methods utilizing magnetic field gradients – magnetic resonance imaging (MRI) and pulsed-field-gradient (PFG) NMR. The second part (Chapter 5) presents enhancements to dynamic nuclear polarization, an intensity enhancement approach for magnetic resonance techniques.

In Chapter 2, I illustrate a characterization method to quantify free polymer chain content in a polymer/DNA complex (polyplex) formulation via one-dimensional proton NMR experiments. This assessment of free polymer quantity has critical impacts on *in vivo* gene transfection efficiency, cellular uptake, as well as toxicity of polycationic gene delivery vectors. Specifically, I investigated the complexation properties of three different polymeric “theranostic” agents, which combine an imaging functionality on the polymer as well as a DNA/RNA complexation component. These agents are under development to allow real time clinical monitoring of drug delivery and efficacy using MRI. Our NMR method provides simple and quantitative assessment of free and DNA-complexed polymers, including the actual polymer amine to DNA phosphate molar ratio (N/P ratio) within polyplexes. The NMR results are in close agreement with the stoichiometric number of polymer/DNA binding obtained by isothermal titration

calorimetry. The noninvasive nature of this method allows broad application to a range of polyelectrolyte coacervates, for understanding and optimizing polyelectrolyte complex formation.

Chapter 3 demonstrates a time-resolved MRI approach for measuring diffusion of drug-delivery polymeric nanoparticles on mm to cm scales as well as monitoring nanoparticle concentration distribution in bulk biological hydrogels. Our results show that as the particle size and surface charge become larger, collagen gel at tumor relevant concentration (1.0 wt.%) presents a more significant impediment to the diffusive transport of negatively charged nanoparticles. These results agree well with those obtained by fluorescence spectroscopies (neutral or slightly positively charged diffusing particles) as well as the proposed electrostatic bandpass theory of tumor interstitium (negatively charged particles). This study provides fundamental information for the design of polymeric theranostic vectors and carries implications that would benefit the understanding of nanoparticle transport in solid tumors. Furthermore, this work takes a significant step toward developing quantitative and real time *in vivo* monitoring of clinical drug delivery using MRI.

Chapter 4 addresses the application of PFG-NMR for the determination of weight-average molar mass ( $M_w$ ) for polyanions that have anti-HIV activity through the measurement of polymer diffusion coefficients in solutions. The effective characterization of molecular weights of polyelectrolytes has been a general and growing problem for the polymer industry, with no clear solutions in sight. In this study, we obtained the molar masses ( $M_w$ ) for two series of sulfonated copolymers using sodium polystyrene sulfonate samples as molecular weight standards. PFG-NMR has notable

advantages over conventional techniques for the characterization of charged polymers and shows great promise for becoming an effective alternative to chromatography methods.

Chapter 5 is devoted to experimental and theoretical studies of liquid state dynamic nuclear polarization (DNP) via the Overhauser effect. Based on the adventurous work done by previous Dorn group members, we show that for  $^1\text{H}$ -nuclide-containing systems, the dipolar DNP enhancement can be significantly improved by decreasing the correlation time ( $\tau_c$ ) of the interaction by utilizing a supercritical fluid (SF  $\text{CO}_2$ ) which allows for greater dipolar enhancements at higher magnetic fields. For molecules containing the ubiquitous  $^{13}\text{C}$  nuclide, we show that previously unreported sp hybridized (H-C) alkyne systems represented by the phenylacetylene-nitroxide system exhibit very large scalar-dominated enhancements. Furthermore, we show for a wide range of molecular systems that the Fermi contact interaction can be computationally predicted via electron-nuclear hyperfine coupling and correlated with experimental  $^{13}\text{C}$  DNP enhancements. For biomedical applications, the enhancement of metabolites in SF  $\text{CO}_2$  followed by rapid dissolution in water or biological fluids is an attractive approach for future hyperpolarized NMR and MRI applications. Moreover, with the aid of density functional theory calculations, solution state DNP provides a unique approach for studying intermolecular weak bonding interaction of solutes in normal liquids and SF fluids.

## **Acknowledgement**

I began my graduate study in Dr. Harry Dorn's research group in the summer of 2009 and started working in Dr. Louis Madsen's lab in early 2012. I appreciate my PhD research advisor Dr. Madsen for the patience, encouragement, trainings and advice I received from him. I appreciate Dr. Dorn for his inspiration, support, and guidance when we worked together in the unknown area of research. I sincerely respect Dr. Madsen and Dr. Dorn for their generosity and dedication to science and education, which will guide me through my career in the future.

I also would like to give my earnest appreciation to my advisory committee – Dr. Harry Gibson, Dr. Daniel Crawford, and Dr. Chenming Zhang from Biological Systems Engineering. Dr. Gibson and Dr. Crawford have been my inspiration due to their academic dedication and modesty since I joined Chemistry Department. The recognition and encouragement given by Dr. Gibson and Dr. Crawford on my graduate research and examinations have truly helped me build confidence in conducting science along the way, especially during my difficult times. Dr. Chenming Zhang offered me his warm welcome and honest advice on graduate study when I arrived at Virginia Tech, and it is unfortunate that I could not keep him on my committee after 2011.

None of my work could have been done without the support and help from research collaborators at Virginia Tech and outside the University. I want to give my thanks to Dr. Theresa Reineke, Dr. Judy Riffle, Dr. Richard Turner, Dr. Richard Gandour, Dr. Sneha Kelkar, Dr. Nipon Pothyaee, Dr. Alice Savage, Dr. Lian Xue, Rui Zhang, and Amanda Hudson. I also want to give special thanks to William Isley III and Dr. Christopher Cramer, my collaborators at University of Minnesota.

I feel deeply grateful for the friendship and support from the Madsen group, the Dorn group, the NMR facility and the Department. I want to thank Ying Chen, Ying Wang, Dr. Zhiyang Zhang, Dr. Kyle Wilmsmeyer, Dr. Mark Lingwood, Dr. Mithun Goswami, Dr. Jianyuan Zhang, Dr. Liaosa Xu, Dr. James Duchamp, Dr. Yaoying Wu and Shuang Fan for their kind help and encouragements. I also sincerely thank Dr. Hugo Azurmendi, Geno Iannaccone, Ken Knott and Dr. Narasimhamurthy Shanaiah for their consistent assistance and advice. The company of those and many other people I met in graduate school has become one of the best parts of my experience.

Last but not least, I sincerely appreciate my family in China for their love over the years. I want to give my deepest thanks to my mother. Without her trust and support, I could never have had the opportunity to study in college or graduate school, or to learn any of the things I have learned here.

# **Applications of MRI and NMR for Transport Investigations in Soft Materials and Explorations of Electron-Nuclear Interactions for Liquid State Dynamic Nuclear Polarization**

## **Chapter 1: Introduction to Magnetic Resonance Imaging and Pulsed-Field-Gradient NMR for Multi-Scale Studies of Polymeric Systems**

1.1 Chapter Overview	1
Part I Basic Concepts in NMR and MRI	2
1.2 Brief Introduction to Nuclear Magnetic Resonance	2
1.3 Principles of Magnetic Resonance Imaging	6
1.3.1 Two Basic Aspects of Magnetic Resonance	6
1.3.2 Fourier Transform	9
1.3.3 <b>K</b> -Space	12
1.3.4 Slice Selection and Spatial Encoding	13
1.3.5 Data Matrices	23
Part II MRI Contrast and Practical Aspects of Contrast Agents	25
1.4 Image Contrast	25
1.5 Two MRI Pulse Sequences Utilized in Diffusion Study	33
1.6 General Aspects of MRI Contrast Agents	40
1.7 Brief Introduction to Polymeric Theranostic Nanoparticles	44
1.8 Overview of Transport of Nanoparticles in Solid Tumors	52
Part III PFG-NMR and Polymer Molecular Weight Determination	56
1.9 Introduction to Pulsed-Field-Gradient NMR	56
1.10 Overview of Translational Diffusion in Liquids	59
1.11 Brief Introduction to Molecular Weight Measurement of Polymer	63
1.12 References	68

## **Chapter 2: Quantitation of Complexed versus Free Polymers in Interpolyelectrolyte Polyplex Formulations**

2.1 Chapter Overview	74
2.2 Background	76
2.3 Experimental Section	80
2.4 Results and Discussion	82
2.5 Conclusion	86
2.6 References	87
2.7 Supplementary Information	89

### **Chapter 3: Diffusion Studies of Nanoparticles into Biogels by Time-Resolved MicroMRI**

3.1 Chapter Overview	99
3.2 Background	101
3.3 Experimental Section	102
3.4 Results and Discussion	106
3.5 Conclusion	113
3.6 References	114
3.7 Supplementary Information	117

### **Chapter 4: Molecular Weight Determination of Sulfonated Polyanions by Pulsed-Field-Gradient NMR**

4.1 Chapter Overview	123
4.2 Background	123
4.3 Experimental Section	126
4.4 Results and Discussion	129
4.5 Conclusion	131
4.6 References	132

### **Chapter 5: Optimization and Prediction of Molecular Interactions in $^1\text{H}$ and $^{13}\text{C}$ Liquid State Dynamic Nuclear Polarization**

5.1 Chapter Overview	134
5.2 Introduction	136
5.3 Experimental Section	143
5.4 Results and Discussion	147
5.5 Conclusion	169
5.6 References	172

### **Appendices**

1. Properties of Polyelectrolyte Solutions	178
2. Supporting Information for Chapter 5	186



## List of Figures

### Chapter 1: Introduction to Magnetic Resonance Imaging and Pulsed-Field-Gradient NMR for Multi-Scale Studies of Polymeric Systems

Figure 1-1. Windows of transparency for imaging techniques.	7
Figure 1-2. Representation of Imaging process.	9
Figure 1-3. Illustration of convolution effect.	11
Figure 1-4. Relationship between bandwidth, gradient strength, and slice thickness, and simplified slice selection process.	15
Figure 1-5. A symbolic representation of hard pulse.	16
Figure 1-6. A symmetric SINC pulse and the frequency profile after Fourier transform.	17
Figure 1-7. Pulse shapes of Gaussian function and hyperbolic secant.	18
Figure 1-8. Simple spin-echo pulse sequence with slice-selective and frequency encoding gradients.	19
Figure 1-9. Effect of a magnetic gradient on the phase evolution of nuclear spin magnetizations.	23
Figure 1-10. Symbolic representation of inversion-recovery pulse sequence and its working mechanism.	27
Figure 1-11. NMR spectral peak amplitude in the inversion-recovery experiment.	28
Figure 1-12. Symbolic representation of spin echo pulse sequence and its working mechanism.	30

Figure 1-13. NMR spectral peak amplitude in the spin echo experiment as a function of time $\tau$ .	31
Figure 1-14. An example of RARE rf pulse sequence.	35
Figure 1-15. Symbolic representation of a 2D RARE sequence.	37
Figure 1-16. Symbolic representation of inversion-recovery pulse sequence and the working mechanism of <i>null</i> .	39
Figure 1-17. Illustration of <i>null</i> time differences between water and fat signals.	40
Figure 1-18. Structures of polymers of G4 and N <sub>4</sub> La.	46
Figure 1-19. Schematic presentation of polyplex formation and transmission election micrograph of polyplexes.	47
Figure 1-20. Intracellular barriers to gene delivery by polyplexes.	48
Figure 1-21. Symbolic representation of proton-sponge hypothesis.	50
Figure 1-22. Structure and synthesis of MBICs.	51
Figure 1-23. Schematic representation of transport steps in a tumor tissue unit.	53
Figure 1-24. A symbolic illustration of measuring diffusion using the Stejskal and Tanner sequence.	58
<b>Chapter 2: Quantitation of Complexed versus Free Polymers in Interpolyelectrolyte Polyplex Formulations</b>	
Figure 2-1. Polyplex formation and <sup>1</sup> H NMR spectra of PEI/DNA polyplexes.	79
Figure 2-2. Structures and <sup>1</sup> H NMR spectra of polyplexes of G4 and N <sub>4</sub> La in H <sub>2</sub> O.	82
Figure 2-3. Percentage of unbound polymer in polymer and polyplex solutions.	85
Figure 2-S1: Suppressed water signal simulated using asymmetric Gaussian and Lorentzian functions.	92

Figure 2-S2: ITC thermogram and binding isotherm of 172 $\mu\text{g}/\text{mL}$ PEI titrated into 132 $\mu\text{g}/\text{mL}$ pDNA in 10 mM Tris buffer pH 7.4 at 37 $^{\circ}\text{C}$ .	94
Figure 2-S3: Overlay of light scattering, refractive index and QELS traces for PEI and $\text{N}_4\text{La}$ polymers.	95
Figure 2-S4: The hydrodynamic diameters of G4 polymer (red curve) and its complexes with pDNA.	96
Figure 2-S5: The size distribution of PEI polymer and its polyplexes in buffer.	97
Figure 2-S6: The particle size measurements using DLS for $\text{N}_4$ polymer and its polyplexes in pure water.	97
Figure 2-S7. Gel electrophoresis shift assay by mixing pDNA with $\text{N}_4\text{La}$ and PEI	98
<b>Chapter 3: Diffusion of Drug Delivery Nanoparticles into Biogels using Time-Resolved MicroMRI</b>	
Figure 3-1. Structure of $\text{N}_4\text{Gd}$ and MBIC, and their DLS size distribution.	103
Figure 3-2. Sample setup for MRI measurements and model for one-dimensional diffusion, and time-resolved $T_2$ -weighted and $T_1$ -null-weighted images.	105
Figure 3-3. $\text{N}_4\text{Gd}$ ingress into gels measured at progressive time points.	107
Figure 3-4. Plots of $T_1$ -null-weighted data of $\text{N}_4\text{Gd}$ diffusing into 0.5 wt.% agarose gel measured at different time points.	108
Figure 3-5. Representation of diffusion-driven transport of $\text{N}_4\text{Gd}$ nanoparticles into 0.5 wt.% agarose gel and MBICs into 1.0 wt.% collagen gel.	113
Figure 3-S1. Fitting of experimental data of MBICs into 0.5 wt.% agarose gel.	122
Figure 3-S2. Fitting of experimental data of MBICs into 0.2 wt.% collagen gel.	122

Figure 3-S3. Fitting of experimental data of MBICs into 1.0 wt.% collagen gel. 123

#### **Chapter 4: Molecular Weight Determination of Sulfonated Polyanion by Pulsed-Field-Gradient NMR**

Figure 4-1. The structures of the alternating copolymers and block copolymers NaSS-*alt*-SPMI, and (NaSS-*alt*-SPMI)-*b*-PEG. 125

Figure 4-2. Proton spectra of NaSS-*alt*-SPMI and (NaSS-*alt*-SPMI)-*b*-PEG polymers; Plot of normalized signal attenuation against the field gradient parameters 128

Figure 4-3. Calibration plot of the diffusion coefficients of four PSS standards measured by PFG-NMR. 129

#### **Chapter 5: Optimization and Prediction of the Electron-Nuclear Dipolar and Scalar Interaction in $^1\text{H}$ and $^{13}\text{C}$ Liquid State Dynamic Nuclear Polarization**

Figure 5-1. Schematic diagram of energy level and transition probabilities for electron-nuclear ( $^{13}\text{C}$ ) spin systems for benzene/TEMPO and phenylacetylene/TEMPO. 140

Figure 5-2. Coupling factor of the Overhauser effect enhancement dependence on the electron Larmor frequency for rotational motion with correlation time. 140

Figure 5-3. Immobilized nitroxide material I and II used in SLIT  $^1\text{H}$  DNP in normal liquids and SF  $\text{CO}_2$ . 144

Figure 5-4. Schematic drawing of apparatus for continuous-flow HPLC-DNP-NMR coupled with SF  $\text{CO}_2$ . 145

Figure 5-5.  $^1\text{H}$  spectra of benzene/TEMPO dissolved in SF  $\text{CO}_2$  at 4.7 T. 150

Figure 5-6. Coupling factor derived from  $^{13}\text{C}$  LLIT DNP absolute enhancements of toluene, diphenylmethane, and triphenylmethane ( $\text{Ph}_Y\text{CH}_X$ , X=1-3, Y=4-X). 155

Figure 5-7. Coupling factor derived from scalar and dipolar dominant $^{13}\text{C}$ LLIT DNP absolute enhancements of small molecules.	156
Figure 5-8. The electronic spin density distribution of the largest $^{13}\text{C}$ -H HFC contributing orientation between benzene and TEMPO.	159
Figure 5-9. The electronic spin density distribution of the second largest $^{13}\text{C}$ -H HFC contributing orientation between benzene and TEMPO.	159
Figure 5-10. The electronic spin density distribution for the lowest energy orientation between nitrobenzene and TEMPO.	161
Figure 5-11. $^{13}\text{C}$ spectra of benzaldehyde/TEMPO in cyclohexane at 4.7 T.	162
Figure 5-12. The electronic spin density distribution for the largest $^{13}\text{CHO}$ - and $^{13}\text{C}$ - <i>ortho</i> HFC contributing orientation between benzaldehyde and TEMPO.	163
Figure 5-13. $^{13}\text{C}$ spectra of phenylacetylene/TEMPO at 4.7 T.	166
Figure 5-14. The electronic spin density distribution of the largest $^{13}\text{C}$ - $\beta$ HFC contributing orientation between phenylacetylene and TEMPO.	167
Figure 5-15. Correlation between experimentally determined $^{13}\text{C}$ LLIT DNP scalar dominated enhancements and their calculated AFC for the phenylacetylene/TEMPO, benzaldehyde/TEMPO, and nitrobenzene/TEMPO systems.	169
<b>Appendix 2: Supporting Information for Chapter 5</b>	
Figure 5-S1. Apparatus of continuous-flow HPLC-DNP-NMR with SF $\text{CO}_2$ .	191
Figure 5-S2 and 5-S3. LLIT $^1\text{H}$ DNP saturation plots of benzene/TEMPO system in SF $\text{CO}_2$ and normal solvents.	194
Figure 5-S4 to 5-S7. Considered lowest-energy molecular configurations of benzene/TEMPO system.	195, 196

Figure 5-S8 to 5-S12. Considered lowest-energy molecular configurations of phenyl acetylene/TEMPO system.	197-199
Figure 5-S13 to 5-S18. Considered lowest-energy molecular configurations of benzaldehyde/TEMPO system.	200, 201
Figure 5-S19 to 5-S23. Considered lowest-energy molecular configurations of nitrobenzene/TEMPO system.	202, 203
Figure 5-S24. LLIT <sup>13</sup> C spectra of nitrobenzene/TEMPO system.	204

## List of Tables

Table 1-1. Common characterization methods of polymer molar mass.	65
Table 2-1. Hydrodynamic diameter of polyplexes by DLS size measurement.	81
Table 3-S1. Diffusion coefficients and distribution of N <sub>4</sub> Gd into agarose and collagen gels.	121
Table 3-S2. Diffusion coefficients measured by <i>T<sub>2</sub>-weighted</i> imaging <i>T<sub>1</sub>-null weighted</i> imaging of N <sub>4</sub> Gd in 0.5 wt.% agarose gel.	121
Table 4-1. Molar mass and antiviral activity of sulfonated polyanions.	130
Table 5-1. LLIT <sup>1</sup> H DNP enhancements polarized at 0.33 T for benzene/TEMPO in C <sub>6</sub> D <sub>6</sub> and SF CO <sub>2</sub> .	150
Table 5-2. SLIT <sup>1</sup> H DNP enhancements polarized at 0.33 T for benzene/Nitroxide in C <sub>6</sub> D <sub>6</sub> and SF CO <sub>2</sub> .	152
Table 5-3. LLIT <sup>13</sup> C DNP enhancements polarized at 0.33 T for nitrobenzene/cyclohexane/0.1 M TEMPO <sup>33</sup> and <i>a<sub>FC</sub></i> via DFT modeling.	160
Table 5-4. LLIT <sup>13</sup> C DNP enhancements polarized at 0.33 T for benzaldehyde/cyclohexane/0.1 M TEMPO <sup>34</sup> and <i>a<sub>FC</sub></i> via DFT modeling.	162
Table 5-5. LLIT <sup>13</sup> C DNP enhancements polarized at 0.33 T for phenylacetylene/0.001 M and 0.14 M TEMPO <sup>19</sup> and <i>a<sub>FC</sub></i> via DFT modeling	165
Table 5-6. LLIT <sup>13</sup> C DNP enhancements polarized at 0.33 T for substrate/TEMPO systems and acid dissociation constants (p <i>K<sub>a</sub></i> ) at 25 °C of <sup>13</sup> C-H protons.	168
Table 5-S1. Electron saturation factor <i>s</i> of benzene/TEMPO system in SF CO <sub>2</sub> and C <sub>6</sub> D <sub>6</sub> .	193

Table 5-S2. LLIT $^{13}\text{C}$ DNP enhancements for benzene/ $\text{C}_6\text{D}_6$ /0.16 M TEMPO and $a_{FC}$ via DFT modeling.	195
Table 5-S3. LLIT $^{13}\text{C}$ DNP enhancements for phenylacetylene/0.001 M TEMPO and $a_{FC}$ via DFT modeling.	197
Table 5-S4. LLIT $^{13}\text{C}$ DNP enhancements for benzaldehyde/cyclohexane/0.1 M TEMPO and $a_{FC}$ via DFT modeling.	199
Table 5-S5. LLIT $^{13}\text{C}$ DNP enhancements for nitrobenzene/cyclohexane/0.1 M TEMPO and $a_{FC}$ via DFT modeling.	202
Table 5-S6 to 5-S13. LLIT $^{13}\text{C}$ DNP enhancements of benzonitrile, phenylamine, anisole, toluene, diethyl malonate, ethyl acetoacetate, acetone, and acetonitrile with TEMPO.	204-207



# **Chapter 1: Introduction to Magnetic Resonance Imaging and Pulsed-Field-Gradient NMR for Multi-Scale Studies of Polymeric Systems**

## **1.1 Chapter Overview**

Part I of this chapter covers fundamental concepts and aspects of nuclear magnetic resonance (NMR) and magnetic resonance imaging (MRI) corresponding to their applications in Chapter 2 to Chapter 4, with an emphasis on the use of magnetic field gradients. In section 1.3, basic principles of MRI are introduced from the source of magnetic resonance signal to data processing and image reconstruction. Furthermore, in Part II, I first describe the origin of image contrast including nuclear spin relaxation, following by illustrations of MRI pulse sequences that are actually applied for the study of nanoparticle diffusion in Chapter 3, in order to set the background for the MRI experiments carried out in the same Chapter. Also as background for Chapter 3, general knowledge of MRI contrast agents is introduced from the materials point of view using an example of gadolinium-based small molecule contrast agents, including description of their working mechanism. The specific materials that have been investigated in Chapter 2 and 3 – polymeric nanoparticles functionalized as theranostic (combined therapeutic and diagnostic) agents are also described in Part II. This includes a short review on the transport of such agents in solid tumor tissue, presented as motivation for investigating the complexation and transport properties of those agents. Part III of this chapter is focused on the principles of pulsed-field-gradient (PFG) NMR diffusometry and its application in molecular weight measurements of polymers in solution. This

technique shows its beneficial implementation in the determination of polyelectrolyte molar masses (presented in Chapter 4), which can be an effective alternative to conventional chromatographic characterization methods.

This introductory chapter includes content from the basic concepts of magnetic resonance focused on two distinct applications (MRI and PFG-NMR). Note that Chapter 5 presents a study on dynamic nuclear polarization (DNP) – an effective and well-recognized hyperpolarization method for signal enhancement in NMR and MRI. The introduction of DNP is not covered in Chapter 1, but is instead incorporated into the beginning of Chapter 5 to keep those concepts in close proximity.

## **Part I. Basic Concepts in NMR and MRI**

### **1.2 Brief Introduction to Nuclear Magnetic Resonance**

This section introduces where the magnetic resonance (MR) signal originates in simplified systems. The foundation on which the MR signal can be manipulated using radio frequency pulses and magnetic field gradients is also summarized. Section 1.2 provides enough information for understanding the principles involved in section 1.3, which are later employed for applications in subsequent chapters.

Nuclear magnetic resonance (NMR) in condensed-phase samples was simultaneously discovered by Purcell, Torrey, and Pound(1) at Harvard and Block, Hansen, and Packard(2) at Stanford in 1946. Nuclear spin is intrinsic angular momentum possessed by atomic nuclei. The spin  $I$  is quantized in integral or half-integral units, which depends on whether the atomic number is even (integral) or

odd (half-integral). For nuclei of  $I \geq \frac{1}{2}$ , the spin will possess an intrinsic magnetic dipole moment, and in an external magnetic field ( $B_0$ ) will experience a precession about the magnetic field axis. The precessional motion is caused by the magnetic field torque applied to the spin angular momentum. The rate of precession is proportional to the strength of the magnetic field, and is known as the Larmor frequency  $\omega_0$  expressed by Equation 1-1,

$$\omega_0 = -\gamma B_0 \quad (1 - 1)$$

where  $\omega_0$  is in  $\text{rad s}^{-1}$ ,  $B_0$  is in Tesla, and  $\gamma$  is the gyromagnetic ratio in  $\text{rad s}^{-1}\text{T}^{-1}$ .

Quantum mechanically, for a nuclear spin in a magnetic field of strength  $B_0$  applied along the z-axis, the Hamiltonian representing the energy of interaction between the spin and the magnetic field is shown by Equation 1-2,(3)

$$\hat{H}_{one\ spin} = -\gamma B_0 \hat{I}_z \quad (1 - 2)$$

where  $\hat{I}_z$  represents the z-component of *nuclear spin angular momentum*. For a single spin-half nucleus, the spin is in a superposition state. This can be explained by the fact that the wavefunction of a single spin can be described as a linear combination of the eigenfunctions of the Hamiltonian of the spin. The eigenfunction of spin operator  $\hat{I}_z$  with eigenvalue  $+\frac{1}{2}$  is commonly denoted as  $\alpha$ , and the state with eigenvalue  $-\frac{1}{2}$  as  $\beta$ .  $c_\alpha$  and  $c_\beta$  are the coefficients for the states  $\alpha$  and  $\beta$  in the superposition wavefunction. Thus the average z-component of nuclear spin angular momentum, equivalent to the expectation value of  $\hat{I}_z$ , is presented by  $\frac{1}{2} c_\alpha^* c_\alpha - \frac{1}{2} c_\beta^* c_\beta$ , where  $c_\alpha^* c_\alpha$  is the probability of obtaining  $+\frac{1}{2}$ , and  $c_\beta^* c_\beta$  is the probability of obtaining  $-\frac{1}{2}$ .

For an ensemble of  $N$  spins, the total z-magnetization is the sum of the z-component of each spin multiplied by  $\gamma$  as in Equation 1-3.(3)

$$M_z = \frac{1}{2} \gamma N \overline{(c_\alpha^* c_\alpha - c_\beta^* c_\beta)} \quad (1 - 3)$$

The quantity  $\overline{c_\alpha^* c_\alpha - c_\beta^* c_\beta} = \frac{1}{N} (n_\alpha - n_\beta)$ , also known as the spin polarization, is computed from  $n_\alpha$  and  $n_\beta$ , the populations of the levels  $\alpha$  and  $\beta$ , respectively. These populations are predicted by the *Boltzmann distribution* at equilibrium shown by Equation 1-4(3),

$$n_{\alpha/\beta,eq} = \frac{1}{2} N \exp(-E_{\alpha/\beta}/k_B T) \quad (1 - 4)$$

where  $E_\alpha$  and  $E_\beta$  are energies of level  $\alpha$  and  $\beta$ . Hence at equilibrium, the z-magnetization  $M_0$  is proportional to the population difference between the two energy levels and can be acquired using the Boltzmann distribution:

$$M_0 = \frac{1}{2} \gamma N [\exp(-E_\alpha/k_B T) - \exp(-E_\beta/k_B T)] \quad (1 - 5)$$

The NMR and MRI experiments described in Chapters 2 through 4 are entirely based on manipulations of the equilibrium net magnetization  $M_0$ .

The energy of the allowed transition between  $\alpha$  and  $\beta$  states is proportional to the Larmor frequency and can be written in frequency units as  $\omega_0$  defined by Equation 1-1. Hence by application of a radio-frequency magnetic field at  $\omega_0$ , nuclear spin transitions can be excited and  $M_0$  can be changed from its equilibrium state. There is a net absorption of energy by the spin ensemble, as a result of the Boltzmann prediction  $n_\alpha > n_\beta$  at equilibrium. The radio-frequency magnetic field is commonly applied as a pulse of radio-frequency (rf) energy. Absorption of the rf

energy at frequency  $\omega_0$  causes  $M_0$  to rotate away from the equilibrium orientation (in parallel with  $B_0$  along  $z$ -axis).

Spin angular momentum also has components in other directions that are presented by  $\hat{I}_x$  as  $x$ -component and  $\hat{I}_y$  as  $y$ -component of the nuclear spin angular momentum. Using the same argument made for  $M_z$ , the  $x$ -magnetization and  $y$ -magnetization can be written as(3)

$$M_x = \frac{1}{2} \gamma N \overline{(c_\alpha^* c_\beta + c_\beta^* c_\alpha)} \quad (1 - 6)$$

$$M_y = \frac{1}{2} i \gamma N \overline{(c_\beta^* c_\alpha - c_\alpha^* c_\beta)} \quad (1 - 7)$$

Time evolution of the spin wavefunction depends on the Hamiltonian introduced in Equation 1-2. And this time variation is a component of the coefficients  $c_\alpha$  and  $c_\beta$  with the forms  $c_\alpha(t) = c_\alpha(0) \exp\left(-\frac{1}{2} i \Omega t\right)$  and  $c_\beta(t) = c_\beta(0) \exp\left(\frac{1}{2} i \Omega t\right)$ . By the substitution of those two coefficients into Equation 1-3, 1-6 and 1-7, we found that  $M_z$  is not affected by such free (precession) evolution, while on the other hand,

$$M_x(t) = \cos(\Omega t) M_x(0) - \sin(\Omega t) M_y(0) \quad (1 - 8)$$

$$M_y(t) = \cos(\Omega t) M_y(0) + \sin(\Omega t) M_x(0) \quad (1 - 9)$$

where  $M_x(0)$  and  $M_y(0)$  are  $M_x$  and  $M_y$  at time zero.(3)

With the free evolution of  $M_x$  and  $M_y$  in mind, it is not hard to understand that after  $M_0$  is rotated away from the  $z$ -axis by rf energy and the rf pulse is turned off, the magnetization begins to evolve in a precessional motion. The net magnetization returns back to align with  $B_0$  along the  $z$ -axis in such a precessional

motion through a process named spin relaxation after the rf excitation. Meanwhile, the rf signal produced by the nuclear spins, known as the free induction decay (FID), is detected by a sufficiently sensitive receiver coil. Although for an ensemble of nuclear spins, magnetization components along three directions are present, only the  $M_+ = M_x + iM_y$  component contributes to the NMR signal. The signal decays with time due to spin relaxation, which will be revisited in Section 1.4.

Considering the scope of this chapter, signal acquisition and data processing as well as relevant NMR spectrometer components will not be introduced here. However, the Fourier transform as a data processing method to obtain NMR spectra from the FID will be described in section 1.3.2.

### **1.3 Principles of Magnetic Resonance Imaging**

This section delivers important principles of magnetic field gradients, which are the basis of the two techniques utilized in Chapters 3 and 4. The Fourier transform and the concept of **k**-space set the foundation to realize the microscopy function of magnetic resonance methods. Furthermore, section 1.3.4, especially the description for phase encoding, illustrates the key rationale behind both MRI and PFG-NMR diffusometry methods – correlating spatial information with MR signal.

#### **1.3.1 Two Basic Aspects of Magnetic Resonance**

Ernst discussed three windows of ‘non-invasive’ transparency, which are X-ray, low frequency ultrasound, and radio frequency.<sup>(4)</sup> As shown in Figure 1-1, for X-rays, the quantum photon energy is sufficiently high at short wavelengths to cause harm to biological samples. Hence, strictly speaking X-ray penetration cannot be

defined as non-invasive. On the other hand, in the radio-frequency window of large wavelengths, different from optical microscopy, the resolution of magnetic resonance microscopy is not limited by wavelength.(5)

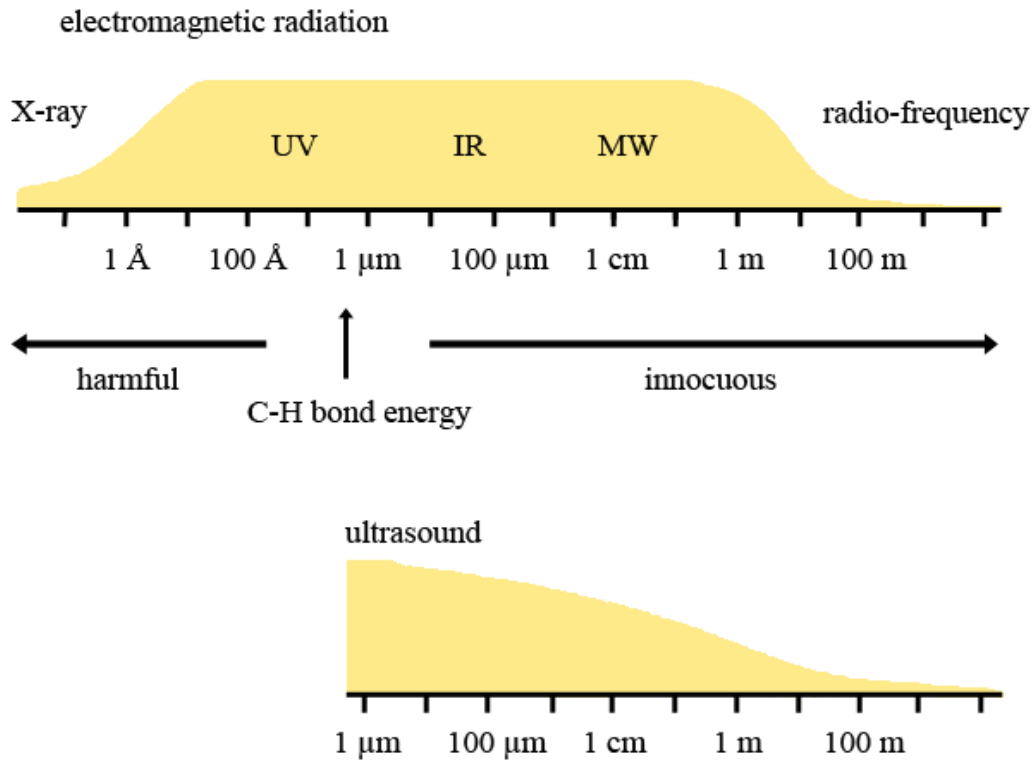


**Figure 1-1.** Windows of transparency for imaging techniques. The vertical scale measures the attenuation of radiation by biological tissue, and the horizontal scale shows frequency windows. The wavelength corresponding to C-H bond dissociation energy with radiation is sufficiently high to cause significant damage to biological specimens and tissues. Figure adapted from Ernst.(4)

The other feature of magnetic resonance that has significance for tomographic applications as well as for the study of translational diffusion (pulsed-

field-gradient NMR) is that the Larmor frequency of the nuclear spin is proportional to the magnetic field strength  $B_0$ , as shown by Equation 1-1. Consequently, one can use this field strength dependence to precisely encode the spatial origin of signal by a magnetic field that varies with position (a magnetic field gradient). In conventional NMR spectroscopy, the magnetic field is made as homogenous as possible across the sample, so that chemically identical nuclei can give nuclear precession frequencies that vary as little as possible. By contrast, in MRI and PFG-NMR experiments, a linearly varying field known as a *magnetic field gradient* is applied independently of the much larger static field  $\mathbf{B}_0$ .(5)

In MRI, magnetic field gradients are relatively small perturbations superimposed on the static magnetic field  $\mathbf{B}_0$ . Hence the effective magnetic field in the presence of gradient  $\mathbf{g}$  ( $\text{Tm}^{-1}$ ) becomes spatially dependent on the nuclear spin coordinate  $\mathbf{r}$  as described by Equation 1-10.

$$B_{eff}(\mathbf{r}) = B_0 + \mathbf{g} \cdot \mathbf{r} \quad (1 - 10)$$

As a result, the nuclear Larmor frequency becomes a spatial label with respect to the directions of three physical gradients ( $x, y$ , and  $z$ ) as shown by Equations 1-11 and 1-12.

$$\omega_{eff}(\mathbf{r}) = \omega_0 + \gamma(\mathbf{g} \cdot \mathbf{r}) \quad (1 - 11)$$

$$\mathbf{g} = \nabla B_0 = \frac{\partial B_z}{\partial x} \mathbf{i} + \frac{\partial B_z}{\partial y} \mathbf{j} + \frac{\partial B_z}{\partial z} \mathbf{k} \quad (1 - 12)$$

where  $\mathbf{g}$  is the gradient field component parallel to  $\mathbf{B}_0$  and  $\mathbf{i}$ ,  $\mathbf{j}$ , and  $\mathbf{k}$  are unit vectors of the laboratory frame of reference. Therefore, each nucleus precesses at a unique frequency depending on its exact position within the gradient field.



This gives a direct correspondence between NMR resonance frequency and spatial position in the sample. In addition to the non-invasive nature of radio waves, this frequency-position correspondence provides the other key feature of NMR necessary for imaging of spin positions and displacements in a sample or a living organism.

### 1.3.2 Fourier Transform

The Fourier transform is of fundamental significance in medical image reconstruction, including implementations in MRI, X-ray computed tomography (CT), and ultrasound imaging. Figure 1-2(5) shows the basic imaging process scheme that applies to MRI, photon intensity tomography such as CT and PET, as well as to optical microscopy.

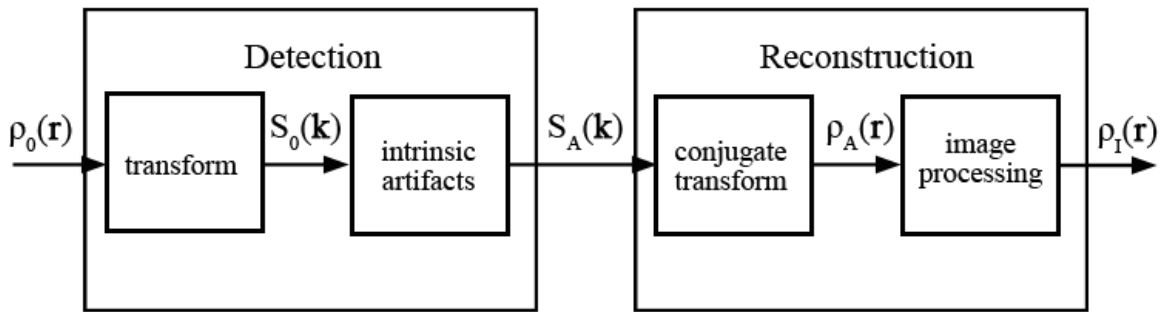


**Figure 1-2.** Representation of the Imaging process.  $\rho(r)$  represents image density,  $\rho_0(r)$  is the initial image density while  $\rho_I(r)$  is the final image density.  $S(k)$  represents the signal,  $S_0(k)$  is the detected signal and  $S_A(k)$  is the signal containing artifacts. Figure adapted from Callaghan.(5)

The function  $\rho(\mathbf{r})$  in Figure 1-2 can represent nuclear spin density in MRI as well as photon absorber density in X-ray CT. And  $\rho_0(\mathbf{r})$  is the initial (ideal) image density while  $\rho_I(\mathbf{r})$  is the final detected and processed image density. In a form analogous to magnetization components defined by Equations 1-8 and 1-9, for imaging we have  $A \exp(i\omega t)$  ( $A$  as amplitude), frequency  $\omega$  and time  $t$  are conjugate variables, where  $\omega = 2\pi/T$  ( $T$  as period) and  $|\mathbf{k}| = 2\pi/\lambda$  ( $\lambda$  as wavelength). Thus the equivalent expression of  $A \exp(i\omega t)$  in the time domain is  $A \exp(i\mathbf{k} \cdot \mathbf{r})$  in the space domain, where wave vector  $\mathbf{k}$  and spatial coordinate  $\mathbf{r}$  are also conjugate. Without further detailed derivation, we define  $S(\mathbf{k})$  as the detected signal for either MRI or X-ray CT, then  $S(\mathbf{k})$  and  $\rho(\mathbf{r})$  are bound by Fourier transformation (FT) as shown by Equations 1-13 and 1-14.(5)

$$S(\mathbf{k}) = \iiint \rho(\mathbf{r}) e^{-i\mathbf{k} \cdot \mathbf{r}} d\mathbf{r} \quad (1 - 13)$$

$$\rho(\mathbf{r}) = \frac{1}{2\pi} \iiint S(\mathbf{k}) e^{i\mathbf{k} \cdot \mathbf{r}} d\mathbf{k} \quad (1 - 14)$$

Conventionally, spatial cyclic frequency  $k$  is used instead of  $\kappa$ , where  $k = \kappa/2\pi$ , to obtain a symmetric form of the FT.

$$F(\mathbf{k}) = \iiint f(\mathbf{r}) e^{-i2\pi\mathbf{k} \cdot \mathbf{r}} d\mathbf{r} \quad (1 - 15)$$

$$f(\mathbf{r}) = \iiint F(\mathbf{k}) e^{i2\pi\mathbf{k} \cdot \mathbf{r}} d\mathbf{k} \quad (1 - 16)$$

For applications of the FT in MRI, the concept of convolution based on the basic FT is critical. Generally, the Fourier transformation of the multiplication of  $f(\mathbf{r})$  by  $g(\mathbf{r})$  is the convolution of the two transformed functions in conjugate space

$F(\mathbf{k})G(\mathbf{k})$ . The effect of such convolution is that the signal can be truncated or shifted as illustrated in Figure 1-3.(5)

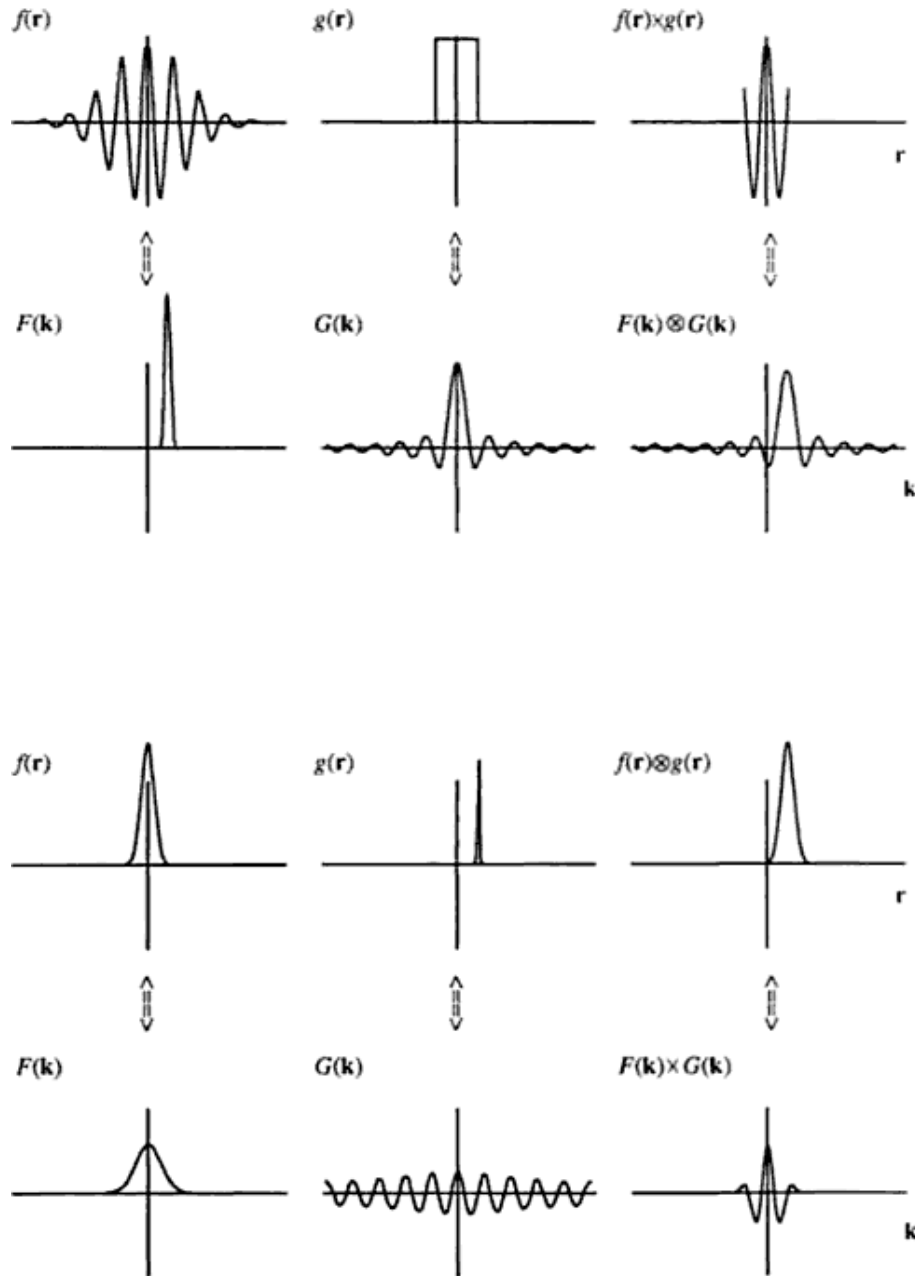


**Figure 1-3.** Illustration of convolution effect. The top part shows the window effect where the signal in the original domain is multiplied by a hat function and leads to a SINC function in the Fourier domain. The bottom figure shows the shift effect.

Multiplication with a displaced spike can shift the signal in original (position) space, which leads to the multiplication by an oscillation in Fourier ( $\mathbf{k}$ ) space. Figure reproduced from Callaghan.(5)

### 1.3.3 k-Space

To continue the discussion in the preceding section,  $\rho(\mathbf{r})$  represents the local spin density of a small element of volume  $dV$  in the presence of a field gradient  $\mathbf{g}$ . Then there are a total of  $\rho(\mathbf{r})dV$  spins in the element contributing to the NMR signal, which can be written as  $\rho(\mathbf{r})dV\exp[i\omega(\mathbf{r})t]$ , according to the oscillatory nature of magnetization. Now by substituting Equation 1-11 into the NMR signal from the small element, one has

$$dS(\mathbf{g}, t) = \rho(\mathbf{r})dV\exp[i(\gamma B_0 + \gamma \mathbf{g} \cdot \mathbf{r})t] \quad (1 - 17)$$

where the effect of transverse relaxation is ignored. Furthermore, by setting  $\gamma B_0$  as the reference frequency, one can neglect the term  $\gamma B_0$  in the parentheses, so that the integrated signal  $S(t)$  becomes

$$S(t) = \iiint \rho(\mathbf{r})\exp[i\gamma \mathbf{g} \cdot \mathbf{r}t]d\mathbf{r} \quad (1 - 18)$$

where  $d\mathbf{r}$  represents volume integration. Mansfield(6) introduced the concept of a vector  $\mathbf{k}$  in the unit of reciprocal space ( $\text{m}^{-1}$ ) defined by Equation 1-19,

$$\mathbf{k} = \gamma \mathbf{g}t/2\pi \quad (1 - 19)$$

so that Equation 1-18 has the format of the Fourier transform analogous to Equation 1-13 and 1-15,

$$S(\mathbf{k}) = \iiint \rho(\mathbf{r})\exp[i2\pi \mathbf{k} \cdot \mathbf{r}]d\mathbf{r} \quad (1 - 20)$$

with its inverse in a similar format as Equation 1-14 and 1-16,

$$\rho(\mathbf{r}) = \iiint S(\mathbf{k})\exp[-i2\pi\mathbf{k} \cdot \mathbf{r}]\mathrm{d}\mathbf{k} \quad (1 - 21)$$

Equation 1-20 and 1-21 are the fundamental relationships for real space and conjugate (Fourier)  $\mathbf{k}$ -space in MRI. In an MRI experiment, data collected from the nuclear spin signals are stored in this  $\mathbf{k}$ -space, which is a graphic matrix of digitized magnetic resonance data representing an image prior to Fourier transform, in the detection process in Figure 1-2. By sampling  $\mathbf{k}$ -space and applying the Fourier transform, an image can then be constructed (reconstruction process in Figure 1-2).  $\mathbf{k}$ -space normally has two axes: one presents the frequency information and the other presents the phase information, which will be introduced in the following section.

#### **1.3.4 Slice Selection and Spatial Encoding**

The idea introduced in 1.3.1 represented by Equation 1-11 states that each nuclear spin resonates at a unique frequency that depends on its specific position within the gradient field along three directions ( $x$ ,  $y$ , and  $z$ ). In short, elements of a magnetic resonance (MR) image (pixels) constitute a map of frequency and phase generated by field gradients corresponding to spins at different magnetic fields in each volume element of the sample.

Gradients along  $x$ ,  $y$ , and  $z$  directions are required in order to obtain spatial information in each direction. Depending on the effects of the three gradients on the signal and image, they are called the slice-select gradient, readout/frequency-

encoding gradient, and phase-encoding gradient, all of which will be considered in this section.

### **Slice Selection**

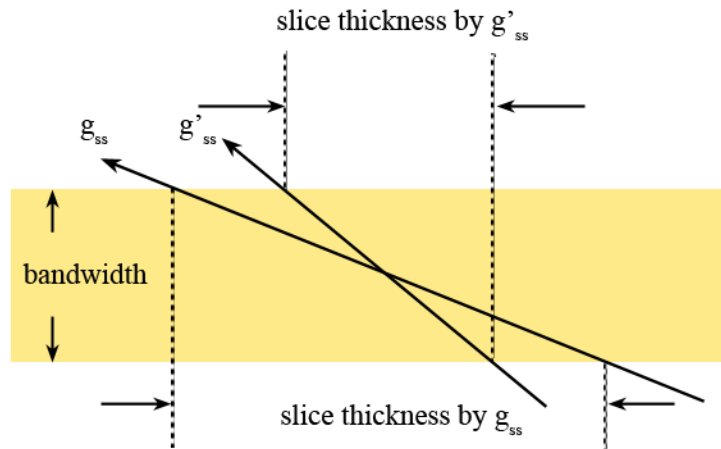
The initial step for obtaining an MR image is to localize the rf excitation pulse to excite a region of space, hence requiring the excitation of a specific range of frequencies. This is realized by the use of frequency-selective excitation in conjunction with a gradient along the slice-selection direction.

In contrast with “hard” rf pulses commonly used in NMR spectroscopy that excite all frequencies equally in the spectrum, frequency-selective excitation uses time-varying, called “shaped” or “soft” rf pulses, which can only excite part of the spectrum if used in NMR experiments. The range of frequencies that are affected by a selective rf pulse is called the excitation or pulse bandwidth. The center frequency and bandwidth of a selective pulse determine the slice position and slice thickness, respectively. Meanwhile, the amplitude of a slice-select gradient (usually along z-axis) affects the frequency variation along the slice selection direction, and hence also determines the slice thickness as shown by Equation 1-22

$$\Delta\omega = \gamma\Delta(g_{SS}\times\textit{Slice Thickness}) \quad (1 - 22)$$

where  $g_{SS}$  is the amplitude of slice-select gradient, and  $\Delta\omega$  is the bandwidth, usually set to a fixed value. According to Equation 1-22, larger gradient values are required for thinner slices within the machine limitation. A simplified slice selection process is shown in Figure 1-4.

(a) One slice



(b) Multiple slices

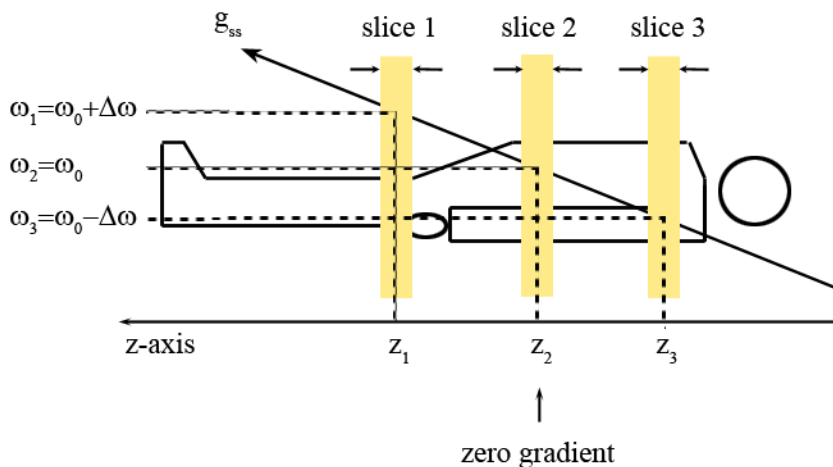


**Figure 1-4.** (a) Relationship between pulse bandwidth, gradient strength, and slice thickness as shown mathematically in Equation 1-22. For a given bandwidth (which is usually the case), the slice thickness is determined by the amplitude of slice-selection gradient. (b) Simplified slice selection process.  $\omega_0$  is the central frequency of the selective rf pulse, which is also the frequency of the slice in the center that experiences zero gradient field. Slices on both sides experience positive and negative gradient field.  $\Delta\omega$  is the bandwidth of the frequency selective rf pulse.

Compared with a nonselective pulse, the transmitter duration of a soft pulse is longer, in order to create a narrower bandwidth, which is desirable for medical imaging applications because it can focus the excitation on narrow regions of tissue. A hard pulse is normally shaped in the form of a rectangular (RECT) function in the time domain, as shown by Figure 1-5. The rectangular pulse is of very short length and applied without a parallel gradient, so that the bandwidth is broad enough to affect a wide range of resonant frequencies.

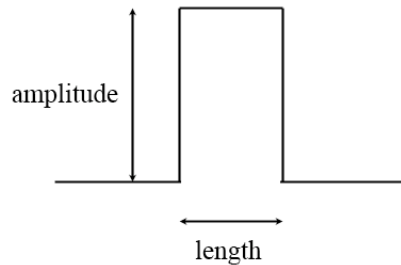


**Figure 1-5.** A symbolic representation of hard pulse.

On the other hand, amplitude-modulated pulses are commonly used for slice selection, for the purpose of achieving uniform amplitude and phase excitation throughout a single slice. SINC pulses are an example of widely used amplitude-modulated pulses, which consist of several adjacent lobes of alternating polarity given by the formula of Equation 1-23(7). In Equation 1-23,  $A$  is the peak amplitude occurring at  $t = 0$ ,  $t_0$  is one-half width of the central lobe, and  $N_L$  and  $N_R$  are the number of zero-crossings in the SINC pulse to the left and right of the central lobe, respectively. The amplitude of the central lobe is the highest and the outlying lobes gradually decrease in amplitude on both sides of the central lobe as their polarity



alternates, as shown in Figure 1-6. The Fourier transform of a SINC pulse in the time domain gives the frequency profile shown in Figure 1-6. The FT of an infinitely long SINC pulse gives a RECT function frequency profile, which can give an ideal slice-selection profile. Therefore the greater the number of lobes included, the better the approximation to the ideal frequency profile.(7, 8)

$$B_1(t) = \begin{cases} A \operatorname{SINC} \left( \frac{\pi t}{t_0} \right) \equiv At_0 \frac{\sin \left( \frac{\pi t}{t_0} \right)}{\pi t} & -N_L t_0 \leq t \leq N_R t_0 \\ 0 & \text{elsewhere} \end{cases} \quad (1 - 23)$$

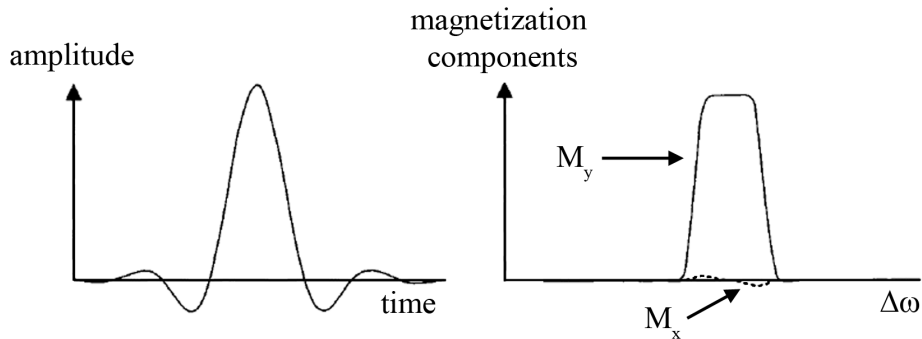


**Figure 1-6.** A symmetric SINC pulse of 4 zero-crossings (right) and the frequency profile (left) after Fourier transform.  $M_x$  is indicated by the dotted line and  $M_y$  is indicated by the solid line. Figure adapted from Bernstein et al.(7)

Unfortunately, SINC pulses do not always meet the requirements for specific applications. For example, the frequency excitation profiles of SINC pulses are significantly nonrectangular for large angle pulses such as  $90^\circ$  and  $180^\circ$  pulses. In this case, Gaussian pulses are frequently used for frequency-selective saturation such as fat suppression due to their narrower bandwidth. In fact  $180^\circ$  Gaussian-shape pulses are used for refocusing and inversion-recovery for the MRI application

of nanoparticle diffusion tracking presented in Chapter 3. Besides the above, hyperbolic secant pulses are often used for inversion-recovery sequences. Examples of Gaussian and hyperbolic secant pulses are illustrated in Figure 1-7.

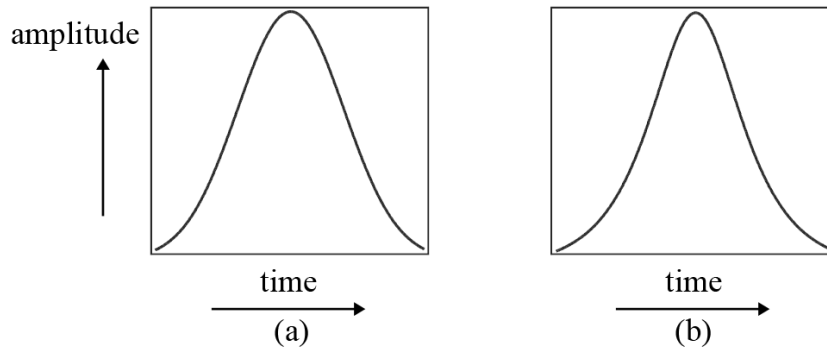


**Figure 1-7** Gaussian function (a) and hyperbolic secant (b) pulse shapes. Figure adapted from Brown and Semelka.(8)

### Frequency Encoding

In an imaging pulse sequence, the gradient  $g_{SS}$  is applied during selective rf pulses for slice selection, for example along the  $z$ -axis. Subsequently, a frequency-encoding or more commonly called a readout gradient is turned on during the detection of signal from the entire selected slice. For example, in a simple spin echo sequence shown in Figure 1-8, a  $90^\circ$  slice-selective pulse is used for excitation, following which the nuclear spins within the slice precess uniformly at a certain frequency and the net magnetization is transverse to  $B_0$ . The dephasing and signal decay due to relaxation after the  $90^\circ$  rf pulse can be partially reversed by the  $180^\circ$  rf pulse. The readout gradient is turned on when the echo signal is forming, along a direction perpendicular to the slice direction ( $x$ -axis in this case). Again, given the

relationship described by Equation 1-11, the nuclear spins begin to precess at different frequencies depending on their position along the x-axis due to the effect of this magnetic field gradient. As a result, the frequency and position have a one-to-one relationship that maps one of the two dimensions (x axis) of an MR image.

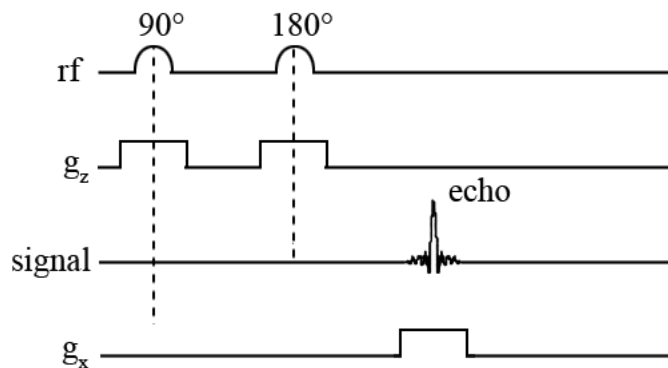


**Figure 1-8.** Simple spin-echo pulse sequence with slice-selective ( $g_z$ ) and frequency encoding ( $g_x$ ) gradients.

Considering the scope of this chapter, the mathematical relationship between the frequency encoding gradient and imaging parameters such as field of view, spatial resolution and frequency resolution will be skipped here. However, one important message derived from those relationships is that independent of spatial resolution, frequency resolution can be improved by increasing the number of sample points, which means increasing the total sampling time.

### Phase Encoding

In addition to using a gradient along z for slice selection and the readout gradient along x for frequency encoding, a third gradient is used to phase encode

along the  $y$  direction. The phase-encoding gradient is usually applied between the rf pulses and the echo/frequency encoding gradient in a pulse sequence such as that shown in Figure 1-8.

As a matter of fact, as stated in the second aspect of magnetic resonance in section 1.3.1, a field gradient is the fundamental tool for MRI as well as the measurement of molecular motion using PFG-NMR diffusometry. In other words, both techniques use magnetic field gradients to determine molecular position and share their basic principle, which will be described below. Different from the application of phase encoding for MRI application, which is perpendicular to  $B_0$ , the gradient used for PFG-NMR is often applied along  $z$  (parallel with  $B_0$ ) to encode each nucleus with a unique phase.

Here the effect of a field gradient on phase evolution is illustrated for the case of PFG-NMR (gradient parallel with  $B_0$ ), to benefit further introduction of PFG-NMR in section 1.9. Consider an ensemble of spins spread along  $z$  originally in a homogenous field  $B_0$ , as shown in Figure 1-9. (9) As briefly mentioned in section 1.2, a  $90_x^\circ$  rf pulse rotates the magnetization of the ensemble of spins away from the  $z$ -axis into the transverse plane to the  $y$ -axis. The first column of spin magnetization vectors in Figure 1-9 shows those vectors have identical phase immediately after the  $90_x^\circ$  pulse. Here we reasonably ignore the effect of transverse relaxation in the time period of phase encoding. By adding this  $z$ -axis gradient promptly after this  $90_x^\circ$  pulse, the time evolution of the NMR signal  $M_+$  can be written as

$$M_+(z, t) = M_+(z, 0) \exp(i\gamma g z t) \quad (1 - 24)$$

Equation 1-24 is in accordance with Equation 1-11 and 1-17, except we replace vector  $\mathbf{r}$  with the displacement along the  $z$ -axis as the scalar  $z$  in the exponential term. It can be shown by the exponential term that the phase accumulated at time  $t$  is proportional to displacement along  $z$ , which is also illustrated by the overall phase evolution pattern of magnetization vectors in a helix in Figure 1-9. The wavelength  $\lambda$  of the magnetization helix decreases with increasing gradient duration as shown by Equation 1-25.

$$\lambda = \frac{2\pi}{\gamma g t} \quad (1 - 25)$$

In section 1.3.3, we defined vector  $\mathbf{k}$  by Equation 1-19 (shown below again). It is easy to see that  $\mathbf{k}$  is actually the reciprocal of  $\lambda$  in units of cyclic spatial frequency ( $\text{m}^{-1}$ ).

$$\mathbf{k} = \gamma \mathbf{g} t / 2\pi \quad (1 - 19)$$

So Equation 1-24 can be rewritten as

$$M_+(z, t) = M_+(z, 0) \exp(i\mathbf{k} \cdot \mathbf{r}) \quad (1 - 24)$$

which is in the same form as Equation 1-20 and 1-21 given in section 1.3.3.

For the application of such a gradient along the  $y$ -axis in the MRI case, according to Equation 1-24, by either moving in time or in gradient magnitude, the  $\mathbf{k}$ -space we defined in section 1.3.3 as a graphic matrix of digitized MR data representing an image prior to Fourier transform can be sampled. In MRI, the approach of changing gradient magnitude is used. By repeating slice selection and signal detection (frequency encoding) multiple times with different amplitudes of  $\mathbf{k}$  for each time, the image information is recorded for the  $y$ -axis.

Therefore the effect of the phase encoding gradient along the third direction, perpendicular to the slice-selective gradient and the frequency encoding gradient, shares exactly the same mechanism as that illustrated above for PFG-NMR. Once this gradient along  $y$  is turned off, and before the readout/frequency encoding gradient along  $x$  is turned on (see Figure 1-15), the distinct phase shift within each volume unit caused by the encoding process persists as the code of every unit along the other visualization axis ( $y$ -axis), together with the frequency-spatial encoding for the  $x$ -axis of an MR image. In short, the magnetic resonance signal originating from nuclear spins in each spatial unit of the sample now has a unique frequency and a unique phase for  $x$  and  $y$  coordinates for each unit (pixel) of the image.

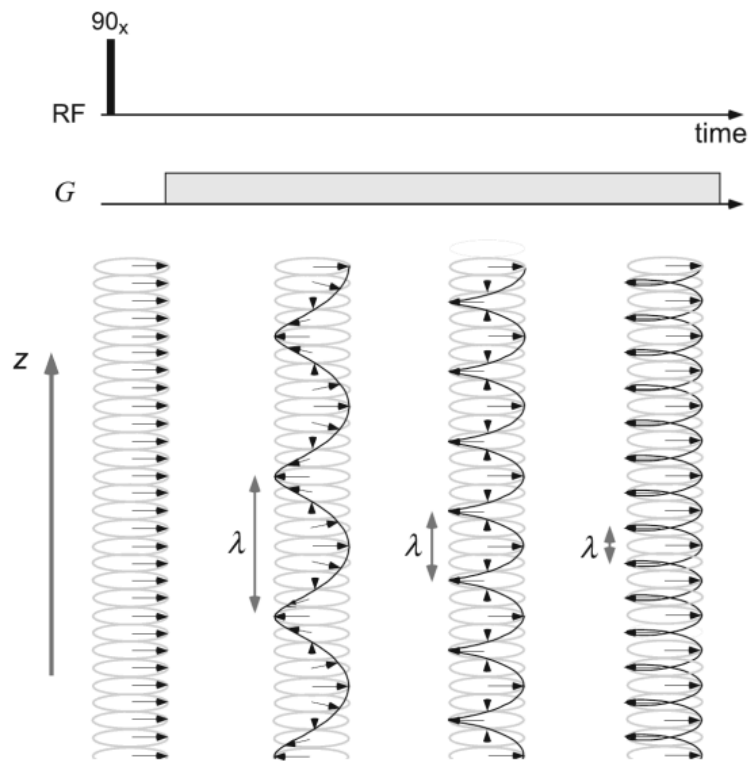


**Figure 1-9.** Effect of a magnetic gradient on the phase evolution of nuclear spin magnetization components within an ensemble along the gradient direction, which is parallel with  $B_0$ . Figure reproduced from Callaghan.(5)

Sequence loops defined as repetitive execution in a MRI measurement are skipped in this section. In general, various encoding loop structures are used for different samples according to specific requirements about the image. However, a balance needs to be found between desired resolution and sufficient sensitivity while maintaining acceptable scan times.

### 1.3.5 Data Matrices

Based on the introduction of  $\mathbf{k}$ -space in section 1.3.3 and what has been discussed previously regarding phase encoding, it is easy to understand that  $\mathbf{k}$ -space is a digitized version of the MR data space. To continue the discussion in the paragraph above Figure 1-9, the complex array of raw data points are ordered as a grid of points  $(k_x, k_y)$  in the  $\mathbf{k}$ -space formalism,

$$k_x = \gamma g_x t_x \quad (1 - 25)$$

$$k_y = \gamma g_y t_y \quad (1 - 26)$$

Where  $k_x$  corresponds to a complex point in the readout (frequency encoding) axis with the readout gradient duration of  $t_x$ , whereas  $k_y$  corresponds to a phase encoding gradient with duration  $t_y$ .

The contrast (intensity) in an MRI images comes primarily from data in the center of  $\mathbf{k}$ -space, whereas the edge definition (resolution) comes from data at the edge of  $\mathbf{k}$ -space.(8) Therefore when filling up  $\mathbf{k}$ -space, the MR data should be sampled continuously with a uniform density (constant  $\Delta k_x$  and  $\Delta k_y$ ). There are various ways to traverse  $\mathbf{k}$ -space, for example the sequential filling used in traditional MRI scanning. It is clear that each phase encoding line corresponds to a measured MR signal. In sequential filling phase encoding lines are acquired serially in time with data from maximum negative  $g_y$  to maximum positive  $g_y$ , with  $g_y$  changing by a constant increment from line to line. Compared with the traditional rectilinear sampling, ramped filling and spiral filling are two important nonrectilinear sampling methods, which will not be introduced in detail here.

Besides full sampling of  $\mathbf{k}$ -space, there are approaches using reduced total number of phase encoding amplitudes that can still produce artifact-free images, for example, partial Fourier imaging.(8) Another recent development in reducing sampling time is parallel acquisition utilizing multiple phased-array receiver coils such as sensitivity encoding (SENSE) technique.(10) Along with the development in data acquisition, advanced image reconstruction approaches such as compressed sensing(11) has gained successes in reducing scanning time without great compensation in image resolution and sensitivity.

One field of tremendous contribution to advanced MRI that has not been mentioned specially is the development of fast MRI sequences including SENSE mentioned above. The rapid development in MRI methodology including signal enhancement of multi-isotope imaging with the aid of hyperpolarization, as well as



new detection hardware especially for medical use have facilitated the development of MRI techniques. With these advances and fast and ultrafast imaging pulse sequences and techniques, MR imaging will provide new meanings and opportunities for applications in medicine and chemistry.

## **Part II. MRI Contrast and Practical Aspects of Contrast Agents**

### **1.4 Image Contrast**

Image contrast originates from the variation of local spin density distribution in the sample, as well as the differences of relaxation rates of individual spin ensembles localized in different sample regions. Without introducing comprehensive relaxation theories, simplified relationships of longitudinal relaxation and transverse relaxation processes will be described in this section, with the intention to explain the actual MRI methods and pulse sequences employed in Chapter 3.

In section 1.3.3,  $\rho(\mathbf{r})$  is defined as the local spin density of a small element of volume  $dV$ . Hence the local spin density in each sampling voxel determines the signal magnitude in each pixel of the image and subsequently provides the basic image contrast without the participation of relaxation processes.

In short, relaxation is the process by which the spins return to equilibrium. In terms of net magnetization, equilibrium means the state predicted by the Boltzmann distribution represented by Equation 1-5. An introduction to basic nuclear relaxation theories in liquids is beyond the scope of this chapter, so only the conclusions from simple relaxation theories relevant to image contrast will be

presented here without introducing mathematical representations or thorough derivations for models used in relaxation theories.

The longitudinal relaxation time  $T_1$  is the time needed for the  $z$ -component of net magnetization of a nuclear spin ensemble to return to 63% ( $1 - 1/e$ ) of its original value  $M_0$  defined by Equation 1-5, after excitation by a  $90^\circ$  rf pulse. In an MR experiment, pulsed rf excitation is usually applied to nuclear spins repeatedly with a delay time between the repetitions (scans). The delay time allows nuclear spins to release rf energy to the surroundings and reestablish the population difference at equilibrium through  $T_1$  relaxation.

An NMR technique called inversion recovery is commonly used for the measurement of  $T_1$  relaxation time, whose pulse sequence is shown in Figure 1-10. This technique is essential for the diffusion study in Chapter 3. For actual measurements of  $T_1$ , the inversion-recovery pulse sequence is usually repeated for a number of times with varying interval  $\tau$  between the two rf pulses, in order to obtain the NMR signals (intensities) corresponding to different  $\tau$  values. Also, the delay time between repetitions (mentioned in the previous paragraph) is kept sufficiently long (several times  $T_1$ ) so that the net magnetization relaxes back to a reproducible thermal equilibrium state before the next repetition of the pulse sequence. In this sense, an estimation of  $T_1$  should be made prior to its measurement using inversion recovery.

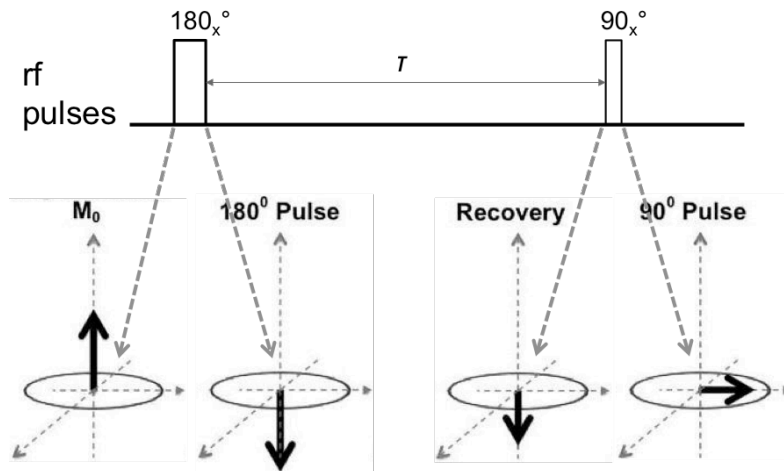


**Figure 1-10.** Symbolic representation of inversion-recovery pulse sequence and its working mechanism.

Figure 1-10 shows the working mechanism of the inversion-recovery pulse sequence in terms of the net magnetization vector. The first  $180^\circ$  rf pulse inverts the net magnetization initially along positive z-direction. Immediately after the  $180^\circ$  pulse, the net magnetization starts to relax toward equilibrium from the negative z-direction during period  $\tau$ . The second  $90^\circ$  rf pulse converts the net magnetization onto xy-plane for detection and generates an NMR signal from the magnitude and direction of net magnetization at the end of  $\tau$ . Therefore, the observed signal is a function of the interval  $\tau$ , and the peak amplitude of each NMR signal reflects the longitudinal relaxation, which is to be measured here.

The spectral peak amplitude  $a(\tau)$  as a function of  $\tau$  is shown in Figure 1-11. For small values of  $\tau$ , the peak amplitude is negative (in the opposite direction with the static field  $B_0$ ). With the increase of  $\tau$ , the peak amplitude goes through zero and becomes positive.

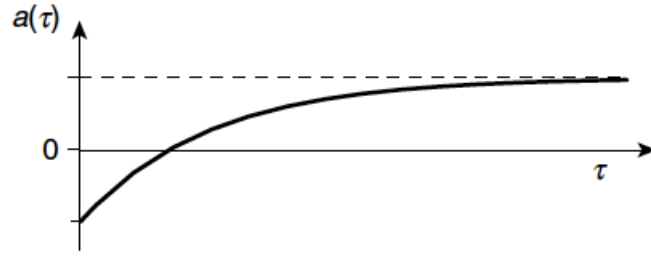


**Figure 1-11.** NMR spectral peak amplitude in the inversion-recovery experiment.

The horizontal dashed line marks the amplitude of signal from initial net magnetization, for example, the signal ideally detected immediately after a 90° excitation pulse without signal loss. Figure reproduced from Levitt.(12)

The value of net magnetization  $M_z$  as a function of  $\tau$  can be expressed by Equation 1-27, where  $M_0$  is the initial magnetization. Since the NMR signal intensity (spectral peak amplitude) is proportional to the net magnetization, the signal as a function of  $\tau$  is shown by Equation 1-28, where  $S_0$  represents the initial signal.

$$\frac{M_z(\tau) - M_0}{-2M_0} = \exp\left(-\frac{\tau}{T_1}\right) \quad (1 - 27)$$

$$\frac{S_z(\tau) - S_0}{-2S_0} = \exp\left(-\frac{\tau}{T_1}\right) \quad (1 - 28)$$

Equation 1-28 implies that a plot of  $\ln\left[\frac{S_z(\tau) - S_0}{-2S_0}\right]$  against  $\tau$  should be a straight line of slope  $-\frac{1}{T_1}$ . Therefore we can extract the value of  $T_1$  from the data of an inversion-recovery experiment.

On the other hand, if rather than varying  $\tau$  systematically during the inversion recovery experiment, one looks for the value of  $\tau$  that results in zero signal, which is termed a *null*, then a quick (but usually less accurate) measurement

of  $T_1$  can be made based on the relationship between *null* time  $t_{null}$  (value of  $\tau$  corresponding to zero signal) and  $T_1$ , which is shown by Equation 1-29.

$$T_1 = \frac{t_{null}}{\ln 2} \quad (1 - 29)$$

The concept and application of a *null* in MRI is of critical importance for the study introduced in Chapter 3, and the imaging technique using the *null* and inversion-recovery pulse sequence will be revisited in succeeding sections.

The transverse relaxation time  $T_2$  is the time required for the transverse component of net magnetization in the  $xy$  plane to decay to 37% ( $1/e$ ) of its initial value after application of a  $90^\circ$  rf pulse. Immediately after a  $90^\circ$  rf pulse, nuclear spins absorb the rf energy and their magnetization vectors are rotated into the transverse plane. If the spins are in homogenous static field  $B_0$ , all spins will precess at the same frequency  $\omega_0$  and with a synchronized phase of precession. . As time elapses, as a result of molecular interactions, the frequencies of individual spins fluctuates, therefore, the precession motion of the spins gradually loses phase coherence, which leads to an irreversible loss of net transverse magnetization. The irreversible process caused only by molecular interactions is termed  $T_2$  relaxation. Other causes for the loss of coherence may include inhomogeneity of static field  $B_0$  or heterogeneity in the sample itself. These sources contribute to the total transverse relaxation time named  $T_2^*$ .

A spin echo(13) pulse sequence is used for measurement of  $T_2$  relaxation. In a spin echo experiment, the so called inhomogeneous part of the signal decay (due to  $T_2^*$  processes) is reversed by the application of an echo pulse, which makes it possible to measure the homogeneous decay constant  $T_2$ , even in the presence of

those inhomogeneous sources described in the preceding paragraph. The spin echo pulse sequence is part of Figure 1-8 and is a key component of the MRI pulse sequence in section 1.5 and the PFG-NMR pulse sequence in section 1.9. Here, the spin echo pulse sequence will be illustrated in Figure 1-12 and introduced in detail.

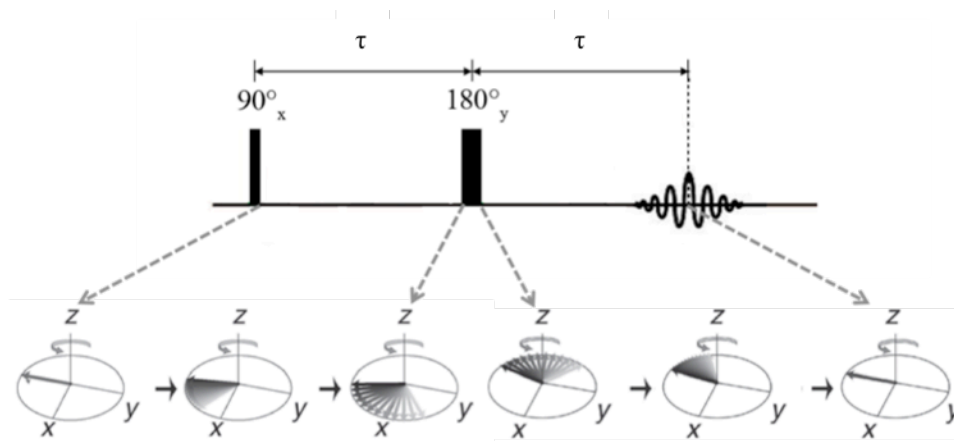


**Figure 1-12.** Symbolic representation of the simple spin echo pulse sequence and its working mechanism. This illustration ignores the signal loss due to  $T_2$  relaxation process during the pulse sequence (assuming ideally very long  $T_2$  and relatively short  $2\tau$ ), in order to only show the refocusing of  $T_2^*$  processes.

The first  $90^\circ$  rf pulse rotates the net magnetization away from the z-direction onto the negative direction along the y-axis. After the  $90^\circ$  pulse the magnetization vectors of nuclear spins from different spatial regions start to evolve out of phase with each other. This is a result of the second aspect of magnetic resonance discussed in section 1.3.1, that spins experiencing different local fields precess with different Larmor frequencies. This dephasing process has been mentioned in section 1.3.4 (frequency encoding), and will be emphasized again in section 1.9. The dephasing leads to a loss in the total signal during the first  $\tau$  interval. The second

180° pulse rotates all magnetization vectors around the  $y$ -axis, as shown in Figure 1-12. In other words, it reverses the direction of nuclear precession and phase evolution of all spins. After the pulse, magnetization vectors with inverted positions of local magnetic fields start to refocus back onto the  $-y$ -axis during the second  $\tau$  interval, and thus an echo forms at this point in the pulse sequence. One thing worth emphasizing again is that the spin echo can refocus signal loss only due to inhomogeneous dephasing, so that signal decay due to pure  $T_2$  relaxation will still be observed. In other words, this feature makes the spin echo capable of measuring the  $T_2$  relaxation time due to molecular interactions without including the effects caused by inhomogeneous processes.

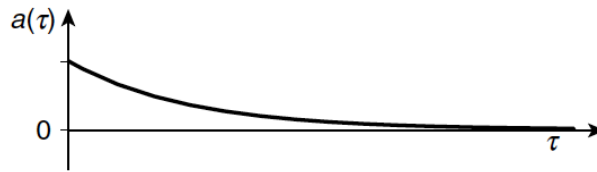


**Figure 1-13.** NMR spectral peak amplitude in the spin echo experiment as a function of time  $\tau$ . Figure reproduced from Levitt.(12)

The net magnetization detected at the end of second  $\tau/2$  interval decays with increasing  $\tau$  values. Therefore, by analyzing such an exponential curve shown by Figure 1-13, one can estimate the value of  $T_2$ . Equation 1-30 gives the mathematical relationship between net magnetization and  $\tau$ , where  $M_0$  is the initial magnetization.

$$\frac{M_z(\tau)}{M_0} = \exp\left(-\frac{\tau}{T_2}\right) \quad (1 - 30)$$

Basically, transverse magnetization ( $x$ - or  $y$ -component) decays exponentially at a rate determined by the transverse relaxation rate constant ( $1/T_2$ ), which will be further illustrated in section 1.5.

Nuclear spins usually have different relaxation times in different environments; hence, by making an MRI signal acquisition sensitive to differences in  $T_1$ ,  $T_2$ , and  $T_2^*$ , intensity contrast can be generated in a image. In a  $T_1$ -weighted image, the delay time between successive excitations is set shorter than  $T_1$ . Therefore the nuclear spins with long  $T_1$  are not allowed to fully release their rf energy, and the  $z$ -component of magnetization cannot relax back to the equilibrium value before the next excitation. As a result, the MR signal detected from these spins will have relatively low magnitude. On the other hand, nuclear spins with shorter  $T_1$  will result in higher signal magnitude due to sufficient  $T_1$  relaxation. In summary, spins with short  $T_1$  (fast  $T_1$  relaxation) create “positive”(higher signal magnitude) image contrast.

In a  $T_2$ -weighted image, the echo repetition time ( $2\tau$ ), which is the time period between  $90^\circ$  excitation pulse and the formation of echo signal in Figure 1-8, is chosen to be long relative to  $T_2$ . This is the time period when  $T_2$  relaxation participates and causes signal loss by dephasing. In this case, spins of short  $T_2$  and fast  $T_2$  relaxation will lead to greater signal loss and create “negative” image contrast with low signal magnitude.

Moreover, MRI contrast agents are used to accentuate the image contrast generated by differences in relaxation times of spin ensembles located in different environments, and these agents are a key part of the studies in Chapters 2 and 3.



Contrast agents and their working mechanisms will be introduced separately in section 1.6.

### **1.5 MRI Pulse Sequences Utilized in Study of Nanoparticle Diffusion**

In this section, the MRI sequences utilized in Chapter 3 will be presented. With the knowledge of MR image construction through the use of gradients from section 1.3.4 and 1.3.5, as well as the relaxation processes covered in section 1.4, those pulse sequences can be explained in detail.

MRI pulse sequences usually comprise radio frequency pulses, gradients and the resulting detected signal waveforms, as well as data acquisition. Schematic representations of MRI pulse sequences show these events in parallel as in Figure 1-8. After three decades of development, MRI pulse sequence design is still an active field of research and has received increasing attention in the area of medical imaging, especially for use in combination with the rapid evolution of hardware construction as well as other signal enhancement techniques.

The MRI pulse sequences applied in Chapter 3 are basic fast imaging pulse sequences routinely used for clinical diagnosis. Those pulse sequences utilize a train of refocusing pulses (instead of only one refocusing  $180^\circ$  pulse in Figure 1.8), in order to produce multiple rf spin echoes for signal detection, and are termed rapid acquisition with relaxation enhancement (RARE) pulses.(14, 15) In short, sampling **k**-space from multiple rf spin echoes produced by RARE can reduce the total imaging time by several fold compared with conventional spin echo sequences, especially for the generation of  $T_2$ -weighted images. RARE is widely accepted for

clinical use and has almost replaced the conventional spin echo sequences for  $T_2$ -weighted imaging. Since to thoroughly understand a basic RARE sequence as well as common variations and modifications from spatial encoding (gradients applications) and image reconstruction aspects will require knowledge on theories of advanced pulse sequence techniques, only key concepts of fast imaging utilizing echo trains will be introduced through an MRI 2D RARE sequence below without detailed explanations on each component from the pulse sequence diagram.

An example of rf pulses in the RARE sequence is shown by Figure 1-14 aiming to show the relationship between RARE and the conventional single spin echo. As explained in section 1.4, a spin echo refocuses inhomogeneous signal decay (due to  $T_2^*$  processes) and forms an echo for detection. In a RARE rf pulse sequence, another  $180^\circ$  is added at time  $3\tau$ , where  $\tau$  is the time interval between the excitation  $90^\circ$  and first refocusing  $180^\circ$  pulse as shown in Figure 1-14. Consequently another spin echo forms at time  $4\tau$  due to the dephasing and rephasing processes about the second  $180^\circ$  through the same mechanism as for the first spin echo illustrated previously. It has also been discussed that homogeneous dephasing cannot be refocused and so signal decay due to pure  $T_2$  relaxation is still observed. Although once the excitation pulse generates a transverse magnetization the lifetime of this net magnetization decays as a result of  $T_2$  relaxation at the rate of  $\exp(-t/T_2)$ , the first (conventional) spin echo occupies only a small fraction of this lifetime. Therefore instead of wasting the lifetime before and after the acquisition window of a single spin echo, a considerable portion of the signal can be acquired by adding

additional  $180^\circ$  refocusing pulses (echoes). And this is the basic rationale of an echo train rf pulse sequence.(16, 17)

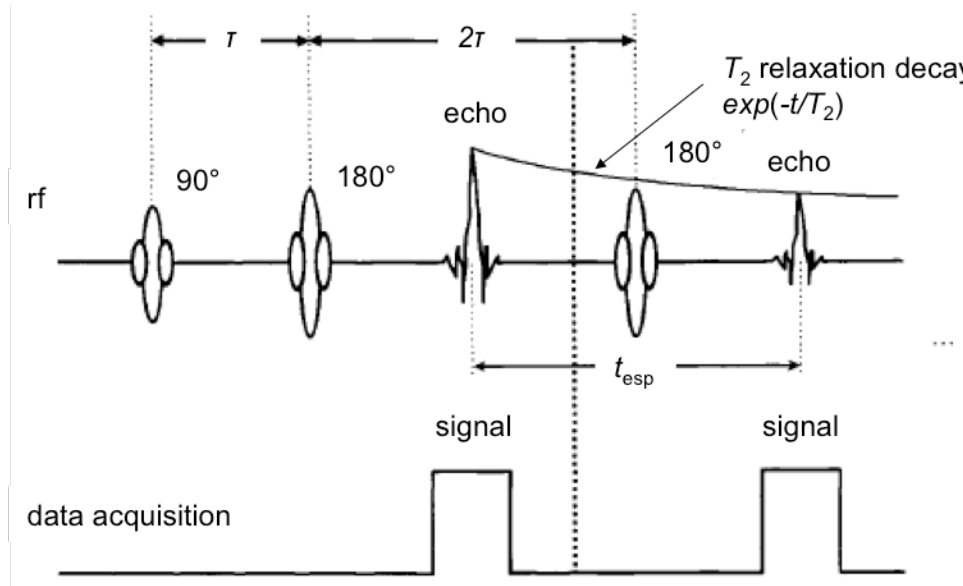


**Figure 1-14.** An example RARE rf pulse sequence. The pulses on the left side of the dotted vertical line represent a conventional spin echo as Figure 1-12. With additional  $180^\circ$  focusing pulses and echo signal acquisitions added to the right of the vertical line, the RARE sequence is constructed. The symbol of pulse shape here is different from those used in Figure 1-8, as a better representation of pulse shapes used in actual MRI pulse sequences.  $t_{esp}$  is the echo spacing time, which is the interval between the peaks of two consecutive spin echoes. Figure adapted from Bernstein et al,(7)

Combining an echo train rf pulse sequence with gradients, one can construct a 2D RARE MRI sequence, which is shown schematically in Figure 1-15. In section 1.3.3 and 1.3.5 it has been shown that an MRI image can be constructed by sampling  $\mathbf{k}$ -space and applying the Fourier transform. In other words, data collected from the

spin echo signals are stored in **k**-space as a graphic matrix of digitized magnetic resonance data representing an image prior to Fourier transform. In fact, the reduction of the total imaging time by RARE is realized by sampling multiple **k**-space lines from the echo train generated by a single excitation of magnetization, instead of one line by each excitation conventionally. This is possible because each echo in RARE is distinctively spatially encoded. For example, 4 echoes shown in Figure 1-15 are distinctively phase encoded by applying different amplitudes of  $k_y$  for each echo. Therefore, 4 lines along  $k_y$  (in **k**-space) are filled following each excitation pulse, compared to only one line at a time in a conventional single spin echo sequence. In this way, the total acquisition time needed for the full sampling of **k**-space can be considerably reduced. There are alternative **k**-space sampling schemes briefly introduced in section 1.3.5. For example, using a second echo in RARE can also be used as a second frequency-encoded line along  $k_x$ . As long as the transverse magnetization does not significantly decay through  $T_2$  relaxation, additional  $180^\circ$  refocusing pulses can be applied to form a train of echoes to realize fast acquisition.

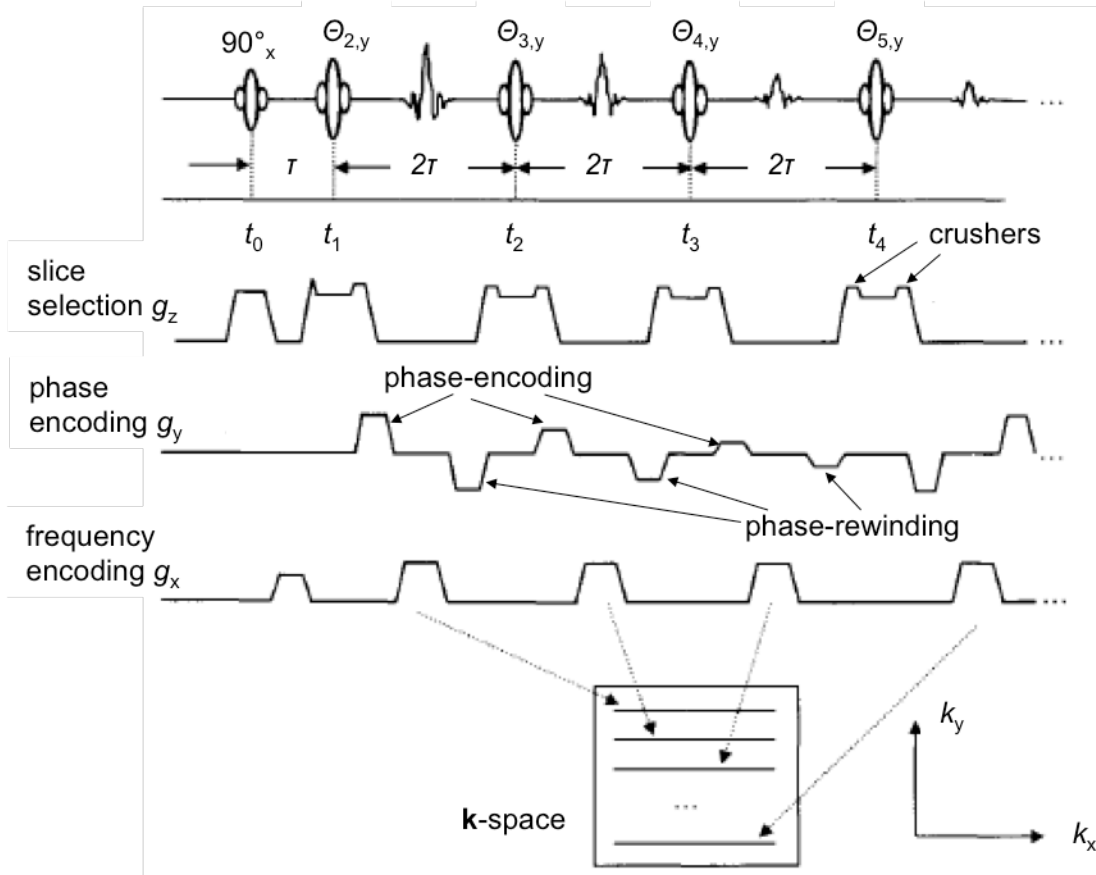


**Figure 1-15.** Symbolic representation of a 2D RARE sequence. The  $90^\circ_x$  is an excitation pulse along the  $x$ -axis and  $\theta_{2,y}$  through  $\theta_{5,y}$  are refocusing pulses ( $180^\circ$  or smaller angle pulses) along the  $y$ -axis. Figure adapted from Bernstein et al.(7)

It is worth mentioning that the rf pulse train shown in Figure 1-15 (timing and rf pulse phase relationship) is called a Carr-Purcell-Meiboom-Gill (CPMG)(16, 17) train, which is routinely used for measuring the  $T_2$  relaxation time.  $\theta_y$  is the flip angle of the refocusing pulse which is usually set to be smaller than  $180^\circ$  in practice. As shown in Figure 1-15, the slice-selection gradient is combined with a pair of straddling gradient crushers in order to select the desired signals (in frequency space) while eliminating the unwanted ones. As illustrated for phasing encoding in

section 1.3.4, a phase-encoding gradient is applied after each refocusing pulse and before the readout gradient. In order to ensure signal coherence, an accompanying phase-rewinding gradient is usually applied.

Considering the limited scope of this section, further illustration on RARE pulse sequences and experimental parameters as well as their applications will be left out.

The second pulse sequence used in Chapter 3 is an inversion-recovery (IR) pulse sequence that combines the basic inversion-recovery experiment illustrated in section 1.4 with a fast echo train acquisition technique such as RARE. Considering the scope of this section, an example of major applications of the IR pulse sequence in medical imaging will be covered instead of the more complicated IR-RARE pulse sequence. Although the IR pulse sequence was used in the study in Chapter 3 for a different application, the mechanism of utilizing a *null* point, which is sensitive to  $T_1$  relaxation time, is basically the same as the example here.

An important clinical application of IR is lipid/fat suppression. In section 1.4, the *null* concept has been introduced without any demonstration of its application. In a nutshell, the lipid suppression is achieved by nulling the signal in the image that originate from lipids.(19, 20) Based on the relationship of Equation 1-29, the null time of a certain spin population can be determined by measuring its  $T_1$  relaxation time. It is the time point after the first  $180^\circ$  rf pulse where MR signal amplitude crosses zero while recovering from negative to positive amplitude along the z-axis, as shown in Figure 1-11. If the second  $90^\circ$  pulse is applied exactly at the *null* point (setting the interval between pulses  $\tau$  as the *null* time  $t_{null}$ ), then the zero net

magnetization for that spin population along the  $z$ -axis is converted to the  $xy$ -plane and the detected signal (transverse magnetization) should be close to zero magnitude and appear dark on the image (signal is nulled). This process is presented in Figure 1-16 below.

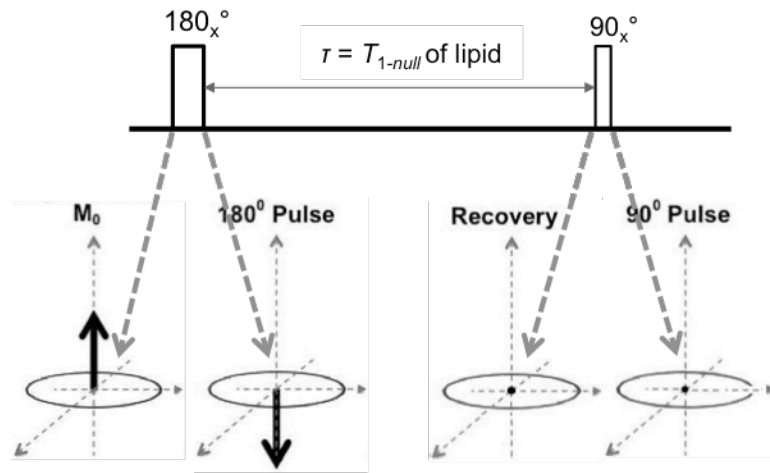


**Figure 1-16.** Symbolic representation of inversion-recovery pulse sequence and the working mechanism of a *null* point.

Specifically, by setting the IR interval  $\tau = t_{null}$  as the *null* time of nuclear spins in the environment of lipid or fat, unwanted signals of lipid or fat can be suppressed while maintaining the desired signals, e.g., water, as shown in Figure 1-17. There are drawbacks of suppression techniques utilizing inversion recovery sequences. For example, it may be difficult to distinguish fat from different compartments or tissue that has  $T_1$  similar to that of fat. It turns out this is not a problem for the application in Chapter 3. Other variations and applications of IR pulse sequences in medical imaging will not be introduced here.

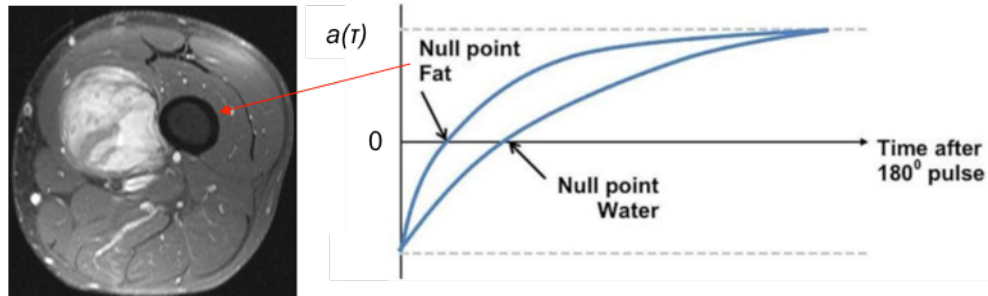


**Figure 1-17.** Illustration of *null* time differences due to different  $T_1$  relaxation times between water and fat signals. This is the basis of fat suppression using IR pulse sequences, and also is used to study nanoparticle diffusion (Chapter 3).(18)

### 1.6 General Aspects of MRI Contrast Agents

MRI contrast agents are widely used in clinical imaging. They provide extra contrast to the image by affecting relaxation times. The *in vivo* behavior of contrast agents is rather complicated and Chapter 3(18) involves their *in vitro* simple linear effects only. Therefore, only basic knowledge of contrast agents is introduced here, which is adequate for understanding their effects combined with those two pulse sequences illustrated in section 1.5.

MRI contrast agents shorten both  $T_1$  and  $T_2$ , or in other words, increase both longitudinal relaxation ( $1/T_1$ ) and transverse relaxation rates ( $1/T_2$ ). However, contrast agents are usually classified based on which relaxation process they affect more than the other.  $T_1$  agents are referred to those that increase the longitudinal relaxation rate to a much greater extent than transverse relaxation rate. As explained in section 1.4, the dominant  $T_1$  lowering effect gives rise to increases in signal intensity and thus they are called positive contrast agents. On the contrary,  $T_2$



agents largely increase the transverse relaxation rate ( $1/T_2$ ) by the surrounding environment and cause a reduction in signal intensity, which causes negative contrast in the image. Generally, paramagnetic gadolinium and manganese-based contrast agents are in the catalogue of  $T_1$  agents, including the first theranostic agent studied in both Chapters 2 and 3 (see section 1.7).<sup>(18, 21)</sup> The second theranostic agent used in Chapter 3 is an example of a  $T_2$  agent, which are mainly ferromagnetic and superparamagnetic iron oxide particles.

The theories of nuclear spin relaxation in paramagnetic and superparamagnetic systems are rather complicated and are outside the scope of this chapter.<sup>(22)</sup> The *in vitro* mechanisms by which contrast agents of both types behave have been the subject of extensive research, along with the development of new composites containing paramagnetic and superparamagnetic ions for MRI contrast agent applications.<sup>(23)</sup> Contrast agent behavior *in vivo* is quite complex and its effects can vary dramatically from *in vitro* observations. Considering the scope of this chapter, only the simple mechanism of gadolinium based contrast agents will be briefly explained below without introducing relaxation theories. The chemistry and *in vivo* physics of both  $T_1$  and  $T_2$  contrast agents will not be illustrated in great detail either. However, several key factors that are worth considering from the design aspects for gadolinium contrast agents will be summarized from studies of lanthanide chemistry, biophysics and molecular imaging.

In spite of different working mechanisms of contrast agents, in most cases the effect of these mechanisms can be evaluated by a single constant called relaxivity. The common way to quantify this effect is to consider the relaxation rates,

termed  $1/T_1$  ( $R_1$ ) and  $1/T_2$  ( $R_2$ ), and the concentration of contrast agent, as shown by Equation 1-30 and 1-31.

$$\frac{1}{T_1} = \frac{1}{T_{10}} + r_1[CA] \quad (1 - 30)$$

$$\frac{1}{T_2} = \frac{1}{T_{20}} + r_2[CA] \quad (1 - 31)$$

where  $T_1$  and  $T_2$  are the longitudinal and transverse relaxation times observed in the presence of contrast agent, and  $T_{10}$  and  $T_{20}$  are the relaxation times prior to the addition of contrast agent,  $[CA]$  is the concentration of contrast agent usually in the unit of mM, and  $r_1$  and  $r_2$  are longitudinal relaxivity and transverse relaxivity, respectively (usually both called relaxivity). The common unit of relaxivity is  $\text{mM}^{-1}\text{s}^{-1}$ . One cautionary note is that even in the simple case of a single biological compartment with pure linear relaxation, the *in vivo* effect of the contrast agent on the MR image is generally nonlinear due to many reasons such as limitations of the pulse sequence (especially when  $[CA]$  is high). In most cases relaxation itself within tissues is nonlinear even without introducing contrast agents. Therefore, relaxivity is a useful parameter that allows *in vitro* evaluations and ranking of various contrast agents. Increased relaxivity typically equates to greater contrast at an equivalent dose, or equivalent contrast at a lower dose, both of which are preferred situations for clinical applications. However, signal change is more complex *in vivo* than the simple linear relationships of Equation 1-30 and 1-31, due to both chemical and physical reasons. *In vivo* relaxivity is not a constant but depends strongly on the environment. For *in vitro* studies of contrast agents, it is critical and necessary to

measure  $r_1$  and  $r_2$  close to the condition (magnetic field, physiological temperature and pH values, tissues) of the targeted *in vivo* environment.

As an example of a simple mechanism for paramagnetic agents induce contrast in MRI, the conventional inner-sphere and second-sphere pathways by which gadolinium (III) (Gd) ion complexes enhance water relaxation will be introduced below. For most Gd-based contrast agents (both small molecules and macromolecules), the coordinated water molecule is essential to providing contrast.(24) The Gd (III) ion has an  $f^7$  electronic configuration with a high magnetic moment as well as a relatively slow electronic relaxation rate, which makes it most suitable as a relaxation agent for water protons. In a nutshell, there are two pathways by which the Gd-complex enhances water relaxation. There is an inner-sphere effect(25) by which the Gd-bound water is relaxed efficiently owing to the proximity of the coordinated water molecule. This water undergoes rapid chemical exchange with other solvent water molecules, so that the fast exchange enhances the relaxation rate of the bulk water, which is the second pathway. Through the second pathway, water not contained in the first coordination sphere of the Gd-complex can also be relaxed by the metal ion. Those water molecules fall into two groups: second-sphere water(25) and outer-sphere(25) water. Second-sphere water designates water molecules that are in the hydration shell of the complex and have a lifetime in the second sphere longer than the time constant for the water molecule and the Gd-complex to diffuse past each other. The outer-sphere water is not associated with the Gd-complex but is diffusing nearby. Both second- and outer-sphere water are termed outer sphere in many discussions.(24) In summary, both

inner-sphere relaxivity and outer-sphere relaxivity contributes to the total relaxivity, which is an important basis for understanding relaxation enhancement by paramagnetic metals *in vivo*.

In brief, for gadolinium based MRI contrast agents, the most critical parameter influencing relaxivity is rotational motion, as a result of the fact that relaxivity strongly depends on rotational dynamics. Because relaxivity is dependent on molecular motion, which is affected by molecular size, rigidity, and possible binding with biological macromolecules, relaxivity has to be optimized on a case-by-case basis. A contrast agent of high relaxivity by itself may not give expected effects after being conjugated with a targeting molecule or vector. Therefore the rotational dynamics and flexibility of the final complex containing the contrast agent are crucial for practical *in vivo* applications.(26) Furthermore, fast water exchange and high hydration level may enhance relaxivity as well. For example, approaches such as linking multiple gadolinium complexes using polymers have been reported in order to achieve isotropic and slow rotational dynamics (owing to increased molecular weight) and hence increased relaxivity, as well as to achieve molecularly targeted imaging.(27, 28)

### **1.7 Brief Introduction to Polymeric Theranostic Nanoparticles**

Comprising MRI contrast agents in a drug delivery system can incorporate diagnostic functions, which may benefit drug transport and disease treatment. The polymer based drug delivery systems investigated in Chapters 2 to 4 are introduced

in this section. Background and motivation of the quantification study in Chapter 2 are also described here.

The term theranostics was not coined in the academic field, but first used by John Funkhouser, president and CEO of PharmaNetics in addressing his company's business model in developing diagnostic tests directly linked to the application of specific therapies. Although this term was initially used to advertise its distinction from traditional diagnostic products, theranostics has been widely used in recent scientific publications.

In general, theranostics is referred to as a treatment strategy that combines therapeutics with diagnostics, with the intention to monitor the response to treatment as well as to improve drug efficacy and safety. Nanoparticles have several advantageous properties that can provide realization of such theranostic agents: for example, the nanometer size that extends their circulation time (addressed below in section 1.8), and the high surface-area-to-volume ratio that yields high loading capacity for therapeutic drugs and imaging agents as well as provides space for surface functionalization.

In Chapter 2 and 3, two major types of polymer-based nanotheranostic agents are investigated, which will be briefly introduced in the current section. The first type contains two polycation-based DNA delivery systems developed by the Reineke group,<sup>(18, 21, 29, 30)</sup> which are carbohydrate-based poly(amidogalactaramine) G4 and lanthanide-containing theranostic polymers. Their chemical structures are shown in Figure 1-18. Strictly speaking, only the second particle contains the

diagnostic function, but since those two particles have similarities in structure and application, they will be introduced together below.

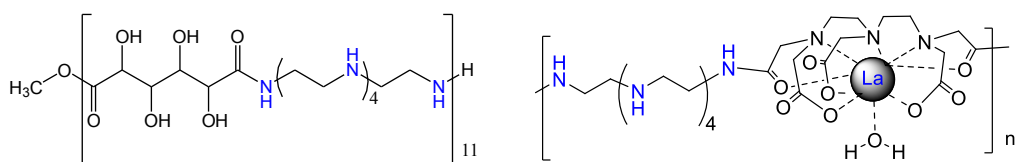


**Figure 1-18.** Structures of polymers G4 (left) and N<sub>4</sub>La containing lanthanide metal ions (right).

Those two polymers are examples of one category of gene-delivery vehicle, synthetic vectors (the other category is recombinant viruses), which can be further divided into polymers and lipids. Non-viral nucleic acid delivery offers promise for a variety of research and therapeutic applications.<sup>(31-33)</sup> Over the last two decades a large variety of polymeric delivery systems have been created and studied.<sup>(34, 35)</sup> In practice, delivery vehicles are needed to compact nucleic acids into small nanoparticles to facilitate cellular uptake,<sup>(36)</sup> protect nucleic acids from enzymatic degradation,<sup>(37, 38)</sup> and can be designed to target delivery to various tissue types.<sup>(39, 40)</sup>

Leaving viral vectors out of the discussion, cationic polymers have great potential for human gene therapy. First of all, DNA binding motifs (primary, secondary, tertiary and quaternary amines and amidines) can reside in the polymer backbone, in pendant groups as well as in grafted oligomers. Secondly, the flexible structures of polymers make multiple functions possible, including efficient gene delivery, biocompatibility and stable formulation.<sup>(32)</sup> However, the major

disadvantage is their insufficient gene-transfer. In fact, the aim of Chapter 2 is to offer a simple and robust quantitative characterization method for one common strategy toward gene transfer efficiency.(21)

Polycationic polymers bind via electrostatic interactions with the negative phosphodiester backbone of the nucleic acid and form nanoparticles termed polyplexes. This process is entropically favored via the release of counterions from both the polycation (delivery vehicle) and polyanion (nucleic acid) backbone.(41, 42) Figure 1-19 shows the symbolic representation of polyplex formation and a TEM image of polyplex particles.

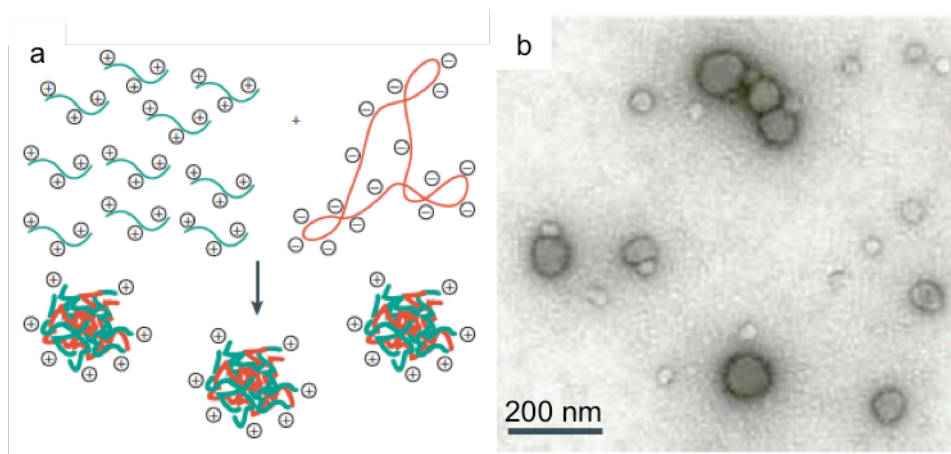


**Figure 1-19.** (a) Schematic presentation of polyplex formation. (b) Transmission electron micrograph of polyplexes. Figure reproduced from Pack et al.(32)

The common strategy for improving gene delivery is to add an excess of polycation in the polyplex formulation.(43, 44) The mechanism of how increasing polycation amount can facilitate gene transfer is explained below. Gene delivery vectors need to face extracellular barriers and intracellular barriers. Figure 1-20 presents schematically the barriers to intracellular trafficking of polyplexes. In

Figure 1-20, endolysosomal escape is the step where adding excess polycationic polymer is proposed to overcome this barrier through a mechanism called proton-sponge. After polyplexes (containing polymers and DNA) are internalized via endocytosis, they become localized within endocytic vesicles that represent a hostile environment for the polyplexes (e.g. high acidity). For example, endocytic vesicles transport the internalized materials back to the cell membrane and out of the cell, or degraded DNA can be trapped inside and destroyed with acidic degradative enzymes. Therefore only DNA that escapes from those endosome vesicles into the cytoplasm (see Figure 1-20) can reach the nucleus.

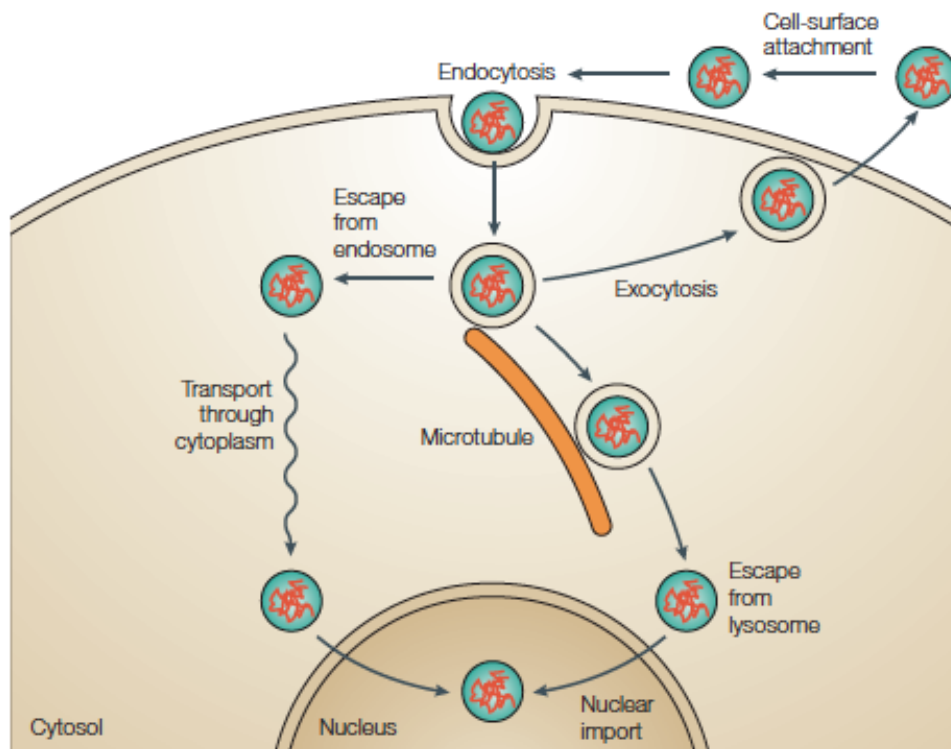


**Figure 1-20.** Intracellular barriers to gene delivery by polyplexes. For successful delivery, polyplexes first need to attach to the cell surface, be internalized by endocytosis, escape from endolysosomes (same term as endosome in figure), move



through the cytoplasm toward the nucleus and cross the nuclear membrane. Figure reproduced from Pack et al.(32)

As illustrated in Figure 1-21, certain polymers containing a large number of secondary and tertiary amines exhibit  $pK_a$  values between physiological pH of  $\sim 7$  and lysosomal (one type of endosome vesicles) pH of  $\sim 4.5$ . The vesicle lysosome is acidified by the action of an ATPase enzyme that actively transports protons from the cytosol (see Figure 1-20) into the vesicle. Certain polymers on the other hand can prevent this acidification process of the vesicle lysosome through their protonation. As a result, ATPase will transport more protons, in order to reach the desired low pH. Eventually the accumulation of protons in the vesicle is balanced by an influx of counter ions, and the increased counter ion concentration causes osmotic swelling and the vesicle membrane ruptures, so that polyplexes containing DNA are able to escape into the cytosol where they can further go on to reach the nucleus. This hypothesis is called the proton-sponge mechanism. The purpose of the study in Chapter 2 is to determine the absolute amount of excess polymer added that would serve to mediate endosomal escape through the proton-sponge mechanism.

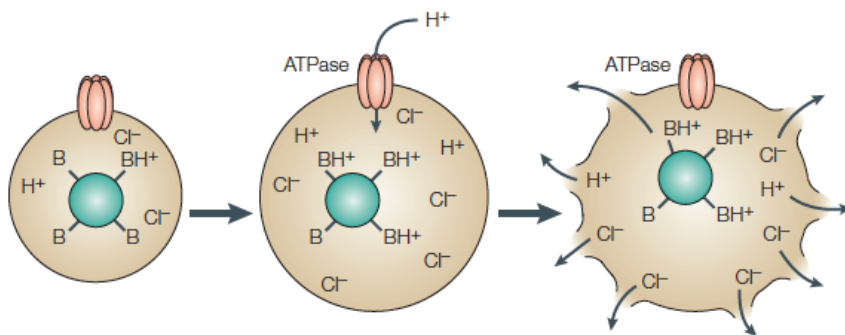


**Figure 1-21.** Symbolic representation of proton-sponge hypothesis. The brown circle represents the endocytic vesicle, inside which the polymer is shown in green. Figure reproduced from Pack et al.(32)

The second theranostic agent (see structure in Figure 1-18, right) developed by the Reineke group combines delivery of nucleic acids and MRI contrast agents. The structure contains a lanthanide-binding domain (diethylenetriamine-pentacetic acid) and an oligoethyleneamine domain that comprises secondary amines (proton-sponge polymers). This vector supports a flexible design so that the lanthanide-binding domain can chelated either gadolinium (Gd), as an MRI contrast agent or luminescent europium (Eu) for visualization with fluorescence microscopy.

Without binding DNA, this polymeric nanoparticle itself is worth investigating because it combines imaging and drug delivery properties. In Chapter 2, the lanthanide-binding domain is chelated to the non-paramagnetic lanthanum ion, for quantitative analysis from observed 1D NMR spectroscopy signals. In Chapter 3, the lanthanide-binding domain is chelated to paramagnetic gadolinium to form a MRI contrast agent, in order to probe its transport through MRI image intensity variations.(18)

In order to study polymer-based nanoparticle diffusive transport in biological hydrogels, a second type of polymer-based theranostic agent developed by the Riffle group(45-47) is also probed in Chapter 3.(18) The second vector (structure shown in Figure 1-22) is a magnetic block ionomer complex (MBIC) comprised of 8-nm diameter magnetite nanoparticles in the core surrounded by a

double corona structure with a nonionic poly(ethylene oxide)-*b*-acrylate (PEO-*b*-PAA) shell and anions are bound to nanomagnetite *via* ligand absorption. The unbound negatively charged carboxylates provide binding sites for drug loading through ionic complexation.(46) The superparamagnetic Fe<sub>3</sub>O<sub>4</sub> particle core provides primarily transverse relaxivity ( $r_2$ ) contrast.

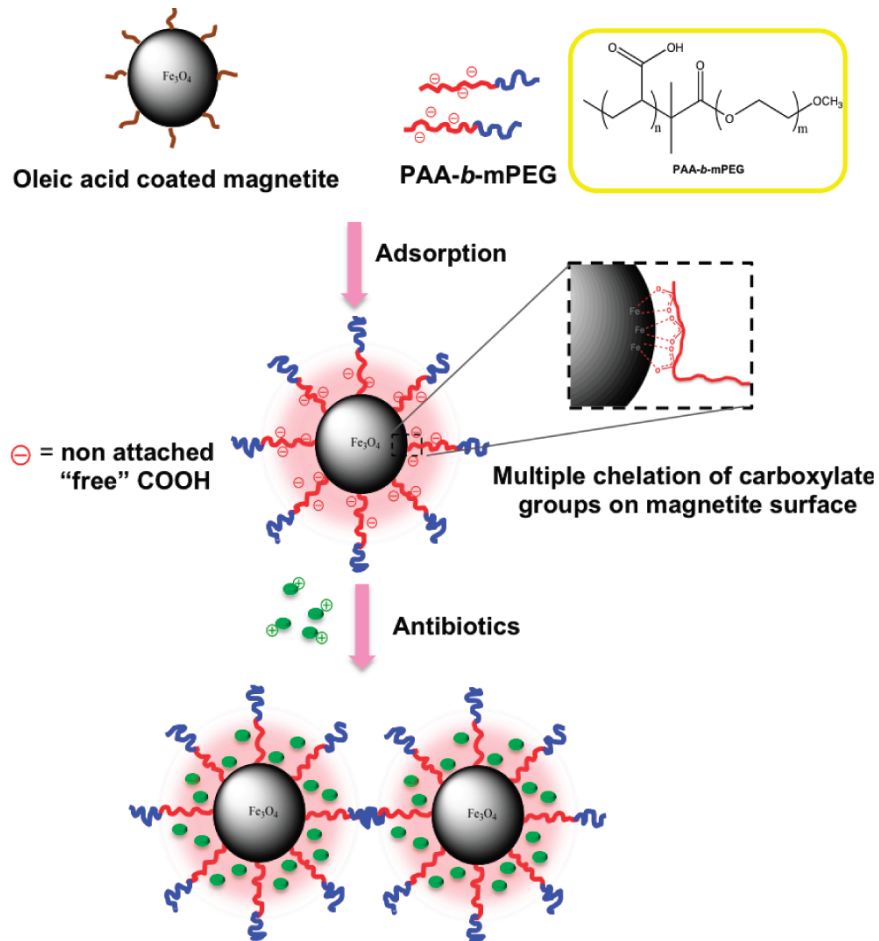


**Figure 1-22.** Structure and synthesis of MBICs. Drug loading can be realized by electrostatic interactions of surplus charged groups. Figure reproduced from Pothayee et al.(46)

The size distribution and the surface charges of the last two nanoparticles introduced in this section will be discussed in Chapter 3, where their transport in hydrogels will be investigated and related to their properties.

### **1.8 Overview of Nanoparticles Transport in Solid Tumors**

The motivation for the diffusion study in Chapter 3 is to provide implications and pilot experiments to support *in vivo* tracking of theranostic nanoparticles transport into the tumor interstitium. This study measures diffusion rates and concentration distributions of two types of polymeric nanoparticles, each of which contain MRI contrast agents, over macroscopic (cm-scale) distances in tumor-tissue-mimetic hydrogels *via* time-resolved MRI. As necessary background, the processes of and barriers to nanoparticle transport in solid tumors will be briefly discussed in this section.

Delivery of small molecules and nanoparticles from systemic (vascular) circulation into cancer cells involves a three step pharmacokinetic process, as shown in Figure 1-23.(48-50) First, particles flow to different regions of tumors via blood vessels. Then those particles need to cross the vessel wall, and finally penetrate through the interstitial space to reach their target cells. The delivery of diagnostic and therapeutic agents in tumor tissue is considerably different compared with that in normal tissue. These principle steps are relatively efficient for normal tissues, whereas the abnormal physiology of tumors causes transport barriers that restrict delivery of therapeutic agents. Considering the scope of this section and the fact that no real biological tissue has been used in Chapter 3, the

discussion below will ignore the effects of agent consumption on drug transport and distribution, including the processes of binding, metabolism and sequestration.

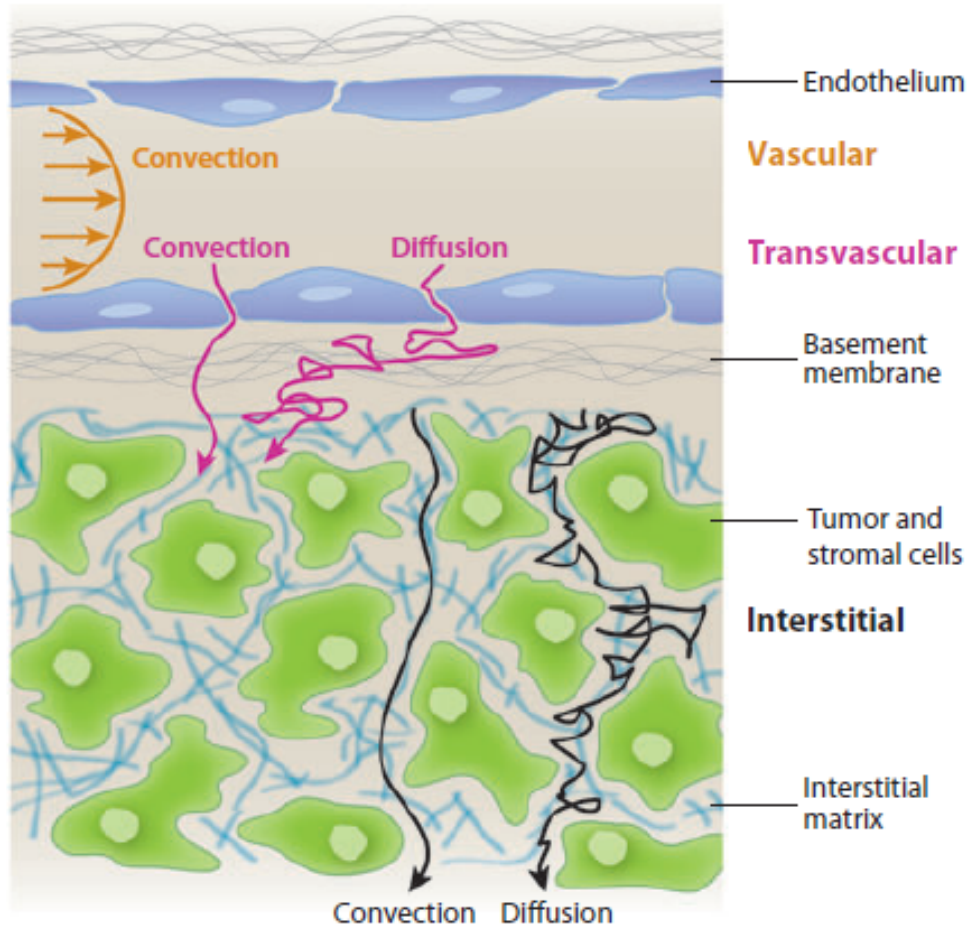


**Figure 1-23.** Schematic representation of transport steps in a tumor tissue unit consisting of blood vessels and surrounding tissue. Figure reproduced from Jain et al.(51)

As shown in Figure 1-23, interstitial transport is the penetration and distribution of drugs through tumor tissue toward their target cells following transvascular transport. Interstitial transport occurs through the combination of diffusion and convection. However, convective transport is negligible except at the

tumor margin, the reasons for which will be explained below. Inside tumors, the lack of functional lymphatic vessels and the vascular hyperpermeability results in interstitial hypertension. This uniformly elevated interstitial fluid pressure (IFP) eliminates pressure gradients inside the tumor, and that significantly reduces the fluid velocity of convection.(52-54) Therefore, the main mechanism of transport within a tumor is not convection but diffusion, which is also the subject of investigation in Chapter 3.

Moreover, the tumor interstitial matrix consists of a highly interconnected network of collagen fibers interacting with other molecules. Small molecules can diffuse rapidly in the tumor interstitial matrix, but the diffusion of nanosized particles (10-200 nanometers for representative theranostic agents) is considerably hindered as a result of their interactions with the dense viscoelastic fiber matrix.(55-57) The diffusion rate of a nanoparticle in the tumor interstitium correlates with its size, surface charge, configuration, as well as the content and structure of collagen fibers.(58-62) In Chapter 3, the effects of size and charge of diffusing nanoparticles as well as the collagen content on diffusion rate are investigated.

Although diffusion of large particles through tumor tissue is decreased due to particle interactions with the interstitial matrix, one remarkable advantage of nanoscale therapeutic agents is that they provide potential selective delivery to tumors due to the enhanced permeability and retention (EPR) effect.(63) In a nutshell, tumor vasculature has abnormal organization, with a structure that leads to tortuous and leaky vessels as well as heterogeneous blood flow. Because tumor

blood vessels have relatively large pores, the vascular permeability and hydraulic conductivity are notably higher in tumor than in normal tissues. Nanoparticles extravasate into a tumor from those large pores in the tumor blood vessels, but cannot enter easily into normal tissues. Therefore the EPR effect enables preferential delivery of nanoparticles to tumor sites via tumor vessels as compared to normal tissues. Enhanced retention of nanoparticles compared to small molecules is also observed due to this effect, but the physiological mechanism will not be explained here.

Caution should be taken when utilizing the EPR effect to argue the preferential application of nanoparticles for anti-cancer drug delivery. First of all, not all tumor vessels are leaky, so the heterogeneous distribution of vessel pore sizes may cause heterogeneous extravasation and transvascular delivery.<sup>(64)</sup> Secondly, for transvascular transport where convection occurs, the transport of large size nanoparticles can be significantly hindered by uniformly elevated IFP, which compromises the benefits of the EPR effect. Lastly, as mentioned above, diffusion of nanoparticles in the tumor interstitial matrix decreases dramatically with the increase of particle size. In many tumors, particles larger than 60 nm in diameter are not able to diffuse through collagen matrix effectively.<sup>(65)</sup> Indeed, the most important implication that the study in Chapter 3 carries is that although countless design and formulations of nanosized therapeutic or theranostic agents for cancer treatment have been proposed and published recently, the majority of those agents do not have sufficient efficacy to reach cancer cells. Therefore, it is critical to consider the transport barriers and develop corresponding strategies to

improve delivery, in order to move the research on nanotherapeutics closer to *in vivo* applications.

### **Part III. PFG-NMR and Polymer Molecular Weight Determination**

#### **1.9 Introduction to Pulsed-Field-Gradient NMR Diffusometry**

Pulsed-field-gradient NMR diffusometry has widespread application in polymer characterization and is commonly used in industrial research on polymeric materials as well. An introduction to the basic principles of PFG-NMR is presented here, with reference to magnetic field gradients described above in section 1.3.

As discussed in section 1.3.1, the Larmor frequency is proportional to the magnetic field strength (Equation 1-1) and this provides the basis for measuring *molecular self-diffusion* using magnetic field gradients by labeling the position of a nuclear spin using the Larmor frequency. The original pulse sequence for PFG-NMR is the Stejskal-Tanner sequence(66) developed on the basis of the Hahn spin-echo pulse sequence.(13) As represented by Equation 1-24 in section 1.3.4, in the presence of a gradient field along the z-axis in parallel with the static field  $\mathbf{B}_0$ , the phase accumulation at time  $t$  is proportional to displacement along the  $z$  direction. Mathematically, based on Equation 1-11, the precession phase accumulation  $\omega t$  is given by

$$\phi(t) = \gamma \mathbf{B}_0 t + \gamma g t, \quad (1 - 32)$$

where the first term corresponds to the phase evolution due to the static field  $\mathbf{B}_0$ , and the second term represents the phase accumulation caused by the gradient  $g$ , in accordance with Equation 1-24. It is shown by Equation 1-32 that the phase



evolution and thus dephasing due to the gradient effect is proportional to the gyromagnetic ratio of the nucleus  $\gamma$ , duration of the gradient  $t$ , as well as the displacement of nuclear spins along the direction of the gradient.

With the effect of gradient field on phase evolution of nuclear spins corresponding to their spatial position/displacement (introduced in section 1.3.4 and restated above), it should not be difficult to qualitatively understand the mechanism of the Stejskal-Tanner sequence. This sequence is shown symbolically in Figure 1-24. Unlike the continuous gradient in Figure 1-9, gradients are applied as pulses in the Stejskal-Tanner sequence for several reasons, including avoiding line broadening, refocusing gradient pulse errors via the echo, as well as allowing the use of large gradients to measure slow diffusion.

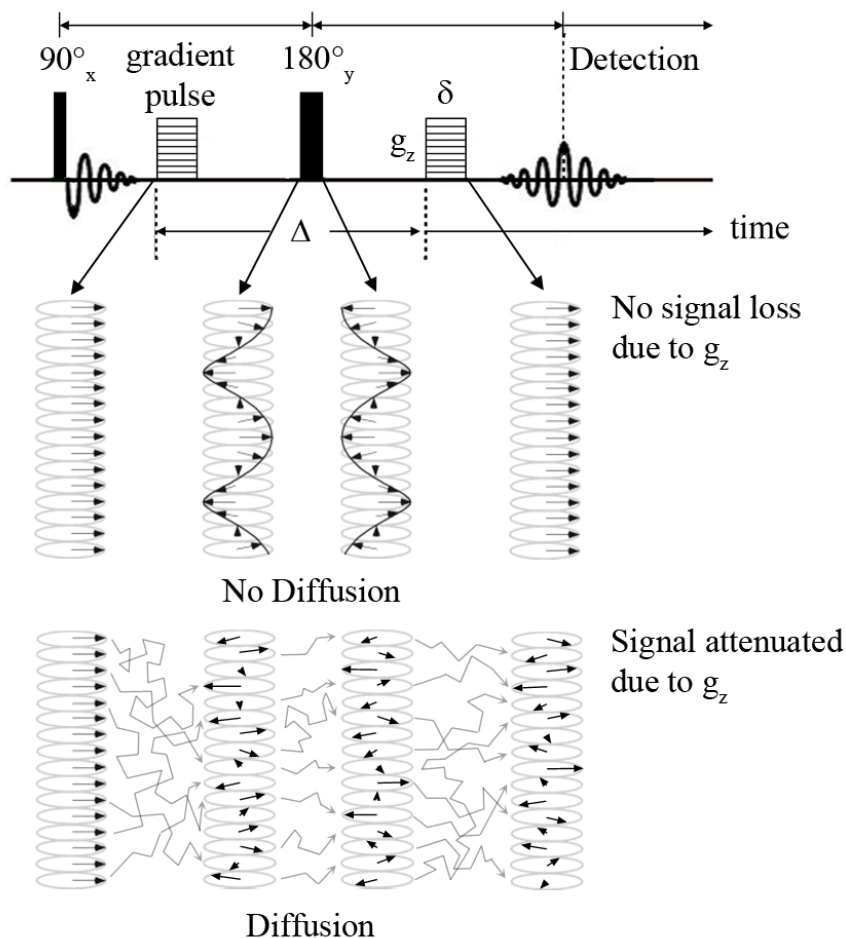


**Figure 1-24.** A symbolic illustration of measurement of diffusion using the Stejskal-Tanner sequence. The pulsed gradient along the  $z$  direction has amplitude  $g_z$  and duration  $\delta$ .  $\Delta$  is the time period between the leading edges of both gradient pulses.

In fact, Figure 1-9 represents the first half of this pulse sequence until the end of the first  $\tau$  period, where spins at different positions along  $z$ -axis have obtained different phase accumulations besides the effect of static field, due to the effect of the first gradient pulse. Subsequently, a  $180^\circ$  rf pulse is applied in order to reverse the direction of nuclear spin precession and phase evolution (a spin echo, see section 1.4), symmetrically in the time domain centered by the  $180^\circ$  rf pulse, a

second gradient pulse of equal magnitude and duration as the first one is applied. This causes the same phase accumulations of the nuclear spins as gained through the effect of the first gradient, only in the opposite direction. The helix formed (shown in Figure 1-9) is unwound and nuclear spins are in phase again, as in their initial state immediately after the  $90^\circ$  rf pulse. In other words, the phase evolutions symmetrically gained on either side of the  $180^\circ$  rf pulse due to the two gradient pulses should cancel and result in unchanged signal for nuclear spins localized at the same position during the pulse, that is, if there is no translational motion along the z-axis. However, in a diffusing liquid, soft solid, or gas, the nuclear spins experience translational diffusion and are displaced along the direction of the gradient. Consequently this leads to the loss of phase coherence (dephasing), whose degree is proportional to the displacement along the gradient direction during the time period between the end of the first and the beginning of the second gradient, termed the diffusion time  $\Delta$ . For the study in Chapter 4, the slightly modified version of Figure 1-24, the pulsed-gradient stimulated echo (PGSTE) pulse sequence(67) is used for diffusion measurements.

Basically, diffusion perturbs the winding and unwinding of the helix shown in Figure 1-9 and 1-24, leading to an increasingly random distribution of phases of nuclear spins as a function of diffusion coefficient and the pulse sequence parameters. This partially randomized phase distribution results in loss of signal. The loss of signal is reflected by attenuated MR signal averaged over the ensemble of nuclear spins in the sample.

Considering the scope of this section, the final equation of the Stejskal-Tanner pulse sequence in the presence of free diffusion will be given without detailed derivation.

$$\ln(E) = -\gamma^2 g^2 D \delta^2 (\Delta - \delta/3), \quad (1 - 33)$$

where  $E$  represents the signal attenuation (ratio between signal with gradients on and off respectively),  $D$  is the diffusion coefficient in units of  $\text{m}^2/\text{s}$  or  $\text{cm}^2/\text{s}$ ,  $\delta$  is the gradient duration, and  $\Delta$  the diffusion time defined above.

Equation 1-33 can be applied to unrestricted isotropic (free) diffusion directly to derive the isotropic diffusion coefficient along the gradient direction. In many cases, diffusion of the probing species is restricted and presents anisotropy on the investigated time scale ( $\Delta$ ) as a result of confined geometry.(5) In these cases, magnetic gradient techniques can also provide structure information of the diffusing media besides molecular motion, with more complicated mathematical treatment and approximations.(68, 69) Since only free diffusion is considered in Chapter 4, the description of PFG-NMR for restricted and anisotropic systems will be omitted here.

### **1.10 Overview of Translational Diffusion in Liquids**

Molecular diffusion coefficients are the subject of investigations for studying polymer motion in solution (Chapter 4), and diffusive transport is an essential factor that determines rates of molecular movement as well as concentration distributions in aqueous environments (Chapter 3), where most biological processes occur. In this section, the concept of free diffusion will be described as well as the Stokes-Einstein equation that correlates diffusion coefficient with diffusing species size.

The modern concept of diffusion is based on Einstein's theoretical study of Brownian motion.(70) It is necessary to introduce Einstein's derivation of the diffusion equation, so the interpretation of this derivation from Callaghan(9) will be borrowed here.

Brownian particles in suspension behave like the molecules in an ideal gas, with pressure  $k_B T n$ , where  $n$  is the number of Brownian particles per unit volume. Considering a small displacement  $\delta x$  of a Brownian particle under a net force, then

$$\delta F = \delta U - T \delta S = 0 \quad (1 - 34)$$

where  $F$  represents the Helmholtz free energy (at constant volume and temperature),  $U$  represents the internal energy,  $S$  represents the entropy, and  $T$  is temperature. Taking a cuboid of unit area normalized along the  $x$ -axis with boundary  $x = 0$  and  $x = l$ , the total energy/work done in this volume is  $-\int_0^l K n \delta x dx$ , where  $K$  is the net force resulting from collisions of surrounding water molecules on Brownian particles. Using the ideal gas result shown by Equation 1-35,

$$\delta S = k_B \frac{\delta V}{V} = k_B \frac{\partial \delta x}{\partial x} \quad (1 - 35)$$

the entropy change can be written as

$$\delta S = k_B \int_0^l n \frac{\partial \delta x}{\partial x} dx = -k_B \int_0^l \frac{\partial n}{\partial x} \delta x dx \quad (1 - 36)$$

By substituting total energy change  $-\int_0^l K n \delta x dx$  and entropy change (Equation 1-36) into Equation 1-34, one has

$$K n = k_B T \frac{\partial n}{\partial x} \quad (1 - 37)$$

where  $K$  is the net force defined above.

Before continuing with the discussion of Brownian motion, the diffusion coefficient will be introduced through Fick's law. Adolf Fick presented the idea that the process of diffusion can be envisaged as a flux of particles arising from a gradient in concentration.(71) The flux of particles may be written for a specified local concentration of particles  $n(\mathbf{r}, t)$  as

$$\mathbf{J} = -D\nabla n(\mathbf{r}, t) \quad (1 - 38)$$

in units of amount of substance per unit area per unit time, for example  $\text{mol m}^{-2}\text{s}^{-1}$ . Here,  $n$  is the mole of particles per unit volume as a function of position vector  $\mathbf{r}$  and time  $t$ , and  $D$  is the *diffusion coefficient* in units of  $\text{length}^2 \text{time}^{-1}$ , for example  $\text{m}^2\text{s}^{-1}$ . The flux along dimension  $x$  can be written as

$$J_x = -D \frac{\partial n}{\partial x} \quad (1 - 39)$$

and Equation 1-39 is known as Fick's first law.

Conservation of number of particles requires that the time rate of concentration change is related to the local flux derived from within the vector field,  $-\nabla \cdot \mathbf{J} = \partial n / \partial t$ . By substituting Equation 1-38 into this relationship, one obtains Fick's second law, represented by Equation 1-40, which is also known as the diffusion equation.

$$\frac{\partial n}{\partial t} = D\nabla^2 n \quad (1 - 40)$$

Fick's laws describe molecular motion as a consequence of concentration gradients, sometimes this process is defined as *mutual diffusion* in the sense that it requires fluxes of both solute and solvent particles in opposite directions to conserve the overall mass density. However, the idea can be applied also to the

motion of Brownian particles in suspension or solution, which is defined as *self-diffusion*.

Returning to the previous discussion on Brownian particles, in analogy to the idea stated in preceding paragraph, the flow of Brownian particles caused by the net force needs to be balanced by a diffusion current in the opposite direction to maintain an equilibrium concentration. Defining  $\zeta$  as the friction, a single particle velocity is  $K/\zeta$ , and the particle current crossing a unit area per unit time is  $nK/\zeta$ . To balance this flow, a self-diffusion flow in the opposite direction is defined by  $-D \partial n/\partial x$ . So the balance between the counteracted flows is

$$\frac{Kn}{\zeta} - D \frac{\partial n}{\partial x} = 0 \quad (1 - 41)$$

By substituting  $Kn$  by Equation 1-37, one obtains

$$D = \frac{k_B T}{\zeta} \quad (1 - 42)$$

By choosing  $\zeta$  of a spherical particle of radius  $R$  in a medium of viscosity  $\eta$ ,  $\zeta = 6\pi\eta R$ , (72) and so one obtains the Stokes-Einstein Equation.

$$D = \frac{k_B T}{6\pi\eta R} \quad (1 - 43)$$

This equation applies well to the diffusion of very large spherical molecules in solvents of low molecular weight(73) and to suspended particles. For the cases where the solute and solvent are similar in size, correlations have been made with the same temperature and viscosity dependence as Equation 1-43.

### 1.11 Brief Introduction to Molecular Weight Measurement of Polymers

In Chapter 4, PFG-NMR has been used to determine the molar mass of the polyanions, which presents another substantial challenge for molecular weight measurements using traditional size exclusion chromatography (SEC). Fundamental concepts of polymer molecular weights and determination methods will be briefly introduced in this section based on Rubinstein's book.<sup>(74)</sup> Basic properties of polyelectrolyte solutions will be briefly sketched in Appendix 1 in order to correlate their distinct properties in solution to the measurement of diffusion coefficients.

One distinguishing property of most polymers compared with small molecules is their polydispersity. Synthetic polymers are composed of individual molecules with a distribution of degrees of polymerization. The polydispersity of a polymer sample is usually represented by its molar mass distribution.

For molecules with a certain molar mass  $M_N$ , its weight fraction over all degrees of polymerization  $N$  can be expressed as

$$w_N = \frac{n_N M_N}{\sum_N n_N M_N} = \frac{c_N}{c} \quad (1 - 44)$$

where  $n_N$  is the number/mole fraction of molecules containing  $N$  monomers,  $c_N$  is the mass per unit volume of molecules with degree of polymerization  $N$ , and  $c$  is the total mass concentration.

Another definition related to molar mass is the  $k$ th moment of the number fraction distribution given by

$$m_k = \sum_N n_N M_N^k \quad (1 - 45)$$

Thus the zeroth moment is



$$m_0 = \sum_N n_N = 1 \quad (1 - 46)$$

Two average molar masses will be introduced here: the number-average molar mass  $M_n$  and the weight-average molar mass  $M_w$ . The number-average molar mass  $M_n$  is defined as the ratio of the first to the zeroth moments of the number fraction distribution, and the expression based on Equation 1-45 and 1-46 is

$$M_n = \sum_N n_N M_N \quad (1 - 47)$$

The weight-average molar mass  $M_w$  is the ratio of the second and the first moments of the number fraction distribution,

$$M_w \equiv \frac{m_2}{m_1} = \frac{\sum_N n_N M_N^2}{\sum_N n_N M_N} = \frac{\sum_N n_N M_N^2}{M_n} \quad (1 - 48)$$

where the definition of  $M_n$  (Equation 1-47) is used in the last relationship. By substituting Equation 1-47 into Equation 1-44, one obtains the relationship between the number fraction  $n_N$  and weight fraction  $w_N$  of a polymer with  $N$  monomers:

$$w_N = \frac{M_N}{M_n} n_N \quad (1 - 49)$$

Using this relationship, Equation 1-48 can be rewritten as

$$M_w = \sum_N w_N M_N = \sum_N \frac{c_N}{c} M_N \quad (1 - 50)$$

The polydispersity index  $P$  is defined as the ratio of the weight-average and number-average molar masses  $M_w/M_n$ . In Chapter 4, polydispersity is not measured due to limited signal intensity from the dilute polyanion samples and the relatively low field NMR spectrometer with a standard probehead. However, with

enough NMR signal-to-noise ratio, one can use PFG-NMR diffusometry to measure the polydispersity of polymers via measuring the molar mass distribution.

Common methods for the determination of average molar masses and molar mass distributions are summarized in Table 1-1.

**Table 1-1. Common characterization methods of polymer molar mass.**

Reproduced from Rubinstein.(74)

Method	Absolute	Relative	$M_n$	$M_w$	$A_2$	Range (g mol <sup>-1</sup> )
End group analysis	×		×			$M_n < 10\,000$
Vapor pressure osmometry	×		×		×	$M_n < 30\,000$
Cryoscopy	×		×		×	$M_n < 30\,000$
Ebulliometry	×		×		×	$M_n < 30\,000$
Membrane osmometry	×		×		×	$20\,000 < M_n$
Light scattering (LS)	×			×	×	$10^4 < M_w < 10^7$
Intrinsic viscosity (IV)		×				$M < 10^6$
SEC <sup>a</sup> with <i>c</i> detector		×	×	×		$10^3 < M < 10^7$
SEC <sup>a</sup> with <i>c</i> and LS detectors	×			×		$10^4 < M < 10^7$
SEC <sup>a</sup> with <i>c</i> and IV detectors		×	×	×		$10^3 < M < 10^6$
MALDI-TOF-MS <sup>b</sup>	×		×	×		$M < 10\,000$

<sup>a</sup>SEC, size exclusion chromatography. <sup>b</sup>MALDI-TOF-MS, matrix-assisted laser desorption/ionization time-of-flight mass spectroscopy.

The molar mass measured by PFG-NMR (not listed in Table 1-1) but as presented in Chapter 4 is the weight-average molar mass  $M_w$ . For polyelectrolytes, the characterization of molecular weights presents a substantial challenge, since polyelectrolytes pose difficulties for traditional size exclusion chromatography (SEC).(75, 76) The strong ionic interactions in polyelectrolyte solutions cause intramolecular chain expansion and electrostatic interactions with the stationary phase, which make it much more difficult to use SEC for the characterization of

polyelectrolytes in aqueous solutions than for neutral polymers. As a consequence, such measurements usually require improved SEC detectors, as well as specific optimal solvents and columns for each polyelectrolyte, and yet still can yield unsatisfying accuracy. Even for neutral polymers, chromatographic methods such as GPC have their drawbacks. For example, GPC measurements usually consume large quantities of organic solvents and require regular calibrations. High cost GPC columns and detectors are also practical disadvantages. PFG-NMR diffusometry shows promise for alleviating many of these problems for both neutral and charged polymers and providing more efficient polymer molecular weight measurements.

For polyelectrolytes, PFG-NMR can be employed to measure molar masses in solution without the influence of the ionic interactions. As a common NMR technique, end group analysis (listed in Table 1-1) has been widely used to measure number-average molar mass  $M_n$ , but this method is limited only to low molecular weight polymers (usually  $\sim 20,000$  g/mol or less), and only on samples without overlapping of end group and backbone NMR signals. PFG-NMR has also been utilized as a powerful tool to study solution-state interactions of macromolecules, and can provide diffusion coefficients that are related to molecular size and weight. The correlation between polymer molar mass and self-diffusion coefficients was originally proposed by Callaghan et al.(77) and was used to measure the size and shape of amylopectin. The dependence of molar mass  $M_w$  on self-diffusion coefficient  $D$  for a monodispersed polymer system(78) is described in Equation 1-51, which can be linearized as Equation 1-52. Parameters  $A$  and  $\alpha$  vary for different polymer systems, and therefore calibrations based on standard polymer samples

with known molar masses (from synthesis) will be needed for different polymer systems prior to the determination of sample molecular weight.

$$D = AM^\alpha \quad (1 - 51)$$

$$\log D = \alpha \log M + \log A \quad (1 - 52)$$

This method has been used to measure the molar masses of uncharged polymers as well as their molecular weight distribution and polydispersity.(78-81) PFG-NMR has been implemented in the study of Chapter 4 to solve a long-standing problem in polymer science – that of measuring molar masses of ionic polymers. This work appears to be the first reported study to apply this technique to measure the molar mass of charged polymers.

## References

1. E. M. Purcell, H. C. Torrey, R. V. Pound, Resonance Absorption by Nuclear Magnetic Moments in a Solid. *Physical Review* **69**, 37-38 (1946).
2. F. Bloch, W. W. Hansen, M. Packard, The Nuclear Induction Experiment. *Physical Review* **70**, 474-485 (1946).
3. J. Keeler, *Understanding NMR spectroscopy*. (John Wiley & Sons, 2011).
4. R. R. Ernst, Methodology of magnetic resonance imaging. *Quarterly Reviews of Biophysics* **19**, 183-220 (1987).
5. P. T. Callaghan, *Principles of nuclear magnetic resonance microscopy*. (Clarendon Press Oxford, 1991), vol. 3.
6. P. Mansfield, P. K. Grannell, NMR 'diffraction' in solids? *Journal of Physics C: Solid State Physics* **6**, L422 (1973).
7. M. A. Bernstein, K. F. King, X. J. Zhou, *Handbook of MRI pulse sequences*. (Elsevier, 2004).
8. M. A. Brown, R. C. Semelka, *MRI: basic principles and applications*. (John Wiley & Sons, 2011).
9. P. T. Callaghan, *Translational dynamics and magnetic resonance: principles of pulsed gradient spin echo NMR*. (Oxford University Press, 2011).
10. K. P. Pruessmann, M. Weiger, M. B. Scheidegger, P. Boesiger, SENSE: sensitivity encoding for fast MRI. *Magnetic Resonance in Medicine* **42**, 952-962 (1999).
11. M. Lustig, D. L. Donoho, J. M. Santos, J. M. Pauly, Compressed sensing MRI. *Signal Processing Magazine, IEEE* **25**, 72-82 (2008).
12. M. H. Levitt, *Spin dynamics: basics of nuclear magnetic resonance*. (John Wiley & Sons, 2001).
13. E. L. Hahn, Spin echoes. *Physical Review* **80**, 580 (1950).
14. J. Hennig, A. Nauerth, H. Friedburg, RARE imaging: A fast imaging method for clinical MR. *Magnetic Resonance in Medicine* **3**, 823-833 (1986).
15. J. Hennig, Multiecho imaging sequences with low refocusing flip angles. *Journal of Magnetic Resonance (1969)* **78**, 397-407 (1988).
16. H. Y. Carr, E. M. Purcell, Effects of diffusion on free precession in nuclear magnetic resonance experiments. *Physical Review* **94**, 630 (1954).
17. S. Meiboom, D. Gill, Modified spin - echo method for measuring nuclear relaxation times. *Review of Scientific Instruments* **29**, 688-691 (1958).
18. X. Wang *et al.*, Diffusion of Drug Delivery Nanoparticles into Biogels Using Time-Resolved MicroMRI. *The Journal of Physical Chemistry Letters* **5**, 3825-3830 (2014).
19. G. Bydder, I. Young, MR imaging: clinical use of the inversion recovery sequence. *Journal of Computer Assisted Tomography* **9**, 659-675 (1985).
20. G. Bydder, R. Steiner, L. Blumgart, S. Khenia, I. Young, MR imaging of the liver using short TI inversion recovery sequences. *Journal of Computer Assisted Tomography* **9**, 1084-1089 (1985).

21. X. Wang *et al.*, Quantitation of Complexed versus Free Polymers in Interpolyelectrolyte Polyplex Formulations. *ACS Macro Letters* **2**, 1038-1041 (2013).
22. J. Kowalewski, L. Maler, *Nuclear Spin Relaxation in Liquids: Theory, Experiments, and Applications*. (CRC Press, 2006).
23. M. M. J. Modo, J. W. M. Bulte, *Molecular and Cellular MR Imaging*. (CRC Press, 2007).
24. P. Caravan, J. J. Ellison, T. J. McMurry, R. B. Lauffer, Gadolinium(III) Chelates as MRI Contrast Agents: Structure, Dynamics, and Applications. *Chemical Reviews* **99**, 2293-2352 (1999).
25. R. B. Lauffer, Paramagnetic metal complexes as water proton relaxation agents for NMR imaging: theory and design. *Chemical Reviews* **87**, 901-927 (1987).
26. P. Caravan, Strategies for increasing the sensitivity of gadolinium based MRI contrast agents. *Chemical Society Reviews* **35**, 512-523 (2006).
27. C. Casali *et al.*, Evaluation of Gd-DOTA-labeled dextran polymer as an intravascular MR contrast agent for myocardial perfusion. *Academic Radiology* **5**, **Supplement 1**, S214-S218 (1998).
28. K. C. P. Li, M. D. Bednarski, Vascular-targeted molecular imaging using functionalized polymerized vesicles. *Journal of Magnetic Resonance Imaging* **16**, 388-393 (2002).
29. J. M. Bryson *et al.*, Polymer beacons for luminescence and magnetic resonance imaging of DNA delivery. *Proceedings of the National Academy of Sciences* **106**, 16913-16918 (2009).
30. Y. Liu, T. M. Reineke, Poly(glycoamidoamine)s for Gene Delivery: Stability of Polyplexes and Efficacy with Cardiomyoblast Cells. *Bioconjugate chemistry* **17**, 101-108 (2005).
31. S. K. Samal *et al.*, Cationic polymers and their therapeutic potential. *Chemical Society Reviews* **41**, 7147-7194 (2012).
32. D. W. Pack, A. S. Hoffman, S. Pun, P. S. Stayton, Design and development of polymers for gene delivery. *Nature Review Drug Discovery* **4**, 581-593 (2005).
33. M. A. Mintzer, E. E. Simanek, Nonviral Vectors for Gene Delivery. *Chemical Reviews* **109**, 259-302 (2008).
34. W. Kim, S. Kim, Efficient siRNA Delivery with Non-viral Polymeric Vehicles. *Pharmaceutical Research* **26**, 657-666 (2009).
35. Y. Lee, K. Kataoka, in *Nucleic Acid Drugs*, A. Murakami, Ed. (Springer Berlin Heidelberg, 2012), vol. 249, chap. 129, pp. 95-134.
36. M. Zhu *et al.*, Physicochemical Properties Determine Nanomaterial Cellular Uptake, Transport, and Fate. *Accounts of Chemical Research* **46**, 622-631 (2012).
37. E. Wagner, in *Polymers in Nanomedicine*, S. Kunugi, T. Yamaoka, Eds. (Springer Berlin Heidelberg, 2012), vol. 247, chap. 148, pp. 1-29.
38. S. K. Cho, Y. J. Kwon, Synthetically engineered viruses: Can synthetic chemistry tame the nature? *Current Opinion in Solid State and Materials Science* **16**, 276-286 (2012).

39. J. D. Byrne, T. Betancourt, L. Brannon-Peppas, Active targeting schemes for nanoparticle systems in cancer therapeutics. *Advanced Drug Delivery Reviews* **60**, 1615-1626 (2008).
40. J. M. Morachis, E. A. Mahmoud, A. Almutairi, Physical and Chemical Strategies for Therapeutic Delivery by Using Polymeric Nanoparticles. *Pharmacological Reviews* **64**, 505-519 (2012).
41. L. E. Prevette, T. E. Kodger, T. M. Reineke, M. L. Lynch, Deciphering the Role of Hydrogen Bonding in Enhancing pDNA–Polycation Interactions. *Langmuir* **23**, 9773-9784 (2007).
42. L. E. Prevette, M. L. Lynch, K. Kizjakina, T. M. Reineke, Correlation of Amine Number and pDNA Binding Mechanism for Trehalose-Based Polycations. *Langmuir* **24**, 8090-8101 (2008).
43. Z. Dai, T. Gjetting, M. A. Matthebjerg, C. Wu, T. L. Andresen, Elucidating the interplay between DNA-condensing and free polycations in gene transfection through a mechanistic study of linear and branched PEI. *Biomaterials* **32**, 8626-8634 (2011).
44. A. Richards Grayson, A. Doody, D. Putnam, Biophysical and Structural Characterization of Polyethylenimine-Mediated siRNA Delivery in Vitro. *Pharmaceutical Research* **23**, 1868-1876 (2006).
45. N. Pothayee *et al.*, Synthesis of 'ready-to-adsorb' polymeric nanoshells for magnetic iron oxide nanoparticles via atom transfer radical polymerization. *Polymer* **52**, 1356-1366 (2011).
46. N. Pothayee *et al.*, Magnetic Block Ionomer Complexes for Potential Dual Imaging and Therapeutic Agents. *Chemistry of Materials* **24**, 2056-2063 (2012).
47. N. Pothayee *et al.*, Magnetic nanoclusters with hydrophilic spacing for dual drug delivery and sensitive magnetic resonance imaging. *Journal of Materials Chemistry B* **1**, 1142-1149 (2013).
48. R. K. Jain, The next frontier of molecular medicine: delivery of therapeutics. *Nature Medicine* **4**, 655-657 (1998).
49. R. K. Jain, T. Stylianopoulos, Delivering nanomedicine to solid tumors. *Nature reviews. Clinical Oncology* **7**, 653-664 (2010).
50. V. P. Chauhan, T. Stylianopoulos, Y. Boucher, R. K. Jain, Delivery of Molecular and Nanoscale Medicine to Tumors: Transport Barriers and Strategies. *Annual Review of Chemical and Biomolecular Engineering* **2**, 281-298 (2011).
51. V. P. Chauhan, T. Stylianopoulos, Y. Boucher, R. K. Jain, Delivery of molecular and nanoscale medicine to tumors: transport barriers and strategies. *Annual Review of Chemical and Biomolecular Engineering* **2**, 281-298 (2011).
52. Y. Boucher, L. T. Baxter, R. K. Jain, Interstitial Pressure Gradients in Tissue-isolated and Subcutaneous Tumors: Implications for Therapy. *Cancer Research* **50**, 4478-4484 (1990).
53. M. F. Milosevic *et al.*, Interstitial fluid pressure in cervical carcinoma. *Cancer* **82**, 2418-2426 (1998).
54. C. H. Heldin, K. Rubin, K. Pietras, A. Ostman, High interstitial fluid pressure - an obstacle in cancer therapy. *Nature reviews. Cancer* **4**, 806-813 (2004).

55. H. F. Dvorak, Tumors: Wounds That Do Not Heal. *New England Journal of Medicine* **315**, 1650-1659 (1986).
56. *Cellular changes involved in conversion of normal to malignant breast: importance of the stromal reaction.* L. Ronnov-Jessen, O. W. Petersen, M. J. Bissell, Eds., (1996), vol. 76, pp. 69-125.
57. P. A. Netti, D. A. Berk, M. A. Swartz, A. J. Grodzinsky, R. K. Jain, Role of Extracellular Matrix Assembly in Interstitial Transport in Solid Tumors. *Cancer Research* **60**, 2497-2503 (2000).
58. A. Pluen *et al.*, Role of tumor–host interactions in interstitial diffusion of macromolecules: Cranial vs. subcutaneous tumors. *Proceedings of the National Academy of Sciences* **98**, 4628-4633 (2001).
59. S. Ramanujan *et al.*, Diffusion and convection in collagen gels: implications for transport in the tumor interstitium. *Biophysical Journal* **83**, 1650-1660 (2002).
60. G. Alexandrakis *et al.*, Two-photon fluorescence correlation microscopy reveals the two-phase nature of transport in tumors. *Nature Medicine* **10**, 203-207 (2004).
61. T. Stylianopoulos *et al.*, Diffusion of particles in the extracellular matrix: the effect of repulsive electrostatic interactions. *Biophysical Journal* **99**, 1342-1349 (2010).
62. O. Lieleg, R. M. Baumgärtel, A. R. Bausch, Selective Filtering of Particles by the Extracellular Matrix: An Electrostatic Bandpass. *Biophysical Journal* **97**, 1569-1577.
63. H. Maeda, J. Wu, T. Sawa, Y. Matsumura, K. Hori, Tumor vascular permeability and the EPR effect in macromolecular therapeutics: a review. *Journal of Controlled Release* **65**, 271-284 (2000).
64. F. Yuan *et al.*, Vascular permeability in a human tumor xenograft: molecular size dependence and cutoff size. *Cancer Research* **55**, 3752-3756 (1995).
65. A. Pluen *et al.*, Role of tumor–host interactions in interstitial diffusion of macromolecules: cranial vs. subcutaneous tumors. *Proceedings of the National Academy of Sciences* **98**, 4628-4633 (2001).
66. E. O. Stejskal, J. E. Tanner, Spin Diffusion Measurements: Spin Echoes in the Presence of a Time - Dependent Field Gradient. *The Journal of Chemical Physics* **42**, 288-292 (1965).
67. J. E. Tanner, Use of the Stimulated Echo in NMR Diffusion Studies. *The Journal of Chemical Physics* **52**, 2523-2526 (1970).
68. E. Stejskal, Use of Spin Echoes in a Pulsed Magnetic - Field Gradient to Study Anisotropic, Restricted Diffusion and Flow. *The Journal of Chemical Physics* **43**, 3597-3603 (1965).
69. J. Tanner, E. O. Stejskal, Restricted self - diffusion of protons in colloidal systems by the pulsed - gradient, spin - echo method. *The Journal of Chemical Physics* **49**, 1768-1777 (1968).
70. A. Einstein, *Investigations on the Theory of the Brownian Movement.* (Courier Corporation, 1956).
71. A. Fick, Ueber diffusion. *Annalen der Physik* **170**, 59-86 (1855).



72. G. G. Stokes, *On the effect of the internal friction of fluids on the motion of pendulums*. (Pitt Press, 1851), vol. 9.
73. A. Polson, The Some Aspects of Diffusion in Solution and a Definition of a Colloidal Particle. *The Journal of Physical and Colloid Chemistry* **54**, 649-652 (1950).
74. M. Rubinstein, R. Colby, *Polymers Physics*. (Oxford, 2003).
75. R. J. Bruessau, Size exclusion chromatography of polyelectrolytes with aqueous elution solvents. *Makromolekulare Chemie. Macromolecular Symposia* **61**, 190-218 (1992).
76. R. García, I. Porcar, J. E. Figueruelo, V. Soria, A. Campos, Solution properties of polyelectrolytes XII. Semi-quantitative approach to mixed electrostatic and hydrophobic polymer-gel interactions. *Journal of Chromatography A* **721**, 203-212 (1996).
77. P. T. Callaghan, J. Lelievre, The size and shape of amylopectin: A study using pulsed-field gradient nuclear magnetic resonance. *Biopolymers* **24**, 441-460 (1985).
78. A. Chen, D. Wu, C. S. Johnson, Determination of molecular weight distributions for polymers by diffusion-ordered NMR. *Journal of the American Chemical Society* **117**, 7965-7970 (1995).
79. S. Augé *et al.*, NMR measure of translational diffusion and fractal dimension. Application to molecular mass measurement. *The Journal of Physical Chemistry B* **113**, 1914-1918 (2009).
80. S. Floquet *et al.*, Molecular weights of cyclic and hollow clusters measured by DOSY NMR spectroscopy. *Journal of the American Chemical Society* **131**, 17254-17259 (2009).
81. W. Li, H. Chung, C. Daeffler, J. A. Johnson, R. H. Grubbs, Application of <sup>1</sup>H DOSY for facile measurement of polymer molecular weights. *Macromolecules* **45**, 9595-9603 (2012).

## Chapter 2 Quantitation of Complexed versus Free Polymers in Interpolyelectrolyte Polyplex Formulations

### 2.1 Chapter Overview

This study has been published on *ACS Macro Lett.* **2013**, *2*, 1038-1041. DOI: 10.1021/mz400500q. Authors are listed below: Xiaoling Wang, Sneha S. Kelkar, Amanda G. Hudson, Robert B. Moore, Theresa M. Reineke, and Louis A. Madsen. Sneha S. Kelkar prepared all polymer DNA complex samples. Amanda G. Hudson conducted isothermal titration calorimetry experiments.

#### **Abstract**

The quantity of free polymer in a polymer/DNA complex (polyplex) formulation critically impacts its gene transfection efficiency, cellular uptake, and toxicity. In this study, the compositions of three interpolyelectrolyte polyplex formulations were quantified by a facile NMR method. Using careful integration of a 1D  $^1\text{H}$  NMR spectrum with a broad spectral width, the quantities of unbound polymer and polyplexes in solution were determined. Linear polyethyleneimine (PEI) mixed with DNA at polymer amine to DNA phosphate molar ratio (N/P ratio) of 5 revealed an effective binding N/P ratio of 3.5 without excess free polymer. This result is in strong agreement with the stoichiometric number of PEI/DNA binding obtained by isothermal titration calorimetry. The noninvasive nature of this method allows broad application to a range of polyelectrolyte coacervates, opening new

opportunities for understanding and optimizing polyelectrolyte complex formation, and providing quantitation of complex formation in a single measurement.

## 2.2 Background

The field of non-viral nucleic acid delivery offers promise for a variety of research and therapeutic applications.<sup>(1-3)</sup> Over the last two decades a large variety of polymeric delivery systems have been created and studied;<sup>(4, 5)</sup> delivery vehicles are needed to compact nucleic acids into small nanoparticles to facilitate cellular uptake,<sup>(6)</sup> protect nucleic acids from enzymatic degradation,<sup>(7, 8)</sup> and can be designed to target delivery to various tissue types.<sup>(9, 10)</sup> Such delivery systems are typically designed to be polycationic in nature in order to bind, via electrostatic interactions, with the negative phosphodiester backbone of the nucleic acid. This process is entropically favored via the release of counterions from both the polycation (delivery vehicle) and polyanion (nucleic acid) backbone.<sup>(11, 12)</sup>

While polymeric delivery systems offer promising properties, low gene-transfer efficiency compared to viral vectors is one of the major limitations towards clinical applications. One of the most common strategies conventionally used to improve delivery (cell transfection) efficiency of nucleic acids *in vitro* is to optimize the N/P ratio, which is simply increasing the amount of the polycation in the polyplex formulation to obtain the most efficient delivery.<sup>(13, 14)</sup> For most published polyplex-based systems, a large excess of free polymer remains in solution during transfection, yet the exact amount of free polycation is rarely known due to difficulties in characterization and in isolating polyplexes from the free polymer. Thus, *in vitro* and *in vivo* assay results (both delivery efficiency and

toxicity) are routinely reported without knowledge of the amount of free polymer in solution. It has been theorized that the free polymer plays a central role in many physiochemical and biological parameters, for example, increasing biological membrane permeability,(15, 16) delivery efficiency,(17, 18) and toxicity.(19) However, the exact role of free polymer concentration is not known.

Several groups have shown that transfection of polyethyleneimine (PEI)-mediated gene delivery in cells is improved at N/P ratios higher than unity (typically 5-7).(20-22) In addition, DNA delivery studies performed on carbohydrate-based poly(amidogalactaramine) G4 and lanthanide-containing theranostic polymers showed increases in transfection efficiency with N/P ratio.<sup>13,(23, 24)</sup> However, PEI polyplexes formed at elevated N/P ratios means that a considerable excess of polymer exists and this clearly contributes to the cellular toxicity profile of PEI polyplex formulations.(25, 26) Therefore, quantifying the concentration of unbound polycation present in polyplex formulations carries deep implications for optimal and non-toxic delivery of nucleic acids in vitro and in vivo.

Researchers have attempted to address the role of free polymer in transfection for PEI/DNA complex using fluorescence spectroscopy(21, 27, 28) and UV-Vis spectroscopy(29). However, sample labeling with probe molecules can significantly affect the solubility and composition of samples, and hence the accuracy of quantitation by these methods. In addition, PEI/DNA polyplexes tend to aggregate(30) and purification was needed prior to spectroscopic analysis due to precipitation,(21) thus requiring constraints on as-delivered sample properties.

Here we describe a new and straightforward NMR peak integration method to accurately determine the concentration of unbound polymer as well as the ratio of this free polymer and polyplexes in solution. For polymer-based gene delivery systems, obtaining this information is critical to optimizing efficacy, as well as to assessing consistency of formulation/quality control for advancing these systems toward animal and clinical studies. In such systems, the ~ 60-200 nm polyplexes in dispersion exhibit broad NMR resonances (Figure 2-1b) while the unbound components show narrow resonances (Figure 2-1c). The concentration of unbound polymer in solution is obtained by comparing the signal intensity of narrow polymer resonances with that of a dilute internal standard (calibrant). The ratio of free polymer to polyplexes is given by the ratio of the narrow resonance intensity to the broad resonance intensity. The latter has been used to determine, e.g., crystalline/amorphous fraction in semi-crystalline polymers.<sup>(31)</sup> Using this method, we can also extract the actual binding molar (N/P) ratio of polymer to DNA for any “as prepared” polyplex formulation. Indeed, this method can be broadly applied to examining coacervates, micelles, and vesicles in solution.

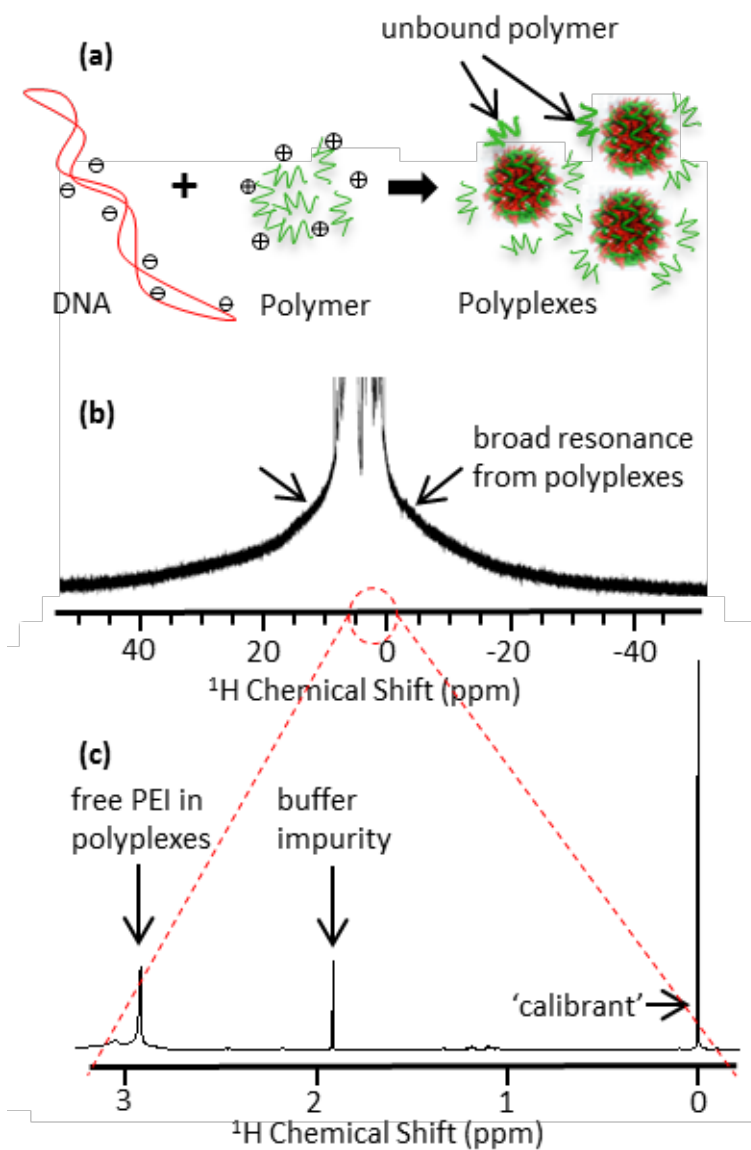


**Figure 2-1.** (a) Polyplex formation. (b) <sup>1</sup>H NMR spectra of PEI/DNA polyplexes in tris buffer with vertical expansion and wide shift range. The broad resonance ranging from -50 to +50 ppm originates from PEI/DNA complexes. (c) “Conventional” narrow shift range <sup>1</sup>H NMR spectrum showing only free PEI in dispersion.

### 2.3 Experimental Section

We apply the described method to three different polyplex formulations: i) 25kg/mol linear PEI, ii) a poly(glycoamidoamine)s (PGAAs) polymer delivery vector (G4),<sup>13,18,(32)</sup> (Figure 2-2a) and iii) a non-paramagnetic (lanthanum, La) analogue of a theranostic polymeric vehicle N<sub>4</sub>La,<sup>(23)</sup> (Figure 2-2b), the latter two developed in our group.

Prior to NMR experiments, we studied plasmid DNA (pDNA) binding ability to PEI and N<sub>4</sub>La using a gel electrophoresis shift assay. Binding and compaction of PEI/pDNA complexes was evident at N/P ratio higher than 2.5. For N<sub>4</sub>La, effective binding took place at N/P ≥ 5 (Figure 2-S7). Dynamic light scattering (DLS) size measurements of PEI/pDNA polyplexes showed a trend consistent with previous reports on branched PEI polyplexes (Table 2-1).<sup>(27, 33)</sup>

For each polymer, polyplex samples were formulated with the same total polymer concentration (170-370 μg/mL), independent of N/P ratio. PEI polyplexes were formulated in tris buffer (10 mM, pH 7), and polyplexes of N<sub>4</sub>La and G4 were prepared in nuclease-free water. The addition of 0.009 wt% of sodium 3-(trimethylsilyl)propionate-2,2,3,3-d<sub>4</sub> to polyplex samples provided the internal standard (calibrant) for NMR measurements. No filtration or other sample pre-treatment was necessary prior to NMR quantitation.

**Table 2-1. Hydrodynamic diameter of polyplexes by DLS size measurement. ( $\infty$  denotes pure polymer)**

<i>Polymer</i>	<i>N/P</i>	<i>D<sub>hyd</sub>/nm</i>	<i>Polymer</i>	<i>N/P</i>	<i>D<sub>hyd</sub>/nm</i>
PEI	5	210	G4	5	79
	10	120		10	66
	20	77		20	67
pure PEI	$\infty$	7	pure G4	$\infty$	162
N <sub>4</sub> La	10	92			
	40	76			
pure N <sub>4</sub> La	$\infty$	250			

We performed all NMR experiments at 310 K using the simple and reproducible presaturation solvent suppression pulse sequence (continuous wave irradiation of 8 mW on water resonance, prior to single pulse acquisition). We experimented with a variety of more complex water suppression NMR pulse sequences, but the results showed equivalent or larger errors.

By comparing intensities of the narrow resonances from free polymer chain and the calibrant, we quantify the absolute amount of unbound polymer in solution. The intensity of the broad resonance (calculated by subtracting the integrals of free polymer resonances from the total integral from -50 to +50 ppm – see SI for further description) further yields the concentration of polyplexes in a given dispersion. Any precipitated polymer/DNA in the sample can be thus ignored, which is desirable since that component would not be delivered during treatment. We



quantitatively characterized PEI, N<sub>4</sub>La and G4 polyplexes at commonly used N/P ratios for transfection studies using <sup>1</sup>H NMR, despite significant aggregation at lower N/P ratios. No broad resonance appears in the spectrum of pure PEI polymer sample, which indicates the complete absence of aggregated components.

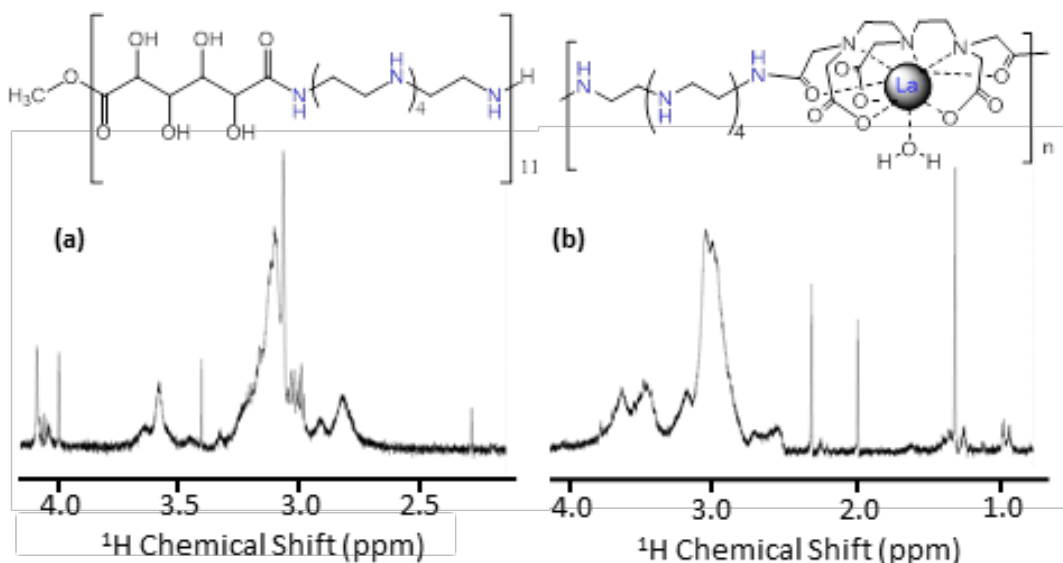


**Figure 2-2.** Structures and <sup>1</sup>H NMR spectra (narrow shift range) of polyplexes of (a) G4 and (b) N<sub>4</sub>La in H<sub>2</sub>O.

## 2.4 Results and Discussion

PEI/DNA polyplexes prepared at N/P = 5 formed significant aggregates (cloudiness in solution) and caused precipitation in buffer. At this N/P ratio, about 70% of polyplexes precipitated to the bottom of NMR tube. This number is determined by comparing the polymer amount initially added to the sample with the total quantity detected through NMR (from both sharp and broad resonances).

The N/P ratio of polyplexes in dispersion without considering free PEI (actual N/P) is 3.5, by comparing the signal intensities of the sharp and broad resonances.

To support the accuracy of this NMR experiment, isothermal titration calorimetry (ITC) measurements were also performed to extract the stoichiometric number of binding between PEI and DNA under the same experimental conditions. Three titrations yielded an averaged stoichiometry of binding,  $n_{\text{bind}}$  of  $3.5 \pm 0.3$  (Table 2-2). This is in excellent agreement with the NMR quantification results above, which show an effective binding N/P ratio = 3.5 for the PEI polyplex sample prepared at N/P = 5.

**Table 2-2. Thermodynamic parameters for PEI-pDNA binding from isothermal titration calorimetry.**

	<i>Average</i>	<i>Std. Dev.</i>	<i>%RSD</i>
$n_{\text{bind}}$	3.5	0.3	8.1
$K \text{ (M}^{-1}\text{)}$	$4.94 \times 10^5$	$2.01 \times 10^5$	40.6
$\Delta H$ (kJ/mol)	2.16	0.56	26.1

Furthermore, we studied higher N/P ratios of 10 and 20 for PEI, as well as a range of N<sub>4</sub>La and G4 polyplex formulations. Figure 2-3 shows a summary of both the unbound polymer percentage and the effective N/P for the polyplexes as a function of polymer type and “as prepared” N/P. For PEI, 16% and 27% of the originally added polymer remained unbound at N/P 10 and 20. Accordingly, the actual or effective N/P ratios of the polyplexes are 8 and 17 instead of N/P 10 and

20, respectively. Interestingly, this indicates that significant over charging of these polyelectrolyte complexes does, in fact, occur. Because precipitation was not observed in these two samples, all polymer species were detected by NMR. Specifically, the sum of signal intensities from the sharp and broad resonances should equal the total quantity of originally added polymer. This equality holds true (with < 10% discrepancy), further validating the use of this broad resonance for quantitation. Indeed, incorporating broad resonances into integration is essential for quantifying compositions of samples exhibiting precipitation. Otherwise, polyplexes in dispersion cannot be quantified separately from those precipitated without isolating each polymer species.

To extend these studies to other polymeric delivery systems, we also investigated G4 and N<sub>4</sub>La polymers. The repeat unit of G4 polymer consists of a galactose sugar and a PEI-like oligoethylene amine group containing four secondary amines along the backbone (Figure 2-2a). G4 has gene delivery efficiency comparable to linear PEI but with lower toxicity.<sup>18</sup> DLS shows (Figure 2-S4) that G4 polymer alone (no pDNA) forms aggregates of 100-200 nm in diameter in dispersion in its pure water solution, but the NMR measurements show that only 60% of the polymer exists in these aggregates and the rest is free unimers. In contrast, for G4/pDNA polyplex solutions, diameters < 100 nm (Table 2-1) were found, indicating that significant compaction of both the pDNA and the polymer aggregates occurs during polyelectrolyte complexation. The complete binding and compaction of DNA by G4 occurs at N/P 4 for the sample prepared at N/P 5 (18% unbound polymer).

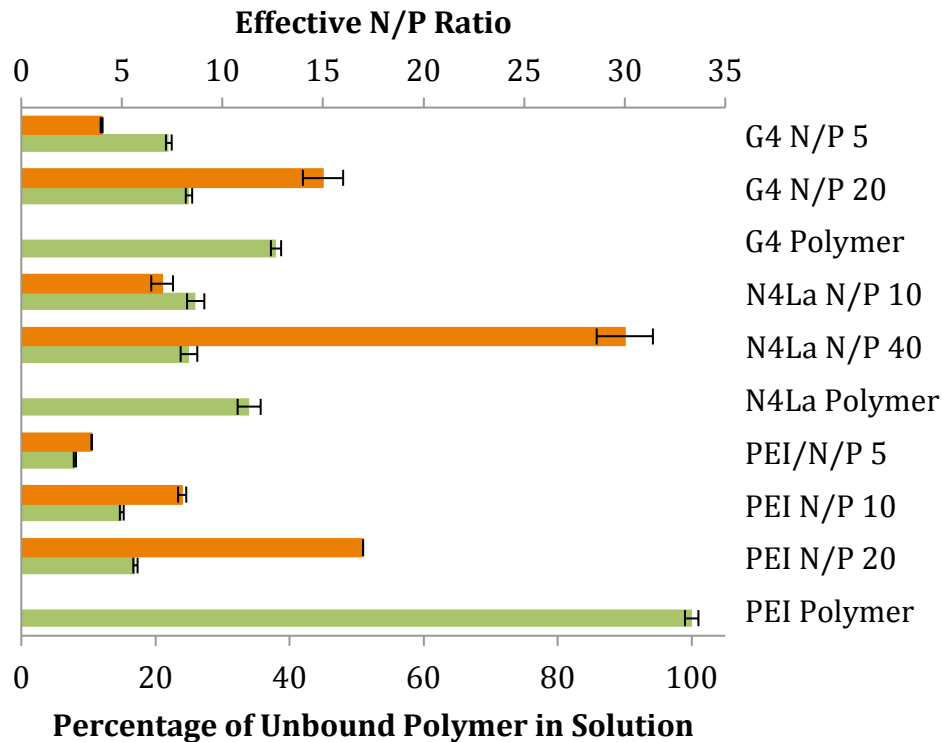


**Figure 2-3.** Percentage of unbound polymer in polymer and polyplex solutions (green) and effective N/P ratios of polyplexes (orange), both as a function of as-prepared N/P.

N<sub>4</sub>La polymer is a non-paramagnetic analog of a previously published paramagnetic gadolinium chelate used for direct tracking of gene delivery via magnetic resonance imaging (Figure 2-2b).<sup>(23)</sup> DLS measurements on of N<sub>4</sub>La polymer in pure water show presence of free polymer (< 10nm) and polymer aggregates (200-300nm) in solution (Figure 2-S6). NMR measurements show that 65% of N<sub>4</sub>La polymer forms aggregates. The concentrations of free polymer in N<sub>4</sub>La polyplex solutions prepared at N/P 10 and N/P 40 are similar (19% and 18%), which indicates enhanced binding between N<sub>4</sub>La and DNA with excess polymer

added at N/P 40. DLS measurements showed smaller particle size of N<sub>4</sub>La polyplex aggregates at N/P 40 compared to N/P 10 (Table 2-1), which also indicates stronger binding of N<sub>4</sub>La polymer to DNA at N/P 40.

## 2.5 Conclusion

This <sup>1</sup>H-NMR quantitation method provides a systematic approach to determine the amount of all polymer species in polyelectrolyte coacervates, in particular, polymer/nucleic acid solutions. This method offers a significantly simplified quantitative analysis of unbound and complexed polymers in polyplex solutions in one measurement, and without the need for disturbing the sample solution. Consequently, it gives better accuracy and more consistent test conditions compared to other spectroscopic methods for systematic investigations of polymer/nucleic acid systems. The relatively short experimental time of NMR measurements (less than 2 hours) is also beneficial for degradable samples. The minimum free polymer concentration detected by NMR in this study is of order 10 µg/mL, and this would be improved significantly through the use of more sensitive NMR instruments (e.g., cryoprobe, higher field).

We have demonstrated the utility of a new protocol for sensitive quantification of free polymer in solutions of polycation/DNA gene delivery vectors and theranostic agents. This method will also allow for characterization of compositions for other vesicles and micelles. For polymer-based gene delivery systems, such a simple quantitative analysis will offer critical information to

optimize drug delivery efficacy, as well as to assess regulatory compliance and quality control.

## 2.6 Reference

1. S. K. Samal *et al.*, Cationic polymers and their therapeutic potential. *Chemical Society Reviews* **41**, 7147-7194 (2012).
2. D. W. Pack, A. S. Hoffman, S. Pun, P. S. Stayton, Design and development of polymers for gene delivery. *Nature Review Drug Discovery* **4**, 581-593 (2005).
3. M. A. Mintzer, E. E. Simanek, Nonviral Vectors for Gene Delivery. *Chemical Reviews* **109**, 259-302 (2008).
4. W. Kim, S. Kim, Efficient siRNA Delivery with Non-viral Polymeric Vehicles. *Pharmaceutical Research* **26**, 657-666 (2009).
5. Y. Lee, K. Kataoka, in *Nucleic Acid Drugs*, A. Murakami, Ed. (Springer Berlin Heidelberg, 2012), vol. 249, chap. 129, pp. 95-134.
6. M. Zhu *et al.*, Physicochemical Properties Determine Nanomaterial Cellular Uptake, Transport, and Fate. *Accounts of Chemical Research* **46**, 622-631 (2012).
7. E. Wagner, in *Polymers in Nanomedicine*, S. Kunugi, T. Yamaoka, Eds. (Springer Berlin Heidelberg, 2012), vol. 247, chap. 148, pp. 1-29.
8. S. K. Cho, Y. J. Kwon, Synthetically engineered viruses: Can synthetic chemistry tame the nature? *Current Opinion in Solid State and Materials Science* **16**, 276-286 (2012).
9. J. D. Byrne, T. Betancourt, L. Brannon-Peppas, Active targeting schemes for nanoparticle systems in cancer therapeutics. *Advanced Drug Delivery Reviews* **60**, 1615-1626 (2008).
10. J. M. Morachis, E. A. Mahmoud, A. Almutairi, Physical and Chemical Strategies for Therapeutic Delivery by Using Polymeric Nanoparticles. *Pharmacological Reviews* **64**, 505-519 (2012).
11. L. E. Prevette, T. E. Kodger, T. M. Reineke, M. L. Lynch, Deciphering the Role of Hydrogen Bonding in Enhancing pDNA-Polycation Interactions. *Langmuir* **23**, 9773-9784 (2007).
12. L. E. Prevette, M. L. Lynch, K. Kizjakina, T. M. Reineke, Correlation of Amine Number and pDNA Binding Mechanism for Trehalose-Based Polycations. *Langmuir* **24**, 8090-8101 (2008).
13. Z. Dai, T. Gjetting, M. A. Mattheberg, C. Wu, T. L. Andresen, Elucidating the interplay between DNA-condensing and free polycations in gene transfection through a mechanistic study of linear and branched PEI. *Biomaterials* **32**, 8626-8634 (2011).
14. A. Richards Grayson, A. Doody, D. Putnam, Biophysical and Structural Characterization of Polyethylenimine-Mediated siRNA Delivery in Vitro. *Pharmaceutical Research* **23**, 1868-1876 (2006).

15. J. P. Behr, The proton sponge: a trick to enter cells the viruses did not exploit. *CHIMIA International Journal for Chemistry* **51**, 1-2 (1997).
16. J. Haensler, F. C. Szoka Jr, Polyamidoamine cascade polymers mediate efficient transfection of cells in culture. *Bioconjugate Chemistry* **4**, 372-379 (1993).
17. N. D. Sonawane, F. C. Szoka, A. Verkman, Chloride accumulation and swelling in endosomes enhances DNA transfer by polyamine-DNA polyplexes. *Journal of Biological Chemistry* **278**, 44826-44831 (2003).
18. A. Akinc, M. Thomas, A. M. Klibanov, R. Langer, Exploring polyethylenimine-mediated DNA transfection and the proton sponge hypothesis. *The Journal of Gene Medicine* **7**, 657-663 (2005).
19. H. Lv, S. Zhang, B. Wang, S. Cui, J. Yan, Toxicity of cationic lipids and cationic polymers in gene delivery. *Journal of Controlled Release* **114**, 100-109 (2006).
20. B. Brissault *et al.*, Synthesis of Linear Polyethylenimine Derivatives for DNA Transfection. *Bioconjugate Chemistry* **14**, 581-587 (2003).
21. S. Boeckle *et al.*, Purification of polyethylenimine polyplexes highlights the role of free polycations in gene transfer. *The Journal of Gene Medicine* **6**, 1102-1111 (2004).
22. K. Kunath *et al.*, Low-molecular-weight polyethylenimine as a non-viral vector for DNA delivery: comparison of physicochemical properties, transfection efficiency and in vivo distribution with high-molecular-weight polyethylenimine. *Journal of Controlled Release* **89**, 113-125 (2003).
23. J. M. Bryson *et al.*, Polymer beacons for luminescence and magnetic resonance imaging of DNA delivery. *Proceedings of the National Academy of Sciences* **106**, 16913-16918 (2009).
24. Y. Liu, T. M. Reineke, Poly(glycoamidoamine)s for Gene Delivery: Stability of Polyplexes and Efficacy with Cardiomyoblast Cells. *Bioconjugate Chemistry* **17**, 101-108 (2005).
25. W. Godbey, K. K. Wu, A. G. Mikos, Poly (ethylenimine)-mediated gene delivery affects endothelial cell function and viability. *Biomaterials* **22**, 471-480 (2001).
26. K. Morimoto *et al.*, Molecular weight-dependent gene transfection activity of unmodified and galactosylated polyethyleneimine on hepatoma cells and mouse liver. *Molecular Therapy* **7**, 254-261 (2003).
27. J. P. Clamme, J. Azoulay, Y. Mély, Monitoring of the formation and dissociation of polyethylenimine/DNA complexes by two photon fluorescence correlation spectroscopy. *Biophysical Journal* **84**, 1960-1968 (2003).
28. T. M. Ketola *et al.*, Role of Polyplex Intermediate Species on Gene Transfer Efficiency: Polyethylenimine– DNA Complexes and Time-Resolved Fluorescence Spectroscopy. *The Journal of Physical Chemistry B* **115**, 1895-1902 (2011).
29. F. Ungaro, G. De Rosa, A. Miro, F. Quaglia, Spectrophotometric determination of polyethylenimine in the presence of an oligonucleotide for the characterization of controlled release formulations. *Journal of Pharmaceutical and Biomedical Analysis* **31**, 143-149 (2003).

30. T. Hellweg, N. Henry-Toulmé, M. Chambon, D. Roux, Interaction of short DNA fragments with the cationic polyelectrolyte poly(ethylene imine): a dynamic light scattering study. *Colloids and Surfaces A: Physicochemical and Engineering Aspects* **163**, 71-80 (2000).
31. L. A. Madsen, Plasticization of Poly(ethylene oxide) in Fluid CO<sub>2</sub> Measured by in-Situ NMR. *Macromolecules* **39**, 1483-1487 (2006).
32. N. P. Ingle, B. Malone, T. M. Reineke, Poly(glycoamidoamine)s: a broad class of carbohydrate-containing polycations for nucleic acid delivery. *Trends in Biotechnology* **29**, 443-453 (2011).
33. P. Erbacher *et al.*, Transfection and physical properties of various saccharide, poly(ethylene glycol), and antibody-derivatized polyethylenimines (PEI). *The Journal of Gene Medicine* **1**, 210-222 (1999).

## 2.7 Supplementary Information

### **Materials:**

25 kDa linear PEI was purchased from Alfa Aesar. Glycofect™ (G4, 5.6kDa) was obtained from Techulon Inc. and plasmid DNA (1.0 mg/mL, 7.5kbp, pcmv, lacz) was purchased from Aldevron. All the reagents were used without any further purification unless specified otherwise DNase and RNase free water used to make polyplexes was purchased from Gibco, Invitrogen (Carlsbad, CA). LaCl<sub>3</sub>·7H<sub>2</sub>O was purchased from Sigma Aldrich.

NMR solvents D<sub>2</sub>O and 0.75 wt% solution of 3-(trimethylsilyl)propionic-2,2,3,3-d<sub>4</sub> acid, sodium salt in D<sub>2</sub>O were purchased from Sigma Aldrich. Tris buffer used to formulate PEI polyplexes was purchased from Fisher Scientific.

### **Methods:**

*Synthesis of N<sub>4</sub>La polymer:* N<sub>4</sub>La polymer was synthesized with some modifications to previously developed synthetic procedure.<sup>1</sup> Briefly, Boc-protected pentaethylenhexamine and diethylenetriamine pentaacetic acid bisanhydride



(DTPA-BA) were polymerized (1:1 stoichiometric ratio) via step growth polymerization in dry DMSO. After the polymerization, the polymer was made water-soluble by deprotection of Boc groups using trifluoroacetic acid, followed by chelation with  $\text{LaCl}_3$  in equivalent molar ratio. Dialysis was performed (3500 MWCO dialysis bags) in pure water after each step during synthesis, to remove any low molecular weight oligomers/excess monomers and excess of  $\text{LaCl}_3$ . Pure polymer was obtained after freeze-drying of the dialyzed solution as a white fluffy solid.

*NMR Integration:* All NMR experiments were performed on a Bruker Avance III spectrometer operating at 600 MHz for  $^1\text{H}$  equipped with a 5 mm triple resonance inverse detection (TBI) probe. The radiofrequency pulse sequence used was a simple presaturation solvent suppression preceding the single excitation-detection pulse. A continuous wave irradiation of 8 mW was applied at the  $\text{H}_2\text{O}$  resonance (4.7 ppm) during the pre-scan delay. The bandwidth of this presaturation pulse was about 1 ppm, which effectively suppressed the water signal without reducing the intensity of the sharp polymer signals ranging from 4.0 to 1.0 ppm. All experiments were performed at 310 K with 512 scans to produce sufficient signal-to-noise ratio (SNR). Spectral width was set to 200 ppm in order to resolve the broad resonance. The rf pulse used for detection was 3 ms ( $30^\circ$ ) at 19 W power, which was optimized to allow for both complete excitation of the broad resonance and best SNR. Phase correction was applied prior to integration in order to obtain a Gaussian shape for the broad resonance. For the integration of broad resonance, sharp peaks and suppressed water signal were integrated and subtracted from the total integral from -50 to +50 ppm. The suppressed water signal was simulated

using asymmetric Gaussian and Lorentzian functions using excel (See Figure 2-S1). The full-width at half maximum (*FWHM*) of the residual water resonance is about 0.4 ppm, while the *FWHM* of the broad polyplex resonance is approximately 25 ppm. Thus, the residual water signal integral in these experiments is actually a small fraction of the broad signal integral. For integration of the narrow polymer peaks, only the  $-CH_2$  proton signal from PEI polymer chain was used, while for  $N_4La$  and G4 polymers, signals from all protons on the polymer chain were included. The ratio of free polymer to polyplexes was then calculated by the ratio of the narrow resonance integration to the broad resonance integration.

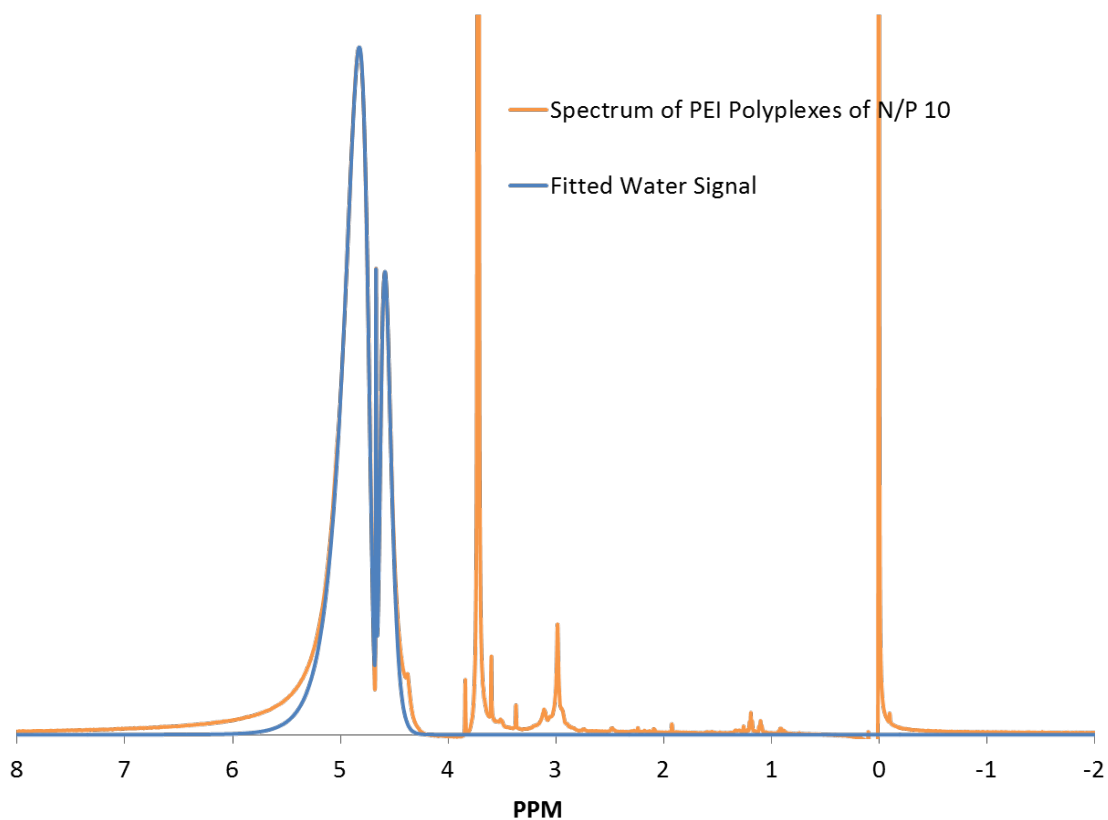


**Figure 2-S2:** Suppressed water signal simulated using asymmetric Gaussian and Lorentzian functions.

*Isothermal Titration Calorimetry (ITC) Measurements:* ITC measurements were performed with a TA Instruments low volume Nano ITC. Prior to ITC experiments, the pDNA solution was dialyzed against 10 mM Tris buffer, with a pH of 7.4. The resulting dialysate solution was used to prepare all polymer solutions. The sample cell, which has a fixed working volume of 170  $\mu\text{L}$ , was filled with a solution of 132  $\mu\text{g}/\text{mL}$  pDNA and the reference cell was filled with water. The buret injection syringe was filled with a total of 50  $\mu\text{L}$  of 172  $\mu\text{g}/\text{mL}$  PEI solution. Triplicate experiments were performed at 37  $^{\circ}\text{C}$  with a 350 rpm stir rate. In each titration, 25 aliquots of 1.96  $\mu\text{L}$  were injected into the sample cell at an interval of 300 s per injection, affording an approximate final N/P of 5. The data was fit with the TA NanoAnalyze Software.

*Results from ITC:* Three titrations yielded an average stoichiometry of binding,  $n_{\text{bind}}$ , of  $3.5 \pm 0.3$ . This is in strong agreement with the NMR experiments showing no free polymer at an N/P of 3.5, while at a higher N/P of 5 free PEI was detected in the solution of polyplexes.

**Table 2-S1: Thermodynamic parameters for the binding of PEI to pDNA, as determined by ITC experiments. Data fit with a standard independent binding sites model.**

	<b>Trial 1</b>	<b>Trial 2</b>	<b>Trial 3</b>	<b>Average</b>	<b>Std. Dev.</b>	<b>%RSD</b>
<b>K (<math>\text{M}^{-1}</math>)</b>	$2.66 \times 10^5$	$6.43 \times 10^5$	$5.75 \times 10^5$	$4.94 \times 10^5$	$2.01 \times 10^5$	40.6
<b><math>\Delta\text{H}</math> (kJ/mol)</b>	2.71	2.18	1.58	2.16	0.56	26.1
<b><math>n_{\text{bind}}</math></b>	3.4	3.3	3.8	<b>3.5</b>	<b>0.3</b>	8.1

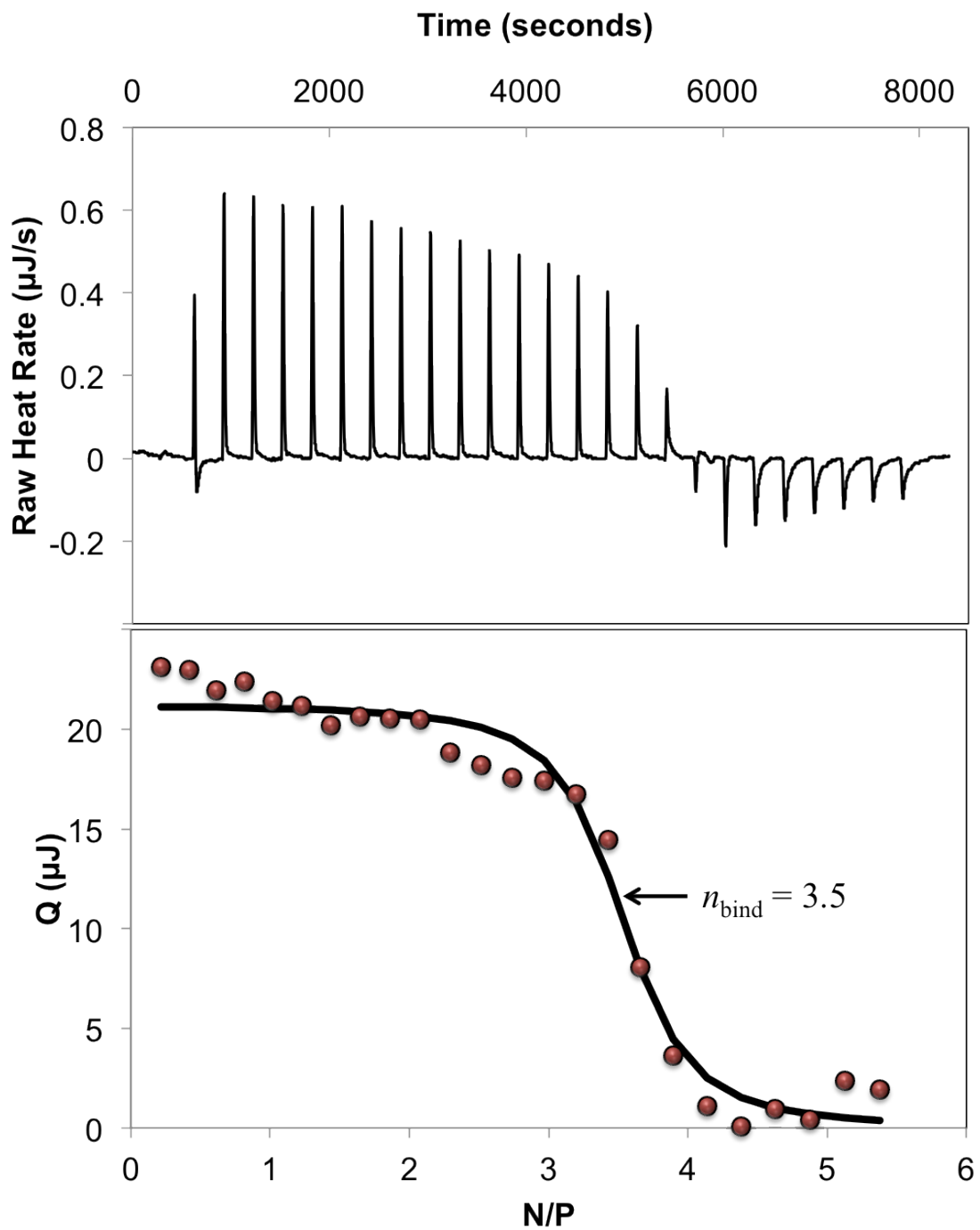
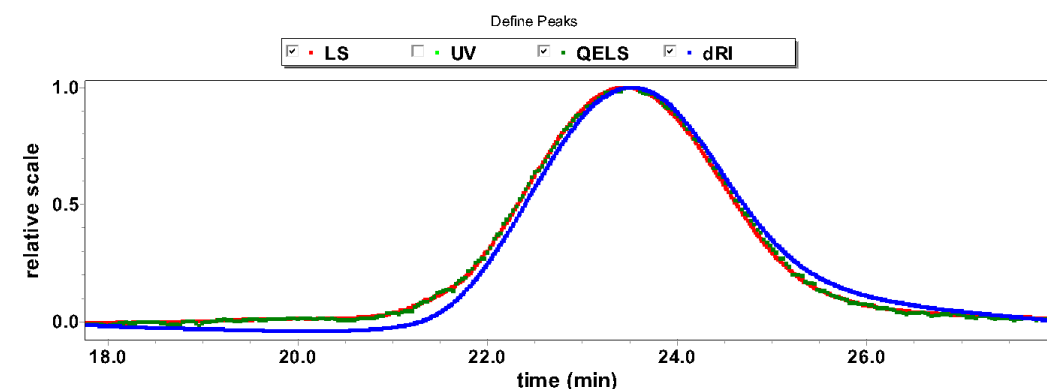


**Figure 2-S2:** ITC thermogram (a) and binding isotherm (b) of 172  $\mu\text{g/mL}$  PEI titrated into 132  $\mu\text{g/mL}$  pDNA in 10 mM Tris buffer pH 7.4 at 37  $^{\circ}\text{C}$ . The data in (b) is the result of the integration of the raw heat rate peaks in the upper panel (a).

*Size exclusion chromatography (SEC) characterization of polymers:* The average molecular weights of PEI and N<sub>4</sub>La was determined using SEC. SEC was performed in aqueous mobile phase- 0.45 M sodium acetate in water with 20v% acetonitrile, pH 7 (for N<sub>4</sub>La) or pH 5 (for PEI) (adjusted using acetic acid), flow rate 0.6 mL/min. Polymer dissolved in mobile phase was separated using GMPW<sub>xL</sub> and G2500PW<sub>xL</sub> (Tosoh Bioscience) columns. This system was equipped with- Waters 2489 UV/vis detector (1 ¼ 274 nm), Wyatt Optilab rex refractometer (1 ¼ 658 nm), and Wyatt DAWN Heleos-II multiangle laser light scattering (MALLS) detector (1 ¼ 662 nm). The data were recorded and analyzed using ASTRA (version 5.3) software.

(a)



(b)

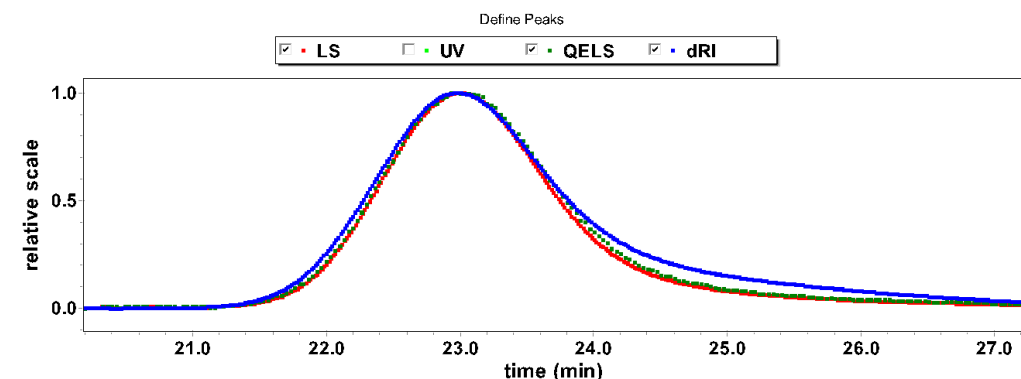


**Figure 2-S3:** Overlay of light scattering (red), refractive index (blue) and QELS (green) traces for PEI (a) and N<sub>4</sub>La (b) polymers.

**Table 2-S2:** SEC analysis was performed on N<sub>4</sub>La and PEI to determine weight average ( $M_w$ ), number average ( $M_n$ ) molecular weights and polydispersities.

The data for G4 polymer (Glycofect™) was obtained from Technulon Inc.

	N <sub>4</sub> La	PEI	G4
<b>Mw (kg/mol)</b>	18.0	26.2	5.6
<b>Mn (kg/mol)</b>	17.1	25.3	-
<b>Mw/Mn</b>	1.1	1.04	-
<b>DP</b>	23	609	11

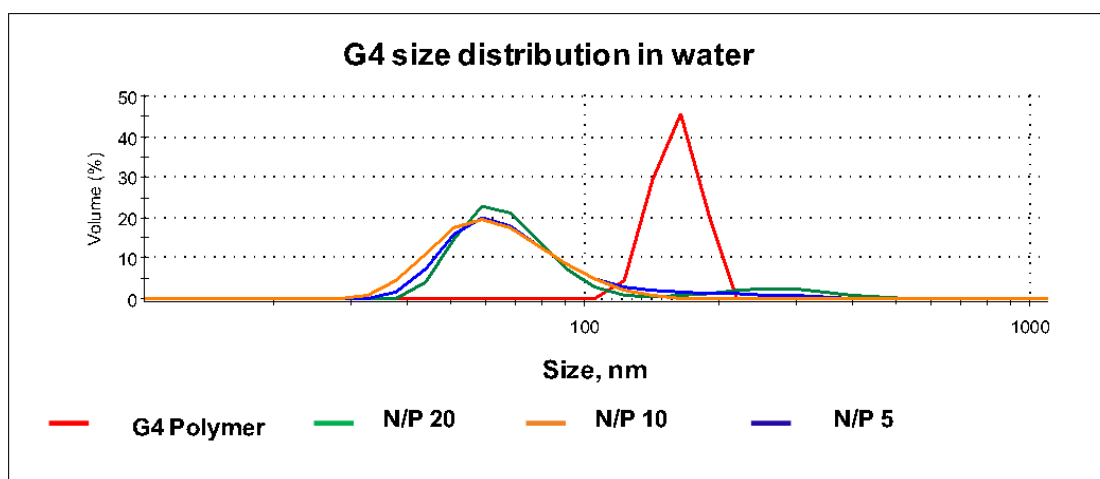


**Figure 2-S4:** The hydrodynamic diameters of G4 polymer (red curve) and its complexes with pDNA at N/P ratios of 5 (green curve), 10 (orange curve) and 20 (green curve) were determined in pure water using DLS.

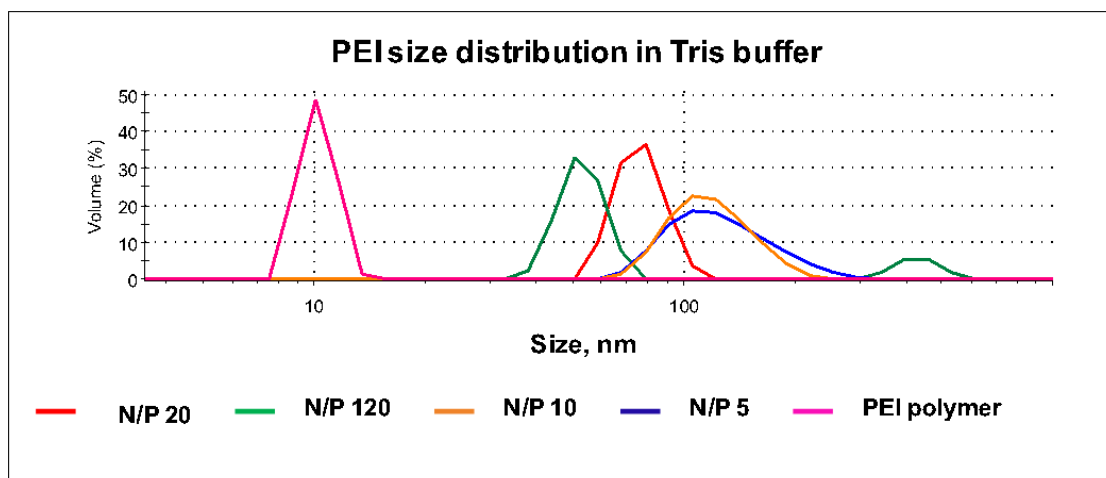


**Figure 2-S5:** The size distribution of PEI polymer (pink curve) and its polyplexes (pH 7 Tris buffer) at N/P ratios of 5 (blue curve), 10 (orange), 20 (red) and 120 (green) were studied using DLS.

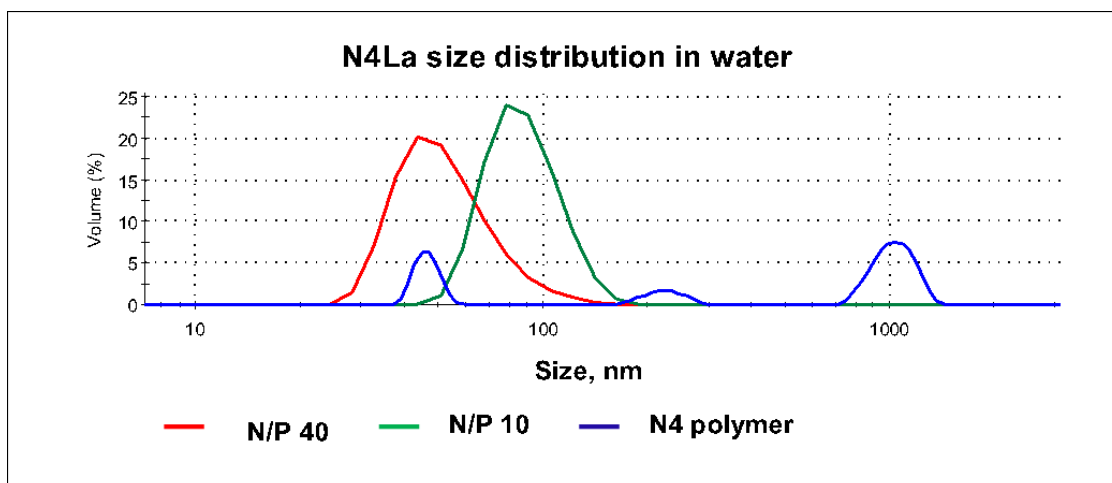


**Figure 2-S6:** The particle size measurements were performed using DLS for N<sub>4</sub> polymer (blue curve) and its polyplexes at N/P ratios of 10 (green curve) and 40 (red curve) in pure water.

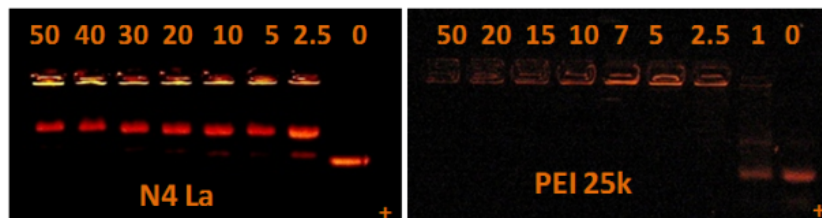


**Figure 2-S7.** Gel electrophoresis shift assay was performed by mixing pDNA (stained with ethidium bromide) with N<sub>4</sub>La (left) and PEI (right) at N/P 0 to 50. The effective binding is indicated by the inhibition of migration of orange-colored DNA band toward positive electrode.

**References of SI:**

(1) J. M. Bryson *et al.*, Polymer beacons for luminescence and magnetic resonance imaging of DNA delivery. *Proceedings of the National Academy of Sciences* **106**, 16913-16918 (2009).



## **Chapter 3 Diffusion of Drug Delivery Nanoparticles into Biogels using Time-Resolved MicroMRI**

### 3.1 Chapter Overview

This work has been published on *J. Phys. Chem. Lett.* **2014**, 5, 3825–3830. DOI: 10.1021/jz501929u. Authors are listed below: Xiaoling Wang, Ying Chen, Lian Xue, Nipon Pothyaee, Rui Zhang, Judy S. Riffle, Theresa M. Reineke and Louis A. Madsen. Ying Chen conducted data processing part using Matlab. Nipon Pothyaee and Rui Zhang prepared magnetite nanoparticle samples, and Lian Xue prepared Gadolinium based particles.

#### **Abstract**

Nanoparticle-based therapeutic agents can in some cases provide selective delivery to tumors, yet this field would greatly benefit from more detailed understanding of particle transport into and within tumor tissue. To provide fundamental information for optimizing interstitial transport of polymeric nanoparticles, we have developed a quantitative approach employing real-time analysis of nanoparticle diffusion into bulk biological hydrogels using microMRI. We use two distinct imaging approaches to probe the migration of two novel “theranostic” polymeric agents (combining drug delivery and contrast agent functions) into bulk hydrogels. Theranostic agent diffusion measured using time-resolved MRI agrees well with diffusion measured for simple probe particles using fluorescence spectroscopies. Furthermore, compared with established fluorescence

techniques, which are restricted by sample thickness, our approach provides three dimensional diffusion rate and concentration distribution of nanoparticles over macroscopic distances in biological media. These results carry implications for *in vivo* tracking of theranostic nanoparticles into tumor interstitium.

### 3.2 Background

Delivery of small molecules and nanoparticles into cancer cells involves a three step pharmacokinetic process: vascular transport, transvascular transport and interstitial transport.(1-3) These principle steps are relatively efficient for normal tissues, whereas the abnormal physiology of tumors causes transport barriers to the adequate delivery of therapeutic agents to tumors. Specifically, elevated interstitial fluid pressure reduces convective mass transport and hence leaves diffusion as the main mechanism of transport into tumors.(4-6) Moreover, the tumor interstitium hinders diffusion as a result of the dense viscoelastic fiber matrix consisting of collagen and interacting molecules.(7-9) The diffusion rate of a nanoparticle in tumor interstitium correlates with its size, charge, configuration, as well as the content and structure of collagen fibers.(10-14) One advantage of nanoscale therapeutic agents is that they provide potential selective delivery to tumors due to the enhanced permeability and retention (EPR) effect. On the other hand, diffusion of large particles through tumor tissue is decreased due to particle interactions with the interstitial matrix. Therefore optimization of nanoparticle size and surface features (such as charge) for different tumor microenvironments is crucial for sufficient interstitial transport. Fluorescence microscopy techniques such as fluorescence recovery after photobleaching (FRAP) have been used to study transport of nanoparticles in interstitial matrix as well as tumor-mimetic gels.(12, 15-18) However, these methods are restricted to measurements of diffusion on the sub-mm scale, e.g., into thin gels and into tumor surfaces with limited depth

penetration even with the aid of spatial Fourier analysis and multiphoton techniques.(12, 19) Magnetic resonance spectroscopy (MRS) and imaging (MRI) approaches, which are not restricted by material thickness, have been applied for investigating *in vivo* water perfusion,(20) and in recent years time-resolved MRI has been employed in quantitative analysis of blood flow with three dimensional spatial resolution.(21, 22) Recent studies report the use of MRI to quantify convective transport of macromolecular contrast agents in hydrogels and tumor tissues.(23, 24) Nevertheless, characterization of diffusion-driven nanoparticle transport using time-resolved MRI has not been reported, and a reliable quantitative assessment of three-dimensional diffusion for polymeric nanomaterials is lacking.

### **3.3 Experimental Section**

In this letter, we describe a non-invasive method for accurate quantitation of diffusion of polymer-based contrast and drug delivery agents, known as theranostic agents, into tumor-tissue-mimetic hydrogels *via* time-resolved MRI. This approach provides three dimensional diffusion rate and concentration distribution of nanoparticles over macroscopic (mm to cm) distances in biological transport media. We examined diffusion of a theranostic polymeric gene-delivery vehicle(25, 26) and a block-copolymer-functionalized magnetite drug delivery vector(27-29) into 0.5-2.0 wt.% agarose and into 0.2-1.0 wt.% collagen type I gels. The first theranostic vehicle (Figure 3-1a) incorporates a paramagnetic gadolinium chelate and oligoethylenamines, so that it offers both transverse and longitudinal relaxivity contrast, as well as the ability to bind and compact nucleic acids for gene

delivery.(25) The second vector (shown in Figure 3-1b) is a magnetic block ionomer complex (MBIC) comprised of 8-nm diameter magnetite nanoparticles in the core surrounded by a double corona structure with a nonionic polyethylene oxide (PEO) shell and anions are bound to nanomagnetite *via* ligand absorption. The unbound negatively charged carboxylates provide binding sites for drug loading through ionic complexation.(28) The superparamagnetic  $\text{Fe}_3\text{O}_4$  particle core provides primarily transverse relaxivity contrast. Figure 3-1c and 3-1d show the vector nanoparticle size distributions measured by dynamic light scattering (DLS). We also included a clinical contrast agent of sub-nm size, gadopentetic acid (marketed as Magnevist®), for comparative analysis of diffusion into hydrogels.

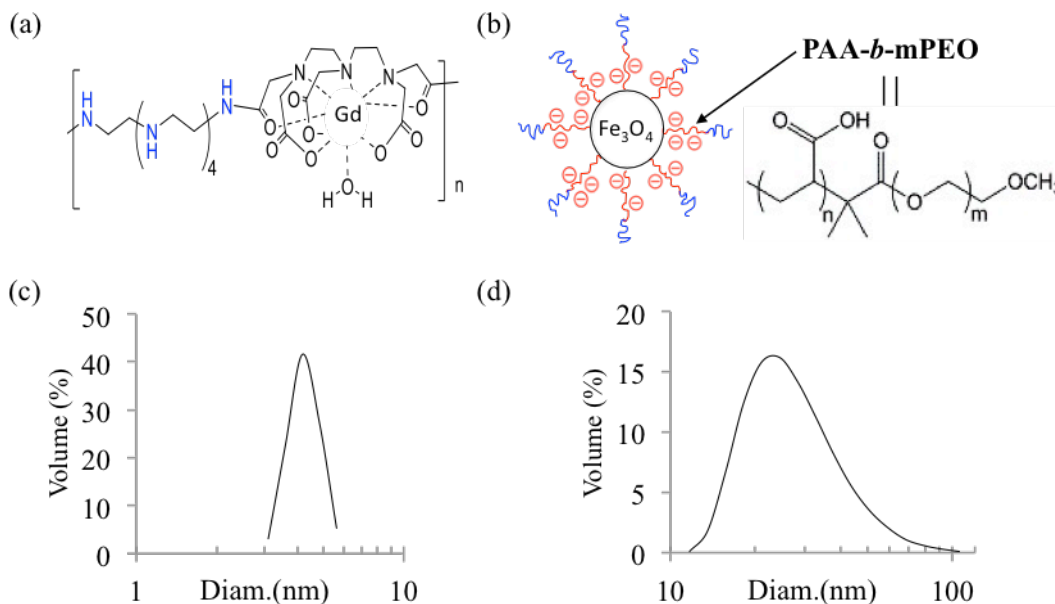


**Figure 3-1.** Structure of  $\text{N}_4\text{Gd}$  (a) and MBIC (b), as well as DLS size distribution of  $\text{N}_4\text{Gd}$  (c) and MBIC (d).

In MR images, contrast is mainly determined by the proton longitudinal relaxation time ( $T_1$ ) and transverse relaxation time ( $T_2$ ). MRI contrast agents containing paramagnetic or superparamagnetic centers have the ability to reduce  $T_1$  and  $T_2$  of their surroundings. In a  $T_1$ -weighted image, shortened  $T_1$  results in positive image contrast (higher signal intensity); while in a  $T_2$ -weighted image, regions of shortened  $T_2$  show negative contrast and appear darker. Additionally, using a suitable MRI pulse sequence, a null time  $t_{null}$  can be determined in which no signal appears in the image due to  $T_1$  relaxation. Thus we can employ a  $T_1$ -null-weighted image based on the correlation between a chosen concentration of contrast agent solution and its corresponding null point (when  $t_{null} \approx \ln 2 T_1$ ) which show near-zero intensity. Hence  $T_1$  null points can be directly encoded into and observed in images as a darkened band or region.

Generally, interference between  $T_1$  and  $T_2$  relaxation processes introduces significant inaccuracy in the determination of the relationship between contrast agent concentration and voxel signal intensity. In common  $T_1$ -weighted imaging method for clinical application, the effect of  $T_2$  relaxation cannot be avoided or effectively minimized by manipulating experiment parameters. Moreover, frequently used  $T_2$ -weighted imaging of scan repetition time smaller than  $5T_1$  can bring serious inaccuracy to the concentration profiles converted from  $T_2$ -weighted images, due to the influence of  $T_1$  relaxation. Thus, we have developed an approach combining time-resolved  $T_2$ -weighted and  $T_1$ -null-weighted imaging methods for the accurate quantitative analysis of diffusive transport, and implemented this comprehensive approach to novel polymeric nanoparticles designed for drug

deliver for the validation of our methodology. Figure 3-2 shows an illustration of the sample setup and the mathematical model for theranostic vehicle diffusion into hydrogels. In contrast to commonly used  $T_1$ -weighted images, both of our methods minimize the interference of  $T_1$  and  $T_2$  relaxation on image signal intensity, and consequently ensure the accuracy of diffusion rates determined from time-resolved MRI experiments.  $T_2$ -weighted images were acquired using the rapid acquisition with relaxation enhancement (*RARE*) sequence(30) with minimized  $T_1$ -weighting effects by applying adequate repetition time ( $>5T_1$ ). The relationship between voxel signal intensity and concentration is expressed in Equation (3-1), where  $S(c_t)$  and  $S(c_0)$  are signal intensities at concentrations  $c_t$  and  $c_0$  of the diffusing molecule,  $r_2$  is the transverse relaxivity of paramagnetic/superparamagnetic species in the medium, and  $TE$  is the echo time in the MRI pulse sequence.(31, 32)

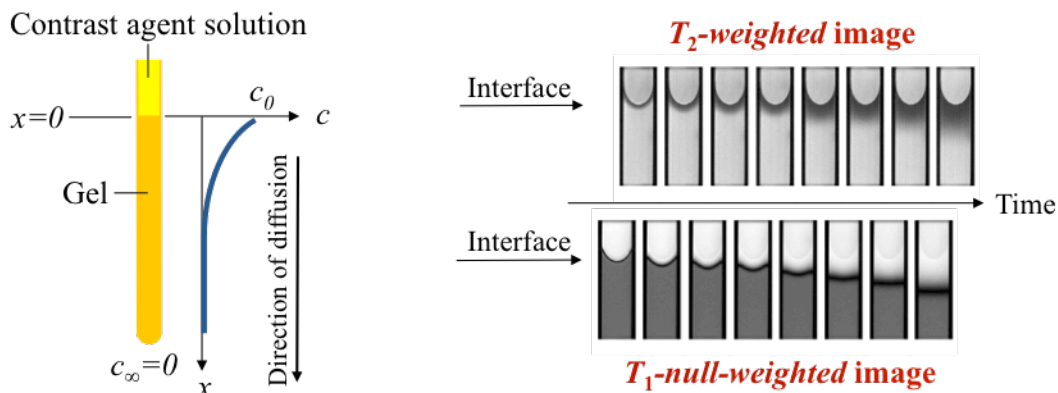


**Figure 3-2.** Sample setup for MRI measurements and model for one-dimensional diffusion (left), and time-resolved  $T_2$ -weighted and  $T_1$ -null-weighted images (right) of  $N_4Gd$  diffusing into 0.5 wt.% agarose gel. White-to-black scale represents decreasing signal intensity. Only data on or near the sample tube axis were used for analysis in  $T_2$ -weighted and  $T_1$ -null-weighted images.

$T_1$ -null-weighted(33) images were obtained using the *RARE* inversion-recovery pulse sequence,(34) yielding a direct measure of nanoparticle concentration over centimeter-scale depth in bulk biogels. The value of  $t_{null}$  was determined by testing  $T_1$  of a gel sample doped with a known reference concentration. By setting the inversion time equal to  $t_{null}$  in the MRI pulse sequence, the migration of voxels of near-zero signal intensity in time-resolved images then represents the movement of this reference concentration, indicating the diffusion of contrast agent into the gels. Time-resolved  $T_2$ -weighted and  $T_1$ -null-weighted images are shown in Figure 3-2.

### 3.4 Results and Discussion

$$c(x, t) = c_0 - \frac{\ln \frac{S(c_t)}{S(c_0)}}{TE \cdot r_2} \quad (3 - 1)$$

$$\frac{c(x, t)}{c_0} = \operatorname{erfc} \left( \frac{x - x_0}{2\sqrt{Dt}} \right) \quad (3 - 2)$$

$$P(D) = \frac{1}{D\sigma\sqrt{2\pi}} \exp \left( -\frac{(\ln(D) - \ln(D_0))^2}{2\sigma^2} \right) \quad (3 - 3)$$

$$c(x, t) = \int_0^{\infty} P(D) c_0 \operatorname{erfc} \left( \frac{x - x_0}{2\sqrt{Dt}} \right) dD \quad (3 - 4)$$

To determine diffusion coefficients ( $D$ ) of polymeric agents through gels *via*  $T_2$ -weighted MRI, we convert signal intensity to concentration using Equation (3-1). By acquiring images at different time points, we map the variation of concentration as a function of position and time,  $c(x, t)$  and then fit using Equation (3-2) to extract  $D$ .



Furthermore, by inserting the lognormal distribution given by Equation (3-3) into Equation (3-2), Equation (3-4) allows us to probe distributions of diffusion coefficients. For comparison, we extracted  $D$  from  $T_2$ -weighted images both with and without the use of a distribution. Figure 3-3 shows fitted curves of  $N_4Gd$  solution diffusing into different concentrations of agarose and collagen gels. Fitting of MBIC particle diffusion data can be found in Supplementary Information (Figure 3-S1-3-S3).

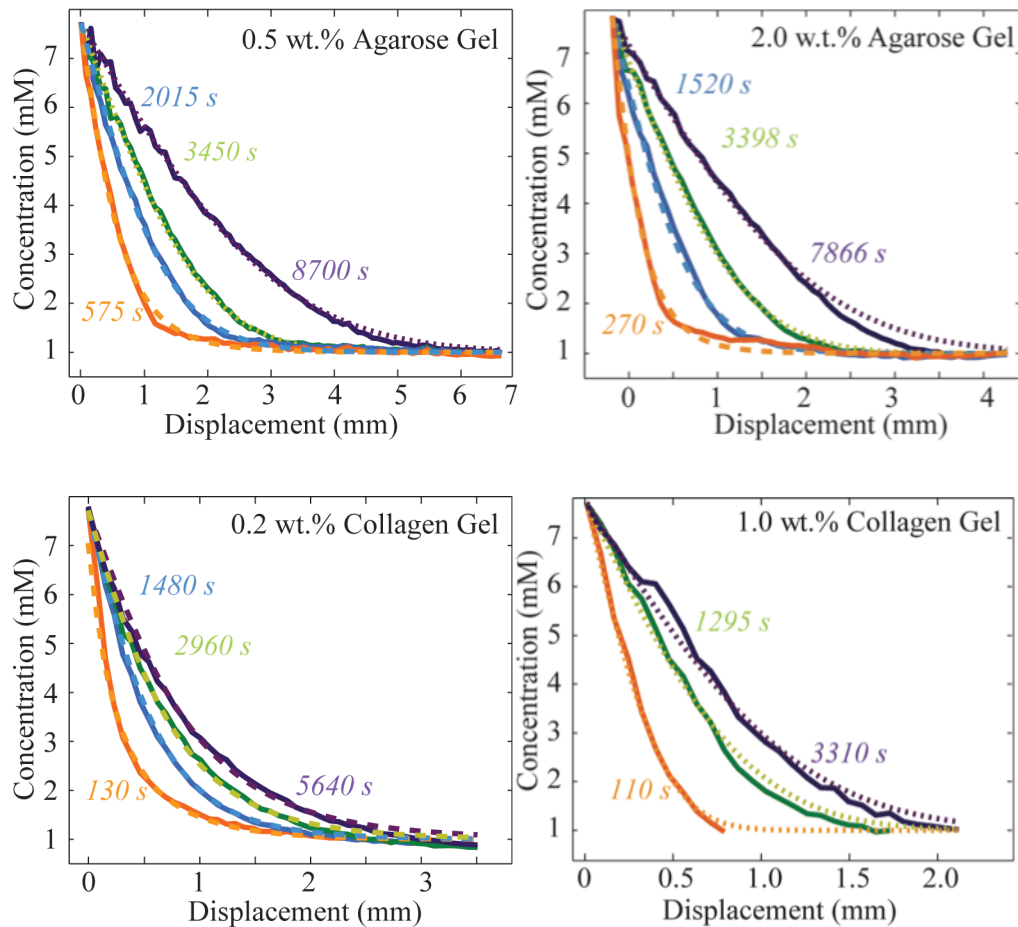


**Figure 3-3.**  $N_4Gd$  ingress into gels measured at progressive time points. Solid lines are concentrations as a function of displacement converted from intensity using

Equation (3-1). Dotted lines are fits using Equation (3-2) with no distribution. Dashed lines are fits using Equation (3-4) assuming a distribution of diffusion coefficients  $D$ . Table 3-S1 in SI shows  $D$  values (estimated error  $\pm 10\%$ ) and distribution widths extracted from each curve.

For analysis of  $T_1$ -null-weighted images, we plotted signal intensity directly versus displacement  $x$  for individual images as a function of elapsed time  $t$  (Figure 3-4). The magnitude of displacements of null points labeling the chosen concentration can then be read from the near-zero positions on the curves corresponding to every measurement time point. A diffusion coefficient (estimated error  $\pm 5\%$ ) at each time point can be directly calculated using Equation (3-2) (see Table 3-S2, SI). Additional details of the signal intensity profile versus time for this  $T_1$ -null experiment are included in SI.

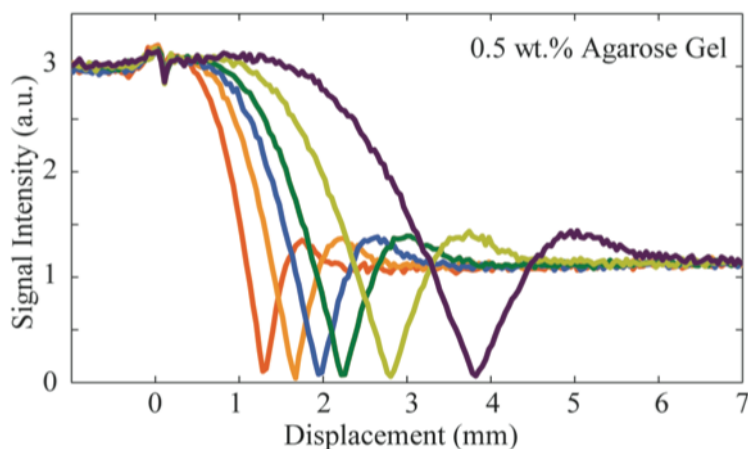


**Figure 3-4.** Plots of  $T_1$ -null-weighted data of  $N_4Gd$  diffusing into 0.5 wt.% agarose gel measured at different time points (from left to right: 950 s, 1670 s, 2390 s, 3110 s, 4780 s, and 8370 s).

We achieved agreement between diffusion coefficients of  $\text{N}_4\text{Gd}$  particles in 0.5 wt.% agarose gels measured using both methods with a discrepancy < 10% (see Table 3-S2, SI). The consistency between the two methods for all particles and diffusing media provides confidence in our approach to measuring  $D$  for a wide variety of theranostic particles into gels and other biological materials. The longitudinal and transverse relaxivity of sample solutions need to be constant throughout the volume of measurement, for the effective employment of  $T_1$ -*null-weighted* and  $T_2$ -*weighted* method, respectively. Although our study meets this requirement, heterogeneity in some other biological media may cause fluctuations in relaxivity across sampling volume. However, a variation of transverse relaxivity would not significantly affect accuracy using  $T_1$ -*null-weighted* method, as long as the longitudinal relaxivity remains consistent. Similarly, fluctuations of longitudinal relaxivity should not affect the successful application of  $T_2$ -*weighted* method through a sample of homogenous transverse relaxivity. These two methods thus provide flexibility in future studies designed to measure *in vivo* nanoparticle diffusion in tissues.

All diffusion data obtained using  $T_2$ -*weighted* images of the three agents in the four different agarose and collagen gels are listed in Table 3-1. Agarose is a neutrally charged matrix with well-characterized pore size, which provides a measure of steric and hydrodynamic interactions that hinder the movement of nanoparticles in biological media.(35-37) A reduction of median  $D$  of  $\text{N}_4\text{Gd}$  by 45% is observed with an increase of agarose content from 0.5 to 2.0 wt.%, corresponding to a decrease of  $\sim 70\%$  in average gel pore size.(35) The median  $D$  for  $\text{N}_4\text{Gd}$  into 2.0

wt.% agarose gel agrees well with the  $D$  for neutral particles of the same size measured by FRAP.(36) Negligible displacement was observed during the measurement of MBICs diffusing into 2.0 wt.% agarose gel after a 25 hour experiment duration, indicating a  $D < 1 \times 10^{-10} \text{ cm}^2/\text{s}$ , set by our spatial resolution of 40 to 80  $\mu\text{m}$ .

**Table 3-1 Diffusion coefficients of Gd-DTPA,  $\text{N}_4\text{Gd}$  and MBICs into agarose gels of 0.5 and 2.0 wt.% at 25 °C, and into collagen gels of 0.2 and 1.0 wt.% at 37 °C.<sup>a</sup> Estimated D error =  $\pm 10\%$ .**

Diffusing Medium	Sample	Diffusion Time $t$ (s)	Median Diffn. Coeff. $D$ ( $\text{cm}^2 \cdot \text{s}^{-1}$ )	Distribution	Std. Dev. $\sigma$
0.5 wt.% Agarose at 25 °C	Gd-DTPA	all	$3.7 \times 10^{-6}$	mono	
	$\text{N}_4\text{Gd}$	**575	$3.0 \times 10^{-6}$	1.0	
		8700	$3.5 \times 10^{-6}$	mono	
	MBICs	**7880	$4.5 \times 10^{-8}$	1.3	
52650		$4.0 \times 10^{-8}$	mono		
2.0 wt.% Agarose at 25 °C	Gd-DTPA	all	$3.5 \times 10^{-6}$	mono	
	$\text{N}_4\text{Gd}$	**270	$1.6 \times 10^{-6}$	1.0	
		7866	$2.0 \times 10^{-6}$	mono	
	MBICs	all	$< 1.0 \times 10^{-10}$	mono	
0.2 wt.% Collagen at 37	Gd-DTPA	all	$1.9 \times 10^{-5}$	mono	
	$\text{N}_4\text{Gd}$	**1480	$1.2 \times 10^{-6}$	0.9	

°C			**5640	$0.8 \times 10^{-6}$	0.9
		MBICs	all	$2.1 \times 10^{-8}$	mono
1.0	wt.%	Gd-DTPA	all	$2.7 \times 10^{-6}$	mono
Collagen	at 37	N <sub>4</sub> Gd	all	$1.3 \times 10^{-6}$	mono
°C		MBICs	all	$3.0 \times 10^{-9}$	mono

a Diffusion data (denoted with \*\*) fitted with the Equation (3-3) distribution are listed in the form of the median  $D$  value and standard deviation of the lognormal distribution.

Pluen and coworkers(36) observed that for 2.0 wt.% agarose gel there is a critical nanoparticle hydrodynamic radius ( $\sim 30$  nm) above which  $D$  decreases drastically. Our observation may also be due to the idea that the mean pore radius reported for 2.0 wt.% agarose gel(35, 37) does not include a distribution of pore sizes, where smaller interconnected pores in a continuous network would limit the transport of particles, though they are larger than the mean pore size. Furthermore, other measurements of pore size may not correspond to what the diffusing MBIC particles experience, when accounting for specific particle surface charge and morphology.

$D$  for MBICs in 0.5 wt.% agarose gel is two orders of magnitude lower than that of the  $\sim 8\times$  smaller N<sub>4</sub>Gd, due to steric hindrance and the influence of hydrodynamic interactions in porous gels.(38, 39) We observe a distribution of  $D$  for N<sub>4</sub>Gd in agarose gels in early time period measurements, as shown in Figure 3-3 and Table 3-1. Moreover, diffusion coefficients detected during later time periods are larger, and the fit better to Equation (3-2) instead of Equation (3-4). This likely

results from the larger MBIC particles that move more slowly through the gel and hence contribute less to the image intensity at later times.

Diffusion rates of positively charged  $N_4Gd$  particles ( $\zeta$ -potential  $+34.1 \pm 4.7$  mV from DLS measurement) match very closely with the diffusivity of neutrally charged particles of about the same size ( $\sim 2$  nm in radius) reported using FRAP methods(11) in collagen gels of both concentrations. On the other hand, the diffusion of negatively charged MBIC particles ( $\zeta$ -potential  $-67.6 \pm 4.0$  mV) was significantly hindered compared to neutral particles of similar size measured in reference 11. Within 0.2 wt.% collagen gels, the diffusion of MBICs is approximately 10 times slower than neutrally charged particles, and the diffusivity of MBICs decreases roughly two orders of magnitude compared to neutral particles in 1.0 wt.% collagen gel. This drastic decrease in diffusion rate arises from the electrostatic interaction between the slightly positively charged collagen fibers at neutral pH ( $\zeta$ -potential  $\sim +4$  mV)(40) and negatively charged MBIC nanoparticles. Combined with hydrodynamic and steric interactions, electrostatic effects influence diffusion of nanoparticles of both positive and negative surface charge, owing to their repulsion from or attraction to collagen fibers.(13) Based on Johnson and Deen's model of electrostatic energy between a spherical particle and a fiber(41), the electrostatic interactions increase with the size of diffusing particles as well as the surface charge density of the particle within a given medium. Accordingly, MBICs experience more significant electrostatic interactions than  $N_4Gd$ . Our results show that as the particle size and surface charge become larger, collagen gel at tumor relevant concentration (1.0 wt.%) presents a more significant impediment to

the diffusive transport of negatively charged nanoparticles, as illustrated in Figure 3-5. Furthermore, our observations support the idea that collagen is the main diffusive hindrance to nanoparticles, and hence determines their transport in tumor interstitium,(11) where collagen is the major component and an electrostatic bandpass is proposed.(14)

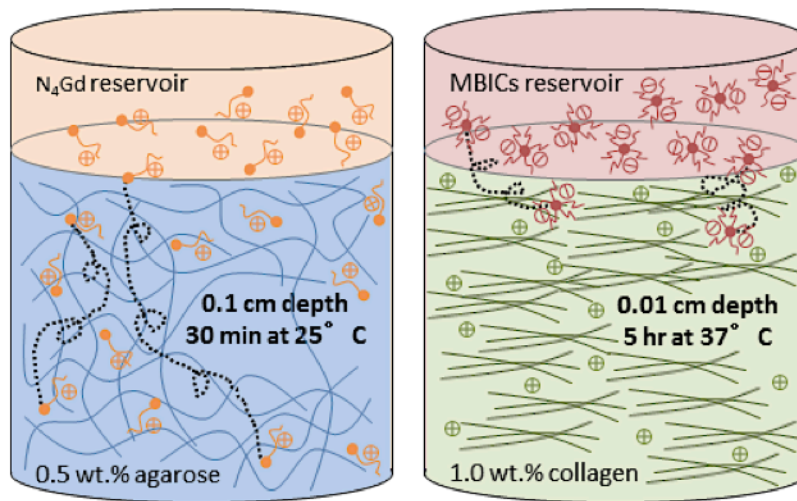


**Figure 3-5.** Representation of diffusion-driven transport of N<sub>4</sub>Gd nanoparticles into 0.5 wt.% agarose gel and MBICs into 1.0 wt.% collagen gel.

### 3.5 Conclusion

In summary, we have established and validated a simple and accurate approach for quantitative study of nanoparticle diffusive penetration into hydrogels. To the best of our knowledge, this is the first work that combines time-resolved MRI experiments to reliably quantify diffusivity of paramagnetic and superparamagnetic nanoparticles in bulk biological media. Our results agree closely with those obtained from fluorescence techniques, yet the capability of our approach allows the analysis

of actual delivery vehicle diffusion through biogels on mm to cm scales. Accordingly, this method also promises to greatly expand examinations of the transport properties of drug delivery systems into the realm of *in vivo* studies in normal and tumor tissues.



### 3.6 Reference

1. R. K. Jain, The next frontier of molecular medicine: delivery of therapeutics. *Nature Medicine* **4**, 655-657 (1998).
2. R. K. Jain, T. Stylianopoulos, Delivering nanomedicine to solid tumors. *Nature reviews. Clinical Oncology* **7**, 653-664 (2010).
3. V. P. Chauhan, T. Stylianopoulos, Y. Boucher, R. K. Jain, Delivery of Molecular and Nanoscale Medicine to Tumors: Transport Barriers and Strategies. *Annual Review of Chemical and Biomolecular Engineering* **2**, 281-298 (2011).
4. Y. Boucher, L. T. Baxter, R. K. Jain, Interstitial Pressure Gradients in Tissue-isolated and Subcutaneous Tumors: Implications for Therapy. *Cancer Research* **50**, 4478-4484 (1990).
5. M. F. Milosevic *et al.*, Interstitial fluid pressure in cervical carcinoma. *Cancer* **82**, 2418-2426 (1998).
6. C. H. Heldin, K. Rubin, K. Pietras, A. Ostman, High interstitial fluid pressure - an obstacle in cancer therapy. *Nature Reviews Cancer* **4**, 806-813 (2004).
7. H. F. Dvorak, Tumors: Wounds That Do Not Heal. *New England Journal of Medicine* **315**, 1650-1659 (1986).
8. *Cellular changes involved in conversion of normal to malignant breast: importance of the stromal reaction.* L. Ronnov-Jessen, O. W. Petersen, M. J. Bissell, Eds., (1996), vol. 76, pp. 69-125.
9. P. A. Netti, D. A. Berk, M. A. Swartz, A. J. Grodzinsky, R. K. Jain, Role of Extracellular Matrix Assembly in Interstitial Transport in Solid Tumors. *Cancer Research* **60**, 2497-2503 (2000).
10. A. Pluen *et al.*, Role of tumor-host interactions in interstitial diffusion of macromolecules: Cranial vs. subcutaneous tumors. *Proceedings of the National Academy of Sciences* **98**, 4628-4633 (2001).
11. S. Ramanujan *et al.*, Diffusion and convection in collagen gels: implications for transport in the tumor interstitium. *Biophysical Journal* **83**, 1650-1660 (2002).
12. G. Alexandrakis *et al.*, Two-photon fluorescence correlation microscopy reveals the two-phase nature of transport in tumors. *Nature Medicine* **10**, 203-207 (2004).
13. T. Stylianopoulos *et al.*, Diffusion of particles in the extracellular matrix: the effect of repulsive electrostatic interactions. *Biophysical Journal* **99**, 1342-1349 (2010).
14. O. Lieleg, R. M. Baumgärtel, A. R. Bausch, Selective Filtering of Particles by the Extracellular Matrix: An Electrostatic Bandpass. *Biophysical Journal* **97**, 1569-1577.
15. D. Axelrod, D. E. Koppel, J. Schlessinger, E. Elson, W. W. Webb, Mobility measurement by analysis of fluorescence photobleaching recovery kinetics. *Biophysical Journal* **16**, 1055-1069 (1976).
16. S. R. Chary, R. K. Jain, Direct measurement of interstitial convection and diffusion of albumin in normal and neoplastic tissues by fluorescence photobleaching. *Proceedings of the National Academy of Sciences* **86**, 5385-5389 (1989).

17. K. M. Berland, P. T. So, E. Gratton, Two-photon fluorescence correlation spectroscopy: method and application to the intracellular environment. *Biophysical Journal* **68**, 694-701 (1995).
18. V. P. Chauhan *et al.*, Multiscale Measurements Distinguish Cellular and Interstitial Hindrances to Diffusion In Vivo. *Biophysical Journal* **97**, 330-336.
19. D. A. Berk, F. Yuan, M. Leunig, R. K. Jain, Fluorescence photobleaching with spatial Fourier analysis: measurement of diffusion in light-scattering media. *Biophysical Journal* **65**, 2428-2436 (1993).
20. B. R. Rosen, J. W. Belliveau, J. M. Vevea, T. J. Brady, Perfusion imaging with NMR contrast agents. *Magnetic Resonance in Medicine* **14**, 249-265 (1990).
21. M. Markl *et al.*, Time-resolved three-dimensional phase-contrast MRI. *Journal of Magnetic Resonance Imaging* **17**, 499-506 (2003).
22. M. Markl *et al.*, Time-resolved 3D MR velocity mapping at 3T: Improved navigator-gated assessment of vascular anatomy and blood flow. *Journal of Magnetic Resonance Imaging* **25**, 824-831 (2007).
23. X. Chen, G. W. Astarly, H. Sepulveda, T. H. Mareci, M. Sarntinoranont, Quantitative assessment of macromolecular concentration during direct infusion into an agarose hydrogel phantom using contrast-enhanced MRI. *Magnetic Resonance Imaging* **26**, 1433-1441 (2008).
24. G. M. Bernal *et al.*, Convection-enhanced delivery and in vivo imaging of polymeric nanoparticles for the treatment of malignant glioma. *Nanomedicine: Nanotechnology, Biology and Medicine* **10**, 149-157 (2014).
25. J. M. Bryson *et al.*, Polymer beacons for luminescence and magnetic resonance imaging of DNA delivery. *Proceedings of the National Academy of Sciences* **106**, 16913-16918 (2009).
26. X. Wang *et al.*, Quantitation of Complexed versus Free Polymers in Interpolyelectrolyte Polyplex Formulations. *ACS Macro Letters* **2**, 1038-1041 (2013).
27. N. Pothayee *et al.*, Synthesis of 'ready-to-adsorb' polymeric nanoshells for magnetic iron oxide nanoparticles via atom transfer radical polymerization. *Polymer* **52**, 1356-1366 (2011).
28. N. Pothayee *et al.*, Magnetic Block Ionomer Complexes for Potential Dual Imaging and Therapeutic Agents. *Chemistry of Materials* **24**, 2056-2063 (2012).
29. N. Pothayee *et al.*, Magnetic nanoclusters with hydrophilic spacing for dual drug delivery and sensitive magnetic resonance imaging. *Journal of Materials Chemistry B* **1**, 1142-1149 (2013).
30. J. Hennig, A. Nauerth, H. Friedburg, RARE imaging: A fast imaging method for clinical MR. *Magnetic Resonance in Medicine* **3**, 823-833 (1986).
31. A. Abragam, *The principles of nuclear magnetism*. The International series of monographs on physics (Clarendon Press, Oxford, 1961), pp. 599 p.
32. E. M. Haacke, R. W. Brown, M. R. Thompson, R. Venkatesan, *Magnetic Resonance Imaging*. (Wiley-Liss New York; 1999).
33. B. J. Balcom, A. E. Fischer, T. A. Carpenter, L. D. Hall, Diffusion in aqueous gels. Mutual diffusion coefficients measured by one-dimensional nuclear magnetic

- resonance imaging. *Journal of the American Chemical Society* **115**, 3300-3305 (1993).
34. J. N. Rydberg, S. J. Riederer, C. H. Rydberg, C. R. Jack, Contrast optimization of fluid - attenuated inversion recovery (flair) imaging. *Magnetic Resonance in Medicine* **34**, 868-877 (1995).
  35. ZhouZhou, ZhouZhou, R. A. Caruso, Agarose Template for the Fabrication of Macroporous Metal Oxide Structures. *Langmuir* **22**, 3332-3336 (2006).
  36. A. Pluen, P. A. Netti, R. K. Jain, D. A. Berk, Diffusion of Macromolecules in Agarose Gels: Comparison of Linear and Globular Configurations. *Biophysical Journal* **77**, 542-552 (1999).
  37. N. Fatin-Rouge, K. Starchev, J. Buffle, Size effects on diffusion processes within agarose gels. *Biophysical Journal* **86**, 2710-2719 (2004).
  38. W. M. Deen, Hindered transport of large molecules in liquid-filled pores. *AIChE Journal* **33**, 1409-1425 (1987).
  39. E. M. Johnson, D. A. Berk, R. K. Jain, W. M. Deen, Hindered diffusion in agarose gels: test of effective medium model. *Biophysical Journal* **70**, 1017-1023 (1996).
  40. Y. Li, A. Asadi, M. R. Monroe, E. P. Douglas, pH effects on collagen fibrillogenesis in vitro: Electrostatic interactions and phosphate binding. *Materials Science and Engineering: C* **29**, 1643-1649 (2009).
  41. E. M. Johnson, W. M. Deen, Electrostatic effects on the equilibrium partitioning of spherical colloids in random fibrous media. *Journal of Colloid and Interface Science* **178**, 749-756 (1996).

### 3.7 Supplementary Information

#### Table of Contents:

Experimental Section

Table 3-S1. Diffusion coefficients and distribution of  $N_4Gd$  into agarose and collagen gels.

Table 3-S2. Median coefficients of  $N_4Gd$  measured by  $T_2$ -weighted imaging and diffusion coefficients measured by  $T_1$ -null weighted imaging of  $N_4Gd$  diffusing into 0.5 wt.% agarose gel.

Figure 3-S1. Fitting of experimental data (solid line) into Equation (4) with consideration of distribution (dash line) or without (dotted line) fitted using Equation (1) for diffusing of MBICs into 0.5 wt.% agarose gel.

Figure 3-S2. Fitting of experimental data (solid line) into Equation (1) without consideration of distribution (dotted line) for diffusing of MBICs into 0.2 wt.% collagen gel.

Figure 3-S3. Fitting of experimental data (solid line) into Equation (1) without consideration of distribution (dotted line) for diffusing of MBICs into 1.0 wt.% collagen gel.

Complete reference of (10), (21), and (24) from main paper

#### Experimental Section

MRI experiments were performed on a Bruker Avance III 400 spectrometer equipped with a Micro5 imaging probe featuring 5 cm rf coil. Experiments in agarose gels were carried at 25°C and the temperature for experiments in collagen gels were done at 37°C. Experimental data were acquired and processed using

ParaVision 5.0 (Bruker Biospin, Germany). Data analysis was done with MATLAB R2012a.

Reservoir concentrations ( $c_0$ ) for Gd-DTPA,  $N_4Gd$ , and MBICs are 5.0 mM, 8.0 mM and 0.3 mM, and the reference (tracker) concentration for Gd-DTPA and  $N_4Gd$  are 1.0 mM and 0.8mM.

For  $T_2$ -weighted experiments, acquisition parameters for *RARE* pulse sequence are as follows:  $TR$  (repetition time): 16000 to 20000 msec depending on the  $T_1$  relaxation time of pure hydrogels;  $TE$  (echo time): 50 to 100 msec depending on the concentration and relaxivities of contrast agent solutions;  $FOV$ : 1.00 cm; slice thickness: 1.00 mm; and resolution: 0.0078 cm/pixel.

2D selective slices centered at the midpoint of the sample tube with 1.00 mm thickness were used for the purpose of studying one-dimensional diffusion. As a result of the meniscus interface of gels in the NMR tube, penetration of contrast agent solution showed diffusion along three directions. Since we are only interested in one-dimensional diffusion along  $z$ , we analyzed data on or near the sample tube axis in every system, and the diffusion from such analysis obeys the model of Equation 3-2.

We note that this diffusion measurement technique does not require any specific assumptions about surface charge properties of the diffusing particles and/or the media, but probes actual particle diffusion that is of course affected by any such interactions.

For the  $T_1$ -null-weighted experiments, in Inversion Recovery (IR) *RARE* pulse sequence, the null time is calculated by

$$t_{null} = T_1 \left[ \ln 2 - \ln \left( 1 + e^{-\frac{TR-TE}{T_1}} \right) \right] \quad (3 - S1)$$

Taking acquisition parameters in N<sub>4</sub>Gd in 0.5 wt.% agarose gel for example, *TR*: 2000 msec, *TE*: 8.1 msec, and *T*<sub>1</sub> in doped gel of reference N<sub>4</sub>Gd concentration: 395 msec, hence *t*<sub>null</sub> is 271 msec from Equation (3-S1). *T*<sub>1</sub> relaxation time is measured using an inversion recovery NMR pulse sequence.

Inversion time was also determined by running the doped reference gel sample using IR *RARE* MRI pulse sequence and adjusting *t*<sub>null</sub> around 271 msec to until lowest signal intensity is observed. *t*<sub>null</sub> was set to 280 msec, and the discrepancy between this actual parameter and theoretical calculated value is about 3 %.

Note that one observes broadening of signal intensity and a minimum but nonzero intensity near the *T*<sub>1</sub>-null points. Because a large concentration gradient around the reference concentration results in *T*<sub>1</sub> variation over a single pixel, the signal intensity of null points is close to but not precisely zero, as suggested by Balcom et al.<sup>33</sup> Moreover, spreading of the curves near the null points in Figure 3-4 increases over time, as the spatial concentration gradient decreases as the reference concentration migrates further away from the interface.<sup>33</sup> This motivates proper selection of reference concentration and optimized experiment duration to accurately resolve diffusion rates and account for concentration gradients using the *T*<sub>1</sub>-null-weighted method.

Agarose powder was purchased from Sigma-Aldrich. Collagen I, Rat Tail was purchased from Life Technology. Agarose gels were prepared by dispersing agarose powder in water followed by heating solutions of desired concentrations to boil and

cooled down in 5 mm NMR tubes at room temperature overnight to allow complete gelation. Collagen gels of low concentration were prepared in phosphate buffered saline (PBS) and left gelling in NMR tubes at pH 7.4 and 37 °C. The collagen solution was ultracentrifuged at 10 °C for 48 hours before use for concentrated gels, and the concentration was determined from volume difference between precentrifugation and supernatant collagen solutions. Preparations were conducted in sterilized environments.

**Table 3-S1. Diffusion coefficients and distribution of N<sub>4</sub>Gd into agarose and collagen gels. Estimated error ±10%.**

Diffusing Medium	Diffusing Time/s	Median Diffusion Coefficient / cm <sup>2</sup> •s <sup>-1</sup>	Distribution Standard Deviation $\sigma$
0.5 wt.% Agarose at 25 °C	575	3.0×10 <sup>-6</sup>	1.0
	2015	3.0×10 <sup>-6</sup>	0.5
	3450	3.2×10 <sup>-6</sup>	mono
	8700	3.5×10 <sup>-6</sup>	mono
2.0 wt.% Agarose at 25 °C	270	1.6×10 <sup>-6</sup>	1.0
	1520	1.6×10 <sup>-6</sup>	0.5
	3398	1.8×10 <sup>-6</sup>	mono
	7866	2.0×10 <sup>-6</sup>	mono
0.2 wt.% Collagen at 37 °C	130	2.1×10 <sup>-6</sup>	0.9
	1480	1.2×10 <sup>-6</sup>	0.9
	2960	1.0×10 <sup>-6</sup>	0.9
	5640	0.8×10 <sup>-6</sup>	0.9
1.0 wt.% Collagen at 37 °C	110	2.3×10 <sup>-6</sup>	mono
	1295	1.8×10 <sup>-6</sup>	mono
	3310	1.3×10 <sup>-6</sup>	mono

**Table 3-S2. Median coefficients of N<sub>4</sub>Gd measured by T<sub>2</sub>-weighted imaging (estimated error ±10%) and diffusion coefficients measured by T<sub>1</sub>-null-**

**weighted imaging (estimated error  $\pm 5\%$ ) of  $N_4Gd$  diffusing into 0.5 wt.% agarose gel.**

Diffusing Time/s	Median Diffusion Coefficient / $cm^2 \cdot s^{-1}$ measured by $T_2$ -weighted	Diffusion Coefficient / $cm^2 \cdot s^{-1}$ measured by $T_1$ -null-weighted
575	$3.0 \times 10^{-6}$	
950		$3.1 \times 10^{-6}$
1670		$3.3 \times 10^{-6}$
2015	$3.0 \times 10^{-6}$	
2390		$3.4 \times 10^{-6}$
3110		$3.5 \times 10^{-6}$
3450	$3.2 \times 10^{-6}$	

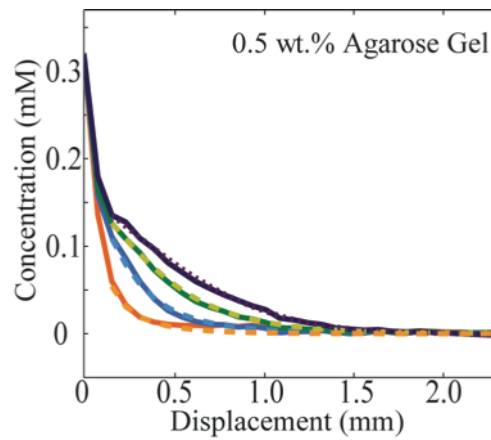


**Figure 3-S1.** Fitting of experimental data (solid line) both with consideration of a diffusion coefficient distribution (dashed line, using Equation (4)) or with no distribution (dotted line, using Equation (1)) for diffusing of MBICs into 0.5 wt.% agarose gel.



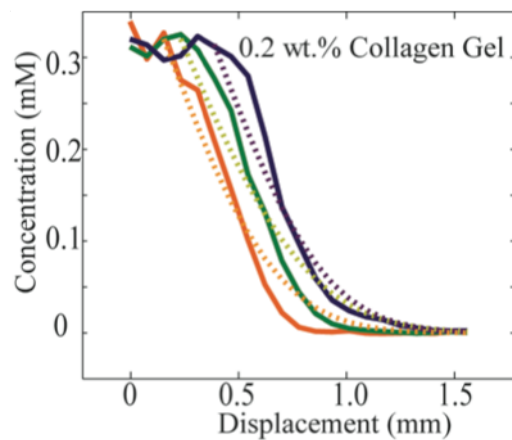


**Figure 3-S2.** Fitting of experimental data (solid line) using Equation (1) (dotted line) for diffusing of MBICs into 0.2 wt.% collagen gel.

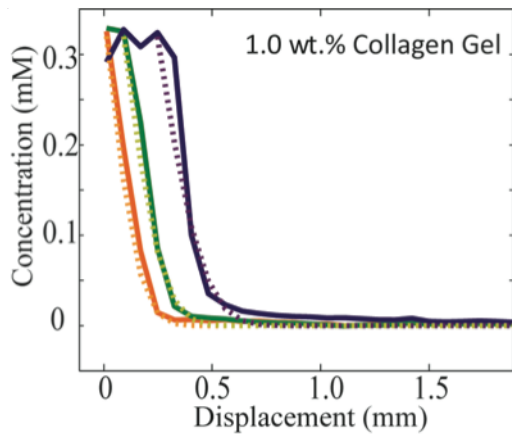


**Figure 3-S3.** Fitting of experimental data (solid line) using Equation (1) (dotted line) for diffusing of MBICs into 1.0 wt.% collagen gel.

## **Chapter 4: Molecular Weight Determination of Sulfonated Polyanion by Pulsed-Field-Gradient NMR Diffusometry**

### 4.1 Chapter Overview and Attribution

After synthesis and purification of sodium *p*-styrenesulfonate (NaSS) and sodium *N*-(4-sulfophenyl)maleimide (SPMI), PFG-NMR diffusometry was used to evaluate the weight-average molar mass ( $M_w$ ) of these polyanions. Issues related to polymer dilution in the PFG-NMR  $M_w$  determination are discussed, as well as careful use of NaSS standards to calibrate the measurements of the SPMI  $M_w$ . The effects of copolymer or block copolymer molar mass on antiviral activity are assessed. These semi-rigid, sulfonated polyanions appeared to improve anti-viral activity compared to that reported for the more flexible polystyrene sulfonate (PSS).

This work is in collaboration with Dr. Turner's and Dr. Gandour's groups at Virginia Tech. A manuscript based on this work is in preparation and close to submission. Related to the work described below, Dr. Alice M. Savage performed all the synthesis of polyanions and the anti-HIV activity characterization of those polymers.

### **4.2 Background**

Synthetic polyelectrolytes (aqueous-soluble polymers with a high degree of ionizable groups of anionic, cationic, or ampholytic nature) have a robust history of seemingly countless structural varieties and potential applications, e.g., anti-HIV

microbicides,(1) water treatment,(2) oil recovery,(3) viscosity enhancers for drilling muds,(4, 5) drug(6) and nonviral gene(7) delivery vehicles, and cosmetics(8) . Over the past decades, interest in synthesizing sequence-controlled polyelectrolytes has increased due to a need for defect-free, precisely defined, sequenced polymers for biological applications.(9, 10) Hence, characterizing these polymers presents a critical need as well as a substantial challenge.

Anti-HIV microbicides have been developed in recent decades(1) to reduce the amount of newly infected people with HIV-1 (nearly 2.3 million people per year).(11) Polyanions (anionic polyelectrolytes) have displayed potential as anti-HIV microbicides for preventing infection by HIV-1.[REF?] More recently, a study of carboxylated, semi-rigid, polyanions indicated that statistical segment lengths of 5–12 nm enhanced anti-HIV activity.[REF]

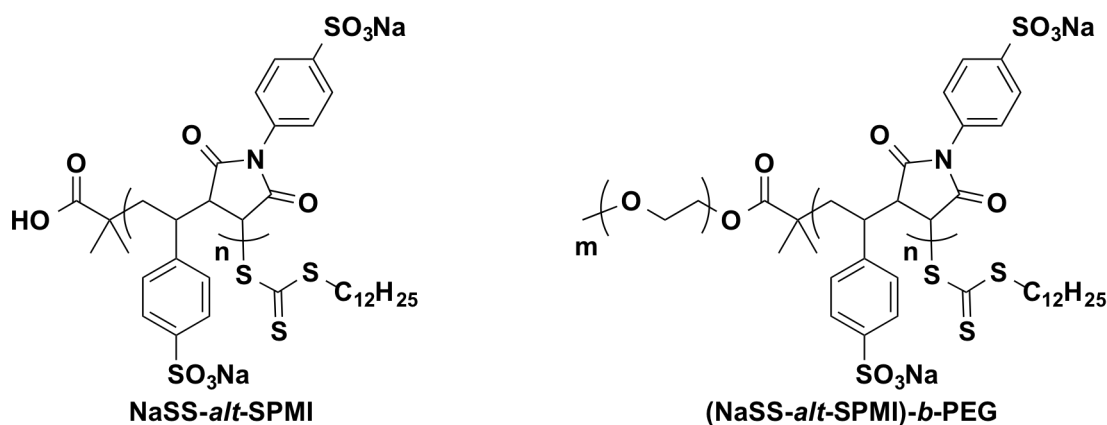


**Figure 4-1.** Structures of the alternating copolymers and block copolymers NaSS-*alt*-SPMI and (NaSS-*alt*-SPMI)-*b*-PEG.

In this study, characterization by PFG-NMR diffusometry (sometimes called DOSY, for *diffusion-ordered spectroscopy*) of a family of sulfonated alternating polyanions and block polyanions with a poly(ethylene glycol) unit (Figure 4-1) is reported. Because these copolymers are semi-rigid, they have potential application as anti-HIV microbicides.(12) Characterizing these copolymers presents a substantial challenge, since polyelectrolytes pose difficulties for traditional size exclusion chromatography (SEC).(13, 14) The strong ionic interaction in polyelectrolyte solutions causes intramolecular chain expansion and electrostatic interactions with the stationary phase, which make it much more difficult using SEC for the characterization of polyelectrolytes in aqueous solutions than for neutral polymers. As a consequence, polyelectrolyte analysis can require improved SEC detectors, as well as specific optimal solvents and columns for each polyelectrolyte, yet often still yields unsatisfying accuracy. As a result of failed SEC trials, PFG- NMR diffusometry was employed here to measure the molar masses of a family of sulfonated, semi-rigid polyanions.

The correlation between polymer molar mass and self-diffusion coefficients was originally proposed Callaghan et al.(15) and this method was used to measure the size and shape of the neutral polymer amylopectin. Subsequently, this method has been used several times to measure the molar masses of uncharged polymers.(16-19) Here we implement PFG-NMR (see Chapter 1, Part III) to solve a long-standing problem in polymer science – that of measuring molar masses of ionic polymers. This appears to be the first reported study to apply this NMR technique to measure the molar mass of charged polymers.

### 4.3 Experimental Section

Previously, the molar masses of uncharged polymers were measured with PFG-NMR(16-19) on the basis of the correlation between polymer molar mass and self-diffusion coefficients.(15) The dependence of molar mass  $M$  on self-diffusion coefficient  $D$  for a monodispersed polymer system(16) is described in Equation 4-1, which can be linearized to give Equation 4-2. Parameters  $A$  and  $\alpha$  vary for different polymer systems.

$$D = AM^\alpha \quad (4 - 1)$$

$$\log D = \alpha \log M + \log A \quad (4 - 2)$$

All diffusion measurements were performed at 25 °C in dilute aqueous solutions of polymers with a concentration of 1 mg/mL. Standards of polystyrene sulfonate (PSS) sodium salts were used to construct a linear calibration curve between  $\log D$  and  $M_w$ . Substituting measured  $D$ 's for these unknown  $M_w$  copolymers into the resulting equation from the linear regression analysis of the calibration curve with the determined coefficients  $\alpha$  and  $\log A$  gave values of  $M_w$ . Diffusion of water molecules was also measured for each sample, and the consistency of water diffusion coefficients ensured quantitative knowledge of the viscosity variation in all polymer solutions.

For both the copolymers of Figure 4-1 and the calibration polymer samples, all diffusion measurements were performed at 25 °C in dilute salt-free aqueous solutions of polymers with a concentration of 1 mg/mL. Diffusion coefficients were determined by fitting with the Stejskal-Tanner equations. Figure 4-2 shows example

proton spectra for the copolymers and a Stejskal-Tanner plot for three example polymers, where the slopes give  $-D$  for each polymer. Standards of polystyrene sulfonate sodium salts (NaPSS) were used to construct the linear calibration curve between  $\log D$  and  $M_w$  (Figure 4-3). PFG-NMR experiments were performed on a Bruker Avance III WB 400 MHz (9.4 T) NMR equipped with a single-axis diffusion probe (Diff60) having a maximum gradient of 2982 G/cm at 50 A current. Pulsed-gradient stimulated echo (PGSTE) experiments(20, 21) were used with half-sinusoid-shaped gradient pulses with effective durations  $\delta$  of 1 ms (actual duration 1.57 ms) and diffusion times  $\Delta$  of 20 ms for all samples. The number of gradient steps was set in the range 8 to 12 with selection of maximum gradient strength from 250 to 1000 G/cm to produce 50 to 70% NMR signal attenuation. The starting gradient strength value was set to 250 G/cm in order to effectively suppress H<sub>2</sub>O signal in PFG-NMR experiments, which ensured accurate determination of polymer diffusion coefficients. The number of scans was varied from 4096 to 40960 in order to achieve sufficient signal-to-noise ratio (SNR) due to differences in signal intensity among samples. Polystyrene sulfonate sodium salt (NaPSS) SEC standards were purchased from Polymer Standards Service-USA with  $M_w$  6.52, 15.8, 65.4, and 148 kDa and MWDs <1.20.  $M_w$ s for these standards were measured by SEC in dihydrogen phosphate buffer at pH 11.

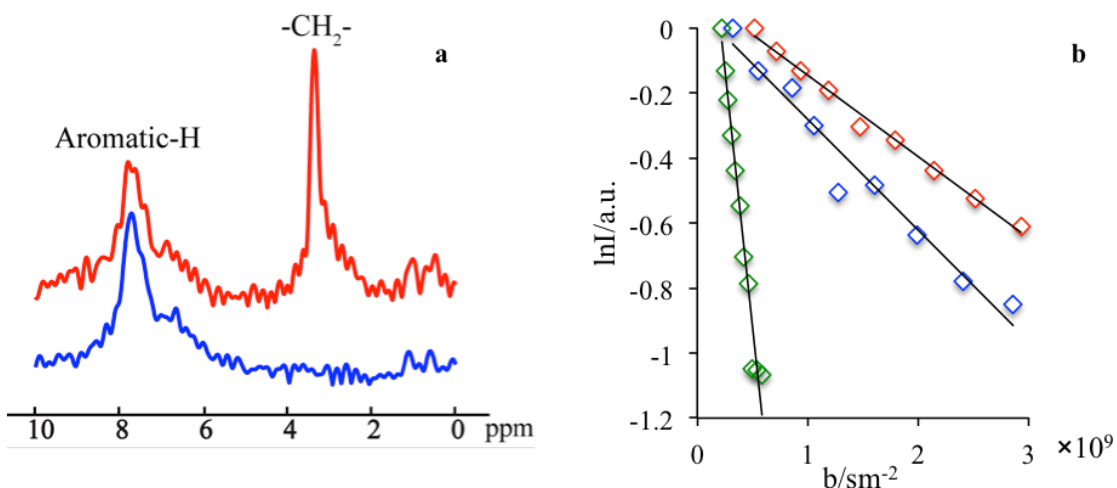


**Figure 4-2.** (a) Proton spectra of NaSS-*alt*-SPMI (blue) and (NaSS-*alt*-SPMI)-*b*-PEG (red) polymers; (b) Plot of normalized signal attenuation against the PFG NMR attenuation parameter  $b$  ( $b$  representing the term of  $-\gamma^2 g^2 \delta^2 (\Delta - \delta/3)$  in eq. 1-33) for determining diffusion coefficients of NaPSS polymer ( $M_w$  6.52 kDa) in green, NaSS-*alt*-SPMI ( $M_w$  125 kg/mol) in blue, and (NaSS-*alt*-SPMI)-*b*-PEG of ( $M_w$  154 kg/mol) in red. The solvent peak of water was suppressed by using a sufficiently large initial gradient value.

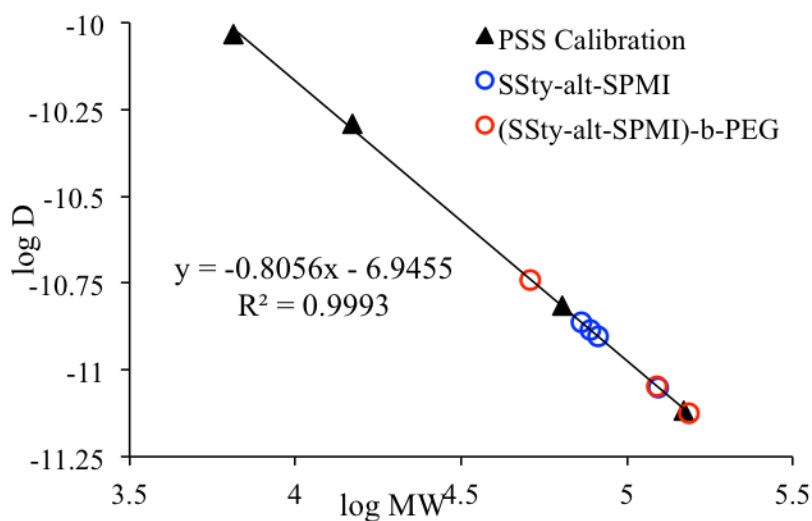


**Figure 4-3.** Calibration plot of the diffusion coefficients of four NaPSS standards measured by PFG-NMR. Using the calibration NaPSS linear fit as a reference, the NaSS-*alt*-SPMI and (NaSS-*alt*-SPMI)-*b*-PEG polyanion samples were analyzed and overlaid on this calibration plot.

Linear regression analysis of the NaPSS data ( $\log D$  vs.  $\log M_w$ ) forms the calibration curve shown in Figure 4-3, with slope  $\alpha = 0.8$  and  $A = 10^{6.9455}$ . Substituting measured  $D$  values for the NaSS-*alt*-SPMI and (NaSS-*alt*-SPMI)-*b*-PEG copolymers into the resulting equation from the calibration regression yields  $M_w$  for each copolymer sample, and these values are also incorporated into the Figure 4-3 plot.

#### 4.4 Results and Discussion

The resulting copolymers were soluble in aqueous solvent but numerous attempts to use SEC were unsuccessful, even with the use of various column sets including neutral highly cross-linked spherical polystyrene/divinylbenzene or hydroxylated polymethacrylate-based gel columns in water/acetonitrile/sodium acetate and water/methanol/acetic acid aqueous solvent mixture. Therefore, the molar masses for all polyanion samples were measured with PFG-NMR and are shown in Table 4-1.



**Table 4-1. Molar Mass and Antiviral Activity of Sulfonated Polyanions**

Copolymer [CTA], mol%	$M_w$ (kg/mol)	DP	IC <sub>50</sub> (μg/mL)		IC <sub>50</sub> (nM) <sup>b</sup>		Selectivity Index <sup>a</sup>	
			IIIb	BaL	IIIb	BaL	IIIb	BaL
NaSS- <i>alt</i> -SPMI	73	152	0.44	1.8	6.0	25	>230	>56
	78	162	0.32	1.5	4.0	19	>320	>69
	82	170	0.38	2.4	4.6	30	>260	>43
	125	260	0.43	2.2	3.4	17	>230	>46
(NaSS- <i>alt</i> -SPMI)- <i>b</i> -PEG	51	101	0.35	1.6	6.9	31	>290	>65
	123	250	0.32	2.0	2.6	15	>320	>51
	154	315	0.40	2.3	2.6	15	>250	>44
PSS <sup>b</sup> (ref 22)	864	4190	30	7	35	8.1	-	-
CSty- <i>alt</i> -CPMI <sup>b,c</sup> (ref (12))	94( $M_n$ )	197	0.23	1.0	2.9	12	>440	>100
<sup>a</sup> CC <sub>50</sub> (cytotoxicity)/IC <sub>50</sub> , where CC <sub>50</sub> (cytotoxicity) >100 μg/mL for all polyanions. <sup>b</sup> Results from previously reported assays.(12, 22) <sup>c</sup> carboxystyrene- <i>alt</i> -carboxy- <i>N</i> -phenylmaleimide								

Directly polymerizing water-soluble, ionized monomers with RAFT controlled radical techniques produces high yields of sulfonated polyanions. Unfortunately, neither SEC nor <sup>1</sup>H NMR end group analysis can be used to measure the molar masses of these polyanions due to column interactions and aggregation in SEC, and broad peaks in <sup>1</sup>H NMR. However, PFG-NMR diffusometry provides a solution to measuring the molar masses. Surprisingly, our studies are the first example of using PFG-NMR for this purpose with charged polymers.

Calibrating molar masses of PSS standards with measured diffusion coefficients by PFG-NMR enables measuring molar masses of these polyanions from their measured diffusion coefficients. Notably, the measured molar mass is  $M_w$  (weight-

average molar mass), and unfortunately, PDIs are not measured at this time due to low NMR signal-to-noise ratio (SNR). Future higher SNR experiments using higher field NMR instruments and/or cryoprobe technology will allow measurement of full molecular weight distributions in systems such as these. Typical controlled radical polymerizations can produce polymers with PDI's <1.2, and conventional radical polymerizations typically produce polymers with PDI ~ 2. Unfortunately, for comparison with our previous study,(12) the number average molar mass ( $M_n$ ) cannot be estimated, and  $M_n$  could be substantially less than  $M_w$ .

For NaSS-*alt*-SPMI, the small molar mass differences among polyanions sensibly result in only minor differences in efficacies against infection by either viral strain. For (NaSS-*alt*-SPMI)-*b*-PEG, the anti-HIV activities for the BaL strain improve slightly with lower molar mass, but they remain similar for the IIIb strain. Synthesizing copolymers with lower molar mass (< 40 kg/mol) may result in lower IC<sub>50</sub>s for both NaSS-*alt*-SPMI and (NaSS-*alt*-SPMI)-*b*-PEG as seen for other polyanion systems.(23)

#### **4.5 Conclusion**

This is the first successful use of PFG-NMR diffusometry to measure the molar masses of polyelectrolytes. The molecular weight distribution and polydispersity of the polyanions can in the future be measured if one can obtain enhanced signal intensity of polyelectrolyte samples using higher sensitivity NMR instrumentation or more concentrated samples.

These measurements were carried out in dilute salt-free aqueous solutions of

electrolytes with a relatively low concentration (1 mg/mL). For the next step, similar measurements should be performed in salt solutions of moderate ionic strength, with the same or slightly higher polymer concentrations. Appendix 1 addresses the key issues involved in such experiments in salt solutions. In that way, polyelectrolytes of larger size can be condensed to a certain extent before reaching the critical condition of aggregation, and hence PFG-NMR can more easily be applied for the characterization of molecular weight and its distribution on polyelectrolytes of larger size. Polyelectrolytes are widely used in conducting polymers for batteries, fuel cells, drug delivery systems, etc, and those materials can be more effectively and quickly analyzed and adapted for technological applications if  $M_w$  is known for those polymers. Compared to chromatographic approaches such as SEC, PFG-NMR has the advantages of short experimental periods, low cost (without the need of SEC columns and detectors, or large quantify organic solvents), as well as high accuracy.

#### 4.6 Reference

1. V. Pirrone, B. Wigdahl, F. C. Krebs, The rise and fall of polyanionic inhibitors of the human immunodeficiency virus type 1. *Antiviral Reseach* **90**, 168–182 (2011).
2. M. Goldblatt, Wastewater treatment. *Chemical Engineering Progress* **104**, 35–36 (2008).
3. W. P. Liao, F. Chen, S. R. Vasconcellos, U. S. P. Office, Ed. (Betz Laboratories, Inc, USA, 1992), pp. 1–6.
4. W. A. Thaler, S. R. Turner, T. O. Walker, E. P. Office, Ed. (EP, 1983).
5. S. R. Turner, R. Wardle, W. A. Thaler, Poly(sodium styrene sulfonate-*alt*-sodium-*N*(4-sulfophenyl) maleimide): A new water-soluble alternating copolymer. *Journal of Polymer Science Part A: Polymer Chemistry* **22**, 2281–2285 (1984).
6. S.-H. Hu, C.-H. Tsai, C.-F. Liao, D.-M. Liu, S.-Y. Chen, Controlled rupture of magnetic polyelectrolyte microcapsules for drug delivery. *Langmuir* **24**, 11811–11818 (2008).

7. S. T. Hemp, M. H. Allen, M. D. Green, T. E. Long, Phosphonium-containing polyelectrolytes for nonviral gene delivery. *Biomacromolecules* **13**, 231–238 (2011).
8. G. E. Deckner, B. S. Lombardo. (Google Patents, USA, 1998), pp. 1–6.
9. E. F. Palermo, S. Vemparala, K. Kuroda, in *ACS Symposium Series* (2013), vol. 1135, pp. 319–330.
10. J. F. Lutz, M. Ouchi, D. R. Liu, M. Sawamoto, Sequence-Controlled Polymers. *Science* **341**, 628–635 (2013).
11. Report on the Global AIDS Epidemic WHO/UNAIDS. (2013).
12. A. M. Savage *et al.*, Anti-HIV activities of precisely defined, semi-rigid, carboxylated alternating copolymers. *Journal of Medicinal Chemistry* **57**, 6354–6363 (2014).
13. R. J. Bruessau, Size exclusion chromatography of polyelectrolytes with aqueous elution solvents. *Makromolekulare Chemie. Macromolecular Symposia* **61**, 190–218 (1992).
14. R. García, I. Porcar, J. E. Figueruelo, V. Soria, A. Campos, Solution properties of polyelectrolytes XII. Semi-quantitative approach to mixed electrostatic and hydrophobic polymer-gel interactions. *Journal of Chromatography A* **721**, 203–212 (1996).
15. P. T. Callaghan, J. Lelievre, The size and shape of amylopectin: A study using pulsed-field gradient nuclear magnetic resonance. *Biopolymers* **24**, 441–460 (1985).
16. A. Chen, D. Wu, C. S. Johnson, Determination of molecular weight distributions for polymers by diffusion-ordered NMR. *Journal of the American Chemical Society* **117**, 7965–7970 (1995).
17. S. Augé *et al.*, NMR measure of translational diffusion and fractal dimension. Application to molecular mass measurement. *J. Phys. Chem. B* **113**, 1914–1918 (2009).
18. S. Floquet *et al.*, Molecular weights of cyclic and hollow clusters measured by DOSY NMR spectroscopy. *Journal of the American Chemical Society* **131**, 17254–17259 (2009).
19. W. Li, H. Chung, C. Daeffler, J. A. Johnson, R. H. Grubbs, Application of <sup>1</sup>H DOSY for facile measurement of polymer molecular weights. *Macromolecules* **45**, 9595–9603 (2012).
20. J. E. Tanner, Use of the stimulated Echo in NMR diffusion studies. *The Journal of Chemical Physics* **52**, 2523–2526 (1970).
21. R. M. Cotts, M. J. R. Hoch, T. Sun, J. T. Markert, Pulsed field gradient stimulated echo methods for improved NMR diffusion measurements in heterogeneous systems. *Journal of Magnetic Resonance* **83**, 252–266 (1989).
22. N. Cheshenko *et al.*, Candidate topical microbicides bind herpes simplex virus glycoprotein B and prevent viral entry and cell-to-cell spread. *Antimicrobial Agents and Chemotherapy* **48**, 2025–2036 (2004).
23. A. G. Bellettini, Bellettini, Richard J., Method for the treatment of HIV infected cells; USA Patent US 6,210,653 B, (USA, 2001), pp. 4

## Chapter 5 Optimization and Prediction of the Electron-Nuclear Dipolar and Scalar Interaction in $^1\text{H}$ and $^{13}\text{C}$ Liquid State Dynamic Nuclear Polarization

### 5.1 Chapter Overview

This work has been submitted to *Chemical Sciences*. Authors are listed below:

Xiaoling Wang, William C. Isley III, Sandra I. Salido, Ziqi Sun, Li Song, Kun-Hsiang Tsai, Christopher J. Cramer, and Harry C. Dorn. William C. Isley III refined all DFT calculations and calculated all hyperfine coupling constants reported in this study. Sandra I. Salido conducted the SF CO<sub>2</sub>-DNP experiments. Ziqi Sun, Li Song, and Kun-Hsiang Tsai contributed to all other experimental results presented in this work.

#### **Abstract**

In the last decade, considerable interest has focused on approaches for the hyperpolarization of NMR and MRI nuclides. One significant hyperpolarization approach is dynamic nuclear polarization (DNP) which involves polarization transfer from an electron to a nuclear spin system in solids and liquids. Although most recent DNP studies have focused on solid systems, solution-state Overhauser (Oe) DNP provides a unique way of studying intermolecular interactions in solutions as well as signal enhancement. In this paper, we illustrate new approaches for optimizing and predicting solution-state DNP. For the  $^1\text{H}$  nuclide containing systems, the solution state Oe enhancement is nearly exclusively dominated by a dipolar interaction of a  $^1\text{H}$  spin system with a unpaired electron spin system (nitroxide), but unfortunately the dipolar dominated DNP enhancement significantly decreases at

commonly used high magnetic fields ( $> 0.3$  T). We show that the dipolar DNP enhancement can be significantly improved by decreasing the correlation time ( $\tau_c$ ) of the interaction by utilizing a supercritical fluid (SF  $\text{CO}_2$ ) which allows for greater dipolar enhancements at higher magnetic fields. For biomedical applications, the enhancement of metabolites in SF  $\text{CO}_2$  followed by rapid dissolution in water or biological fluids is an attractive approach for future hyperpolarized NMR and MRI applications. For molecules containing the ubiquitous  $^{13}\text{C}$  nuclide, the solution state  $\rho_{\text{e}}$  enhancement is usually a profile of both scalar and dipolar interactions. However, the scalar interaction is dependent on a Fermi contact interaction which does not have the magnetic field dependence inherent in the dipolar interaction. Previous work has established that nitroxides are excellent probes of systems containing weakly acidic H-C groups ( $\text{H}-\text{CCl}_3$ ) and exhibit large scalar dominated DNP enhancements that are amenable to high field DNP studies. In this paper, we show a comprehensive range of molecular systems that exhibit weakly acidic complexation interaction(s) with nitroxides and provide corresponding large scalar dominated DNP enhancements. For example, we show that previously unreported sp hybridized (H-C) alkyne systems represented by the phenylacetylene-nitroxide system exhibit very large scalar dominated enhancements. Finally, we show for a wide range of molecular systems that the Fermi contact interaction can be computationally predicted via electron-nuclear hyperfine coupling and correlated with experimental  $^{13}\text{C}$  DNP enhancements.

## 5.2 Introduction

During the last two decades, significant advances have been made in the field of hyperpolarization of nuclear magnetic resonance nuclides (e.g.  $^1\text{H}$ ,  $^{15}\text{N}$ ,  $^{31}\text{P}$ ,  $^{13}\text{C}$ ). One approach pioneered by Weitekamp, Bhattacharya, and coworkers involves spin polarization transfer from para-hydrogen ( $p\text{-H}_2$ ) to another molecular entity after a hydrogenation reaction, which is described as PASADENA (para hydrogen and synthesis allow dramatically enhanced nuclear alignment).<sup>(1, 2)</sup> In another approach, polarization transfer from an electron to nuclear spin system, dynamic nuclear polarization (DNP) has advantages for numerous biological applications. For example, a seminal approach reported by Ardenkjaer-Larsen and coworkers involved contact of stable radicals (e.g., trityl, nitroxides) to hyperpolarize small molecules endogenous to biological systems (e.g., urea, pyruvate, and carbon dioxide) at low temperatures (<4K) that are then rapidly transferred to an NMR or MRI instrument.<sup>(3, 4)</sup> For solution-state DNP, there has also been a resurgence of interest in ameliorating solution-state high magnetic field DNP enhancements.<sup>(5-7)</sup>

In dynamic nuclear polarization, the electron-nucleus dipolar and scalar couplings can be described by the Hamiltonian,

$$\hat{H} = h \cdot \hat{S} \cdot D \cdot \hat{I} + h \cdot \hat{I} \cdot A \cdot \hat{S} \quad (5 - 1)$$

where  $h$  is the Planck constant,  $\hat{I}$  is the nuclear spin angular momentum operator,  $\hat{S}$  is the electronic spin angular momentum operator,  $D$  is the dipolar coupling tensor, and  $A$  is the hyperfine coupling tensor (typically in units of MHz).

One can compute the dipolar coupling tensor  $D$ ; however, knowledge of the electron-nucleus dipole-dipole correlation function is required to determine the enhancement factor.(8) Computation of this dipole-dipole correlation function can be achieved with a molecular dynamic simulation. However, such simulations are typically limited to select parameterized systems, and are very computationally intensive.(8)

Scalar relaxation originates from the coupling of the magnetic moments of electrons and nuclei via the hyperfine coupling interaction.(9) Although  $A$  in eq. 5-1 is the isotropic Fermi contact hyperfine coupling constant, henceforth it is labeled as  $a_{FC}$ , in order to avoid confusion with the DNP enhancement, *A* *vida infra*. The hyperfine coupling is directly proportional to the unpaired electron spin density at the nucleus of interest, and is readily computed from electronic structure calculations (both wave-function based and density-functional based) using the variationally determined density matrix. Barone et al. have demonstrated the effect of hydrogen bond between nitroxide radicals and water molecules on hyperfine coupling constants.(10) Qualitatively, scalar coupling involves the transfer of angular momentum from unpaired electron spin density at the target nucleus to that nucleus' magnetic angular momentum (the Fermi contact interaction). In the case of the scalar DNP interaction, the transition probability  $W_0$  is much larger than both  $W_1^D$  and  $W_2^D$ , as shown by the lower diagram in Figure 5-1. The Fermi contact interaction and corresponding hyperfine coupling constant ( $a_{FC}$ ), which is given by

$$a_{FC} = (8\pi/3)\gamma_S\gamma_I\hbar^2|\psi(0)|^2 \quad (5 - 2)$$

where  $|\psi(0)|^2$  represents the unpaired spin density at the nucleus X.



For solution-state DNP, the drawbacks for obtaining significant DNP enhancements ( $A$ ) are well recognized since the time-dependent electron-nuclear interaction is dominated by the Overhauser effect (Oe).<sup>(11-16)</sup> This can be derived from eqs. 5-3-5-5, where  $\gamma_S$  and  $\gamma_I$  are the magnetogyric ratios for the electron and nuclear spins, respectively, and the coupling ( $\rho$ ) and leakage ( $f$ ) factors are defined in terms of the nuclear transition probabilities in the presence of a free radical,  $W_2^D$ ,  $W_0^D$ ,  $W_1^D$ , which represent dipolar relaxation, and  $W_0^{Sc}$  due to scalar relaxation, as well as the transition probability in the absence of a free radical  $W_{10}$  (Figure 5-1).<sup>(16)</sup> The subscript illustrates the change of total magnetic quantum number by each transition. For all time-dependent Oe enhancements, the dipolar interaction is always present between the substrate and the paramagnetic (electron) spin system. For molecular liquid systems, the time-dependent electron-nuclear Oe coupling interaction only dominates at low magnetic fields and/or short correlation times ( $\tau_c$ ), in the extreme narrowing limit  $\omega_S^2 \tau_c^2 \ll 1$  ( $\omega_S$  electron Larmor frequency).

Unfortunately, at high magnetic fields (3-12 T) commonly employed in NMR the coupling factor approaches zero (shown in Figure 2). In addition, it is experimentally difficult to achieve a high electron spin saturation factor ( $s$ ) especially at high microwave frequencies (90-360 GHz) at high magnetic fields due to short electron spin relaxation times.

$$A = \frac{A_Z - A_0}{A_0} = \frac{-\rho f s |\gamma_S|}{\gamma_I} \quad (5 - 3)$$

$$\rho = \frac{W_2^D - W_0^D - W_0^{Sc}}{W_2^D + W_0^D + W_0^{Sc} + 2W_1^D} \quad (5 - 4)$$

$$f = \frac{W_0^D + 2W_1^D + W_2^D + W_0^{Sc}}{W_0^D + 2W_1^D + W_2^D + W_0^{Sc} + W_{10}} \quad (5 - 5)$$

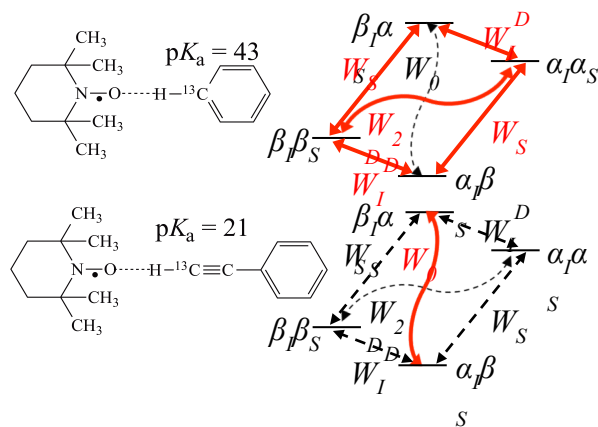


**Figure 5-1.** Schematic diagram of energy level and transition probabilities for electron-nuclear (<sup>13</sup>C) spin systems for benzene/TEMPO (above) and phenylacetylene/TEMPO (below).  $\alpha_S$  and  $\beta_S$  are the spin states of the unpaired nitroxide electron spin, and  $\alpha_I$  and  $\beta_I$  are for nuclear spins.  $W_S$  represents the electron relaxation;  $W_0$ ,  $W_1^D$  and  $W_2^D$  are zero, single and double quantum transition, respectively.  $W_0$  is equal to the sum of  $W_0^{Sc}$  and  $W_0^D$  in eq. 5-4 and eq. 5-5, which are transition rates of scalar and dipolar relaxation, respectively. <sup>13</sup>C DNP enhancement of benzene is mainly due to dipolar relaxation, while scalar relaxation is the dominant mechanism for the  $\beta$  carbon of phenylacetylene.

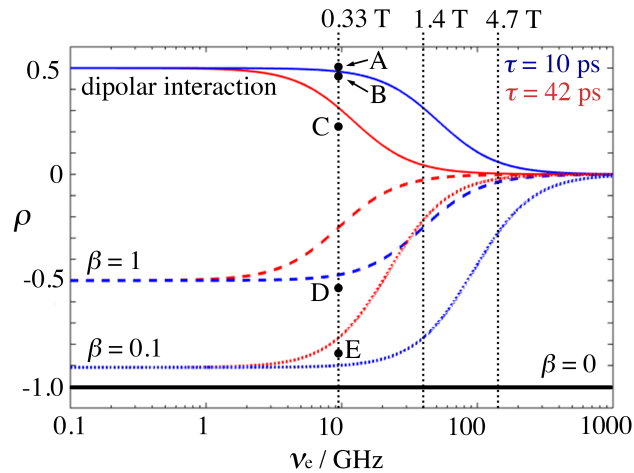


**Figure 5-2.** Coupling factor ( $\rho$ ) of the Overhauser effect enhancement depends on the electron Larmor frequency for rotational motion with correlation time 10 ps (blue solid) and 42 ps (red solid); mixed with scalar enhancement of  $\beta = 1$  (blue dash for  $\tau_c = 10$  ps and red dash for  $\tau_c = 42$  ps), and  $\beta = 0.1$  (blue dotted for  $\tau_c = 10$  ps and red dotted for  $\tau_c = 42$  ps), where  $\beta$  values define different contributions from dipolar relaxation competing with pure scalar relaxation(15). Pure scalar enhancement (black solid line) is independent of magnetic field strength. Points A-E represent coupling factor values calculated from extrapolated experimental LLIT DNP enhancements polarized at 0.33 T: (A)  $^1\text{H}$  of 9% benzene/0.001 M TEMPO/SF  $\text{CO}_2$ ,<sup>(17)</sup> (B)  $^1\text{H}$  of chloroform/0.0015 M TEMPO<sup>(18)</sup>, (C)  $^1\text{H}$  of 9% benzene/0.01 M TEMPO/ $\text{C}_6\text{D}_6$ ,<sup>(17)</sup> (D)  $^{13}\text{C}$ - $\beta$  of phenylacetylene/0.01 M TEMPO<sup>(19)</sup>, and (E)  $^{13}\text{C}$  of chloroform/0.0052 M TEMPO<sup>(18)</sup>. The relative standard deviation for  $\rho$  is about 15%. The two correlation times were estimated from  $^1\text{H}$  DNP coupling factors of benzene in SF  $\text{CO}_2$  and normal solvent by a rotational diffusion modulated dipolar interaction mechanism shown by eq. 5-6 and 5-7. (See SI for derivation)

For most liquid systems, the dipolar interaction dominates the electron-<sup>1</sup>H interaction. Although a translational correlation time is possible, it is convenient to assume that a rotationally modulated mechanism dominates this dipolar interaction; the corresponding rotational correlation time ( $\tau_r$ ) can be estimated from the expression for exclusive rotational dipolar diffusion(15, 16, 20),

$$\rho_D^r = \frac{1}{1.4 + 0.6 \left[ \frac{J_D^r(\omega_I)}{J_D^r(\omega_S)} \right]} \quad (5 - 6)$$

$$J_D^r(\omega) = \left( \frac{1}{2\pi r^6} \right) \left[ \frac{\tau_r}{1 + \omega^2 \tau_r^2} \right] \quad (5 - 7)$$

where  $r$  is the nucleus-electron distance in the complex and  $J_D^r(\omega)$  is the rotational dipolar spectral density.

However, a notable exception is a nitroxide-trifluoroacetic acid system reported by Bates where the scalar interaction dominates the <sup>1</sup>H DNP enhancement.<sup>(21)</sup> On the other hand, for the <sup>13</sup>C nuclide, the coupling interaction can be dominated by a strong scalar interaction ( $W_{\sigma^{Sc}} \gg W_{2^D}, W_{1^D}, W_{0^D}$ ) or a dipolar interaction ( $W_{\sigma^{Sc}} \ll W_{2^D}, W_{1^D}, W_{0^D}$ ), or by a mixture of scalar and dipolar interactions. As illustrated in Figure 1, it is well recognized that molecules with a (C-H) group can exhibit weak hydrogen bonding with nitroxides and exhibit modest to large scalar enhancements.<sup>(16, 18, 22-25)</sup> Griffin and coworkers have pointed out the importance of the scalar interaction for certain other nuclides (<sup>19</sup>F, <sup>15</sup>N, <sup>31</sup>P) besides <sup>13</sup>C for high-field liquid-state DNP studies.<sup>(26)</sup> Unfortunately, it is difficult to estimate the corresponding scalar correlation time  $\tau_{sc}$ . It can be estimated from determination of the nuclear relaxation rates,  $1/T_1$  and  $1/T_2$ , the value of the hyperfine coupling

constant  $a$ , and the mole fraction obtainable from the NMR contact shift measurements. However, it is commonly believed that the scalar correlation times are longer than dipolar correlation times. For the case of acetonitrile/TEMPO, we previously reported  $^{13}\text{C}$  DNP  $\tau_{sc}$  values 2-3 times longer than the dipolar correlation time ( $\tau_r$ ).<sup>(25)</sup>

In the current study, we demonstrate that  $^1\text{H}$  LLIT (liquid-liquid intermolecular transfer) and  $^1\text{H}$  SLIT (solid-liquid intermolecular transfer) DNP solutes dissolved in supercritical fluid (SF)  $\text{CO}_2$  result in enhanced electron-nuclear dipolar interactions and exhibit significant Oe DNP enhancements at higher magnetic fields as a result of reduced correlation times. For the case of the  $^{13}\text{C}$  NMR nuclide, significant scalar interactions and corresponding large positive enhancements are obtained at high magnetic fields for cases where weak hydrogen bonding interactions are present in nitroxide-substrate complex. For example, we show that  $sp$  hybridized (H-C) alkyne systems, such as, the phenylacetylene-nitroxide system exhibit very large scalar dominated enhancements. It is also possible to directly compare liquid-liquid intermolecular scalar (Fermi contact) hyperfine couplings ( $a_{FC}$ ) with experimental scalar DNP data utilizing density functional theory (DFT) modeling.<sup>(25)</sup> We will subsequently demonstrate that computational predictions of the scalar hyperfine coupling constants (HFCs) across a wide set of nitroxide-substrate systems correlates strongly with the DNP enhancements for systems dominated by the scalar interaction.

### 5.3 Experimental Section

**Samples.** All reagents and solvents for the LLIT DNP experiments were obtained commercially.  $C_6D_6$  was purchased from the Isotec Inc, and other chemicals were purchased from Aldrich Chemical Co. and used without further purification. Sample solutions for the LLIT DNP experiments were prepared with TEMPO of varied concentrations from 0.005 to 0.14 M. The immobilized nitroxide materials used for the SLIT DNP experiments were synthesized in our lab by Holger Fischer and Rossi Gitti.(27) The sample solutions were degassed by bubbling  $N_2$  gas through during DNP experiments.

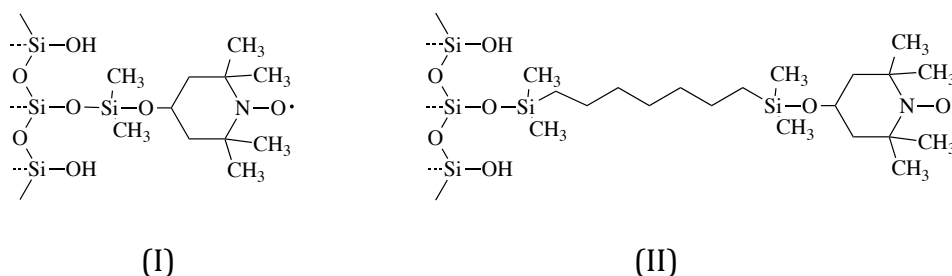


**Figure 5-3.** Immobilized nitroxide material I (left) and II (right) used in SLIT  $^1H$  DNP in normal liquids and SF  $CO_2$ .

**Dynamic Nuclear Polarization Instrument.** The instrument used for the LLIT DNP experiments was described previously.(18) The flow transfer DNP apparatus for normal liquids and supercritical fluid  $CO_2$  is shown in Figure 5-4, where SF  $CO_2$  can be used as the flowing solvent. For flow  $^1H$  DNP performed under supercritical fluid conditions,  $N_2$  degassed neat liquid benzene containing free radical TEMPO (0.1 M-0.01 M) originates at the HPLC pump and flows at a rate of 0.1 mL/min. The typical sample volumes inside the low field microwave cavity and high field NMR

detector are 160 and 60  $\mu\text{L}$ , respectively, and the volume of the transfer region is 80  $\mu\text{L}$ .  $\text{CO}_2$  is pumped from a syringe pump of a Suprex SFC/200A Multipurpose Unit and equilibrated to a flow rate of 1.01 mL/min and 165 atm. The liquid sample is introduced into the  $\text{CO}_2$  flow, and at a total flow rate of 1.11 mL/min the sample solution enters the SFC oven where it is heated to 40  $^\circ\text{C}$ . The flow rate maintains the liquid sample concentration ensuring the liquid solutes solubility and also maintains the optimum conditions based on transfer and residence times for the flow  $^1\text{H}$  DNP apparatus.

The instruments for the SLIT DNP performed in normal liquids and SF  $\text{CO}_2$  were reported in our previous studies.(27-30) The immobilized nitroxide radical is contained in a flow cell and located in the 0.33 T low field cavity, where electron spins are polarized. The experimental procedure of SLIT  $^1\text{H}$  DNP is similar to that of LLIT  $^1\text{H}$  DNP. The rate of liquid flow containing the sample was adjusted accordingly to obtain preferred concentrations in normal liquids or SF  $\text{CO}_2$  as the flowing solvents.

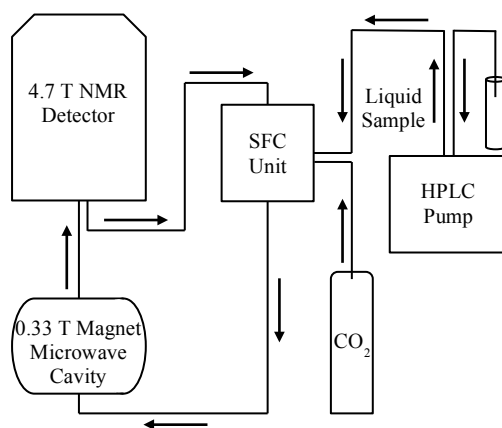


**Figure 5-4.** Schematic drawing of apparatus for continuous-flow HPLC-DNP-NMR coupled with SF CO<sub>2</sub> (adapted from Ref. 17, with the original figure shown in SI).

**Determination of Experimental Parameters.** The determination of the leakage factor  $f$  and the electron spin saturation factor  $s$  is described previously for the DNP flowing system.<sup>(18)</sup> In Ref. 18, we reported a theoretical model for determining the absolute enhancement for the low to high magnetic field transfer experiments, which is scaled according to the observed enhancement considering relaxation losses during the transfer. For most systems reported in this study, the DNP data were processed based on this model, and absolute DNP enhancements were calculated using the method we applied previously.<sup>(27, 31, 32)</sup> For the benzaldehyde and nitrobenzene systems, the absolute enhancements of <sup>13</sup>C LLIT DNP are obtained using a ratio method<sup>(33-35)</sup> using <sup>13</sup>C of cyclohexane as the reference nucleus, with detailed procedures illustrated in the SI.

**Theory: Geometry Optimization, Solvation, and Thermochemistry.** Geometry optimizations were performed for all species at the unrestricted M06-L<sup>(36)</sup> level of density functional theory. The def2-SVP basis set<sup>(37)</sup> was used for all atoms during optimization. The nature of stationary points was assessed in all cases by computation of analytic vibrational frequencies, which were also used to compute the molecular partition functions necessary to predict 298.15 K thermochemical quantities using the conventional ideal-gas, rigid-rotator, quantum-mechanical quasi-harmonic-oscillator<sup>(38)</sup> approximation.<sup>(39)</sup> Improved electronic energies were computed with the M06-2X density functional<sup>(40)</sup> and the SMD continuum



solvation model(41) to account for the effects of the solvation environment, as single-point calculations, using the def2-TZVPP basis set(37) on all atoms. Benzene was used for SMD solvent parameters on nitroxide /benzene and nitroxide/phenylacetylene systems; whereas cyclohexane SMD solvent parameters were specified for nitroxide/ benzaldehyde and nitroxide/nitrobenzene systems.

**Theory: Isotropic Hyperfine Coupling.** The  $^{13}\text{C}$  hyperfine coupling constants were computed in the gas phase at the unrestricted B3LYP level of DFT employing the EPR-III basis(42) for C, N, H, O. We chose to use the B3LYP functional(43) based on previously demonstrated good EPR performance for a nitroxide in aqueous system.(8) Hyperfine coupling constants were computed using the spin orbit mean field approximation SOMF(1X).(44) For all substrate/TEMPO systems, Boltzmann weighted isotropic HFCs for nucleus  $j$ ,  $a_{iso}^j$ , are determined from low-energy intermolecular configurations,  $c_i$ , as computed from eq. 8.  $a_{iso}^{j, c_i}$  is the isotropic HFC for nucleus  $j$  in geometrical configuration  $c_i$ ,  $\Delta G^{c_i}$  is the relative free energy of geometrical configuration  $c_i$ ,  $R$  is the universal gas constant, and  $T$  is the temperature (taken to be 298.15 K). Symmetry equivalent atoms are averaged together.

$$a_{iso}^j = \sum_{c_i} a_{iso}^{j, c_i} \left( \frac{e^{-\Delta G^{c_i}/RT}}{\sum_{c_i} e^{-\Delta G^{c_i}/RT}} \right) \quad (8)$$

**Software.** All optimization, thermochemistry, and solvation computations were accomplished using the Gaussian09 Rev D.01 suite of electronic structure programs.(45) All EPR computations were accomplished in the gas phase using the ORCA 3.0.2 suite(46) of electronic structure programs.

## 5.4 RESULTS AND DISCUSSION

**LLIT  $^1\text{H}$  DNP Experiments in Supercritical Fluid (SF)  $\text{CO}_2$ .** The dipole-dipole transition probabilities and the coupling factor (eq. 5-4) can be evaluated as products of dipolar coupling constants and spectral densities.(13) It is convenient to use the reduced spectral density function(47) for a given correlation time as a function of electron Larmor frequency shown by eq. 5-9, which under the extreme narrowing condition where  $\omega^2\tau_c^2 \ll 1$  is independent of the magnetic field. Assuming a DNP enhancement is due to pure dipolar relaxation modulated by exclusive rotational diffusion, the corresponding coupling factor (eq. 5-6) then gives the magnetic field dependence shown in Figure 5-2 by colored solid lines. It can be shown theoretically(13) from Figure 5-2 and eq. 5-9 that as the molecular correlation time becomes shorter, dipolar relaxation results in useful DNP enhancement at high magnetic fields for electron polarization (blue versus red lines).

$$j(\omega) = \frac{1}{2\pi} \frac{\tau_c}{(1 + \omega^2\tau_c^2)} \quad (5 - 9)$$

Solutes dissolved in supercritical fluids exhibit significantly shorter molecular correlation times than in most common liquid solvents.(48) The solubility of SFs can be readily adjusted by changes in temperature and pressure, which affect the SF density, and more importantly for DNP studies, the molecular correlation times. In order to operate in the supercritical region, temperatures and pressures at or above the critical point ( $T_c$  and  $P_c$ ) must be used. SF  $\text{CO}_2$  has the advantage of relatively low

critical point parameters,  $T_c = 31\text{ }^\circ\text{C}$  and  $P_c = 74\text{ atm}$  (1072 psi), with a corresponding critical density of  $\rho_c = 0.468\text{ g/mL}$  and viscosity  $\eta_c = 0.03\text{ cP}$ . The use of SF CO<sub>2</sub> as a solvent has salient other features as a hyperpolarization fluid since it does not contain abundant spins (<sup>1</sup>H) which would allow alternative relaxation pathways for hyperpolarized nuclides. In addition, samples are easily recovered from this fluid either by simple evaporation of liquid SF CO<sub>2</sub> at atmospheric pressure or bubbling into a different solvent (e.g., H<sub>2</sub>O).<sup>(25, 26, 49, 50)</sup>

Studies of molecular correlation times of small molecules in supercritical fluids and gases have shown narrowed NMR lines (shorter correlation times  $\tau_c$ ) of quadrupolar nuclei in NO and CO<sub>2</sub> under supercritical conditions<sup>(48)</sup>, and the line narrowing effect makes <sup>1</sup>H NMR a potential monitoring detector for supercritical fluid chromatography<sup>(51, 52)</sup>. The line narrowing originates from reduced quadrupolar interactions as a result of the shortened molecular correlation time, which is directly proportional to the solution viscosity<sup>(53)</sup>. However, there is a paucity of SF DNP experiments reported to date, with the notable exception of the <sup>1</sup>H DNP enhancement of supercritical ethylene by Wind and coworkers.<sup>(54)</sup> Therefore, for flow transfer <sup>1</sup>H DNP using SF CO<sub>2</sub> as the flowing solvent, as a consequence of shorter correlation times, larger absolute DNP enhancements of small molecules due to enhanced dipolar relaxation are expected.

In the current study, we report the SF <sup>1</sup>H DNP enhancements of benzene in supercritical CO<sub>2</sub>. The static and flow <sup>1</sup>H NMR, and flow <sup>1</sup>H DNP spectra for 9% benzene/0.001 M TEMPO dissolved in SF CO<sub>2</sub> is illustrated in Figure 5-5.<sup>(17)</sup> The LLIT <sup>1</sup>H DNP absolute enhancements of benzene dissolved in deuterated benzene

and SF CO<sub>2</sub> are presented in Table 5-1.(17) DNP data were collected for the benzene samples at TEMPO concentration of 0.01 and 0.001 M. The values of electron spin saturation factor *s* are smaller in SF CO<sub>2</sub> compared with normal liquids (see Table 5-S1). This is because of increased broadening of the EPR signal in SF CO<sub>2</sub>, which makes it more difficult to saturate the electron transitions by the microwave power and can affect optimal DNP enhancements (saturation curves shown in Figure 5-S2 and Figure 5-S3). Batchelor(55), as well as Randolph and Carrier(56) suggest a large increase of Heisenberg electron-electron exchange rates and hence the increased line widths of nitroxides in SF's may be due to critical clustering between solute and solvent molecules.

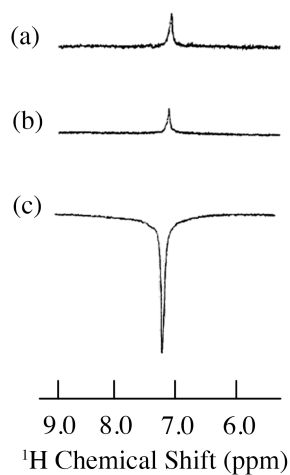


**Figure 5-5.** <sup>1</sup>H spectra of 9% benzene/0.001M TEMPO dissolved in SF CO<sub>2</sub> at 4.7 T. (a) Static <sup>1</sup>H NMR (S/N = 20), (b) flow <sup>1</sup>H NMR (S/N = 17) and (c) flow <sup>1</sup>H DNP (S/N = 124). Total flow of SF CO<sub>2</sub> was 1.1 mL/min. SF CO<sub>2</sub> conditions: d = 0.805 g/mL, SFC oven temperature 40 °C, P = 165 atm. All Spectra were collected at 32 scans.

**Table 5-1. LLIT  $^1\text{H}$  DNP Enhancements Polarized at 0.33 T for Benzene/TEMPO in  $\text{C}_6\text{D}_6$  and SF  $\text{CO}_2$**

system	absolute enhancement
9% benzene/ $\text{C}_6\text{D}_6$ /0.001 M TEMPO	-120±18
9% benzene/SF $\text{CO}_2$ /0.001 M TEMPO	-341±36
9% benzene/ $\text{C}_6\text{D}_6$ /0.01 M TEMPO	-146±20
9% benzene/SF $\text{CO}_2$ /0.01 M TEMPO	-293±44

Benzene and chloroform have been extensively used as model systems in DNP studies: both molecules present negative  $^1\text{H}$  DNP enhancements due to a dipolar-dominated Overhauser effect.<sup>(23, 49, 57-65)</sup> The  $^1\text{H}$  DNP absolute enhancement of chloroform gives a coupling factor approaching the dipolar enhancement limit (point B in Figure. 5-2). A comparison of the absolute enhancement values between 9% benzene in  $\text{C}_6\text{D}_6$  and SF  $\text{CO}_2$  mixed with same TEMPO concentration shows a significant increase in the DNP signal. The increased  $^1\text{H}$  DNP enhancement of benzene in SF  $\text{CO}_2$  over benzene in liquid  $\text{C}_6\text{D}_6$  is attributed to increased mobility of benzene provided by the supercritical fluid. There is an approximately 2-3 fold increase in the DNP enhancement of SF  $\text{CO}_2$  in comparison with liquid  $\text{C}_6\text{D}_6$ , which is in agreement with the decrease factor of molecular correlation times of small molecules in SF  $\text{CO}_2$ .<sup>(48, 52, 66)</sup> Assuming a rotational dominated correlation (eq. 5-6 and 5-7), provides the prediction of 10 and 42 ps, respectively for SF  $\text{CO}_2$  and liquid  $\text{C}_6\text{D}_6$ . Furthermore, when the experimental error is taken into account, the absolute enhancement of 9% benzene in SF  $\text{CO}_2$  with 0.001 M TEMPO approaches

the dipolar limiting value of -330 corresponding to a coupling factor  $\rho = 0.5$ , leading to nearly the highest possible dipolar-dominant enhancement in the  $^1\text{H}$  DNP experiment (point A in Figure 5-2). This indicates that fast molecular motion of benzene in SF  $\text{CO}_2$  satisfies the extreme narrowing limit  $\omega_s^2 \tau_c^2 \ll 1$  shown as the flat region at the low magnetic field strength in Figure 5-2, for the pure dipolar relaxation model at 0.33 T. For the case of mixed scalar and dipolar relaxation, with different values of  $\beta$  that define different contributions from dipolar relaxation competing with pure scalar relaxation, (15) three sets of scalar-dominant coupling factor dependence curves were plotted. It can be shown that molecules of faster motion come out of the extreme narrowing regime at a higher field (blue versus red curves). Consequently, by conducting flow transfer  $^1\text{H}$  DNP using SF  $\text{CO}_2$ , both dipolar and scalar relaxation can result in substantial DNP Oe enhancements even at relatively high magnetic fields for the polarization of electron transitions.

**Table 5-2. SLIT  $^1\text{H}$  DNP Enhancements Polarized at 0.33 T for Benzene/Nitroxide in  $\text{C}_6\text{D}_6$  and SF  $\text{CO}_2$**

system	absolute enhancement
9% benzene/ $\text{C}_6\text{D}_6$ /nitroxide (I)	-67±15
9% benzene/SF $\text{CO}_2$ /nitroxide (I)	-205±24
9% benzene/ $\text{C}_6\text{D}_6$ /nitroxide (II)	-61±17
9% benzene/SF $\text{CO}_2$ /nitroxide (II)	-246±36

**SLIT  $^1\text{H}$  DNP Experiments in Supercritical Fluid (SF)  $\text{CO}_2$ .** As first reported in the late 1980's, the solid-liquid intermolecular (SLIT) DNP experiment has certain

advantages when the radical is not present in the solution.(28, 29) Firstly, in the SLIT DNP experiments,  $^{13}\text{C}$  contact shifts and spectral line broadening are avoided in the high field detection magnet. The SLIT approach also has the advantage of improved low to high magnetic field transfer efficiencies allowing the transfer of radical free hyperpolarized metabolites for biological uses.(27, 30) The use of immobilized radicals for DNP approaches has recently been reconsidered and utilized to generate hyperpolarized water for clinical MRI applications.(67-71) However, one disadvantage of the SLIT in comparison with the LLIT approach is that the longer correlation times with the immobilized nitroxide radicals solid-liquid interaction result in lower DNP enhancement for systems dominated by dipolar relaxation. The efficiency of interactions between the radical and nuclei in immobilized radical flow methods can be in fact improved through better design of immobilizing methods,(68, 72) as well as the optimum synthesis of new radicals.(73, 74) Another strategy for improving dipolar-dominated DNP enhancements in SLIT type experiments is to use supercritical liquids as the flowing solvent. In the current study, we present SLIT  $^1\text{H}$  DNP enhancements of benzene in supercritical  $\text{CO}_2$  with the application of two immobilized radicals that have been reported by our group.(27) Table 5-2 presents the SLIT  $^1\text{H}$  DNP absolute enhancements of benzene dissolved in deuterated benzene and  $\text{SF}_6/\text{CO}_2$  using the immobilized nitroxides(17)(I) and (II) as illustrated in Figure 5-3. The absolute enhancements were obtained by estimating a transfer efficiency of ~80% (the efficiency with which the polarized sample bolus is transferred from the low to high field strength magnet).(17) For I and II, a 3 to 4 fold increase is observed for the  $^1\text{H}$  SLIT DNP enhancement for  $\text{SF}_6$

CO<sub>2</sub>, in comparison with normal liquid benzene, which is due to an increase in molecular motion of the immobilized nitroxide/benzene complex. The absolute DNP enhancement from nitroxide II is slightly higher ( $A = -246$ ) in comparison with radical I ( $A = -205$ ) presumably due to the increased mobility (shorter correlation time  $\tau_c$ ) of the radical attached to a longer flexible chain off the surface of the silica gel for nitroxide II.

**LLIT <sup>13</sup>C DNP Experiments of Molecular Nitroxide-Substrate Systems and Density Functional Theory Computations: Background.** The <sup>13</sup>C nuclide in molecules with C-H groups readily form weak complexes with nitroxides providing interactions ranging from relatively strong dipolar to strong scalar interaction(s) dependent on the hydrocarbon acidity.(18, 22, 26) For the case of hydrocarbons with sp<sup>3</sup> hybridized (C-H) bonds not bound to electronegative elements, the <sup>13</sup>C DNP present modest dipolar enhancements as illustrated for the case of cyclohexane ( $A = -270$ ) and adamantane ( $A = -254$  and  $-209$ ) (Table 5-6). It is well recognized that there is increasing acidity for the sp<sup>3</sup> hybridized carbon (-C-H<sub>x</sub>) group in progressing from toluene ( $pK_a = 41.2$ ) to diphenylmethane ( $pK_a = 33.4$ ), and triphenylmethane ( $pK_a = 31.4$ ). This trend results in a significant change in the DNP enhancement from a modest dipolar ( $A = -209$ ) to scalar interaction ( $A = +129$ ) (Figure 5-6). Although the sp<sup>2</sup> aromatic *ipso* carbon exhibits a nearly constant dipolar enhancement, ( $A = -423$  to  $-429$ ), the aromatic *ortho*, *meta* and *para* carbons reflect nearly the same dipolar to scalar trend as the sp<sup>3</sup> hybridized (-C-H<sub>x</sub>) group. This trend is especially relevant in view of the significant change in the molecular size (and corresponding correlation time) in progressing from toluene to



triphenylmethane. Clearly, spin delocalization from the  $sp^3$  hybridized ( $-C-H_X$ ) group to the aromatic  $\pi$  system is an important factor dictating this trend. However, a second factor is the expected longer correlation time for the nitroxide/triphenylmethane complex in comparison with the toluene complex, which results in a larger scalar component in the overall coupling factor. For the case of electron withdrawing groups attached to  $sp^3$  hybridized carbon ( $X-C-H_X$ ) groups, it is well recognized that these weakly acidic hydrocarbons lead to very significant scalar enhancements as represented by the well know chloroform ( $HCCl_3$ ) example with a very large scalar enhancement,  $A = +2200$  which is close to the scalar limit. However, there are numerous other examples of large scalar enhancements for electron withdrawing  $sp^3$  hybridized carbon ( $X-C-H_X$ ) groups including nitromethane, diethyl malonate, ethylacetoacetate, and acetonitrile as illustrated in Figure 5-7a and Table 5-6. All of these examples have acidic (C-H) groups with  $pK_a$  values ranging from 10-25. Thus,  $sp^3$  hybridized carbon hydrocarbons exhibit a wide range of DNP enhancements ranging from those with  $pK_a$ s 40-50 (e.g., toluene, cyclohexane) that exhibit modest dipolar interactions to hydrocarbons with C-H groups exhibiting  $pK_a$  acidities between 10-30 with large ( $A = +400$  to  $+2200$ ) scalar enhancements. Even molecules with weakly acidic (C-H) sites exhibit significant scalar enhancements, for example, the C-1 carbon in 1-chlorobutane ( $A = +460$ ) even when the remaining non-acidic (C-H) sites ( $C_2-C_4$ ) exhibit dipolar enhancements (Table 5-6).

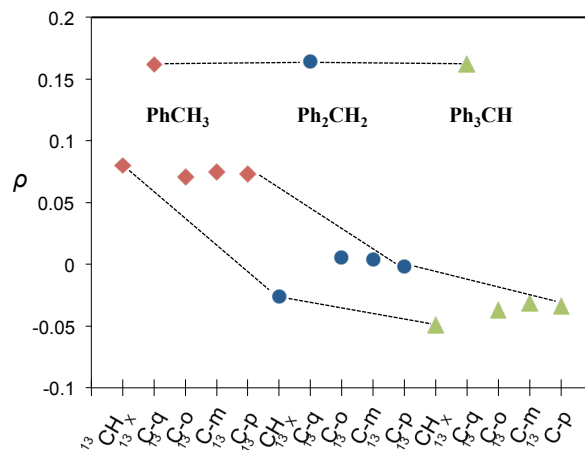


**Figure 5-6.** Coupling factor derived from  $^{13}\text{C}$  LLIT DNP absolute enhancements of the indicated carbon (i.e.  $^{13}\text{C}\text{H}_x$ ,  $X=1-3$ ,  $^{13}\text{C}$ -quaternary,  $^{13}\text{C}$ -*ortho*,  $^{13}\text{C}$ -*meta*, and  $^{13}\text{C}$ -*para*) for the series of toluene (red diamond), diphenylmethane (blue circle), and triphenylmethane (green triangle) ( $\text{Ph}_Y\text{CH}_X$ ,  $X=1-3$ ,  $Y=4-X$ ).<sup>(33)</sup> Dashed lines illustrate motif trends for different molecules. The relative standard deviation for  $\rho$  is about 15%.

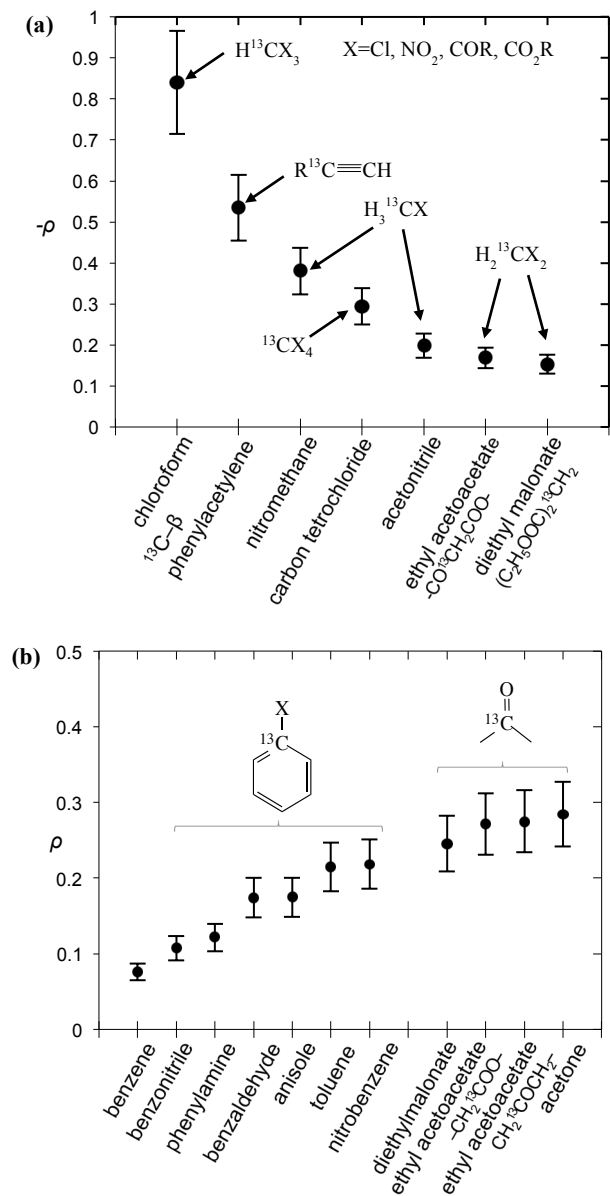


**Figure 5-7.** (a) Coupling factor (negative) derived from scalar dominant  $^{13}\text{C}$  LLIT DNP absolute enhancements of small molecules. (b) Coupling factor derived from dipolar dominant  $^{13}\text{C}$  LLIT DNP absolute enhancement of the indicated *ipso* carbons of monosubstituted benzenes and carbonyls of small molecules. The relative standard deviation for  $\rho$  is about 15%.

**Benzene/TEMPO.** For the case of hydrocarbons with  $sp^2$  hybridization, benzene has been an archetypal system for many previous solution state DNP studies. In addition, earlier NMR contact shift studies have clearly established a small scalar contribution to the dipolar dominated DNP enhancement for the benzene/TEMPO system,  $A = -220$ .(25, 35, 75, 76) Electron withdrawing groups attached to  $sp^2$  hybridized quaternary carbons dramatically increase this dipolar interaction. For example, the aromatic *ipso* (quaternary)  $sp^2$  carbons ( $^{13}C-X$ ) of monosubstituted benzenes such as benzonitrile, phenylamine, benzaldehyde, anisole, and nitrobenzene exhibit increasing dipolar enhancements with increasing electron withdrawal of the X substituent as illustrated in Figure 5-7b. This implies a corresponding decrease in the scalar interaction assuming similar correlation times for these monosubstituted benzenes. This trend is even more pronounced for  $sp^2$  hybridized carbonyl carbons with electronegative oxygens directly attached (Figure 5-7b). The highest dipolar enhancement in this trend is for the carbonyl carbon of acetone with a dipolar enhancement of  $A = -744$  representing a coupling factor of ~55% of the dipolar limit at 0.33 T. For comparison, the significantly larger fullerene  $C_{60}$  molecule with  $sp^2$  hybridized quaternary carbons exhibits a solution state enhancement of  $A = -250$  and does not have a significant scalar component (no significant NMR contact shift).(32) These results suggest that substrate molecules (100-700 Daltons) with  $sp^2$  hybridized carbons that do not have a significant scalar contribution exhibit dipolar enhancements with TEMPO ranging from  $A = -250$  to  $-740$  at 0.33 T. As previously noted, at the lower end of this range, the benzene/TEMPO system represents a molecule of considerable interest because

of both dipolar and scalar  $^{13}\text{C}$  interactions in contrast with the dipolar-dominated  $^1\text{H}$  DNP *vide supra* for this system. We have previously reported DFT calculations that the formation of weak hydrogen bonding between C-H bond of substrate molecules and nitroxides results in unpaired spin density at the substrate carbon nuclei and results in non-trivial scalar contributions to the  $^{13}\text{C}$  DNP enhancements for acetonitrile/TEMPO and acetamide/TEMPO(25). It is of considerable interest to establish the orientation and site(s) interaction of the important conformations of the electron-nuclear interaction for the case of benzene/TEMPO. We have obtained the Boltzmann weighted  $^{13}\text{C}$   $a_{FC} = 0.80$  MHz via DFT computations using eq. 5-8 and considering the four lowest-energy molecular configurations. (See Figure 5-S4-S7 and Table 5-S2 for optimized orientations and their parameters.) The two important conformations with the largest contributions to the hyperfine coupling are shown in Figures 5-8 and 5-9. It is important to note that in both conformations the nitroxide N-O bond vector is either orthogonal to one C-H bond vector or orthogonal between (T shape) two C-H bond vectors with interaction distances of 0.230 and 0.239 nm, respectively. This orthogonal approach of the N-O and C-H bond is also consistent for the lowest energy conformations found below for other monosubstituted benzene/TEMPO complexes *vide infra*. The computational average  $a_{FC}$  value ( $a_{FC} = 0.80$  MHz) indicates a non-trivial scalar contribution to the  $^{13}\text{C}$  DNP NMR signal of benzene, which has an absolute enhancement of  $-220$  in 0.16 M TEMPO solution(18) and supports the reported modest  $^{13}\text{C}$  contact shifts of benzene in the presence of nitroxide radicals.(35, 75, 76)

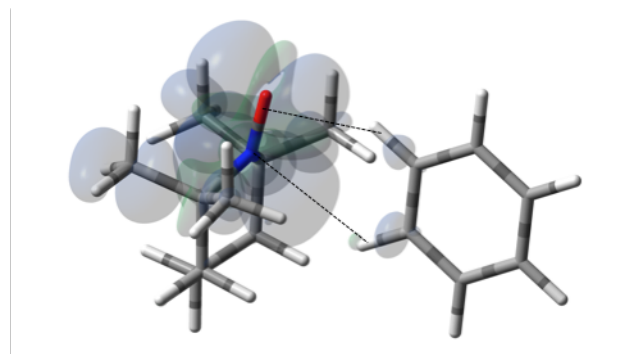


**Figure 5-8.** The electronic spin density distribution of the largest  $^{13}\text{C}$ -H HFC contributing orientation between benzene and TEMPO where two C-H moieties bite the TEMPO N-O group. Dashed lines are given as guides for intermolecular distances, which are 2.39 Å for O---H (of C-H moiety with closest approach to TEMPO oxygen) and 2.86 Å for N---H (of C-H with closest approach to TEMPO nitrogen).

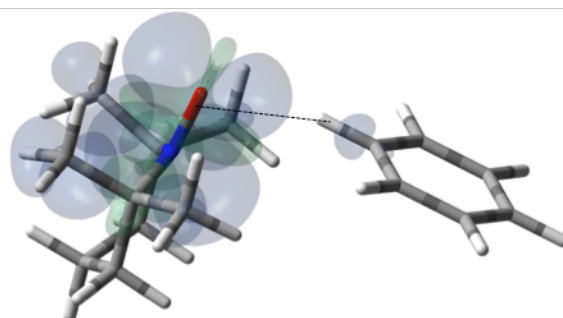


**Figure 5-9.** The electronic spin density distribution of the second largest  $^{13}\text{C}$ -H HFC contributing orientation between benzene and TEMPO where one C-H moiety points at the N-O group. The dashed line is given as a guide for intermolecular distance, which is 2.30 Å between the oxygen atom of TEMPO and the hydrogen atom of benzene C-H moiety.

**Nitrobenzene/TEMPO.** For the case of nitrobenzene/TEMPO, the introduction of the strong electron withdrawing nitro group to replace a hydrogen atom on the

aromatic ring leads to a lowest energy conformation with an orthogonal approach of the N-O and C-H bond vectors between the *ortho* and *meta* carbons (Figure 5-10). The weighted Boltzmann averaging of HFC for the *ortho* carbon ( $a_{FC} = 1.424$ ) is in strong agreement with the large scalar enhancement,  $A = +587$  observed for this site. The large  $^{13}\text{C}$ -*para* and  $^{13}\text{C}$ -*meta* contribution appears to originate from a slightly higher energy configuration (Figure 5-S21) where the *para* C-H bond vector is orthogonal to the nitroxide, N-O bond vector. However, delocalization of polarized spin from the dominant *ortho* conformation to the *meta* and *para* sites can not be excluded. It is interesting to note in this regard that the strong electron withdrawing nitro group leads to scalar enhancements, whereas, electron donating groups such as the amino group of phenylamine leads to dipolar enhancements at all *ortho*, *meta*, and *para* carbon positions (Table 5-S7).

**Table 5-3. LLIT  $^{13}\text{C}$  DNP Enhancements Polarized at 0.33 T for Nitrobenzene/Cyclohexane/0.1 M TEMPO(33) and  $a_{FC}$  via DFT Modeling**

system	nucleus	absolute enhancement	$a_{FC}$ <sup>a</sup>
nitrobenzene	$^{13}\text{C}$ - <i>ipso</i>	-572±86	0.399
	$^{13}\text{C}$ - <i>ortho</i>	+587±88	1.424
	$^{13}\text{C}$ - <i>meta</i>	+198±30	0.329
	$^{13}\text{C}$ - <i>para</i>	+366±55	0.418

<sup>a</sup> $a_{FC}$  is the Fermi Contact HFC in units of MHz computed as described

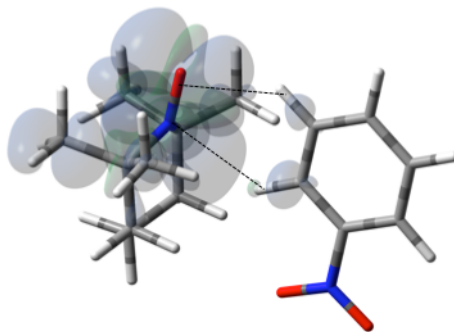


**Figure 5-10.** The electronic spin density distribution for the lowest energy orientation between nitrobenzene and TEMPO where *ortho* and *meta* C-H moieties complex with the TEMPO N-O group. Dashed lines are given as guides for intermolecular distances, which are 2.45 Å for O...H (of *ortho* C-H) and 2.53 Å for N...H (of *para* C-H).

**Benzaldehyde/TEMPO.** In contrast with benzene and nitrobenzene, the benzaldehyde/TEMPO system provides a system where two different weak  $sp^2$  hybridized C-H bonds complex with TEMPO (Figure 5-12 and Table 5-4). The weighted Boltzmann averaging of hyperfine couplings continues to show strong agreement with the scalar enhancements measured by DNP (see Table 5-S4 for details). In this case the *ortho* aromatic C-H bond and the aldehyde, O=C-H bonds both contribute as a “dual complexation site” with TEMPO for the lowest energy conformation. In addition, this conformation is similar to the orthogonal bond vector conformations found for benzene and nitrobenzene. However, the more acidic aldehyde O=C-H site exhibits a larger hyperfine coupling ( $a_{FC} = 1.155$ ) and corresponding larger scalar enhancement ( $A = +373$ ) in comparison with the modest hyperfine coupling and DNP enhancement found for aromatic C-H site,  $a_{FC} =$



0.442 and  $A = +131$ , respectively. It is also interesting to note that the modest electron withdrawing aldehyde group leads to modest scalar enhancements at all *ortho*, *meta*, and *para* carbon positions (Table 5-4).

**Table 5-4. LLIT  $^{13}\text{C}$  DNP Enhancements Polarized at 0.33 T for Benzaldehyde/Cyclohexane/0.1 M TEMPO(34) and  $a_{FC}$  via DFT Modeling**

system	nucleus	absolute enhancement	$a_{FC}^a$
benzaldehyde	$^{13}\text{CHO}$ -	$+373 \pm 56$	1.155
	$^{13}\text{C}$ - <i>ipso</i>	$-456 \pm 20$	0.284
	$^{13}\text{C}$ - <i>ortho</i>	$+131 \pm 20$	0.442
	$^{13}\text{C}$ - <i>meta</i>	$+93 \pm 14$	0.063
	$^{13}\text{C}$ - <i>para</i>	$+78 \pm 12$	0.099

<sup>a</sup> $a_{FC}$  is the Fermi Contact HFC in units of MHz computed as described

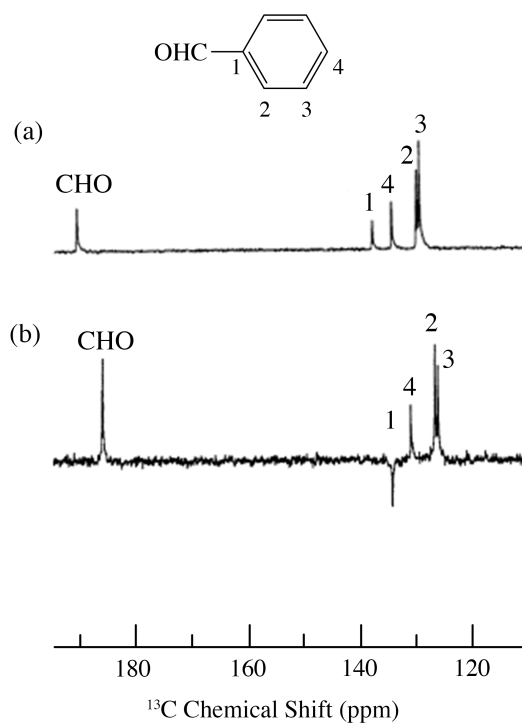


**Figure 5-11.**  $^{13}\text{C}$  spectra of benzaldehyde/TEMPO in cyclohexane at 4.7 T (a) 0.1 M TEMPO without flow DNP, (b) 0.1 M TEMPO with flow DNP. (a) 3000 scans; (b) 735 scans. (34)

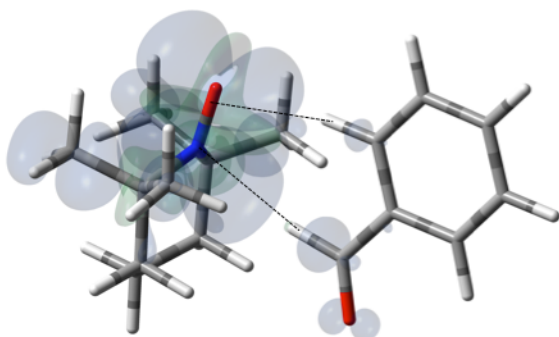


**Figure 5-12.** The electronic spin density distribution for the largest  $^{13}\text{CHO-}$  and  $^{13}\text{C-ortho}$  HFC contributing orientation between benzaldehyde and TEMPO where the aldehyde and *ortho* C-H moieties bite the N-O group. Dashed lines are given as guides for intermolecular distances, which are 2.39 Å for O---H (of *ortho* C-H) and 2.46 Å for N---H (of aldehyde C-H).

**Phenylacetylene/TEMPO** For the case of  $sp$  hybridized carbons there is a paucity of data for the complexation of alkynes with nitroxides. For cyano  $sp$  hybridized carbons modest  $^{13}\text{C}$  dipolar DNP enhancements have been reported for benzonitrile and acetonitrile (Table 5-6 and 5-S13). However, for the acidic  $sp$  hybridized C-H carbons there is a paucity of examples reported. In one notable early NMR shift study, a transient hydrogen bonding between phenylacetylene and di-*tert*-butyl nitroxide was proposed,(35) since the former is a good proton donor with a  $pK_a$  of 21 (Figure 5-1). It should be noted that alkynes are key components in the widely employed “click” reaction extensively employed in organic, polymer, and biomedical

functionalization studies(77). Phenylacetylene has an acetylenic proton of relatively high acidity ( $pK_a$  of 21)(78) compared with benzene as shown in Figure 5-1. The DFT and DNP results for phenylacetylene/TEMPO are shown in Figure 5-14 and Table 5-5. As predicted, the phenylacetylene/TEMPO exhibits a large hyperfine coupling,  $a_{FC} = 3.28$  and corresponding large scalar dominated enhancement ( $A = +1400$ ) for the  $sp$  hybridized C-H  $\beta$  carbon (shown in Table 5-5). Moreover, the  $\beta$  carbon exhibits the largest scalar-dominant DNP enhancement observed to date for a molecule not containing halogens, corresponding to a DNP coupling factor of -0.53 (point D in Figure. 5-2). In analogous fashion to the previous examples above, the lowest energy conformation has the N-O bond vector orthogonal to the  $sp$  hybridized C-H bond vector (Figure 5-14), but the interaction distance is considerably shorter (0.204 nm) than the previous examples, *vide supra*. It is also interesting to note that the  $\alpha$   $sp$  hybridized carbon also exhibits a notable scalar enhancement ( $A = +290$ ), also consistent with the relatively large computational derived hyperfine coupling ( $a_{FC} = 0.871$ ). The  $o$ ,  $m$ ,  $p$  carbons on the benzene ring of phenylacetylene show very small dipolar-dominated (negative) enhancements that are nearly zero. Clearly there is a large difference in the spin-lattice  $T_1$  relaxation time of the scalar dominated  $\beta$  carbon relative to the  $o$ ,  $m$ , and  $p$  carbons of the aromatic ring. At low radical (TEMPO) concentrations (0.01 M), the  $\beta$  carbon polarization is clearly enhanced, but the other carbon atoms are barely observable. For the ring carbons having dipolar-dominated interactions, whereas, at higher radical concentrations (0.14 M) dipolar enhancements become observable, but the  $\beta$  carbon is barely observed because of the very short nuclear relaxation times at this

concentration which limits the transfer efficiency from the low (0.33T) to the high observable magnetic field (4.7 T). However, the lower radical concentration used (0.01 M) may diminish the observed DNP enhancements for the  $\beta$  carbon and other carbons because of a lower leakage factor and three-spin effects(79) (Figure 5-13b). These results suggest that for molecules having specific strong scalar complexation sites, it is possible to detect independently enhancements contributed by the scalar and dipolar interactions by varying the radical concentration.

**Table 5-5. LLIT  $^{13}\text{C}$  DNP Enhancements Polarized at 0.33 T for Phenylacetylene/0.001 M and 0.14 M TEMPO(19) and  $a_{FC}$  via DFT Modeling**

system	nucleus	absolute enhancement	$a_{FC}$ <sup>a</sup>
phenylacetylene <sup>b</sup>	$^{13}\text{C}-\beta^c$	+1400±210	3.281
	$^{13}\text{C}-\alpha$	+290±44	0.871
	$^{13}\text{C}-ipso$	-280±42	0.277
	$^{13}\text{C}-ortho$	-36±5	0.579
	$^{13}\text{C}-meta$	-32±5	0.117
	$^{13}\text{C}-para$	N/A <sup>d</sup>	0.181

<sup>a</sup> $a_{FC}$  is the Fermi Contact HFC in units of MHz computed as described <sup>b</sup>inverse gated  $^1\text{H}$  decoupling was employed. <sup>c</sup>C- $\beta$  results are based on measurements of 0.01 M TEMPO solution, while C- $\alpha$  and C-1~3 results are from 0.14 M TEMPO solution. <sup>d</sup>C-4 signal is close to zero.

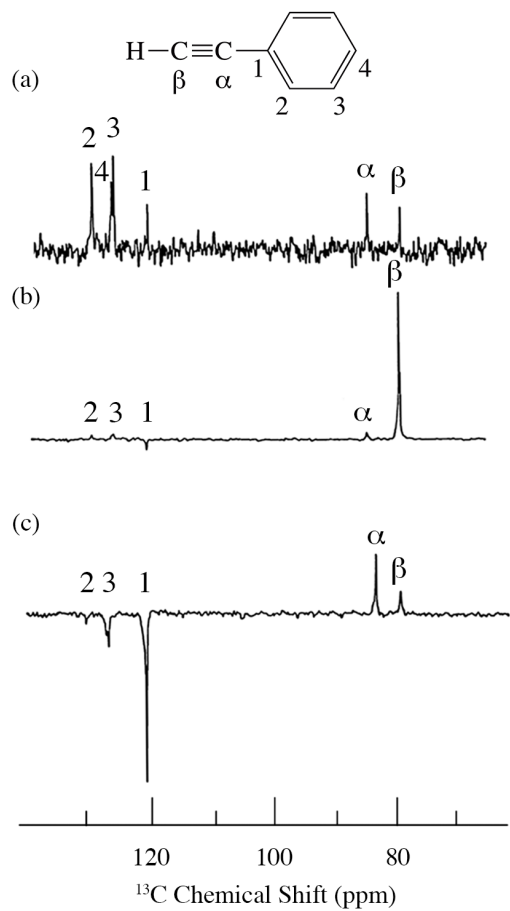


**Figure 5-13.** <sup>13</sup>C spectra of phenylacetylene/TEMPO at 4.7 T (a) 0.01 M TEMPO without flow DNP, (b) 0.01 M TEMPO with flow DNP and (c) 0.14 M TEMPO. (a) 16 scans; (b) 16 scans; (c) 64 scans. (19)

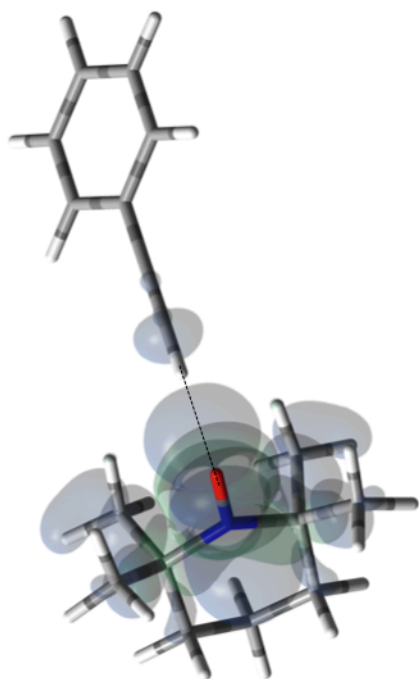


**Figure 5-14.** The electronic spin density distribution of the largest  $^{13}\text{C}$ - $\beta$  HFC contributing orientation between phenylacetylene and TEMPO where the alkyne points at N-O group. The dashed line is given as guide for intermolecular distance, which is 2.03 Å between oxygen atom of TEMPO and the hydrogen atom of acetylene group of phenylacetylene

**Table 5-6. LLIT  $^{13}\text{C}$  DNP Enhancements Polarized at 0.33 T for Substrate/TEMPO Systems and Acid Dissociation Constants ( $\text{p}K_{\text{a}}$ )(80, 81) at 25**

**$^{\circ}\text{C}$  of  $^{13}\text{C}$ -H protons.**

system (solute/solvent/TEMPO conc.)	nucleus	absolute enhancement	$\text{p}K_{\text{a}}$	type of carbon hybridization
phenylacetylene/NA/0.01 M(19)	$^{13}\text{C}-\beta$	+1400±210	21	sp
phenylacetylene/NA/0.14 M(19)	$^{13}\text{C}-\alpha$	+290±44	-	
benzaldehyde/cyclohexane/0.1 M(34)	$^{13}\text{CHO}-$	+373±56	14.9	sp <sup>2</sup>
	$^{13}\text{C}-\text{ortho}$	+131±20	-	
nitrobenzene/cyclohexane/0.1 M(33)	$^{13}\text{C}-\text{ortho}$	+587±88	-	sp <sup>2</sup>
	$^{13}\text{C}-\text{meta}$	+198±30	-	
	$^{13}\text{C}-\text{para}$	+366±55	-	
chloroform/0.0052 M(18)	$^{13}\text{CHCl}_3$	+2200±330	15.5	sp <sup>3</sup>
nitromethane/benzene/0.1 M(33)	$^{13}\text{CH}_3\text{NO}_2$	+996±149	10	
carbon tetrachloride/1-chlorobutane/0.08M(18)	$^{13}\text{CCl}_4$	+770±115	-	
acetonitrile/carbon tetrachloride/0.1 M(82)	$^{13}\text{CH}_3\text{CN}$	+520±100	25	
1-chlorobutane/carbon tetrachloride/0.08 M(18)	$\text{Cl}^{13}\text{CH}_2\text{CH}_2\text{CH}_2\text{CH}_3$	+460±70	-	
ethyl acetoacetate/benzene/cyclohexane/0.1 M(33)	$\text{CH}_3\text{CO}^{13}\text{CH}_2\text{COOCH}_2\text{CH}_3$	+440±66	11	
diethyl malonate/benzene/cyclohexane/0.1 M(33)	$(\text{CH}_3\text{CH}_2\text{OOC})_2^{13}\text{CH}_2$	+401±60	13	
triphenylmethane/cyclohexane/0.1 M(33)	$^{13}\text{CH}(\text{Ph})_3$	+129±19	31.4	
diphenylmethane/cyclohexane/0.1 M(33)	$^{13}\text{CH}_2(\text{Ph})_2$	+67±10	33.4	
benzene/0.1 M(33)	$^{13}\text{C}_6\text{H}_6$	-200±30	43	
$\text{C}_{60}/\text{C}_6\text{D}_6/0.1$ M(32)	$^{13}\text{C}_{60}$	-250±20	-	sp <sup>2</sup>
benzonitrile/cyclohexane/0.1 M(34)	$^{13}\text{C}-\text{ipso}$	-281±42	-	
phenylamine/cyclohexane/0.1 M(34)	$^{13}\text{C}-\text{ipso}$	-318±48	-	
benzaldehyde/cyclohexane/0.1 M(34)	$^{13}\text{C}-\text{ipso}$	-456±20	-	
anisole/cyclohexane/0.1 M(34)	$^{13}\text{C}-\text{ipso}$	-457±69	-	
toluene/cyclohexane/0.1 M(33)	$^{13}\text{C}-\text{ipso}$	-562±69	-	
nitrobenzene/cyclohexane/0.1 M(33)	$^{13}\text{C}-\text{ipso}$	-572±86	-	
diethyl malonate/benzene/cyclohexane/0.1 M(33)	$(\text{CH}_3\text{CH}_2\text{OO}^{13}\text{C})_2\text{CH}_2$	-642±96	-	
ethyl acetoacetate/benzene/cyclohexane/0.1 M(33)	$\text{CH}_3\text{COCH}_2^{13}\text{COOCH}_2\text{CH}_3$	-711±107	-	
	$\text{CH}_3^{13}\text{COCH}_2\text{COOCH}_2\text{CH}_3$	-720±108	-	
acetone/carbon tetrachloride/cyclohexane/0.1 M(33)	$(\text{CH}_3)_2^{13}\text{CO}$	-744±112	-	
toluene/cyclohexane/0.1 M(33)	$^{13}\text{CH}_3\text{Ph}$	-209±31	41.2	sp <sup>3</sup>
adamantane/benzene/0.1 M(33)	$^{-13}\text{CH}_2-$	-209±13	-	
	$^{-13}\text{CH}-$	-254±14	-	
cyclohexane/NA/0.1 M(19)	$^{13}\text{C}_6\text{H}_{12}$	-270±40	45	
1-chlorobutane/carbon tetrachloride/0.08 M(18)	$\text{ClCH}_2^{13}\text{CH}_2\text{CH}_2\text{CH}_3$	-200±30	-	
	$\text{ClCH}_2\text{CH}_2^{13}\text{CH}_2\text{CH}_3$	-400±60	-	
	$\text{ClCH}_2\text{CH}_2\text{CH}_2^{13}\text{CH}_3$	-290±44	-	

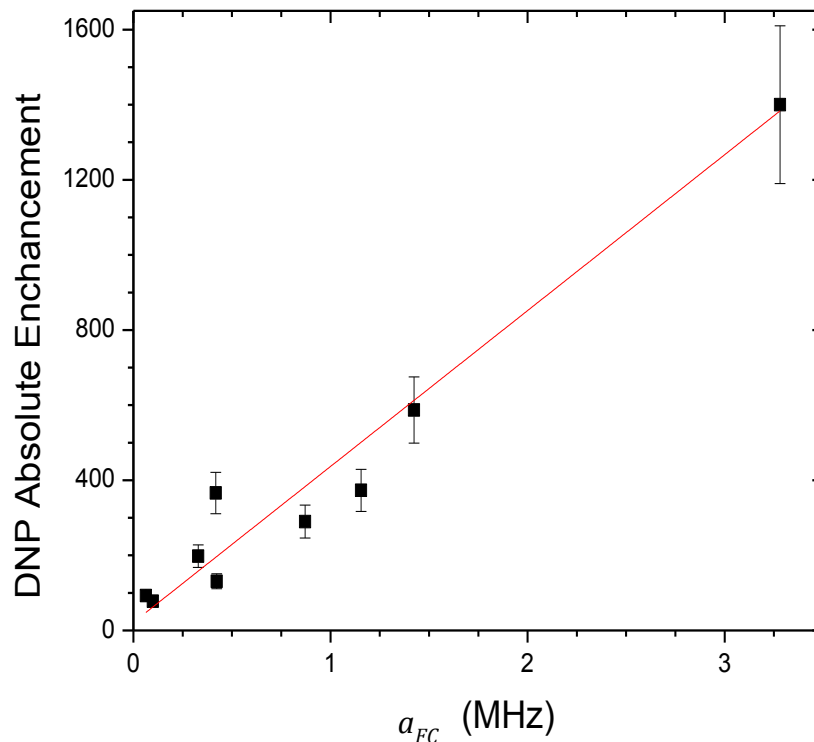


**Figure 5-15.** Correlation between experimentally determined  $^{13}\text{C}$  LLIT DNP scalar dominated enhancements and their calculated AFC (Boltzmann weighted DFT computed Fermi Contact hyperfine coupling constant) for the phenylacetylene/TEMPO, benzaldehyde/TEMPO, and nitrobenzene/TEMPO systems. After performing a linear regression with direct weighting of the DNP enhancement error, a line of best fit ( $y = mx + b$ ) was determined having parameters  $m = 415 \pm 23$ ,  $b = 21 \pm 52$ , and the goodness of the fit is computed as having an adjusted  $R^2 = 0.97$ .

## 5.5 Conclusion

In summary, we have found that for  $^1\text{H}$  DNP, supercritical fluids provide a convenient approach for decreasing the correlation time for solutes and provide an



alternative approach for improving dipolar enhancements at high magnetic fields without the need for polarization at low temperatures ( $\sim 4$  K). For the system SF CO<sub>2</sub>/benzene/TEMPO, the DNP enhancement approaches the dipolar limiting value of  $-330$  ( $\rho = 0.5$ ) at 0.33 T. For biomedical applications, there has been considerable interest in the DNP enhancement of water as reviewed by Gunther.<sup>(7)</sup> For example, Bennati and coworkers have experimentally reported an Oe dipolar DNP enhancement  $A = -170$  for the water/ TEMPONE-D-<sup>15</sup>N system at 9.7 GHz (0.33 T).<sup>(83)</sup> It is easy to predict enhancements at the dipolar limit ( $-330$ ) for the same system in SF CO<sub>2</sub> and even very significant enhancements at higher magnetic fields based on the results reported in the current study.

For <sup>13</sup>C DNP at 0.33 T, we have found that molecules (100-700 Daltons) dissolved in liquids containing carbon sites without a significant scalar contribution (e.g., carbonyls) exhibit dipolar enhancements ranging from,  $A = -250$  to  $-740$  with TEMPO *vide supra*. It is easy to predict that <sup>13</sup>C DNP for these carbon sites could also exhibit <sup>13</sup>C DNP enhancements 2 to 3 times greater if conducted in SF CO<sub>2</sub>. For the biomedical metabolites, the enhancement in SF CO<sub>2</sub> followed by rapid dissolution in water or saline solutions and transfer to high magnetic fields could be a viable approach for NMR nuclides with long  $T_1$  relaxation times for both NMR and MRI applications. Furthermore, other SF fluids, such as, supercritical water and nitrous oxide represent alternative fluids for decreasing correlation times at higher magnetic fields for DNP at high magnetic fields. For the case of <sup>13</sup>C DNP where both dipolar and scalar interactions are important, it is clear from DFT computational results for the monosubstituted benzene/TEMPO system that DFT approaches

provide an excellent predictive framework that correlates computational hyperfine couplings with the experimental scalar dominated DNP enhancements. The correlation between experimental scalar DNP enhancements ( $A$ ) and the Boltzmann weighted hyperfine coupling constants ( $a_{FC}$ ) calculated using the DFT methods provides a predictive tool for any substrate/radical systems exhibiting a non-trivial scalar interaction as illustrated in Figure 5-15. A cautionary note of these predictions is the importance of the scalar and/or dipolar correlation time(s) that is not included in the current computational approach. For this work, we assume similar correlation times for the monosubstituted benzenes. Finally, of critical importance, molecules with  $sp$  hybridized C-H groups, such as, the  $\beta$  carbon of phenylacetylene deserve further study because of the large scalar enhancements observed for this system. The intermolecular distance between the hydrogen attached to  $\beta$  C-H group and the orthogonal O-N bond of the nitroxide, TEMPO is about 2.0 Å (see Figure 5-14). The shorter intermolecular distance is an indication of stronger hydrogen bonding between the acetylene group and the radical, and hence a greater effect on the scalar interaction, compared with other  $sp^3$  and  $sp^2$  hybridized carbon systems. Furthermore, compared with  $sp^2$  carbons such as the aldehyde carbon of benzaldehyde, phenylacetylene  $\beta$  carbon has a greater  $s$  character of the bonding carbon hybrid orbital caused by  $sp$  hybridization. The hyperfine coupling constant ( $a_{FC}$ ) is directly proportional to the unpaired electron spin density at the investigating carbon nucleus, hence the increased HFC value of phenylacetylene  $\beta$  carbon indicates the contribution of increased  $s$  character and corresponding greater spin density transfer from the radical to the  $sp$  carbon

nucleus,  $|\psi(0)|^2$ . This conclusion is consistent with the observation of experimental and computed increasing s character for  $^{13}\text{C}$ - $^1\text{H}$  coupling constants ( $J_{\text{CH}}$ ) which increases markedly as a result of Fermi contact contributions(84) with the trend, 159 Hz for benzene(85), 173.7 Hz for the carbonyl group in benzaldehyde(86), ( $\text{C}_6\text{H}_5^{13}\text{C}^1\text{HO}$ ) and 251 Hz for the sp  $\beta$  carbon in phenylacetylene(87) ( $\text{C}_6\text{H}_5\text{C}^{13}\text{C}^1\text{H}$ ). In conclusion, solution state DNP provides a unique approach for studying intermolecular weak bonding interaction of solutes in normal liquids and SF fluids. Supporting information of this chapter can be found in Appendix 2.

## 5.6 References

1. C. R. Bowers, D. P. Weitekamp, Parahydrogen and synthesis allow dramatically enhanced nuclear alignment. *Journal of the American Chemical Society* **109**, 5541-5542 (1987).
2. E. Y. Chekmenev *et al.*, PASADENA Hyperpolarization of Succinic Acid for MRI and NMR Spectroscopy. *Journal of the American Chemical Society* **130**, 4212-4213 (2008).
3. J. H. Ardenkjær-Larsen *et al.*, Increase in signal-to-noise ratio of > 10,000 times in liquid-state NMR. *Proceedings of the National Academy of Sciences of the United States of America* **100**, 10158-10163 (2003).
4. K. Golman, J. H. Ardenkjær-Larsen, J. S. Petersson, S. Månsson, I. Leunbach, Molecular imaging with endogenous substances. *Proceedings of the National Academy of Sciences of the United States of America* **100**, 10435-10439 (2003).
5. P. Höfer *et al.*, Field Dependent Dynamic Nuclear Polarization with Radicals in Aqueous Solution. *Journal of the American Chemical Society* **130**, 3254-3255 (2008).
6. M. J. Prandolini, V. P. Denysenkov, M. Gafurov, B. Endeward, T. F. Prisner, High-Field Dynamic Nuclear Polarization in Aqueous Solutions. *Journal of the American Chemical Society* **131**, 6090-6092 (2009).
7. U. Günther, in *Modern NMR Methodology*, H. Heise, S. Matthews, Eds. (Springer Berlin Heidelberg, 2013), vol. 335, chap. 229, pp. 23-69.
8. D. Sezer, M. J. Prandolini, T. F. Prisner, Dynamic nuclear polarization coupling factors calculated from molecular dynamics simulations of a nitroxide radical in water. *Physical Chemistry Chemical Physics* **11**, 6626-6637 (2009).
9. E. Fermi, Über die magnetischen Momente der Atomkerne. *Z. Physik* **60**, 320-333 (1930).
10. V. Barone *et al.*, Assessment of a Combined QM/MM Approach for the Study of Large Nitroxide Systems in Vacuo and in Condensed Phases. *Journal of the American Chemical Society* **120**, 7069-7078 (1998).
11. A. Overhauser, Polarization of Nuclei in Metals. *Physical Review* **92**, 411-415 (1953).
12. T. Carver, C. Slichter, Polarization of Nuclear Spins in Metals. *Physical Review* **92**, 212-213 (1953).
13. I. Solomon, Relaxation Processes in a System of Two Spins. *Physical Review* **99**, 559-565 (1955).
14. P. Hubbard, Theory of electron-nucleus Overhauser effects in liquids containing free radicals. *Proceedings of the Royal Society of London. Series A. Mathematical and Physical Sciences* **291**, 537-555 (1966).
15. K. Hausser, D. Stehlik, Dynamic nuclear polarization in liquids. *Advanced Magnetic Resonance* **3**, 79-139 (1968).
16. W. Müller-Warmuth, K. Meise-Gresch, Molecular motions and interactions as studied by dynamic nuclear polarization (DNP) in free radical solutions. *Advances in Magnetic Resonance* **11**, 1-45 (1983).

17. S. I. Salido, Ph.D. Thesis, Virginia Polytechnic Institute and State University, (2003).
18. K. H. Tsai, H. C. Dorn, A model for establishing the ultimate enhancements ( $A \infty$ ) in the low to high magnetic field transfer dynamic nuclear polarization experiment. *Applied Magnetic Resonance* **1**, 231-254 (1990).
19. K.-H. Tsai, Ph.D. Thesis, Virginia Polytechnic Institute and State University, (1990).
20. J. Potenza, Measurement and applications of dynamic nuclear polarization. *Advances in Molecular Relaxation Processes* **4**, 229-354 (1972).
21. I. Al-Bala'a, R. D. Bates Jr, Effects of partially fluorinated hydrogen donors on ESR spectra in studies of hydrogen-bonded transient solvent-solute complexes. *Journal of Magnetic Resonance (1969)* **78**, 271-280 (1988).
22. R. D. Bates, B. E. Wagner, E. H. Poindexter, Dynamic fluorine-19 polarization in fluorinated strained cyclic alkanes and alkenes. *The Journal of Physical Chemistry* **80**, 320-323 (1976).
23. R. D. Bates, B. E. Wagner, E. H. Poindexter, Transient intermolecular spin coupling of trichloromethane with di-tert-butyl nitroxide free radical. *The Journal of Physical Chemistry* **81**, 276-279 (1977).
24. J. N. Helbert, E. H. Poindexter, B. E. Wagner, Scalar dynamic nuclear polarization of protons in trifluoroacetic acid solutions. *Chemical Physics Letters* **52**, 546-548 (1977).
25. J. L. Russ *et al.*, Nitroxide/Substrate Weak Hydrogen Bonding: Attitude and Dynamics of Collisions in Solution. *Journal of the American Chemical Society* **129**, 7018-7027 (2007).
26. N. M. Loening, M. Rosay, V. Weis, R. G. Griffin, Solution-State Dynamic Nuclear Polarization at High Magnetic Field. *Journal of the American Chemical Society* **124**, 8808-8809 (2002).
27. H. C. Dorn, T. E. Glass, R. Gitti, K. H. Tsai, Transfer of  $^1\text{H}$  and  $^{13}\text{C}$  dynamic nuclear polarization from immobilized nitroxide radicals to flowing liquids. *Applied Magnetic Resonance* **2**, 9-27 (1991).
28. R. Gitti *et al.*, Solid/liquid intermolecular transfer of dynamic nuclear polarization. Enhanced flowing fluid proton NMR signals via immobilized spin labels. *Journal of the American Chemical Society* **110**, 2294-2296 (1988).
29. H. C. Dorn, R. Gitti, K. H. Tsai, T. E. Glass, The flow transfer of a bolus with  $^1\text{H}$  dynamic nuclear polarization from low to high magnetic fields. *Chemical Physics Letters* **155**, 227-232 (1989).
30. S. Stevenson, T. Glass, H. C. Dorn,  $^{13}\text{C}$  Dynamic Nuclear Polarization: an Alternative Detector for Recycled-Flow NMR Experiments. *Analytical Chemistry* **70**, 2623-2628 (1998).
31. K. H. Tsai, T. E. Glass, H. C. Dorn, Dipolar-dominated  $^{29}\text{Si}$  dynamic nuclear polarization overhauser enhancements for hexamethyldisiloxane. *Journal of Magnetic Resonance (1969)* **89**, 362-366 (1990).
32. H. C. Dorn, J. Gu, D. S. Bethune, R. D. Johnson, C. S. Yannoni, The nature of fullerene solution collisional dynamics. A  $^{13}\text{C}$  DNP and NMR study of the  $\text{C}_{60}/\text{C}_6\text{D}_6/\text{TEMPO}$  system. *Chemical Physics Letters* **203**, 549-554 (1993).

33. Z. Sun, Ph.D. Thesis, Virginia Polytechnic Institute and State University, (1996).
34. L. Song, M.S. Thesis, Virginia Polytechnic Institute and State University, (1997).
35. I. Morishima, T. Matsui, T. Yonezawa, K. Goto, Studies on the nuclear magnetic resonance contact shifts induced by interaction with free radicals. Part IV. Utility of  $^{13}\text{C}$  contact shifts for the study of weak hydrocarbon-radical interaction. *Journal of the Chemical Society, Perkin Transactions 2*, 633-635 (1972).
36. Y. Zhao, D. G. Truhlar, A new local density functional for main-group thermochemistry, transition metal bonding, thermochemical kinetics, and noncovalent interactions. *The Journal of Chemical Physics* **125**, - (2006).
37. F. Weigend, R. Ahlrichs, Balanced basis sets of split valence, triple zeta valence and quadruple zeta valence quality for H to Rn: Design and assessment of accuracy. *Physical Chemistry Chemical Physics* **7**, 3297-3305 (2005).
38. R. F. Ribeiro, A. V. Marenich, C. J. Cramer, D. G. Truhlar, Use of Solution-Phase Vibrational Frequencies in Continuum Models for the Free Energy of Solvation. *The Journal of Physical Chemistry B* **115**, 14556-14562 (2011).
39. C. J. Cramer, *Essentials of computational chemistry : theories and models*. (Wiley, Chichester, West Sussex, England ; Hoboken, NJ, ed. 2nd, 2004)
40. Y. Zhao, D. G. Truhlar, The M06 suite of density functionals for main group thermochemistry, thermochemical kinetics, noncovalent interactions, excited states, and transition elements: two new functionals and systematic testing of four M06-class functionals and 12 other functionals. *Theoretical Chemistry Accounts* **120**, 215-241 (2007).
41. A. V. Marenich, C. J. Cramer, D. G. Truhlar, Universal Solvation Model Based on Solute Electron Density and on a Continuum Model of the Solvent Defined by the Bulk Dielectric Constant and Atomic Surface Tensions. *The Journal of Physical Chemistry B* **113**, 6378-6396 (2009).
42. D. P. Chong, *Recent advances in density functional methods*. Recent advances in computational chemistry (World Scientific, Singapore ; River Edge, N.J., 1995)
43. A. D. Becke, Density-functional thermochemistry. III. The role of exact exchange. *The Journal of Chemical Physics* **98**, 5648 (1993).
44. F. Neese, Efficient and accurate approximations to the molecular spin-orbit coupling operator and their use in molecular g-tensor calculations. *The Journal of Chemical Physics* **122** (2005).
45. M. J. Frisch *et al.* (Gaussian, Inc., Wallingford, CT, USA, 2009).
46. F. Neese, The ORCA program system. *Wiley Interdisciplinary Reviews: Computational Molecular Science* **2**, 73-78 (2012).
47. A. Abragam, R. Pound, Influence of electric and magnetic fields on angular correlations. *Physical Review* **92**, 943 (1953).
48. J. M. Robert, R. F. Evilia, High-resolution nuclear magnetic resonance spectroscopy of quadrupolar nuclei: nitrogen-14 and oxygen-17 examples. *Journal of the American Chemical Society* **107**, 3733-3735 (1985).

49. H. C. Dorn, J. Wang, L. Allen, D. Sweeney, T. E. Glass, Flow dynamic nuclear polarization, a novel method for enhancing NMR signals in flowing fluids. *Journal of Magnetic Resonance (1969)* **79**, 404-412 (1988).
50. S. Stevenson, H. C. Dorn, <sup>13</sup>C Dynamic Nuclear Polarization: A Detector for Continuous-Flow, Online Chromatography. *Analytical Chemistry* **66**, 2993-2999 (1994).
51. H. Dorn, <sup>1</sup>H-NMR: A New Detector for liquid Chromatography. *Analytical Chemistry* **56**, 747A-758A (1984).
52. L. Allen, T. Glass, H. Dorn, Direct monitoring of supercritical fluids and supercritical chromatographic separations by proton nuclear magnetic resonance. *Analytical Chemistry* **60**, 390-394 (1988).
53. A. Abragam, *The principles of nuclear magnetism*. The International series of monographs on physics (Clarendon Press, Oxford,, 1961), pp. 599 p.
54. R. A. Wind *et al.*, <sup>1</sup>H Dynamic Nuclear Polarization in Supercritical Ethylene at 1.4 T. *Journal of Magnetic Resonance* **143**, 233-239 (2000).
55. S. N. Batchelor, Free Radical Motion in Super Critical Fluids Probed by EPR Spectroscopy. *The Journal of Physical Chemistry B* **102**, 615-619 (1998).
56. T. W. Randolph, C. Carlier, Free-radical reactions in supercritical ethane: a probe of supercritical fluid structure. *The Journal of Physical Chemistry* **96**, 5146-5151 (1992).
57. R. D. Bates, W. S. Drozdowski, Use of nitroxide spin labels in studies of solvent-solute interactions. *The Journal of Chemical Physics* **67**, 4038-4044 (1977).
58. W. Müller-Warmuth, E. Oztekin, R. Vilhjalmsson, A. Yalciner, Dynamic polarization molecular motion and solvent effects in several organic solutions as studied by proton-electron double resonance. *Z. Naturforsch*, 1688-1695 (1970).
59. H. Grützediek, W. Müller-Warmuth, R. Van Steenwinkel, The nuclear-electron Overhauser effect of carbon-13 as studied by multi-field dynamic polarization experiments in solutions. *Zeitschrift Naturforschung Teil A* **25**, 1703 (1970).
60. R. L. Glazer, E. H. Poindexter, Dynamic Nuclear Polarization by Nitroxide, Perhalocarbon, Semiquinone, and Verdazyl Radicals. *The Journal of Chemical Physics* **55**, 4548-4553 (1971).
61. R. D. Bates Jr, B. E. Wagner, E. H. Poindexter, Dynamic polarization of carbon-13 nuclei in free radical solutions. *Chemical Physics Letters* **17**, 328-331 (1972).
62. W. Müller-Warmuth, R. Vilhjalmsson, P. A. M. Gerlof, J. Smidt, J. Trommel, Intermolecular interactions of benzene and carbon tetrachloride with selected free radicals in solution as studied by <sup>13</sup>C and <sup>1</sup>H dynamic nuclear polarization. *Molecular Physics* **31**, 1055-1067 (1976).
63. J. Trommel, *Molecular motions and collisions in organic free radical solutions as studied by dynamic nuclear polarization*. (Rodopi, 1978).
64. R. D. Bates Jr, Polarization of solvent nuclei by nitroxide spin labels at low magnetic fields. *Journal of Magnetic Resonance (1969)* **48**, 111-124 (1982).

65. R. A. Dwek, O. W. Howarth, D. F. S. Natusch, R. E. Richards, Proton-electron double resonance in organic compounds. *Molecular Physics* **13**, 457-460 (1967).
66. W. J. Lamb, G. A. Hoffman, J. Jonas, Self - diffusion in compressed supercritical water. *The Journal of Chemical Physics* **74**, 6875-6880 (1981).
67. E. R. McCarney, B. D. Armstrong, M. D. Lingwood, S. Han, Hyperpolarized water as an authentic magnetic resonance imaging contrast agent. *Proceedings of the National Academy of Sciences* **104**, 1754-1759 (2007).
68. M. D. Lingwood *et al.*, Continuous flow Overhauser dynamic nuclear polarization of water in the fringe field of a clinical magnetic resonance imaging system for authentic image contrast. *Journal of Magnetic Resonance* **205**, 247-254 (2010).
69. M. D. Lingwood, A. J. Sederman, M. D. Mantle, L. F. Gladden, S. Han, Overhauser dynamic nuclear polarization amplification of NMR flow imaging. *Journal of Magnetic Resonance* **216**, 94-100 (2012).
70. Hyperpolarized Water as an MR Imaging Contrast Agent: Feasibility of in Vivo Imaging in a Rat Model. *Radiology* **265**, 418-425 (2012).
71. S. Ebert *et al.*, A Mobile DNP Polarizer for Continuous Flow Applications. *Applied Magnetic Resonance* **43**, 195-206 (2012).
72. D. Gajan *et al.*, Hybrid polarizing solids for pure hyperpolarized liquids through dissolution dynamic nuclear polarization. *Proceedings of the National Academy of Sciences* **111**, 14693-14697 (2014).
73. C. Song, K.-N. Hu, C.-G. Joo, T. M. Swager, R. G. Griffin, TOTAPOL: A Biradical Polarizing Agent for Dynamic Nuclear Polarization Experiments in Aqueous Media. *Journal of the American Chemical Society* **128**, 11385-11390 (2006).
74. M. K. Kieseewetter, B. Corzilius, A. A. Smith, R. G. Griffin, T. M. Swager, Dynamic Nuclear Polarization with a Water-Soluble Rigid Biradical. *Journal of the American Chemical Society* **134**, 4537-4540 (2012).
75. I. Morishima, K. Kawakami, T. Yonezawa, K. Goto, M. Imanari, Interactions between closed- and open-shell molecules. VIII. Carbon-13 contact shift studies on the interaction between aromatic hydrocarbons and nitroxide radical. *Journal of the American Chemical Society* **94**, 6555-6557 (1972).
76. Z. W. Qiu, D. M. Grant, R. J. Pugmire, Paramagnetic carbon-13 shifts induced by the free radical 2,2,6,6-tetramethylpiperidiny-1-oxy. 1. Simple aromatic and paraffinic hydrocarbons. *Journal of the American Chemical Society* **104**, 2747-2753 (1982).
77. H. C. Kolb, K. B. Sharpless, The growing impact of click chemistry on drug discovery. *Drug Discovery Today* **8**, 1128-1137 (2003).
78. J. McMurry, *Fundamentals of Organic Chemistry*. (Cengage Learning, 2010).
79. K. Hausser, F. Reinbold, Dynamic polarisation in a three-spin system. *Physics Letters* **2**, 53-54 (1962).
80. F. A. Carey, R. J. Sundberg, *Advanced Organic Chemistry: Part A: Structure and Mechanisms*. (Springer, 2007).
81. F. G. Bordwell, Equilibrium acidities in dimethyl sulfoxide solution. *Accounts of Chemical Research* **21**, 456-463 (1988).



82. J. Gu, Ph.D. Thesis, Virginia Polytechnic Institute and State University, (1992).
83. M.-T. Turke, I. Tkach, M. Reese, P. Hofer, M. Bennati, Optimization of dynamic nuclear polarization experiments in aqueous solution at 15 MHz/9.7 GHz: a comparative study with DNP at 140 MHz/94 GHz. *Physical Chemistry Chemical Physics* **12**, 5893-5901 (2010).
84. G. E. Maciel, J. W. McIver, N. S. Ostlund, J. A. Pople, Approximate self-consistent molecular orbital theory of nuclear spin coupling. II. Fermi contact contributions to coupling between carbon and directly bonded atoms. *Journal of the American Chemical Society* **92**, 11-18 (1970).
85. N. Muller, D. E. Pritchard, C13 Splittings in Proton Magnetic Resonance Spectra. I. Hydrocarbons. *The Journal of Chemical Physics* **31**, 768-771 (1959).
86. E. R. Malinowski, L. Z. Pollara, J. P. Larmann, Substituent Effects. II. C13-Proton Couplings in Carbon sp<sup>2</sup> Systems. *Journal of the American Chemical Society* **84**, 2649-2650 (1962).
87. H. Dreeskamp, E. Sackmann, G. Stegmeier, Die Vorzeichen der C13 - H Kernspinkopplungskonstanten in Propin. *Berichte der Bunsengesellschaft für physikalische Chemie* **67**, 860-864 (1963).

## Appendix 1: Properties of Polyelectrolyte Solutions

At the end of Chapter 4, it was proposed to measure diffusion of polyelectrolytes in salt solution as an extension of the application of PFG NMR for molecular weight determination. The properties of polyelectrolytes in solutions and relevant insights that affect those measurements will be introduced here.

The properties of polymer solutions are entirely different when the dissolved chains are polyelectrolytes rather than electrically neutral (uncharged) macromolecules. In an aqueous solution, polyelectrolytes dissociate into chain-fixed polyions with positive or negative charges as well as mobile counterions bearing the opposite charge. Here the focus is on small (non polymeric) counterions such as  $\text{Li}^+$ ,  $\text{Na}^+$ ,  $\text{NH}_4^+$ , etc. The Coulomb forces originating from charges in polyelectrolyte solutions are much stronger than intermolecular van der Waals or dipole forces and consequently cause uncommon solution properties. In a nutshell, the repulsive Coulomb forces between the (intramolecular) chain-fixed charges lead to chain stretching, while the equilibrium distances between those chains in solution depend on the concentration of mobile counterions. Moreover, as a result of mobile counterions present, the osmotic pressure in polyelectrolyte solutions is much higher than in solutions of neutral polymers. In order to understand the influence of charges on polymer chain configurations and solution properties, two basic effects of the polyelectrolyte solution need to be illustrated: 1) charge condensation, and 2) screening of charges (Debye-Hückel theory). This discussion draws primarily on material in Strobl's book.(1)

Ideally, the situation for polyelectrolytes in solution would be much simpler if, upon dissolving, the counterions associated with a polyelectrolyte chain would diffuse away and distribute homogeneously in the solution, in which case the polymer chain could fully expand as a result of repulsive Coulomb forces between the chain-fixed charges. In fact, the two effects mentioned above give rise to a situation different from the ideal case.

### Charge Condensation

First, for a polyelectrolyte that has ionizable groups in every monomeric unit, the strong attraction between opposite charges can prevent the counterions from diffusing away. In order to reduce the effective charge density, part of the counterions stay in close proximity to the chain-fixed polyion and this is known as counterion condensation. To be specific, the electrostatic potential developed by a single rod-like chain with monovalent cations of charge  $e$  at regular (average) distance of  $l_{io}$  along the polymer chain is

$$V = \frac{e}{2\pi\epsilon\epsilon_0 l_{io}} \ln \frac{r}{r_0} \quad (A1 - 1)$$

where  $r_0$  is the radius of the single rod-like chain,  $r$  designates the distance from the chain axis assuming cylindrical symmetry of the potential,  $\epsilon$  is the dielectric coefficient of the solvent, and  $\epsilon_0$  is the elementary dielectric constant (permittivity of vacuum).

Using a simplified model of a series of cylindrical shells about the rod-like chain axes, with inner radius  $r_i$  for shell  $i$ , and  $r_0$  as the radius of the chain. Then the electrostatic energy of a single monovalent anion placed in shell  $i$  is

$$u_i = -eV(r_i) \quad (A1 - 2)$$

where  $V(r_i)$  is the electrostatic potential at distance  $r_i$  defined by Equation A1-1.

And the entropy of the anion motion within cell  $i$  is

$$s_i = k \ln \frac{r_i}{r_0} + \text{const} \quad (\text{A1} - 3)$$

Therefore the free energy of an anion in cell  $i$  is

$$f_i = u_i - Ts_i = \left( \frac{e^2}{2\pi\epsilon\epsilon_0 l_{i0}} - kT \right) \ln \frac{r_i}{r_0} + \text{const} = kT(\beta - 1) \ln \frac{r_i}{r_0} + \text{const} \quad (\text{A1} - 4)$$

$$\beta = \frac{e^2}{2\pi\epsilon\epsilon_0 l_{i0} kT} \quad (\text{A1} - 5)$$

Moreover, the number of anions  $n_i$  localized in shell  $i$  at temperature  $T$  follows the Boltzmann distribution, and from Equation A1-4 one obtains

$$n_i \propto \exp \frac{-f_i}{kT} = \left( \frac{r_i}{r_0} \right)^{1-\beta} \quad (\text{A1} - 6)$$

and

$$\frac{n_i}{n_0} = \left( \frac{r_i}{r_0} \right)^{1-\beta} \quad (\text{A1} - 7)$$

where  $n_0$  denotes the number of anions on the chain surface. Therefore the occupation probability for anions to stay at the chain surface is

$$p_0 = \frac{1}{\sum_{i=0}^{\infty} \frac{n_i}{n_0}} \quad (\text{A1} - 8)$$

According to Equation A1-7, and if the increment of  $r_i$  is small enough, one can write

$$\sum_{i=0}^{\infty} \frac{n_i}{n_0} \approx \int_0^{\infty} x^{1-\beta} dx \quad (\text{A1} - 9)$$

where  $x = r_i/r_0$ .

It can be shown from Equation A1-9 that for  $\beta \leq 2$ , the occupation probability at chains surface  $p_0$  vanishes, which means under the condition of  $\beta \leq 2$ , anions do not stay on the chain surface. On the contrary, for  $\beta > 2$ ,  $p_0$  is a non-vanishing value, hence the number of anions on the chain surface is not zero. Substituting the critical value  $\beta = 2$  into Equation A1-5, one has

$$2 = \frac{e^2}{2\pi\epsilon\epsilon_0 l_{io} kT} \quad (A1 - 10)$$

Rearranging Equation A1-10 gives the critical value of the average distance between fixed elementary charges along the chain  $l_{io}$

$$l_{io} = \frac{e^2}{4\pi\epsilon\epsilon_0 kT} \quad (A1 - 11)$$

This critical distance is known as the Bjerrum length  $\xi_B$ . If the distance between fixed charges on the rod-like chain is larger than  $\xi_B$ , then (approximately) all the counterions diffuse away from the chain surface. Otherwise, a fraction of counterions stay in close vicinity to the chain surface, leading to condensation.

The Bjerrum length  $\xi_B$  applies to highly simplified systems of non-interacting mobile anions. In order to take account of the interactions of anions with each other, one can define a spatially varying charge density  $\rho_e(r)$  and a varying electrostatic potential  $V(r)$ . These quantities follow the relationships shown by Equation A1-12 and A1-13.

$$\Delta V(r) = -\frac{\rho_e(r)}{\epsilon\epsilon_0} \quad (A1 - 12)$$

$$\rho_e(r) \propto (-e) \exp -\frac{(-e)V}{kT} \quad (A1 - 13)$$

According to these relationships, electrostatic potential now includes the presence of the anions and the potential determines the charge density distribution. Based on this correction, the conclusion about Bjerrum length  $\xi_B$  does not change for the case of  $l_{io} > \xi_B$ . However for  $l_{io} < \xi_B$ , the effective charge density on the rod due to the partial counterion condensation (by the certain fraction of counterions on the surface) is equal to  $e/\xi_B$ , which means the charge density distribution appears at distance  $\xi_B$  independent of the actual value of  $l_{io}$ .

As mentioned at the beginning of this section, instead of having polyion chains fully stretched in solution, condensation by counterions occurs depending on the charge concentration on the polyelectrolyte chain and this then influences the chain configuration to be more contracted (higher curvature along the chain). This effect has a key role in the chain configuration in solution, and thus can affect the relationship between diffusion coefficient, which gives the polymer particle hydrodynamic radius, and molecular weight.

### **Charge Screening (Debye-Hückel Theory)**

Shells of counterions surrounding an electrolyte ion can alter the electrostatic potential originating from this single (polymer-fixed or isolated) charge. For example, the potential created by an isolated positive elementary charge in a neutral solvent can be modified in the electrolyte solution by a spatial factor according to

$$V(r) = \frac{e}{4\pi\epsilon\epsilon_0 r} \exp - \frac{r}{\xi_D}. \quad (A1 - 14)$$

This dependence means that the Coulomb force from a cation virtually disappears (becomes small) at distance  $r$  above the Debye screening length  $\xi_D$  (defined below). (2) This explanation of the charge screening effect applies to low molar mass electrolyte as well as polyelectrolyte solutions.

Using the interrelated concepts of charge density  $\rho_e(r)$  and electrostatic potential  $V(r)$  defined above, one can derive the Debye length based on the Debye-Hückel theory as

$$\xi_D = \left( \frac{\epsilon \epsilon_0 kT}{I_{io}} \right)^{1/2} \quad (A1 - 15)$$

where  $I_{io}$  is the ionic strength defined by

$$I_{io} = \sum_i \bar{c}_i z_i^2 e^2 \quad (A1 - 16)$$

In Equation A1-16,  $\bar{c}_i$  is the number density of ions  $i$  with charge  $\pm z_i e$  for an electrolyte of arbitrary composition.

The Debye-Hückel theory states that the accumulation of counterions in the vicinity of an ion leads to such a screening effect, so that the Coulomb field of this ion is reduced and eventually (effectively) vanishes at distance above the Debye length. Upon increasing the ionic strength, one can decrease the Coulomb field strongly at very short distances.

Such a charge screening is commonly observed in polyelectrolyte solutions. The charge screening affects the repulsive electrostatic forces between the chain-fixed ions, when those polyions are screened by all mobile ionic species including counterions. The extension of the ion cloud around the charges on the polyion is

described by  $\xi_D$  and determined by the ionic strength (adjustable via salt concentration) in the polyelectrolyte solution.

Therefore, by adding sufficient salt into, for example, aqueous solutions, the charge screening effect can be strong enough to cancel the repulsive effects among polyelectrolyte chains and present a condition similar to neutral polymer solutions. This is in fact the rationale of performing diffusion coefficient measurements in salt-solution of polyelectrolyte by PFG-NMR, which has been proposed at the end of Chapter 4 and restated at the beginning of this section. For such a purpose, the salt concentration needs to exceed the value such that the Debye length drops below the Bjerrum length (Equation A1-11), which is the minimum distance between ions in the solution such that the counterions condense strongly on the polyelectrolyte chains. Meanwhile, the polyelectrolyte must remain in solution without precipitation, which may be induced by very high salt concentration and the resulting counterion condensation.

Here, a set of PFG-NMR diffusometry experiments is proposed as a function of salt concentration, in order to accurately assess polymer molecular weight and probe chain configuration. Since charge condensation can affect the relationship between diffusion coefficient and molecular weight, varied values of parameters  $A$  and  $\alpha$  (defined in eq. 4-1) are expected at different salt concentration for the same polyelectrolyte system.

Regarding the study in Chapter 4, in order to obtain an accurate calibration curve from reference samples for the investigation of polyelectrolyte samples of unknown molar mass, under one salt concentration, a series of measurements



should be made to study the effects of charge condensation on the molecular size/diffusion coefficient on individual reference and unknown samples with different molecular weights. This is necessary because synthesized polyelectrolyte samples may have a range of charge density for molecules from low to high molecular weights. For example, a salt concentration that can sufficiently neutralize the repulsive forces among polymer chains of a molecule with low molecular weight may not be high enough to make the chains of a molecule with high molecular weight behave also like neutral polymers. Therefore in order to assess and minimize the influence of configuration variation in the determination of a wide range of molecular weights of polyelectrolytes, thorough studies are needed in prior to the application of the PFG-NMR diffusometry method in salt solutions.

#### **References:**

1. G. R. Strobl, G. R. Strobl, *The physics of polymers*. (Springer, 1997), vol. 2.
2. P. Debye, E. Hückel, De la théorie des électrolytes. i. abaissement du point de congélation et phénomènes associés. *Physikalische Zeitschrift* **24**, 185-206 (1923).

## Appendix 2 Supporting Information for Chapter 5

### Contents

- Estimation of Benzene Correlation Times in SF CO<sub>2</sub> and Normal Solvents
- Figure 5-S1: Apparatus for Continuous-flow HPLC-DNP-NMR Coupled with SF CO<sub>2</sub>
- Determination of Absolute DNP Enhancement by Ratio Method
- Table 5-S1: Electron Saturation factor  $s$  of Benzene/TEMPO system in SF CO<sub>2</sub> and C<sub>6</sub>D<sub>6</sub>
- Figure 5-S2-S3: LLIT <sup>1</sup>H DNP Saturation Plots of Benzene/TEMPO system in SF CO<sub>2</sub> and Normal Solvents
- Table 5-S2 and Figure 5-S4-S7:  $a_{FC}$  via DFT Modeling and Considered Lowest-Energy Molecular Configurations of Benzene/TEMPO System
- Table 5-S3 and Figure 5-S8-S12:  $a_{FC}$  via DFT Modeling and Considered Lowest-Energy Molecular Configurations of Phenyl Acetylene/TEMPO System
- Table 5-S4 and Figure 5-S13-S18:  $a_{FC}$  via DFT Modeling and Considered Lowest-Energy Molecular Configurations of Benzaldehyde/TEMPO System
- Table 5-S5 and Figure 5-S19-S23:  $a_{FC}$  via DFT Modeling and Considered Lowest-Energy Molecular Configurations of Nitrobenzene/TEMPO System
- Figure 5-S24: LLIT <sup>13</sup>C Spectra of Nitrobenzene/TEMPO System

- Table 5-S6-S13: LLIT  $^{13}\text{C}$  DNP Enhancements of Benzonitrile, Phenylamine, Anisole, Toluene, Diethyl malonate, Ethyl Acetoacetate, Acetone, and Acetonitrile with TEMPO
- XYZ Coordinates of Phenyl acetylene/TEMPO, Benzaldehyde/TEMPO, and Nitrobenzene/TEMPO systems.

Estimation of correlation times corresponding to benzene  $^1\text{H}$  DNP coupling factors in SF  $\text{CO}_2$  and normal solvent by rotational diffusion modulation of dipolar interaction. For rotational diffusion modulation, the radical induced dipolar transition probabilities can be expressed as:

$$2W_1^D = 3W_0^D = W_2^D/2 = (3/10)\gamma_S^2\gamma_I^2h^2\tau_r(n_p N_e/N_p)d_r^{-6}J_r(\omega_i) \quad (5 - S1)$$

$$\tau_r = 4\pi b^3\eta/3kT \quad (5 - S2)$$

$$J(\omega_i) = 1/(1 + \omega_i^2\tau_r^2) \quad (5 - S3)$$

$\tau_r$  is the rotational correlation time;  $n_p$  is the number of receptor nuclei bound near each electron;  $N_e$  is the unpaired electron concentration;  $N_p$  is the total nuclear concentration;  $d_r$  is the shortest distance between the nuclear and electron spins;  $b$  is the effective tumbling radius treating solute-radical complex as a sphere;  $J_r(\omega_i)$  is the rotational spectral density function.

Under the assumption that rotational dipolar interaction dominates DNP enhancement, then the coupling factor can be expressed as:

$$\rho = (W_2^D + W_0^D)/(W_2^D + W_0^D + 2W_1^D) \quad (5 - S4)$$

By relating eq. 5-S4 with eq. 5-S1 and eq. 5-S3, the coupling factor can be further simplified as eq. S5 for dipolar interaction dominant DNP enhancement by rotational diffusion modulation:

$$\rho = \frac{1}{1.4+0.6(1+\omega_e^2\tau_r^2)} \quad (5 - S5)$$

With eq. 5-1 in main text, the absolute enhancement can be converted to coupling factor  $\rho$  for  $^1\text{H}$  DNP of benzene in normal solvent and SF  $\text{CO}_2$ , and the corresponding rotational correlation times can be estimated using eq. 5-S5.

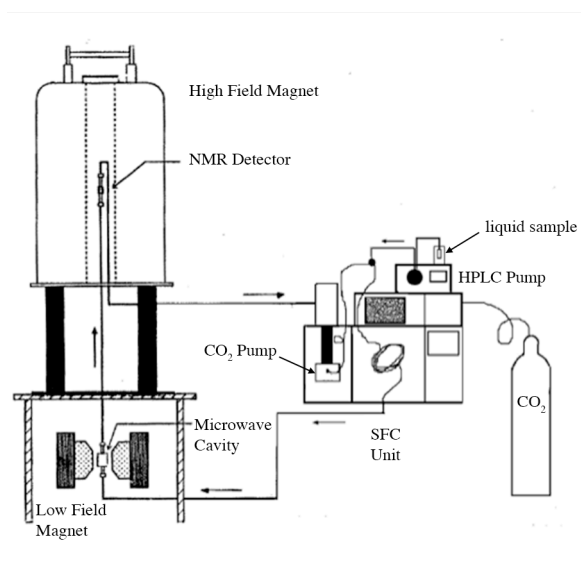


**Figure 5-S1.** Schematic drawing of apparatus for continuous-flow HPLC-DNP-NMR coupled with SF CO<sub>2</sub> from Ref. 17.

Ratio Method. There are two methods for the calculation of absolute DNP enhancements. One is called the exhaustive method, which was applied in most of our previous publications. This method takes into account as many variable factors that may cause an error to the final result as possible, such as the low to high magnetic field strength change,  $f$  and  $s$  factors. It is closely correlated to the flow transfer DNP system, so that the calculated result matches the true value well. One disadvantage of this method is that it requires a stable instrumental condition. Moreover, since the data have to be obtained for a whole range of flow rates, it is very time consuming.

The second method is called the ratio method. In this work, the DNP data of nitrobenzene and benzaldehyde systems were collected and processed by the ratio method. This method is advantageous where sample solutions cannot be readily studied by the exhaustive method due to high demand on instrument stability and experimental time.

The procedure for the ratio method is much simpler. The  $s$  factor is assumed to be same for all the nuclei in a given experiment. In contrast to the exhaustive method, no flow plot or power plot has to be made in the ratio method. The experiment and calculation for the absolute DNP enhancement by using ratio method includes the steps described below.

1. To obtain the peak height of the  $^{13}\text{C}$  static NMR, flow NMR and DNP spectra.
2. To calculate the observed  $^{13}\text{C}$  DNP enhancement  $A_{obs}$  for the flow transfer system using eq. S6, where  $M_Z^*$  is the peak height of the enhanced NMR signal at certain microwave power,  $M_Z^{HL}$  is the peak height of the flow NMR signal in the absence of the microwave power, and  $M_0^H$  is the peak height of the static NMR signal.

$$A_{obs} = \frac{M_Z^* - M_Z^{HL}}{M_0^H} \quad (5 - S6)$$

3. To convert  $A_{obs}$  obtained from the flow transfer system to the static DNP system. The formula for such conversion was given in the exhaustive method as described by eq. S7, where  $T_{1a}$  and  $T_{1c}$  are the nuclear relaxation times in low field microwave cavity and high field NMR detector, respectively, and  $T_{1c}$  is the nuclear relaxation time in between the abovementioned regions. Similarly,  $V_a$ ,  $V_b$  and  $V_c$  are the corresponding sample solution volumes of these three regions.  $F$  is the flow rate and  $K$  is the high to low magnetic field strength ratio.

$$A_s = \frac{K \cdot A_{obs}}{\left[1 - \exp\left(\frac{-v_a}{T_{1a} \cdot F}\right)\right] \cdot \exp\left[-\left(\frac{v_b}{T_{1b}} + \frac{v_c}{T_{1c}}\right) \frac{1}{F}\right]} \quad (5 - S7)$$

$T_{1a}$ ,  $T_{1b}$  and  $T_{1c}$  are assumed equal for simplicity.

4. To get the absolute enhancement by eq. 5-S8, where  $A_\infty^{ref}$  is the absolute DNP enhancement of the reference nucleus ( $^{13}\text{C}$  of cyclohexane here).  $A_s$  and  $A_{ref}$  are the observed static DNP enhancements for the respective nucleus and the reference nucleus.  $f_s$  and  $f_{ref}$  are the leakage factors of the sample and reference nucleus, respectively.

$$A_\infty = A_\infty^{ref} \cdot \frac{A_s}{A_{ref}} \cdot \frac{f_{ref}}{f_s} \quad (5 - S8)$$

**Table 5-S1. Electron Saturation factor  $s$  of Benzene/TEMPO system for LLIT  $^1\text{H}$**

**DNP Enhancements in  $\text{C}_6\text{D}_6$  and SF  $\text{CO}_2$**

system	saturation factor
9% benzene/ $\text{C}_6\text{D}_6$ /0.001 M TEMPO	0.68
9% benzene/SF $\text{CO}_2$ /0.001 M TEMPO	0.28
9% benzene/ $\text{C}_6\text{D}_6$ /0.01 M TEMPO	0.49
9% benzene/SF $\text{CO}_2$ /0.01 M TEMPO	0.21

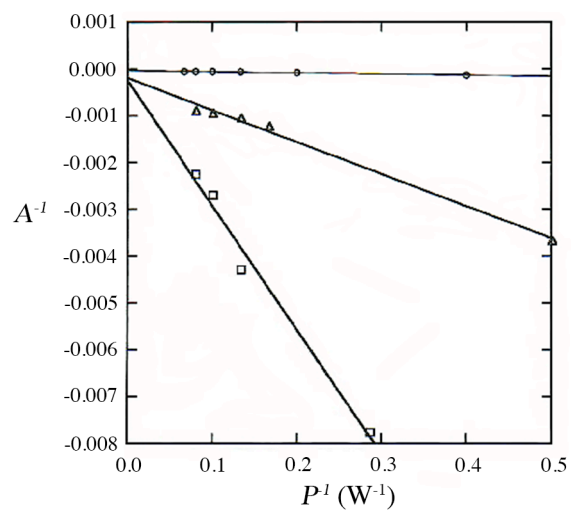


**Figure 5-S2.** LLIT  $^1\text{H}$  DNP saturation plot showing the inverse enhancement versus the inverse microwave power for 9% benzene in deuterated benzene (circle), neat benzene (triangle), and 9% benzene in  $\text{SF}_6/\text{CO}_2$  (square) in 0.001 M TEMPO.

Microwave power was varied from 2 to 15 W. The value of the slope for each sample is given as follow:  $-2.5 \times 10^{-4} \text{ G}^2$ ,  $-5.9 \times 10^{-3} \text{ G}^2$ , and  $-2.7 \times 10^{-2} \text{ G}^2$  for benzene in  $\text{C}_6\text{D}_6$ ,  $\text{C}_6\text{H}_6$ , and  $\text{SF}_6/\text{CO}_2$ , respectively.

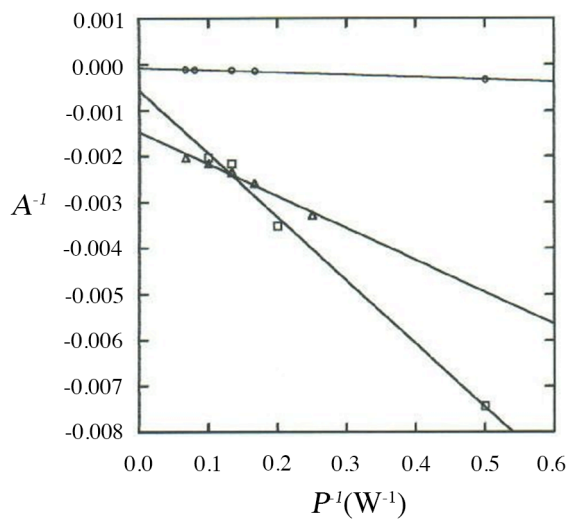




**Figure 5-S3.** LLIT  $^1\text{H}$  DNP saturation plot showing the inverse enhancement versus the inverse microwave power for 9% benzene in deuterated benzene (circle), neat benzene (triangle), and 9% benzene in  $\text{SF}_6/\text{CO}_2$  (square) in 0.01 M TEMPO.

Microwave power was varied from 2 to 15 W. The value of the slope for each sample is given as follow:  $-5.0 \times 10^{-4} \text{ G}^2$ ,  $-7.0 \times 10^{-3} \text{ G}^2$ , and  $-1.4 \times 10^{-2} \text{ G}^2$  for benzene in  $\text{C}_6\text{D}_6$ ,  $\text{C}_6\text{H}_6$ , and  $\text{SF}_6/\text{CO}_2$ , respectively.

**Table 5-S2.** LLIT  $^{13}\text{C}$  DNP Enhancements for Benzene/ $\text{C}_6\text{D}_6$ /0.16 M TEMPO [15](#) and  $a_{FC}$  via DFT Modeling

Nucleus	Enhancement	$a_{FC}$ (MHz)				
		Average	1	2	3	4
$^{13}\text{C}$	$-220 \pm 33$	0.802	0.025	0.160	0.731	0.021
			0.263	1.896	0.107	0.129
			1.046	0.163	-0.045	-0.127
			0.609	0.146	0.057	0.306
			0.120	0.029	0.862	1.658
			0.002	0.145	3.854	0.171
$\Delta G$ (kcal/mol)			0.00	0.09	0.17	3.83

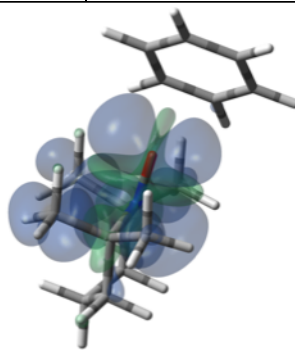


**Figure 5-S4.** Interacting orientation 1 of benzene/TEMPO

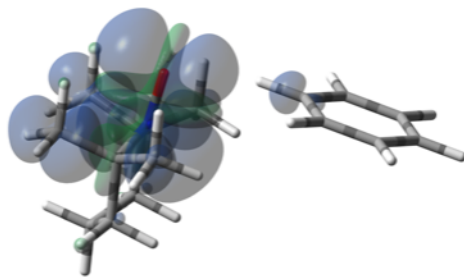


**Figure 5-S5.** Interacting orientation 2 of benzene/TEMPO (Figure 9 in main text)

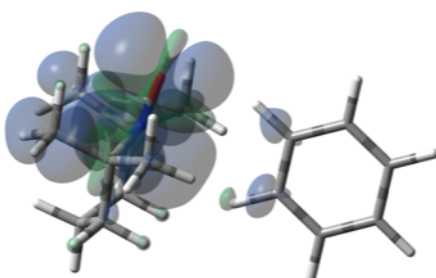


**Figure 5-S6.** Interacting orientation 3 of benzene/TEMPO (Figure 8 in main text)

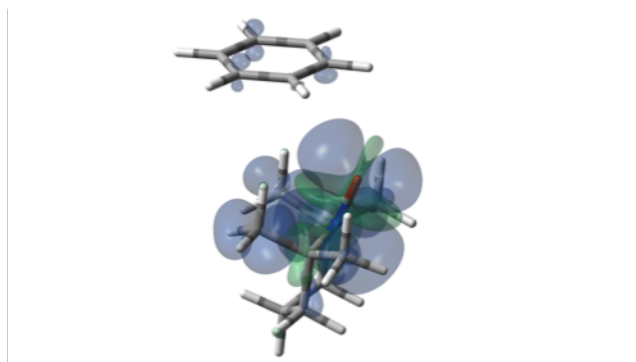


**Figure 5-S7.** Interacting orientation 4 of benzene/TEMPO

**Table 5-S3. LLIT  $^{13}\text{C}$  DNP Enhancements for Phenylacetylene/0.001 M TEMPO and  $a_{FC}$  via DFT Modeling**

Nucleus	Enhancement	$a_{FC}$ (MHz)						
		Average	5	6	7	8	9	10
$^{13}\text{C}-\beta$	+1400±210	3.281	0.256	15.249	-0.001	-0.031	0.066	0.043
$^{13}\text{C}-\alpha$	+290±44	0.871	0.727	2.722	0.028	0.063	-0.105	-0.026
$^{13}\text{C}-\text{Ipso}$	-280±42	0.277	0.540	0.227	-0.004	-0.162	0.195	0.200
$^{13}\text{C}-\text{Ortho}$	-36±5	0.579	2.493	-0.082	0.124	0.173	0.313	1.526
			-0.019	-0.114	0.039	0.259	-0.100	0.040
$^{13}\text{C}-\text{Meta}$	-32±5	0.117	-0.104	0.021	0.554	-0.111	0.240	0.484
			0.028	0.010	0.299	0.836	0.172	0.099
$^{13}\text{C}-\text{Para}$	N/A	0.181	0.005	-0.023	1.245	-0.061	0.288	-0.058
$\Delta G$ (kcal/mol)			0.00	0.41	0.65	0.77	1.04	1.25

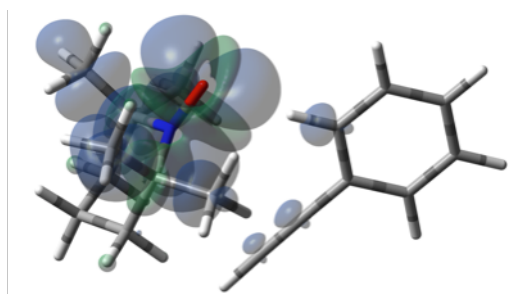


**Figure 5-S8.** Interacting orientation 5 of phenylacetylene/TEMPO

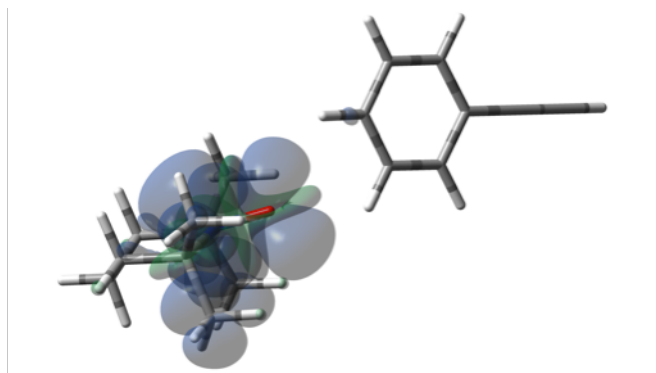


**Figure 5-S9.** Interacting orientation 7 of benzene/TEMPO

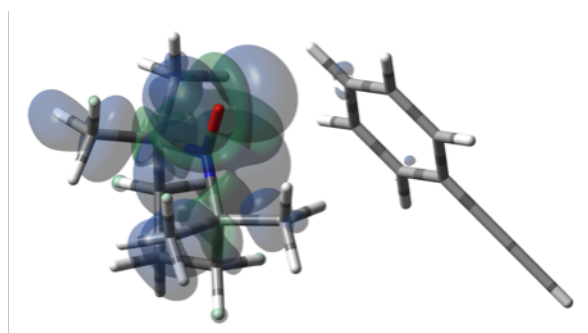


**Figure 5-S10.** Interacting orientation 8 of phenylacetylene/TEMPO

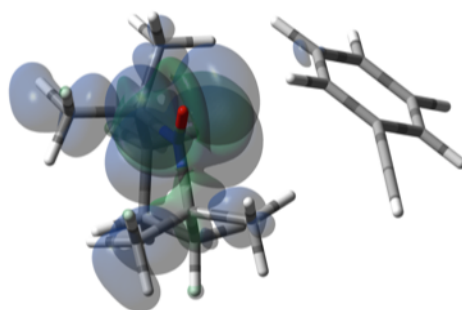


**Figure 5-S11.** Interacting orientation 9 of benzene/TEMPO

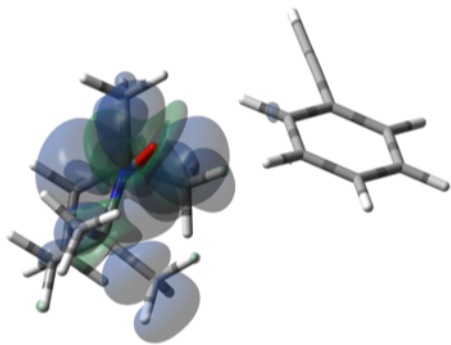


**Figure 5-S12.** Interacting orientation 10 of benzaldehyde/ TEMPO

**Table 5-S4. LLIT  $^{13}\text{C}$  DNP Enhancements for Benzaldehyde/Cyclohexane/0.1 M TEMPO and  $a_{FC}$  via DFT Modeling**

Nucleus	Enhancement	$a_{FC}$ (MHz)								
		Average	11	12	13	14	15	16	17	
$^{13}\text{CHO-}$	+373±56	1.155	-0.356	1.294	-0.178	7.506	0.027	0.003	0.016	
$^{13}\text{C-Ipso}$	-456±20	0.284	0.731	-0.003	-0.083	0.277	0.149	0.147	-0.035	
$^{13}\text{C-Ortho}$	+131±20	0.442	1.532	0.173	0.178	1.580	0.158	0.083	0.048	
			-0.219	0.229	0.204	-0.158	-0.038	0.785	0.240	
$^{13}\text{C-Meta}$	+93±14	0.063	0.206	-0.237	0.010	-0.140	2.632	0.079	-0.135	
			0.231	-0.237	0.050	0.156	0.183	0.567	0.405	
$^{13}\text{C-Para}$	+78±12	0.099	-0.154	0.267	-0.026	0.120	0.177	0.118	2.320	
$\Delta G$ (kcal/mol)			0.00	0.10	0.50	0.62	1.48	1.57	1.60	

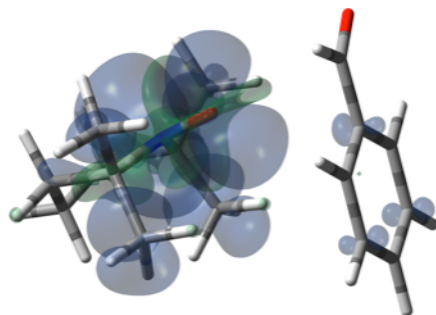


**Figure 5-S13.** Interacting orientation 11 of benzaldehyde/ TEMPO

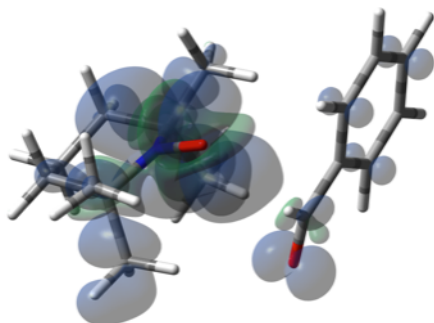


**Figure 5-S14.** Interacting orientation 12 of benzaldehyde/ TEMPO

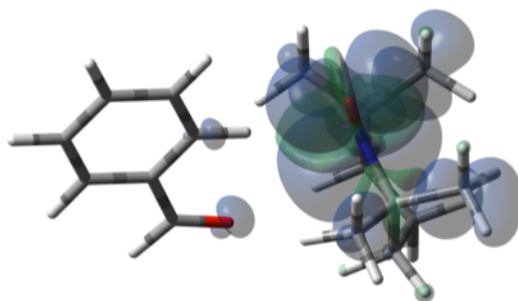


**Figure 5-S15.** Interacting orientation 13 of benzaldehyde/ TEMPO

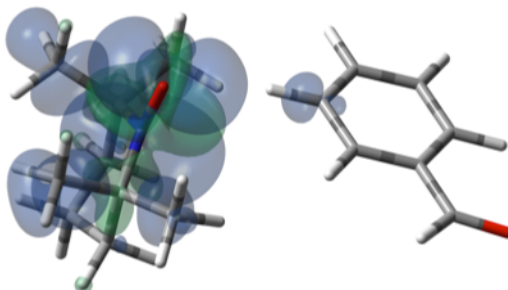


**Figure 5-S16.** Interacting orientation 15 of benzaldehyde/ TEMPO

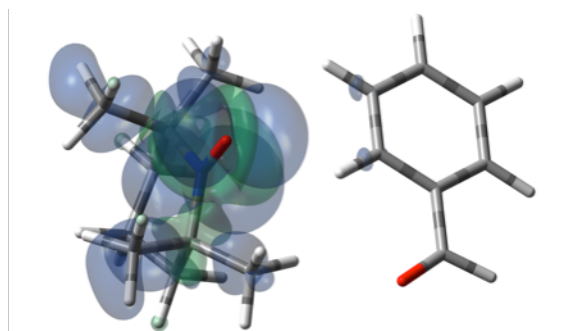


**Figure 5-S17.** Interacting orientation 16 of benzaldehyde/ TEMPO

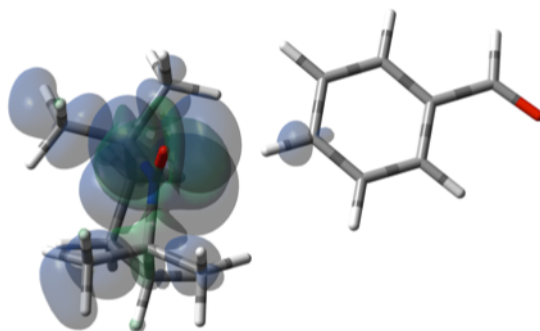


**Figure 5-S18.** Interacting orientation 17 of benzaldehyde/ TEMPO

**Table 5-S5. LLIT  $^{13}\text{C}$  DNP Enhancements for Nitrobenzene/Cyclohexane/0.1 M TEMPO and  $a_{FC}$  via DFT Modeling**

Nucleus	Enhancement	$a_{FC}$ (MHz)						
		Average	18	19	20	21	22	23
$^{13}\text{C}$ -Ipsso	$-572 \pm 86$	0.399	0.792	0.176	0.601	0.040	0.138	0.036
$^{13}\text{C}$ -Ortho	$+587 \pm 88$	1.424	6.549	1.816	0.801	0.218	0.901	0.029
			0.112	0.024	0.476	0.035	0.048	0.007
$^{13}\text{C}$ -Meta	$+198 \pm 30$	0.329	1.638	-0.070	-0.436	1.174	0.743	0.958
			-0.077	0.030	-0.403	0.340	0.107	0.027
$^{13}\text{C}$ -Para	$+366 \pm 55$	0.418	0.558	-0.022	0.490	1.253	0.166	0.006
$\Delta G$ (kcal/mol)			0.00	0.05	0.42	0.49	0.85	1.01

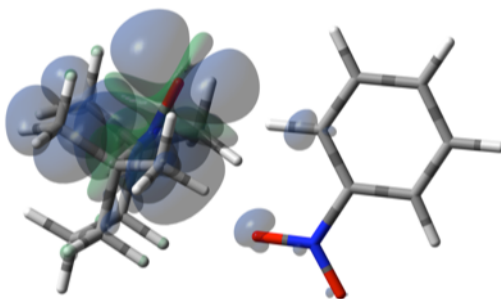


**Figure 5-S19.** Interacting orientation 19 of nitrobenzene/ TEMPO

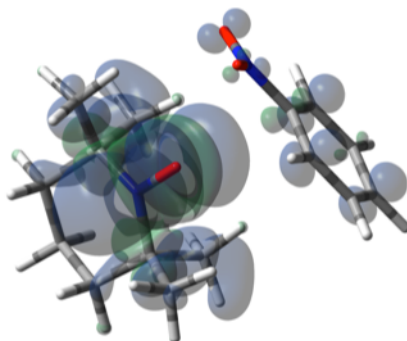


**Figure 5-S20.** Interacting orientation 20 of nitrobenzene/ TEMPO



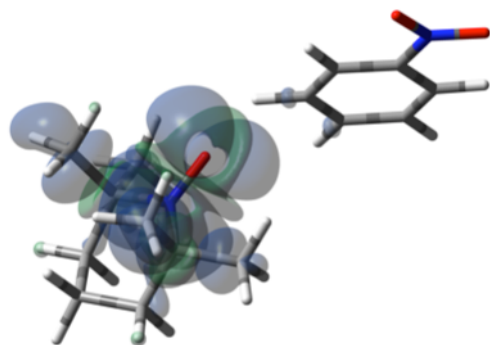


**Figure 5-S21.** Interacting orientation 21 of nitrobenzene/ TEMPO

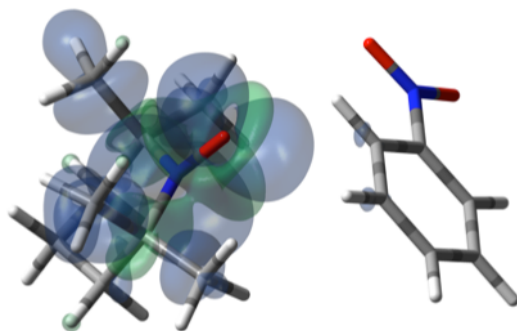


**Figure 5-S22.** Interacting orientation 22 of nitrobenzene/ TEMPO

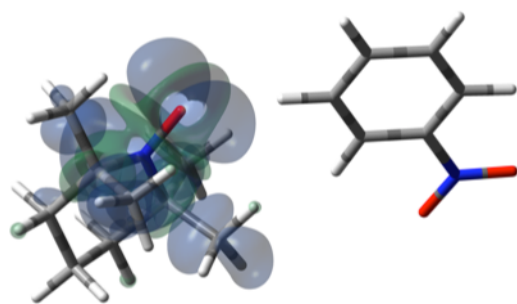


**Figure 5-S23.** Interacting orientation 23 of nitrobenzene/ TEMPO

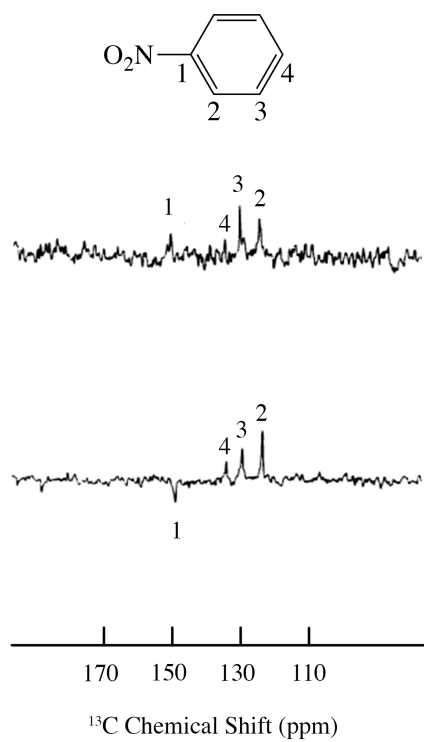


**Figure 5-S24.**  $^{13}\text{C}$  spectra of nitrobenzene/TEMPO in cyclohexane at 4.7 T (a) 0.1 M TEMPO without flow DNP, (b) 0.1 M TEMPO with flow DNP (a) 100 scans; (b) 100 scans.

**Table 5-S6. LLIT  $^{13}\text{C}$  DNP Enhancements for Benzonitrile/Cyclohexane/0.1 M TEMPO**

system	nucleus	absolute enhancement
benzonitrile	$^{13}\text{CN-}$	$-204\pm 31$
	$^{13}\text{C-ipso}$	$-281\pm 42$
	$^{13}\text{C-ortho}$	$+171\pm 26$
	$^{13}\text{C-meta}$	$+98\pm 15$
	$^{13}\text{C-para}$	$+22\pm 2$

**Table 5-S7. LLIT <sup>13</sup>C DNP Enhancements for Phenylamine/Cyclohexane/0.1 M****TEMPO**

system	nucleus	absolute enhancement
phenylamine	<sup>13</sup> C- <i>ipso</i>	-318±48
	<sup>13</sup> C- <i>ortho</i>	-22±2
	<sup>13</sup> C- <i>meta</i>	-131±20
	<sup>13</sup> C- <i>para</i>	-145±22

**Table 5-S8. LLIT <sup>13</sup>C DNP Enhancements for Anisole/Cyclohexane/0.1 M****TEMPO**

system	nucleus	absolute enhancement
anisole	O <sup>13</sup> CH <sub>3</sub> -	+266±31
	<sup>13</sup> C- <i>ipso</i>	-457±69
	<sup>13</sup> C- <i>ortho</i>	-42±6
	<sup>13</sup> C- <i>meta</i>	-61±9
	<sup>13</sup> C- <i>para</i>	-64±10

**Table 5-S9. LLIT <sup>13</sup>C DNP Enhancements for Toluene/Cyclohexane/0.1 M****TEMPO**

system	nucleus	absolute enhancement
toluene	<sup>13</sup> CH <sub>3</sub> -	-187±28
	<sup>13</sup> C- <i>ipso</i>	-562±84
	<sup>13</sup> C- <i>ortho</i>	-179±27
	<sup>13</sup> C- <i>meta</i>	-153±23
	<sup>13</sup> C- <i>para</i>	-207±31

**Table 5-S10. LLIT  $^{13}\text{C}$  DNP Enhancements for  
Diethylmalonate/Benzene/Cyclohexane/0.1 M TEMPO**

system	nucleus	absolute enhancement
diethyl malonate	$^{13}\text{C}$ -1	-642±96
	$^{13}\text{C}$ -2	+401±60
	$^{13}\text{C}$ -1'	+86±13
	$^{13}\text{C}$ -2'	-97±14

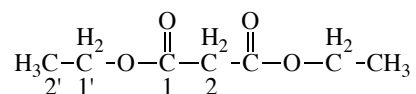


**Table 5-S11. LLIT  $^{13}\text{C}$  DNP Enhancements for Ethyl  
acetoacetate/Benzene/Cyclohexane/0.1 M TEMPO**

system	nucleus	absolute enhancement
ethyl acetoacetate	$^{13}\text{C}$ -1	-711±107
	$^{13}\text{C}$ -2	+440±66
	$^{13}\text{C}$ -3	-720±108
	$^{13}\text{C}$ -4	+73±11
	$^{13}\text{C}$ -1'	+250±38
	$^{13}\text{C}$ -2'	-117±18

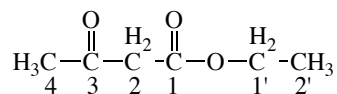


**Table 5-S12. LLIT  $^{13}\text{C}$  DNP Enhancements for Acetone/Carbon tetrachloride/Cyclohexane/0.1 M TEMPO**

system	nucleus	absolute enhancement
acetone	$^{-13}\text{CO-}$	$-84\pm 13$
	$^{13}\text{CH}_3\text{-}$	$-744\pm 112$

**Table 5-S13. LLIT  $^{13}\text{C}$  DNP Enhancements for Acetonitrile/Carbon tetrachloride/0.1 M TEMPO**

system	nucleus	absolute enhancement
acetonitrile	$^{13}\text{CH}_3\text{-}$	$+520\pm 100$
	$^{13}\text{CN-}$	$-620\pm 120$

XYZ Coordinates of Phenyl acetylene/TEMPO, Benzaldehyde/TEMPO, and Nitrobenzene/TEMPO systems.

Orientation #5

phenylacetylene/bite-orthometa/phenylacetylene-tempo-bite-orthometa.freq.out

```
C -4.754403 -1.200578 0.000110
C -3.413655 -1.585041 -0.000026
C -2.402665 -0.628710 -0.000133
C -2.731181 0.740333 -0.000104
C -4.087367 1.120713 0.000029
C -5.087346 0.154859 0.000137
H -5.542373 -1.957332 0.000190
H -3.145891 -2.643984 -0.000050
H -1.355521 -0.942381 -0.000251
H -4.342310 2.182544 0.000044
H -6.135644 0.462184 0.000234
C -1.713248 1.738418 -0.000226
C 1.899014 -0.244690 -1.324793
C 2.420871 1.190285 -1.234489
C 3.259585 1.451286 -0.000084
C 2.420815 1.190507 1.234329
C 1.898959 -0.244455 1.324874
H 2.979130 1.409000 -2.158857
```

H 4.164084 0.818819 -0.000002  
H 3.627701 2.488500 -0.000166  
H 2.979033 1.409400 2.158680  
H 1.555605 1.876041 1.230067  
H 1.555665 1.875826 -1.230397  
C 3.005250 -1.220397 -1.729933  
H 2.639035 -2.252733 -1.647627  
H 3.308030 -1.044305 -2.772051  
H 3.902816 -1.125363 -1.103288  
C 0.757793 -0.315454 -2.330708  
H 1.108279 0.026389 -3.314634  
H 0.380340 -1.340065 -2.430214  
H -0.076678 0.330869 -2.022102  
C 3.005179 -1.220079 1.730249  
H 3.307835 -1.043838 2.772377  
H 2.638989 -2.252433 1.648049  
H 3.902817 -1.125110 1.103695  
C 0.757692 -0.315036 2.330765  
H 0.380315 -1.339646 2.430559  
H 1.108095 0.027142 3.314604  
H -0.076823 0.331118 2.021917  
N 1.350228 -0.678012 0.000075  
O 0.699045 -1.769467 0.000157

C -0.864323 2.610853 -0.000346  
H -0.132316 3.394304 -0.000461

Orientation #6

phenylacetylene/rcontact/phenylacetylene-tempo-rcontact.freq.out

C 6.501361 -0.189869 0.653996  
C 5.551680 -1.138868 1.034059  
C 4.238857 -1.037618 0.585975  
C 3.851179 0.022246 -0.255957  
C 4.818504 0.973618 -0.632782  
C 6.128999 0.864823 -0.180133  
H 7.531594 -0.272641 1.007442  
H 5.837208 -1.967442 1.686379  
H 3.494085 -1.779490 0.881349  
H 4.524401 1.797512 -1.286106  
H 6.867960 1.610756 -0.481767  
C 2.508339 0.132447 -0.718954  
C -2.673368 1.306758 0.315628  
C -3.914886 1.028884 1.166052  
C -3.978430 -0.389514 1.694506  
C -3.992083 -1.356646 0.528597  
C -2.757211 -1.246802 -0.368903  
H -3.941506 1.767053 1.983392



H -3.125404 -0.595773 2.363226  
H -4.877368 -0.526107 2.314029  
H -4.075217 -2.400934 0.869499  
H -4.890694 -1.164050 -0.082985  
H -4.812829 1.221045 0.553330  
C -1.419026 1.433346 1.182009  
H -0.519943 1.490736 0.552922  
H -1.468528 2.351437 1.784889  
H -1.292792 0.591071 1.875339  
C -2.868664 2.587538 -0.483693  
H -3.086743 3.419500 0.200184  
H -1.972215 2.836485 -1.062679  
H -3.708638 2.490921 -1.185211  
C -1.525714 -1.864987 0.295558  
H -1.640109 -2.956635 0.359788  
H -0.623392 -1.653716 -0.294813  
H -1.358462 -1.490722 1.314394  
C -3.018741 -1.941723 -1.697889  
H -2.131058 -1.920438 -2.340083  
H -3.297057 -2.989443 -1.518278  
H -3.841062 -1.456788 -2.241604  
N -2.478361 0.194335 -0.668849  
O -1.684815 0.426271 -1.632976

C 1.364837 0.233744 -1.125024  
H 0.341019 0.322889 -1.465155

Orientation #7

phenylacetylene/para/phenylacetylene-tempo-paraCH.freq.out

C 2.220912 0.989135 -0.748176  
C 2.340055 0.395267 0.509680  
C 3.571190 -0.080239 0.947711  
C 4.710854 0.030761 0.127754  
C 4.579916 0.631650 -1.138377  
C 3.344001 1.105287 -1.567643  
H 1.242855 1.351981 -1.072368  
H 1.452438 0.310839 1.140896  
H 3.669885 -0.544222 1.931471  
H 5.460980 0.720407 -1.777422  
H 3.257969 1.570092 -2.552805  
C 5.974178 -0.456384 0.571748  
C -3.214391 0.981036 0.355988  
C -4.411143 0.346786 -0.355389  
C -4.404190 -1.167580 -0.314433  
C -3.143330 -1.678378 -0.981131  
C -1.858068 -1.188101 -0.311155  
H -5.331291 0.760156 0.087688

H -4.471121 -1.531056 0.725298  
H -5.294137 -1.567293 -0.823096  
H -3.116451 -2.779390 -1.007873  
H -3.139337 -1.349152 -2.034793  
H -4.408608 0.673585 -1.409768  
C -3.354885 0.897599 1.877108  
H -2.418719 1.216020 2.355674  
H -4.159676 1.562035 2.222868  
H -3.591004 -0.116164 2.227785  
C -3.076902 2.439004 -0.060292  
H -4.006433 2.979281 0.166854  
H -2.249529 2.925990 0.468126  
H -2.886671 2.524033 -1.139099  
C -1.605149 -1.911675 1.012730  
H -1.345018 -2.963563 0.826989  
H -0.765019 -1.442701 1.543162  
H -2.478610 -1.899983 1.678501  
C -0.673046 -1.408790 -1.241242  
H 0.274236 -1.139491 -0.759130  
H -0.624600 -2.466915 -1.533888  
H -0.770759 -0.805780 -2.154966  
N -1.951890 0.283953 -0.049875  
O -0.869247 0.867994 0.267017

C 7.052239 -0.872379 0.951300

H 8.002375 -1.238332 1.285808

Orientation #8

phenylacetylene/meta/phenylacetylene-tempo-metaCH.freq.out

C -1.436350 -1.947392 0.216167

C -2.323578 -1.627433 1.243581

C -3.354812 -0.720213 1.026074

C -3.513392 -0.109850 -0.233130

C -2.613587 -0.439876 -1.264430

C -1.587422 -1.351828 -1.036579

H -0.614891 -2.641042 0.404448

H -2.200072 -2.081863 2.229008

H -4.048439 -0.465407 1.829992

H -2.733380 0.028386 -2.243831

H -0.899312 -1.599742 -1.849464

C -4.561612 0.828308 -0.458954

C 2.549249 -0.714920 -0.444263

C 2.473098 0.097829 -1.738152

C 2.411277 1.594084 -1.507717

C 1.192036 1.922788 -0.670223

C 1.186895 1.234886 0.695962

H 3.332018 -0.179912 -2.370218

H 3.332049 1.950834 -1.014992  
H 2.369042 2.126147 -2.469960  
H 1.093046 3.008174 -0.508997  
H 0.285816 1.612444 -1.219813  
H 1.571871 -0.212682 -2.295613  
C 3.933420 -0.620283 0.201826  
H 3.907053 -1.067167 1.205192  
H 4.672453 -1.170327 -0.398385  
H 4.291653 0.413178 0.296318  
C 2.236435 -2.176411 -0.732262  
H 2.948107 -2.569962 -1.471244  
H 2.304443 -2.783293 0.178173  
H 1.224131 -2.290303 -1.143435  
C 2.197425 1.868304 1.654871  
H 1.859370 2.870831 1.953925  
H 2.285860 1.253802 2.561402  
H 3.198014 1.976994 1.215997  
C -0.203170 1.318937 1.308319  
H -0.233543 0.836860 2.292486  
H -0.491999 2.373044 1.422903  
H -0.948188 0.829727 0.666809  
N 1.520966 -0.218181 0.527765  
O 1.289326 -0.967742 1.525868

C -5.456075 1.629167 -0.652619  
H -6.245489 2.333893 -0.822807

Orientation #9

phenylacetylene/ring/phenylacetylene-tempo-ring.freq.out

C 2.000319 -2.301201 0.601917  
C 1.763127 -1.704511 -0.635911  
C 2.462061 -0.561882 -1.008940  
C 3.417553 0.001213 -0.143933  
C 3.652012 -0.609592 1.103323  
C 2.946082 -1.750208 1.469653  
H 1.446941 -3.197466 0.894178  
H 1.011660 -2.111552 -1.315049  
H 2.250605 -0.079977 -1.964971  
H 4.390429 -0.174041 1.779648  
H 3.134017 -2.213992 2.440780  
C 4.116326 1.187219 -0.511956  
C -2.524447 -0.779208 -0.498197  
C -3.109080 -0.904155 0.909652  
C -3.252639 0.425017 1.621833  
C -1.887356 1.069832 1.744816  
C -1.210719 1.332115 0.397791  
H -4.073321 -1.432239 0.835046

H -3.951221 1.085601 1.080417  
H -3.697699 0.279039 2.617506  
H -1.936987 2.024261 2.292891  
H -1.235300 0.409365 2.342668  
H -2.449638 -1.557133 1.507803  
C -3.546437 -0.211143 -1.484526  
H -3.056013 0.006896 -2.443076  
H -4.349691 -0.939524 -1.666760  
H -4.015184 0.713845 -1.122865  
C -2.058555 -2.144813 -0.983195  
H -2.900930 -2.850566 -0.976035  
H -1.658115 -2.087799 -2.002438  
H -1.272822 -2.544964 -0.327087  
C -1.843819 2.520415 -0.328082  
H -1.604195 3.457688 0.194282  
H -1.445424 2.586334 -1.349725  
H -2.938282 2.448136 -0.391112  
C 0.271983 1.599541 0.612799  
H 0.779398 1.830787 -0.331820  
H 0.399709 2.452664 1.294103  
H 0.767898 0.726947 1.061558  
N -1.325149 0.119325 -0.476729  
O -0.618771 0.124390 -1.532053

C 4.704479 2.204405 -0.825828  
H 5.225045 3.099032 -1.103720

Orientation #10

phenylacetylene/ortho/phenylacetylene-tempo-orthoCH.freq.out

C -3.451624 -2.301647 0.165964  
C -2.452213 -1.711955 -0.608729  
C -2.378686 -0.327629 -0.724522  
C -3.303050 0.491637 -0.049806  
C -4.307634 -0.112030 0.730206  
C -4.378540 -1.497448 0.831737  
H -3.509609 -3.389198 0.253131  
H -1.713802 -2.325392 -1.130587  
H -1.583810 0.121166 -1.322544  
H -5.027338 0.519891 1.254755  
H -5.163165 -1.954650 1.439098  
C -3.205945 1.910381 -0.146189  
C 2.503417 -1.181294 -0.056150  
C 3.812670 -0.581327 0.462194  
C 3.618164 0.677119 1.283417  
C 2.913195 1.723794 0.444172  
C 1.540467 1.273421 -0.060937  
H 4.344569 -1.358642 1.034077



H 3.042047 0.459738 2.199051  
H 4.589783 1.058163 1.632036  
H 2.781535 2.665284 1.001086  
H 3.545960 1.970024 -0.426370  
H 4.456763 -0.345685 -0.402807  
C 1.720055 -1.877086 1.059116  
H 0.713191 -2.139119 0.705059  
H 2.228851 -2.804223 1.360269  
H 1.612082 -1.254841 1.957244  
C 2.798693 -2.181440 -1.165441  
H 3.486354 -2.953935 -0.793796  
H 1.882080 -2.667841 -1.517902  
H 3.270122 -1.687407 -2.026059  
C 0.506828 1.260896 1.067247  
H 0.245643 2.289879 1.353394  
H -0.414886 0.763239 0.735717  
H 0.865213 0.748320 1.969702  
C 1.065940 2.202753 -1.169623  
H 0.048327 1.957482 -1.495145  
H 1.067461 3.239626 -0.805088  
H 1.727081 2.144250 -2.045098  
N 1.654735 -0.099751 -0.648838  
O 0.695920 -0.484168 -1.388041

C -3.104884 3.120054 -0.226208  
H -3.026073 4.186270 -0.301700

Orientation #11

benzaldehyde/ring/benzaldehyde-tempo-ring.freq.out

C 3.207391 -1.841368 -1.208712  
C 2.590012 -2.157245 0.003492  
C 2.322058 -1.149450 0.925873  
C 2.661722 0.177383 0.637367  
C 3.282190 0.487820 -0.579809  
C 3.555922 -0.519303 -1.499153  
H 3.419788 -2.631546 -1.932969  
H 1.823044 -1.373514 1.873362  
C -2.386816 -0.669574 0.793566  
C -3.672459 -0.344042 0.029836  
C -3.444970 -0.041093 -1.436952  
C -2.503954 1.139524 -1.566583  
C -1.137951 0.902289 -0.919252  
H -4.374284 -1.182508 0.166027  
H -3.037239 -0.923717 -1.958907  
H -4.402319 0.176505 -1.933594  
H -2.339368 1.410562 -2.621760  
H -2.969456 2.022212 -1.094500

H -4.149182 0.531269 0.503929  
C -1.868245 -2.069338 0.457052  
H -0.867723 -2.211675 0.889188  
H -2.535204 -2.834619 0.879598  
H -1.800526 -2.250829 -0.623898  
C -2.638628 -0.570387 2.291940  
H -3.463223 -1.240057 2.574021  
H -1.747845 -0.850370 2.865468  
H -2.915485 0.453638 2.577535  
C -0.285304 -0.062521 -1.746032  
H 0.064306 0.432883 -2.663822  
H 0.599218 -0.369983 -1.171695  
H -0.830347 -0.967391 -2.047050  
C -0.399252 2.224577 -0.767476  
H 0.625306 2.083088 -0.403876  
H -0.350382 2.729849 -1.742250  
H -0.916229 2.889644 -0.062585  
N -1.329720 0.334786 0.453421  
O -0.319342 0.358697 1.223591  
H 2.317271 -3.192070 0.224629  
H 4.040596 -0.279705 -2.448601  
C 2.349053 1.249827 1.606639  
O 2.556071 2.425256 1.408522

H 1.903070 0.887934 2.568942  
H 3.535812 1.532683 -0.778812

Orientation #12

benzaldehyde/ortho/benzaldehyde-tempo-ortho.freq.out

C -4.299646 1.111616 -0.489090  
C -3.786062 0.292274 -1.496433  
C -2.888994 -0.721305 -1.172906  
C -2.496646 -0.917480 0.156239  
C -3.017712 -0.093366 1.163218  
C -3.916501 0.917469 0.841041  
H -5.004709 1.907442 -0.741657  
H -2.458642 -1.357613 -1.951600  
C 2.552241 -0.782308 -0.348480  
C 3.737076 0.187354 -0.319256  
C 3.509121 1.395433 0.566807  
C 2.284313 2.152252 0.092867  
C 1.008237 1.306518 0.101691  
H 4.633129 -0.374503 -0.010332  
H 3.391964 1.087533 1.619687  
H 4.392491 2.051337 0.549874  
H 2.105044 3.050893 0.704759  
H 2.460684 2.512770 -0.935673

H 3.933508 0.532270 -1.349512  
C 2.443822 -1.584007 0.950344  
H 1.493191 -2.133642 0.990595  
H 3.265518 -2.312462 1.010011  
H 2.500990 -0.952477 1.846435  
C 2.698187 -1.739738 -1.522607  
H 3.665228 -2.257285 -1.455415  
H 1.900573 -2.491295 -1.527168  
H 2.662048 -1.201986 -2.479946  
C 0.507383 1.066321 1.527993  
H 0.054635 1.987086 1.924623  
H -0.256061 0.277193 1.544184  
H 1.307573 0.770071 2.218823  
C -0.082110 1.996278 -0.705974  
H -1.031832 1.450973 -0.646231  
H -0.238630 3.011740 -0.315786  
H 0.197874 2.074136 -1.765562  
N 1.288191 -0.007769 -0.560082  
O 0.288215 -0.655340 -0.994912  
H -4.084831 0.450768 -2.535154  
H -4.325335 1.559262 1.625129  
C -1.520045 -1.974400 0.488728  
O -1.041443 -2.138695 1.591099

H -1.252778 -2.644243 -0.368433

H -2.699143 -0.268768 2.194327

Orientation #13

benzaldehyde/meta2/benzaldehyde-tempo-meta2.freq.out

C 4.583876 -1.353880 0.131573

C 5.095737 -0.061860 -0.003673

C 4.221890 1.016194 -0.106575

C 2.835293 0.807943 -0.075386

C 2.326267 -0.494422 0.060640

C 3.202673 -1.567871 0.163603

H 5.268345 -2.202377 0.212333

H 4.607360 2.035299 -0.212908

C -1.934821 -0.084009 1.336409

C -2.448604 1.335731 1.088496

C -3.285303 1.459866 -0.168523

C -2.441257 1.065405 -1.363327

C -1.924602 -0.372922 -1.293310

H -3.010036 1.654431 1.981592

H -4.193292 0.835004 -0.102314

H -3.647228 2.492723 -0.283651

H -2.997247 1.180850 -2.307802

H -1.575855 1.745078 -1.423592

H -1.582389 2.011908 1.004199  
C -3.047301 -1.006577 1.838781  
H -2.687425 -2.044217 1.865710  
H -3.350924 -0.720706 2.856237  
H -3.943379 -0.971928 1.203925  
C -0.800873 -0.051357 2.352165  
H -1.154219 0.404292 3.287892  
H -0.433682 -1.061270 2.570587  
H 0.037662 0.548305 1.972511  
C -3.032008 -1.385622 -1.593223  
H -3.328031 -1.326935 -2.650601  
H -2.670687 -2.403674 -1.393050  
H -3.933408 -1.217802 -0.987644  
C -0.781831 -0.557711 -2.282896  
H -0.408957 -1.588957 -2.271822  
H -1.128373 -0.319878 -3.298503  
H 0.051465 0.115085 -2.037691  
N -1.381159 -0.660213 0.071061  
O -0.711941 -1.734890 0.191449  
H 6.175607 0.100525 -0.027924  
H 2.804458 -2.579652 0.269153  
C 1.931078 1.961937 -0.188676  
O 0.719772 1.907604 -0.178299

H 2.458272 2.949815 -0.291338

H 1.246134 -0.661215 0.085599

Orientation #14

benzaldehyde/ald/benzaldehyde-tempo-ald.freq.out

C -4.819217 -1.150293 -0.041915

C -3.534492 -1.694833 -0.050969

C -2.424577 -0.853778 -0.015281

C -2.605845 0.536458 0.029890

C -3.899808 1.079179 0.038080

C -5.002817 0.236073 0.002276

H -5.689311 -1.811041 -0.069866

H -1.408223 -1.267018 -0.023573

C 1.941079 -0.172394 -1.332868

C 2.225662 1.324081 -1.181677

C 3.017704 1.663622 0.065422

C 2.247730 1.209874 1.289569

C 1.964962 -0.294408 1.306991

H 2.741642 1.666411 -2.093184

H 4.016613 1.194893 0.034791

H 3.202190 2.746939 0.114003

H 2.779833 1.467366 2.219559

H 1.289535 1.757219 1.328485



H 1.267546 1.872264 -1.153227  
C 3.193783 -0.947075 -1.748929  
H 3.003617 -2.027344 -1.686074  
H 3.459973 -0.706785 -2.788282  
H 4.066823 -0.715461 -1.124479  
C 0.850753 -0.395536 -2.372504  
H 1.160882 0.042022 -3.331571  
H 0.655683 -1.463963 -2.521377  
H -0.093455 0.082413 -2.074477  
C 3.224464 -1.102851 1.625694  
H 3.512503 -0.957324 2.676827  
H 3.031386 -2.173131 1.468804  
H 4.084572 -0.815135 1.006472  
C 0.893802 -0.613453 2.341069  
H 0.699711 -1.691084 2.393032  
H 1.222144 -0.267033 3.330766  
H -0.054612 -0.109596 2.106758  
N 1.439993 -0.726397 -0.030955  
O 0.902684 -1.876918 -0.079115  
H -3.398534 -2.777850 -0.086052  
H -6.013160 0.651774 0.008412  
C -1.422745 1.411239 0.068028  
O -1.435281 2.621824 0.105717

H -0.450959 0.845405 0.057840  
H -4.008214 2.166154 0.073020

Orientation #15

benzaldehyde/meta/benzaldehyde-tempo-meta.freq.out

C -2.339612 1.931636 -0.331472  
C -1.893272 0.680944 -0.762966  
C -2.721145 -0.428251 -0.602047  
C -3.983259 -0.294459 -0.009598  
C -4.419236 0.966592 0.423774  
C -3.599030 2.075517 0.260617  
H -1.698145 2.807360 -0.461193  
H -2.392806 -1.416559 -0.940751  
C 2.563235 1.167085 0.117398  
C 2.951753 0.850818 1.562804  
C 3.551733 -0.529066 1.737632  
C 2.539644 -1.567207 1.298896  
C 2.120546 -1.428281 -0.165755  
H 3.637243 1.639271 1.912181  
H 4.487906 -0.625793 1.161578  
H 3.834722 -0.691963 2.788188  
H 2.916137 -2.591351 1.450461  
H 1.641706 -1.477198 1.934422

H 2.051553 0.928802 2.196729  
C 3.792526 1.464205 -0.742534  
H 3.498417 1.545222 -1.797696  
H 4.251063 2.415936 -0.438480  
H 4.562585 0.684930 -0.661522  
C 1.615682 2.358565 0.086135  
H 2.094676 3.229165 0.555323  
H 1.343306 2.620850 -0.943411  
H 0.691969 2.136841 0.639486  
C 3.213802 -1.925155 -1.112775  
H 3.323367 -3.015958 -1.031373  
H 2.946750 -1.682423 -2.150166  
H 4.193804 -1.477218 -0.898571  
C 0.836025 -2.207996 -0.411651  
H 0.527996 -2.141503 -1.462222  
H 0.985900 -3.265991 -0.155415  
H 0.018415 -1.817914 0.211216  
N 1.831140 0.006846 -0.484722  
O 1.276888 0.224098 -1.607628  
H -0.904981 0.573665 -1.221220  
H -3.935909 3.060365 0.592844  
C -4.848902 -1.476338 0.157353  
O -5.948151 -1.465377 0.660887

H -4.398529 -2.431442 -0.231240

H -5.407963 1.043577 0.882942

Orientation #16

benzaldehyde/ortho2/benzaldehyde-tempo-ortho2.freq.out

C 3.070878 -2.303412 -0.022540

C 4.119830 -1.766575 0.726851

C 4.291932 -0.386365 0.779685

C 3.417081 0.461280 0.086203

C 2.367261 -0.086242 -0.666405

C 2.195613 -1.464179 -0.718357

H 2.934936 -3.387260 -0.065094

H 5.108934 0.050231 1.363221

C -2.300914 -1.250965 -0.054797

C -2.873113 -1.064546 1.351696

C -3.449382 0.316047 1.589147

C -2.361232 1.350420 1.388230

C -1.749642 1.332706 -0.014161

H -3.623910 -1.852622 1.522942

H -4.300125 0.506060 0.912526

H -3.861868 0.387647 2.606704

H -2.729343 2.369583 1.586731

H -1.558571 1.169495 2.124087

H -2.069153 -1.245677 2.086177  
C -3.409941 -1.390964 -1.099400  
H -2.976042 -1.362577 -2.108279  
H -3.930897 -2.351436 -0.976487  
H -4.163965 -0.595582 -1.029332  
C -1.416862 -2.490161 -0.090044  
H -1.989801 -3.363993 0.250686  
H -1.052571 -2.689239 -1.105028  
H -0.545873 -2.372003 0.570084  
C -2.696339 1.942014 -1.049601  
H -2.782932 3.026740 -0.893208  
H -2.299899 1.773253 -2.060087  
H -3.709281 1.519584 -1.003277  
C -0.438429 2.104505 -0.010185  
H -0.003128 2.177964 -1.013394  
H -0.607391 3.124619 0.361597  
H 0.302143 1.625141 0.645103  
N -1.440548 -0.078802 -0.416069  
O -0.716066 -0.220960 -1.450399  
H 4.801187 -2.427051 1.267938  
H 1.368415 -1.875107 -1.300602  
C 3.602856 1.921651 0.159973  
O 2.888226 2.743237 -0.366783

H 4.492911 2.238126 0.772088  
H 1.685205 0.576217 -1.202923

Orientation #17

benzaldehyde/para/benzaldehyde-tempo-para.freq.out

C -1.821175 -0.331722 -1.008812  
C -2.304024 0.977987 -0.979974  
C -3.558104 1.243018 -0.436382  
C -4.336425 0.199922 0.082047  
C -3.848554 -1.115081 0.048816  
C -2.597251 -1.376670 -0.495139  
H -0.831111 -0.525784 -1.430995  
H -3.949495 2.265171 -0.408356  
C 2.394123 1.338379 0.098150  
C 2.757744 1.178562 1.575312  
C 3.582176 -0.059606 1.861732  
C 2.795620 -1.285976 1.447085  
C 2.429723 -1.302836 -0.038441  
H 3.275140 2.095022 1.900966  
H 4.549563 -0.017260 1.332617  
H 3.834175 -0.111713 2.931350  
H 3.342385 -2.214954 1.674490  
H 1.865831 -1.328034 2.040375

H 1.826200 1.129801 2.165378  
C 3.596935 1.791028 -0.731278  
H 3.349353 1.748818 -1.800665  
H 3.864255 2.827616 -0.481048  
H 4.487235 1.170451 -0.561499  
C 1.264552 2.348250 -0.050541  
H 1.561452 3.307323 0.396220  
H 1.020358 2.515246 -1.106300  
H 0.355840 1.998629 0.459655  
C 3.639488 -1.635861 -0.912877  
H 3.938396 -2.683876 -0.768372  
H 3.384174 -1.494249 -1.971833  
H 4.512234 -1.009138 -0.684828  
C 1.326906 -2.323680 -0.283486  
H 1.065667 -2.380136 -1.347391  
H 1.659894 -3.317340 0.047028  
H 0.420479 -2.062975 0.281039  
N 1.895920 0.035864 -0.450240  
O 1.352301 0.090272 -1.597781  
H -1.692799 1.787032 -1.386690  
H -2.216591 -2.401008 -0.525349  
C -5.662289 0.486142 0.659323  
O -6.405254 -0.340807 1.135020

H -5.949754 1.573621 0.627320

H -4.477366 -1.910165 0.457441

Orientation #18

nitrobenzene/tshape/nitrobenzene-tempo-tshape.freq.out

C -2.930927 -2.467273 0.000046

C -1.685357 -1.837405 0.000007

C -1.615523 -0.446728 -0.000064

C -2.796399 0.289479 -0.000066

C -4.048730 -0.322006 0.000000

C -4.106893 -1.712323 0.000040

H -2.987300 -3.558061 0.000079

H -0.754967 -2.412491 0.000023

H -0.653973 0.068302 -0.000165

H -4.945698 0.297074 0.000015

H -5.078026 -2.211421 0.000063

C 2.037971 -0.098693 -1.318630

C 1.695954 1.390870 -1.239067

C 2.241459 2.072870 -0.000172

C 1.695789 1.391110 1.238778

C 2.037782 -0.098435 1.318707

H 2.061230 1.875674 -2.158654

H 3.345376 2.061248 -0.000112



H 1.956603 3.135417 -0.000270  
H 2.060909 1.876126 2.158316  
H 0.597997 1.508034 1.250157  
H 0.598170 1.507808 -1.250621  
C 3.510843 -0.327425 -1.665895  
H 3.766281 -1.388649 -1.539568  
H 3.697287 -0.054826 -2.714508  
H 4.195477 0.267001 -1.047447  
C 1.172825 -0.776416 -2.372117  
H 1.330246 -0.288938 -3.344106  
H 1.422129 -1.839453 -2.469016  
H 0.104588 -0.699130 -2.126901  
C 3.510581 -0.327118 1.666304  
H 3.696819 -0.054298 2.714896  
H 3.766034 -1.388370 1.540247  
H 4.195324 0.267184 1.047858  
C 1.172445 -0.775897 2.372208  
H 1.421719 -1.838917 2.469393  
H 1.329707 -0.288201 3.344111  
H 0.104254 -0.698662 2.126783  
N 1.736846 -0.749817 0.000088  
O 1.664149 -2.019048 0.000217  
N -2.719649 1.760279 -0.000136

O -1.608051 2.270597 -0.000428

O -3.768783 2.380534 0.000122

Orientation #19

nitrobenzene/bite-orthometa/nitrobenzene-tempo-bite-orthometa.freq.out

C -4.372294 1.751384 -0.000068

C -2.984879 1.899252 -0.000316

C -2.155733 0.780231 -0.000342

C -2.751072 -0.479926 -0.000093

C -4.134991 -0.652073 0.000158

C -4.945955 0.477646 0.000165

H -5.014172 2.635261 -0.000040

H -2.533416 2.893376 -0.000477

H -1.069572 0.894544 -0.000556

H -4.546821 -1.661083 0.000350

H -6.031876 0.364382 0.000357

C 2.072814 0.251102 1.322171

C 2.499815 -1.215582 1.235003

C 3.319671 -1.531069 0.000394

C 2.500223 -1.215784 -1.234530

C 2.073144 0.250853 -1.322078

H 3.046859 -1.465709 2.158297

H 4.266927 -0.963942 0.000515

H 3.612537 -2.591677 0.000521  
H 3.047575 -1.466031 -2.157608  
H 1.594710 -1.844651 -1.228972  
H 1.594260 -1.844407 1.229249  
C 3.241827 1.157863 1.713628  
H 2.945218 2.211668 1.620483  
H 3.533906 0.974229 2.757605  
H 4.130920 0.996416 1.088981  
C 0.950902 0.401918 2.340670  
H 1.289270 0.035038 3.319781  
H 0.646411 1.450098 2.445592  
H 0.073233 -0.186547 2.039725  
C 3.242195 1.157593 -1.713455  
H 3.534516 0.973766 -2.757330  
H 2.945542 2.211410 -1.620565  
H 4.131143 0.996282 -1.088567  
C 0.951476 0.401396 -2.340893  
H 0.647055 1.449557 -2.446220  
H 1.290071 0.034213 -3.319811  
H 0.073711 -0.186936 -2.039980  
N 1.540944 0.709048 -0.000064  
O 0.910296 1.813502 -0.000267  
N -1.897774 -1.679124 -0.000064

O -0.684426 -1.511341 -0.000181

O -2.445003 -2.768104 0.000081

Orientation #20

nitrobenzene/ortho/nitrobenzene-tempo-orthoCH.freq.out

C -3.252988 -2.101629 0.734961

C -3.085835 -1.791026 -0.617072

C -2.694026 -0.512308 -0.998427

C -2.464790 0.437945 -0.007126

C -2.619420 0.149049 1.345364

C -3.020931 -1.133461 1.712637

H -3.565315 -3.106555 1.027774

H -3.260813 -2.553327 -1.379360

H -2.538762 -0.234252 -2.040500

H -2.428650 0.928814 2.083149

H -3.155461 -1.376798 2.768617

C 1.657339 -1.392437 -0.460388

C 3.157906 -1.571367 -0.219356

C 3.712855 -0.651594 0.849629

C 3.463939 0.790369 0.454331

C 1.980883 1.122726 0.278427

H 3.343426 -2.630379 0.022099

H 3.254385 -0.871411 1.829104

H 4.790215 -0.831085 0.983239  
H 3.887047 1.489906 1.192707  
H 3.987252 0.996494 -0.495603  
H 3.690767 -1.377701 -1.166535  
C 0.822778 -2.007145 0.665231  
H -0.229774 -1.709772 0.552560  
H 0.873681 -3.104908 0.621983  
H 1.159830 -1.700258 1.664444  
C 1.264620 -2.035999 -1.783470  
H 1.568895 -3.092091 -1.784868  
H 0.181523 -1.984020 -1.946075  
H 1.757714 -1.535468 -2.627974  
C 1.260764 1.205298 1.625805  
H 1.600838 2.092712 2.178800  
H 0.179029 1.308297 1.466871  
H 1.441581 0.329387 2.263310  
C 1.820826 2.444888 -0.459933  
H 0.767390 2.739931 -0.536181  
H 2.362664 3.233750 0.080206  
H 2.232743 2.380500 -1.476379  
N 1.333333 0.065046 -0.561063  
O 0.198145 0.350966 -1.050468  
N -2.054218 1.793602 -0.406017

O -1.676004 2.548610 0.479803  
O -2.131833 2.085156 -1.583774

Orientation #21

nitrobenzene/para/nitrobenzene-tempo-paraCH.freq.out

C 1.806927 1.056703 -0.796680  
C 1.903816 0.368550 0.415190  
C 3.134497 -0.115143 0.848255  
C 4.255242 0.102832 0.049371  
C 4.181271 0.787180 -1.161497  
C 2.942773 1.264981 -1.581163  
H 0.827781 1.422940 -1.113761  
H 1.000483 0.219960 1.010495  
H 3.250072 -0.655611 1.787751  
H 5.089105 0.930909 -1.747209  
H 2.865200 1.804267 -2.527634  
C -3.561773 0.951924 0.482864  
C -4.810798 0.369723 -0.181742  
C -4.797624 -1.142507 -0.270748  
C -3.593583 -1.584410 -1.077119  
C -2.259740 -1.142111 -0.471947  
H -5.692716 0.735751 0.367693  
H -4.780744 -1.593580 0.736106

H -5.724531 -1.505268 -0.739274  
H -3.567319 -2.678857 -1.199641  
H -3.674326 -1.166788 -2.095730  
H -4.894441 0.785211 -1.200970  
C -3.578459 0.737747 1.997409  
H -2.608273 1.023902 2.425921  
H -4.354954 1.362227 2.461709  
H -3.782710 -0.304435 2.277389  
C -3.461081 2.441033 0.182661  
H -4.371607 2.950810 0.526762  
H -2.596960 2.890249 0.684990  
H -3.356759 2.619153 -0.896500  
C -1.901602 -1.972156 0.762109  
H -1.657026 -3.002875 0.468388  
H -1.021855 -1.544447 1.262481  
H -2.719097 -2.022689 1.493622  
C -1.151951 -1.274712 -1.508096  
H -0.169449 -1.043281 -1.079541  
H -1.126909 -2.303540 -1.893196  
H -1.321077 -0.596699 -2.356413  
N -2.334993 0.302083 -0.081634  
O -1.230973 0.868571 0.190851  
N 5.562361 -0.407073 0.500031

O 5.595999 -1.014738 1.557726  
O 6.528606 -0.190108 -0.213004

Orientation #22

nitrobenzene/stackedtshape/nitrobenzene-tempo-stackedtshape.freq.out

C -2.531439 2.652338 -0.024409  
C -1.764271 1.762649 0.728591  
C -2.093046 0.410076 0.761710  
C -3.193204 -0.025156 0.027908  
C -3.972894 0.846278 -0.731065  
C -3.633084 2.195141 -0.752213  
H -2.269741 3.712996 -0.046459  
H -0.893943 2.103378 1.291866  
H -1.496584 -0.295398 1.339057  
H -4.823726 0.452826 -1.286954  
H -4.231034 2.894308 -1.340461  
C 1.825759 -1.391086 0.000472  
C 2.430225 -1.475806 -1.402469  
C 3.626606 -0.568376 -1.601280  
C 3.207250 0.867716 -1.364180  
C 2.657616 1.116515 0.041724  
H 2.683394 -2.529292 -1.601223  
H 4.449393 -0.852098 -0.922935



H 4.030477 -0.685034 -2.618007  
H 4.041326 1.567295 -1.534036  
H 2.429610 1.137246 -2.099855  
H 1.652504 -1.206904 -2.138196  
C 2.702375 -2.099248 1.034768  
H 2.330536 -1.886976 2.046386  
H 2.668686 -3.187045 0.879745  
H 3.755385 -1.790964 0.984137  
C 0.438501 -2.015928 0.000830  
H 0.493967 -3.045607 -0.378633  
H 0.005725 -2.049518 1.007205  
H -0.249792 -1.454365 -0.646898  
C 3.773531 1.132519 1.087873  
H 4.397543 2.029519 0.965934  
H 3.338531 1.151798 2.096452  
H 4.435153 0.258839 1.017332  
C 1.915784 2.445862 0.075274  
H 1.573436 2.684662 1.089407  
H 2.582715 3.250885 -0.263653  
H 1.039588 2.425179 -0.588345  
N 1.672314 0.046100 0.401113  
O 0.963388 0.267621 1.432580  
N -3.545408 -1.456493 0.047016

O -2.838813 -2.203729 0.704312  
O -4.520794 -1.805634 -0.598139

Orientation #23

nitrobenzene/meta/nitrobenzene-tempo-metaCH.freq.out

C 2.562620 2.429222 -0.205845  
C 1.840552 1.237120 -0.301145  
C 2.502020 0.018527 -0.168616  
C 3.876214 0.019103 0.058451  
C 4.610854 1.198180 0.156150  
C 3.940191 2.410394 0.021058  
H 2.042212 3.383743 -0.310806  
H 0.759701 1.258437 -0.477047  
H 1.978092 -0.935735 -0.236931  
H 5.684675 1.143722 0.334362  
H 4.497309 3.346759 0.093557  
C -3.613823 0.808862 0.235120  
C -4.669840 -0.296086 0.169285  
C -4.136966 -1.663047 0.546734  
C -3.014344 -2.038637 -0.398663  
C -1.841607 -1.056087 -0.374424  
H -5.515393 0.000674 0.810087  
H -3.787302 -1.671594 1.593211

H -4.940993 -2.412490 0.500318  
H -2.621164 -3.044558 -0.181885  
H -3.415230 -2.084394 -1.426027  
H -5.069476 -0.341631 -0.858651  
C -3.290059 1.192325 1.680181  
H -2.427091 1.871763 1.701521  
H -4.145051 1.709919 2.138077  
H -3.055844 0.322565 2.308649  
C -4.101797 2.038110 -0.519020  
H -5.058352 2.376724 -0.097375  
H -3.378202 2.858291 -0.451269  
H -4.257637 1.811191 -1.582661  
C -1.000265 -1.222714 0.892752  
H -0.442786 -2.170047 0.860534  
H -0.273977 -0.402421 0.978677  
H -1.608420 -1.230310 1.807253  
C -0.967745 -1.270516 -1.602874  
H -0.097144 -0.604516 -1.601196  
H -0.610620 -2.309472 -1.628769  
H -1.531960 -1.079259 -2.525940  
N -2.353572 0.350494 -0.433184  
O -1.492300 1.254504 -0.668789  
N 4.575613 -1.270543 0.200999

0 5.778184 -1.240323 0.404156

0 3.907159 -2.287373 0.107476